Photodegradation of synthetic organic dyes in water using tungsten disulfide and bismuth-based metal halide perovskite composite materials

By

Tshegofatso Mabilane

2024

A dissertation submitted to the Faculty of Science, University of the Witwatersrand, Johannesburg, in partial fulfilment of the requirements for the degree of Master of Science in Chemistry

Supervisors: Dr Siziwe S. Gqoba
Dr Kalenga P. Mubiayi
Prof Nosipho Moloto

DECLARATION

I declare that this dissertation is my independent work. It is being submitted for the Degree of Master of Science at the School of Chemistry, University of the Witwatersrand, Johannesburg. The work presented in this dissertation has never been submitted for any degree or examination in any other University.

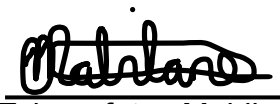

Tshegofatso Mabilane (56484)

Signed on 27/06/2024

Supervisor

(Dr. S.S. Gqoba)

Co-supervisor

(Dr. P. Mubiayi)

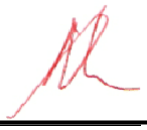

Co-supervisor

(Prof. N. Moloto)

ABSTRACT

Synthetic organic dyes (SODs) are extensively used in the textile, paint, and printing industries. However, these dyes pose significant threats to the ecosystem. The degradation of SODs through photocatalysis has garnered considerable attention from researchers as a promising approach for wastewater treatment and environmental remediation. This research project aims to investigate the photodegradation of methyl red and rhodamine B as anionic and cationic types of SODs respectively, using a metal halide perovskite (MHP), $Cs_3Bi_2Br_9$. Then, the photodegradation efficacy of $Cs_3Bi_2Br_9$ was compared to that of a heterostructure, composed of $Cs_3Bi_2Br_9$ and a transition metal dichalcogenide (TMDC), WS_2. $Cs_3Bi_2Br_9$ and WS_2 were synthesized using hot-injection, and colloidal synthesis methods, respectively. The synthesized materials were characterized using transmission electron microscopy (TEM), scanning electron microscopy (SEM), energy dispersive X-ray spectroscopy (EDS), elemental mapping, ultraviolet-visible (UV-Vis) spectroscopy, Brunauer-Emmett-Teller (BET) analysis, zeta potential, powder X-ray diffraction (PXRD), and thermogravimetric analysis (TGA).

Degradation experiments were conducted under controlled conditions, including varying catalyst loading (0.8 mg/mL, 1.6 mg/mL, and 2.4 mg/mL), initial dye concentrations (20, 40, and 60 ppm), and pH levels (pH 2, 7, and 12) to find the optimum dye photodegradation conditions. Photolysis studies were also carried out to assess the photolytic stability of the dyes. The oxidizing effect of adding 0.3519 M hydrogen peroxide to the photolysis and heterogeneous photocatalytic reactions was also investigated. When compared to $Cs_3Bi_2Br_9$, the heterostructure, $Cs_3Bi_2Br_9/WS_2$, offered the advantages of improved dye degradation efficiency and stability due to enhanced charge separation. This is because WS_2 is a layered material that has pockets that increase catalytic active sites thus making it a good co-catalyst. This project's findings shed light on the photocatalytic degradation of anionic and cationic dyes using a MHP and a heterostructure comprised of a MHP and TMDC. These findings contribute to the development of efficient and environmentally friendly approaches for SOD removal in wastewater.

Keywords: Metal halide perovskite, transition metal dichalcogenide, photocatalysis, photodegradation, synthetic organic dyes, heterostructure

DEDICATION

To my mother (Boitumelo Gaofetoge), my father (Fani Mabilane), and my sisters (Kagiso Tlou and Kgomotso Mabilane) thank you for your unwavering support, love, sacrifices, and prayers. I could not have made it without you.

To my daughter (Khumo Mabilane), my nieces (Masego Tlou and Thoriso Mabilane), and my nephew (Tshiamo Tlou), when doors of opportunity open for you, work hard and take full advantage of every opportunity you get. There are no limits to what you can achieve!

In loving memory of:

My beloved grandmother, Hetti ‘Mamiye’ Gaofetoge, and my nephew, Lereko Tlou.

ACKNOWLEDGEMENTS

I would like to express my gratitude to my amazing supervisors, Dr. S.S. Gqoba, Prof. N. Moloto, and Dr. P.K. Mubiayi. Thank you so much for believing in me, taking me under your wings, and providing me with this wonderful opportunity to work with you on this project. It has been an absolute pleasure. You have been great mentors, and your financial support is greatly appreciated. I look forward to working with you on many more projects in the future.

I would also like to thank the NanoWEBS and CATMAT groups for their support and MMU for their kind assistance with the characterization techniques.

My thanks also go to Petra Dinham and Zaynab Cader for their assistance with SEM and EDS analysis, and to Eric Morifi and his team for their help with mass spectroscopy analysis. I am also grateful to Prof. Neil Coville and his team for their assistance with BET and TGA analysis.

I would like to extend my appreciation to Ms. Namhla Maqubela and Dr. Biyela for assisting with the COD analysis.

A big thank you to Mintek and Dr. Machogo for assisting with the zeta potential analysis.

I want to thank my dear friends, including Thabiso Mokhele, Kgaugelo Mabape, Phumlile Magwirokona, Siyabonga Nkabinde, and many others. Thank you for always being there to encourage me and for cheering me on along this journey.

Finally, gratitude goes to the National Research Foundation for the financial support.

To God Almighty. He has been so faithful. Without Him, I could have never made it to the end! John 5:15 “I am the vine; you are the branches. If you remain in me and I in you, you will bear much fruit; apart from me you can do nothing.”

PRESENTATIONS

1. MSc Poster Presentation SACI Central YCS 2022: 19/08/2022

2. MSc poster presentations School of Chemistry Wits 2022: 28/09/2022

TABLE OF CONTENTS

List of Figures

List of Schemes

List of Tables

List of symbols and abbreviations

AOP - Advanced oxidation process

BET - Brunauer-Emmett-Teller analysis

CB - Conduction band

CFLT – Clothing, fashion, leather, and textiles

COD – Chemical oxygen demand

Cs – Cesium

DE - Degradation efficiency

DMSO – Dimethyl sulfoxide

e^- - electron

E_g - Energy gap

FT-IR - Fourier transformer infrared

GDP – Gross domestic profit

h^+ - hole

hrs - Hours

HOMO - Highest occupied molecular orbital

TEM - Transmission electron microscopy

LUMO - Lowest unoccupied molecular orbital

MHP – Metal halide perovskite

MR – Methyl red

NP - Nanoparticle

OA – Oleic Acid

OLA - Oleylamine

Pb - lead

PXRD - Powdered X-ray diffraction

PL - Photoluminescence

RhB – Rhodamine B

ROS – Reactive oxygen species

SC - Semiconductor

SEM - Scanning electron microscopy

SODs – Synthetic organic dyes

TEM - Transmission electron microscope

TMDC - Transition metal dichalcogenide

UPW – Ultrapure water

UV-Vis - Ultraviolet-visible spectrophotometry

VB - Valence band

WHO – World Health Organization

Synopsis

The study aimed to synthesize $Cs_3Bi_2Br_9$ and WS_2 using the hot injection and colloidal synthesis methods respectively. The synthesized materials were used to create a heterostructure, $Cs_3Bi_2Br_9/WS_2$ via ultra-sonication. The materials were used for the photocatalytic degradation of rhodamine B and methyl red. The degradation efficacies of the materials were investigated and compared. Optimization studies were also carried out to determine the optimum dye degradation conditions. The dissertation outline is given below:

Chapter 1: This chapter introduces the study by discussing the background as well as the environmental and health impact of synthetic organic dyes. This chapter also outlines the aims, objectives, research questions, and novelty of the project.

Chapter 2: This literature review chapter provides a foundational background of the origin and chemistry of synthetic organic dyes. The adverse effects of dye pollution on the environment, animals, and humans will be explained in more depth. Existing dye removal methods will be given along with their advantages and limitations. Solutions to alleviate dye pollution will also be discussed.

Chapter 3: This chapter will explain and illustrate the techniques used for synthesis, characterization, dye degradation studies, and data processing.

Chapter 4: The characterization results for the synthesized WS_2, $Cs_3Bi_2Br_9$, and $Cs_3Bi_2Br_9/WS_2$ materials are given and discussed. The characterization techniques used were PXRD, BET, TGA, TEM, SEM/EDX, EDS mapping, Zeta potential, UV-vis, LC-MS, and COD.

Chapter 5: The synthesized WS_2, $Cs_3Bi_2Br_9$, and $Cs_3Bi_2Br_9/WS_2$ materials were used for dye degradation application. The dyes degraded were rhodamine B and methyl red. The effect of adding H_2O_2 will be discussed. The results from the quantitative and qualitative analyses are discussed. The kinetics and adsorption isotherms were determined. The physical and optical changes of the materials after degradation of the dyes were investigated.

Chapter 6: The conclusion and recommendations for future work are given.

CHAPTER 1: INTRODUCTION

1.1 General background:

Although clean and safe water is an essential source of life, millions of people around the world live without adequate access to clean and safe drinking water. Approximately 70% of the Earth is covered in water, and only 1% of the freshwater is easily accessible for humans and all other living creatures (Mullen, 2019). The 2022 World Health Organization (WHO) statistics state that 10% of people do not have access to sanitary water. Consequently, 368 million people get water from unsafe streams and wells, and 122 million people survive on surface water, including rivers, lakes, streams, and ponds (World Health Organization (WHO) and United Nations Children's Fund (UNICEF), 2021; World Health Organization (WHO), 2022). The Sustainable Development Goal (SDG) target is to ensure that safe drinking water is accessible to the whole world population by 2030, which means that the current rates of water treatment, sanitation, and basic hygiene services need to increase four-fold (Velusamy et al., 2021). However, progress towards achieving this target may be impeded by various challenges including contamination of surface water with dangerous chemicals from urban, agricultural, and industrial waste (Mokif, 2019; World Health Organization (WHO) and United Nations Children's Fund (UNICEF), 2021).

Synthetic organic dyes (SODS), also known as colouring agents, are organic compounds fixed to various materials such as paper, plastic, and fabric to give them colour. Industries prefer to use SODs over natural dyes because they are cheaper, brighter, easily available, stable, long-lasting, and offer a wide variety of colours. They are used in various industries including pharmaceutical, paint, cosmetics, plastic, leather, ceramics, printer inks, hair dyes, and textiles (Shah, 2014; Forgacs, Cserháti and Oros, 2004; Patel and Shah, 2014; Liu et al., 2015; Rani et al., 2016; Piaskowski, Świderska-Dąbrowska and Zarzycki, 2018; Bresolin, Hammouda and Sillanpää, 2019; Mokif, 2019; Tkaczyk, Mitrowska and Posyniak, 2020). With textiles being ranked second, after food, among basic human needs, the fashion industry is one of the biggest industries that utilize SODs to produce clothing with attractive colours and prints. Over 10,000 textile dye compounds exist, and they are classified according to their solubility in water, molecular structure, chemical properties, and chromophores.

The common textile dyes are azo, acidic, basic, and direct dyes (Crini, 2006; Singh and Arora, 2011; Bhattacharya, Goyal and Gupta, 2017; Piaskowski, Świderska-Dąbrowska and Zarzycki, 2018; Bresolin, Hammouda and Sillanpää, 2019; Tkaczyk, Mitrowska and Posyniak, 2020; Velusamy *et al.*, 2021). In this study of interest were methyl blue and Rhodamine blue dyes. Rhodamine B (cationic dye) and methyl red (anionic dye) are both commonly used SODs in the textile industry (Muthuraman and Teng, 2009; Kusrini *et al.*, 2018) to dye various textile materials (Ridjal et al., 2022; Ikram et al., 2022).

The annual production of commercial SODs exceeds 700,000 tons globally, and the textile industry generates 54% of the dye effluents found in wastewater around the world (Shah, 2014; Crini, 2006; Rani et al., 2016; Katheresan, Kansedo, and Lau, 2018; Nidheesh, Zhou and Oturan, 2018; Bresolin, Hammouda and Sillanpää, 2019; Tkaczyk, Mitrowska and Posyniak, 2020; Velusamy et al., 2021). However, these dyes pose negative environmental effects when released into the environment through textile effluents. They are harmful to humans, animals, and aquatic life. Moreover, their elimination from wastewater is challenging, leading to their persistence in the environment and subsequent contamination of the food chain (BM and M, 2015a; Al-Buriahi *et al.*, 2022). Synthetic dyes are made up of heterocyclic and aromatic compounds, which have toxic, carcinogenic, and mutagenic effects that can cause gene mutations, cancer, asthma, and contact allergies in humans and aquatic life (Shakir *et al.*, 2010; Liu *et al.*, 2015; Rani *et al.*, 2016; Tkaczyk, Mitrowska and Posyniak, 2020).

SODs are resistant to conventional chemical and biological treatments because of their complex aromatic chemical structures (Piaskowski, Świderska-Dąbrowska and Zarzycki, 2018; Bresolin, Hammouda and Sillanpää, 2019; Tkaczyk, Mitrowska and Posyniak, 2020). Consequently, SODs cause serious long-term pollution in water (Piaskowski, Świderska-Dąbrowska and Zarzycki, 2018). Additionally, conventional methods have several limitations including high operating costs, time-consuming processes, and production of non-biodegradable secondary products (Rani *et al.*, 2016; Bresolin, Hammouda and Sillanpää, 2019). Therefore, it is crucial to develop water purification solutions that will effectively mitigate water pollution and help achieve the 2030 SDG target.

Photocatalysis has emerged as an attractive and promising advanced oxidation process (AOP) method for the decolourization through degradation of synthetic organic dyes among various dye removal technologies that exist. This method performs better than the conventional method due to its cost-effectiveness, environmental friendliness, ability to operate at ambient temperatures, and complete degradation of dyes without secondary pollution (Rani *et al.*, 2016; Velusamy *et al.*, 2021). In AOP, a photocatalyst is added to dye-contaminated water, which is then irradiated with light (artificial or natural) to trigger the generation of photogenerated reactive oxygen species (ROS) through light absorption. Solar photocatalysis uses sunlight as a light source which is cost-effective, environmentally friendly, and globally applicable. This makes it a great solution for developing countries or areas that have limited access to electricity such as South Africa (World Health Organization (WHO) and the United Nations Children's Fund (UNICEF), 2021). The ROS, such as superoxide anion radical ($\bullet O_2^-$), hydroxyl radical ($\bullet OH$), hydrogen peroxide (H_2O_2), and singlet oxygen ($^1O_2$), facilitate the chemical reactions that degrade SODs to simple and less harmful organic compounds such as CO_2, H_2O, and mineral ions (Rani *et al.*, 2016; Bresolin, Hammouda and Sillanpää, 2019; Tkaczyk, Mitrowska and Posyniak, 2020). Photodegradation can remove various pollutants such as organic materials, organic acids, micro-organisms, inorganic molecules, metals, and SODs (World Health Organization (WHO) and United Nations Children's Fund (UNICEF), 2021).

Photocatalysts are semiconducting materials such as TiO_2, CdS, MgO, and metal halide perovskites. The important characteristics of a good photocatalyst are low toxicity, simple synthesis, reusability, selectivity, stability, photon absorption in the visible light region, large surface area, and surface transfer of photo-induced charge carriers (Li and Wu, 2017; Koe et al., 2020; Sharma and Soni, 2021). In recent years, lead (Pb)-free cesium bismuth halide perovskites ($Cs_3Bi_2X_9$ where X represents halides Cl, Br, or I), have been investigated for their application in photocatalysis due to their impressive properties such as wide optical absorption, quantum-size effect, tuneable bandgap, low toxicity, and low cost (Q. Zhang *et al.*, 2020b; Li *et al.*, 2021). However, there are limitations associated with these MHPs such as charge recombination and stability which can be improved by integrating the MHPs with other materials (Rani *et al.*, 2016; Li *et al.*, 2021). Transition metal dichalcogenides (TMDCs) such as WS_2, are suitable candidates for co-catalysts as they have superior carrier

transport, optoelectronic properties, thermal conductivity, and structural properties (Q. Zhang *et al.*, 2020b). Integrating the materials improves photocatalytic performance by reducing intrinsic defects through passivation of the MHP by the co-catalyst, boosts charge separation via an electric field between the surfaces of the MHP and co-catalyst, and modifying the MHP's redox ability, thus enabling it to initiate some advanced reactions (Li *et al.*, 2021).

1.1.1 Problem statement:

Dye effluents from industries such as the textile, food, paint, and paper industries endanger the environment and health of humans. Even at a small concentration of 1 mg/L, SODs are visible in wastewater, reducing light penetration and oxygen solubility, which negatively impact aquatic plants and species. Dye concentrations in textile wastewater range between 10-200 mg/L (Patel and Shah, 2014; Bhattacharya, Goyal and Gupta, 2017). Rhodamine B (a basic and cationic dye) and methyl red (an anionic azo dye) fall under the classes of dyes that are commonly used in the textile industry (Shakir *et al.*, 2010; Bhattacharya, Goyal and Gupta, 2017). Azo dyes such as methyl red can be extremely resistant to conventional treatment due to the azo groups (-N=N-) which are responsible for the colour (Patel and Shah, 2014; Bhattacharya, Goyal and Gupta, 2017; Bresolin, Hammouda and Sillanpää, 2019). Reactive, acidic, direct, and basic SODs are hard to eliminate from water because of their high-water solubility. SODs are stable in nature and persist throughout the entire food chain (Lellis *et al.*, 2019a). The insistent nature of these dyes is serious and has the potential to introduce emerging diseases and recalcitrant non-biodegradable wastewater pollutants Du et al., 2022). The negative effects on water bodies include high chemical oxygen demand (COD), aesthetic damage that reduces light penetration, reduced photosynthesis, imbalance in ecological function, and less dissolved oxygen (Shah, 2014; Lellis *et al.*, 2019a). For developing countries, water treatment methods can be very costly or energy-intensive which is undesirable. Therefore new, and innovative methods need to be developed to combat these problems. Metal halide perovskites (MHPs) have been used to degrade synthetic dyes in water. However, MHPs have poor stability in water and light. To improve the stability and photodegradation performance of MHPs, researchers have explored strategies to combat this problem such as co-catalysts to enhance stability and doping to enhance the electronic properties of the materials.

1.1.2 Hypothesis:

The superior optical and photoelectronic properties of metal halide perovskites (MHPs) and transition metal dichalcogenides (TMDCs) make them suitable photocatalysts for an environmentally friendly solution to remove SODs from water via the photocatalysis method (Q. Zhang *et al.*, 2020b; Wang *et al.*, 2021). $Cs_3Bi_2Br_9$ (MHP) and WS_2 (TMDC) can be combined into a heterostructure, which will result in a synergistic effect that degrades SODs more effectively. This method will not only encourage industries to remove dyes from the water before releasing waste-containing dyes into waterbodies but also to reuse the water. This will help reduce the current high water usage in the textile industry and improve the quality of water.

1.1.3 Aim and Objectives:

1.1.3.1 Aim

This project aims to compare the efficacy of $Cs_3Bi_2Br_9$ versus the $Cs_3Bi_2Br_9/WS_2$ efficacy for removing dyes from water and to determine the optimum degradation conditions.

1.1.3.2 Objectives

The main aim of the study was achieved by accomplishing a set of specific objectives as highlighted below:

- To synthesize a bismuth-based MHP ($Cs_3Bi_2Br_9$) via hot-injection synthesis and WS_2 via colloidal synthesis.
- To make a $Cs_3Bi_2Br_9/WS_2$ composite via ultrasonication.
- To characterize the synthesized materials using powder X-ray diffraction (PXRD), transmission electron microscopy (TEM), energy-dispersive X-ray spectroscopy (EDS), scanning electron microscopy (SEM), zeta potential, ultraviolet-visible (UV-vis) spectroscopy, Brunauer-Emmett-Teller (BET) analysis, and thermal gravimetric analysis (TGA).
- To use the as-synthesized materials for degrading anionic (methyl red) and cationic (rhodamine B) SODs from water via heterogenous photodegradation using a UV light source.
- To optimize the dye photodegradation conditions by varying different parameters namely: catalyst loading, dye concentration, and solution pH.

- To conduct photolysis studies where the dyes will be degraded in the absence of a photocatalyst i.e. the dyes will be degraded using UV light only.
- To determine the effect of adding H_2O_2 by adding it to the heterogenous photocatalysis and photolysis reactions.

1.1.4 Research questions:

- What is the effect of adding WS_2 as a co-catalyst to $Cs_3Bi_2Br_9$?
- What are the optimum photocatalysis conditions (pH, catalyst loading, and dye concentration) for degrading cationic and anionic dyes?
- How are the photocatalysts' optical and structural properties affected after degrading SODs?
- How will the photolysis efficacy compare with the efficacy of heterogenous photocatalysis?
- What are the effects of adding H_2O_2 to the degradation reactions?

1.1.5 Novelty of the study:

- There is little data available in literature on the use of MHP/WS_2 composites for the photodegradation of SODs.
- There is no known data on the use of $Cs_3Bi_2Br_9/WS_2$ for the degradation of anionic and cationic dyes.
- In this research, $Cs_3Bi_2Br_9/WS_2$ will be synthesized and used for degrading methyl red and Rhodamine B. Although a metal-coupled MHP composite has previously been synthesized, the only existing composite of this nature has been synthesized by using Pb-free MHP. Therefore, this study presents the first MHP/WS_2 heterostructure manufactured by coupling MHP with WS_2 in contrast to the literature-reported use of Pb-free onto MHP.

References:

Al-Buriahi, A.K. et al. (2022) ‘Elimination of rhodamine B from textile wastewater using nanoparticle photocatalysts: A review for sustainable approaches’, Chemosphere, 287, p. 132162. Available at: https://doi.org/10.1016/j.chemosphere.2021.132162.

Bhattacharya, A., Goyal, N. and Gupta, A. (2017) ‘Degradation of azo dye methyl red by alkaliphilic, halotolerant Nesterenkonia lacusekhoensis EMLA3: application in alkaline and salt-rich dyeing effluent treatment’, Extremophiles, 21(3), pp. 479–490. Available at: https://doi.org/10.1007/s00792-017-0918-2.

BM, V. and M, V. (2015) ‘Photocatalytic Degradation of Toxic Methyl Red Dye Using Silica Nanoparticles Synthesized from Rice Husk Ash’, Journal of Environmental & Analytical Toxicology, 05(06). Available at: https://doi.org/10.4172/2161-0525.1000336.

Bresolin, B.M., Hammouda, S. Ben and Sillanpää, M. (2019) ‘Methylammonium iodo bismuthate perovskite $(CH_3NH_3)_3Bi_2I_9$ as new effective visible light-responsive photocatalyst for degradation of environment pollutants’, Journal of Photochemistry and Photobiology A: Chemistry, 376, pp. 116–126. Available at: https://doi.org/10.1016/j.jphotochem.2019.03.009.

Crini, G. (2006) ‘Non-conventional low-cost adsorbents for dye removal: A review’, Bioresource Technology, pp. 1061–1085. Available at: https://doi.org/10.1016/j.biortech.2005.05.001.

Du, H. et al. (2022) ‘Adsorption of rhodamine B on polyvinyl chloride, polystyrene, and polyethylene terephthalate microplastics in aqueous environments’, Environmental Technology and Innovation, 27. Available at: https://doi.org/10.1016/j.eti.2022.102495.

Forgacs, E., Cserháti, T. and Oros, G. (2004) ‘Removal of synthetic dyes from wastewaters: a review’, Environment International, 30(7), pp. 953–971. Available at: https://doi.org/10.1016/j.envint.2004.02.001.

Ikram, M. et al. (2022) ‘Biodegradation of Azo Dye Methyl Red by Pseudomonas aeruginosa: Optimization of Process Conditions’, International Journal of Environmental Research and Public Health, 19(16), p. 9962. Available at: https://doi.org/10.3390/ijerph19169962.

Katheresan, V., Kansedo, J. and Lau, S.Y. (2018) ‘Efficiency of various recent wastewater dye removal methods: A review’, Journal of Environmental Chemical Engineering, 6(4), pp. 4676–4697. Available at: https://doi.org/10.1016/j.jece.2018.06.060.

Koe, W.S. et al. (2020) ‘An overview of photocatalytic degradation: photocatalysts, mechanisms, and development of photocatalytic membrane’, Environmental Science and Pollution Research. Springer, pp. 2522–2565. Available at: https://doi.org/10.1007/s11356-019-07193-5.

Kusrini, E. et al. (2018) ‘Textile Dye Removal from Aqueous Solution using Modified Graphite Waste/Lanthanum/Chitosan Composite’, IOP Conference Series: Materials Science and Engineering, 316, p. 012029. Available at: https://doi.org/10.1088/1757-899X/316/1/012029.

Lellis, B. et al. (2019) ‘Effects of textile dyes on health and the environment and bioremediation potential of living organisms’, Biotechnology Research and Innovation, 3(2), pp. 275–290. Available at: https://doi.org/10.1016/j.biori.2019.09.001.

Li, Q. et al. (2021) ‘Boosting Photocatalytic Activity and Stability of Lead-Free Cs3Bi2Br9Perovskite Nanocrystals via in Situ Growth on Monolayer 2D Ti3C2T xMXene for C-H Bond Oxidation’, ACS Applied Materials and Interfaces, 13(23), pp. 27323–27333. Available at: https://doi.org/10.1021/acsami.1c06367.

Li, W. and Wu, H. (2017) ‘Sodium citrate functionalized reusable Fe3O4@TiO2 photocatalyst for water purification’, Chemical Physics Letters, 686, pp. 178–182. Available at: https://doi.org/10.1016/j.cplett.2017.08.046.

Liu, L. et al. (2015) ‘Simultaneous removal of cationic and anionic dyes from environmental water using montmorillonite-pillared graphene oxide’, Journal of Chemical and Engineering Data, 60(5), pp. 1270–1278. Available at: https://doi.org/10.1021/je5009312.

Mokif, L.A. (2019) ‘Removal Methods of Synthetic Dyes from Industrial Wastewater: A review’, Mesopo. Environ. J, 5(1), pp. 23–40. Available at: https://doi.org/10.31759/mej.2019.5.1.0040.

Mullen, K. (2019) Groundwater | Information on Earth's water, NGWA The Groundwater Association.

Muthuraman, G. and Teng, T.T. (2009) 'Extraction of methyl red from industrial wastewater using xylene as an extractant', Progress in Natural Science, 19(10), pp. 1215–1220. Available at: https://doi.org/10.1016/j.pnsc.2009.04.002.

Nidheesh, P.V., Zhou, M. and Oturan, M.A. (2018) 'An overview on the removal of synthetic dyes from water by electrochemical advanced oxidation processes', Chemosphere, 197, pp. 210–227. Available at: https://doi.org/10.1016/j.chemosphere.2017.12.195.

Patel, B. and Shah, K. (2014) Research review on Biodegradation of Azo Dye compounds. Available at: https://ssrn.com/abstract=2474466.

Piaskowski, K., Świderska-Dąbrowska, R. and Zarzycki, P.K. (2018) 'Dye removal from water and wastewater using various physical, chemical, and biological processes', Journal of AOAC International, 101(5), pp. 1371–1384. Available at: https://doi.org/10.5740/jaoacint.18-0051.

Rand Water (no date) Water Wise - Water Situation in South Africa. Available at: https://waterwise.co.za/site/water/environment/situation.html (Accessed: 18 March 2023).

Rani, S. et al. (2016) 'Removal of methylene blue and rhodamine B from water by zirconium oxide/graphene', Water Science, 30(1), pp. 51–60. Available at: https://doi.org/10.1016/j.wsj.2016.04.001.

Ridjal, A.T.M. et al. (2022) 'Study of Rhodamine B Dyes Content in Snacks of Karuwisi Traditional Market Makassar, South Sulawesi, Indonesia', IOP Conference Series: Earth and Environmental Science, 1027(1), p. 012012. Available at: https://doi.org/10.1088/1755-1315/1027/1/012012.

Shah, K. (2014) Biodegradation of azo dye compounds IRJBB Biodegradation of azo dye compounds. Available at: https://www.researchgate.net/publication/267623559.

Shakir, K. et al. (2010) 'Removal of rhodamine B (a basic dye) and thoron (an acidic dye) from dilute aqueous solutions and wastewater simulants by ion flotation', Water

Research, 44(5), pp. 1449–1461. Available at: https://doi.org/10.1016/j.watres.2009.10.029.

Sharma, J., Sharma, S. and Soni, V. (2021) ‘Classification and impact of synthetic textile dyes on Aquatic Flora: A review’, Regional Studies in Marine Science. Elsevier B.V. Available at: https://doi.org/10.1016/j.rsma.2021.101802.

Singh, K. and Arora, S. (2011) ‘Removal of synthetic textile dyes from wastewaters: A critical review on present treatment technologies’, Critical Reviews in Environmental Science and Technology, 41(9), pp. 807–878. Available at: https://doi.org/10.1080/10643380903218376.

Tkaczyk, A., Mitrowska, K. and Posyniak, A. (2020) ‘Synthetic organic dyes as contaminants of the aquatic environment and their implications for ecosystems: A review’, Science of the Total Environment. Elsevier B.V. Available at: https://doi.org/10.1016/j.scitotenv.2020.137222.

Velusamy, S. et al. (2021) ‘A Review on Heavy Metal Ions and Containing Dyes Removal Through Graphene Oxide-Based Adsorption Strategies for Textile Wastewater Treatment’, Chemical Record. John Wiley and Sons Inc, pp. 1570–1610. Available at: https://doi.org/10.1002/tcr.202000153.

Wang, J. et al. (2021) ‘Recent advances in metal halide perovskite photocatalysts: Properties, synthesis and applications’, Journal of Energy Chemistry. Elsevier B.V., pp. 770–785. Available at: https://doi.org/10.1016/j.jechem.2020.06.024.

World Health Organization (WHO) (2022) Drinking-water. Available at: https://www.who.int/news-room/fact-sheets/detail/drinking-water (Accessed: 18 March 2023).

World Health Organization (WHO) and United Nations Children’s Fund (UNICEF) (2021) Progress on household drinking water, sanitation and hygiene 2000-2020: five years into the SDGs. Available at: https://washdata.org/sites/default/files/2021-07/jmp-2021-wash-households.pdf (Accessed: 18 March 2023).

Zhang, Q. et al. (2020) ‘Enhanced Photocatalytic Property of γ-CsPbI3 Perovskite Nanocrystals with WS2’, ACS Sustainable Chemistry and Engineering, 8(2), pp. 1219–1229. Available at: https://doi.org/10.1021/acssuschemeng.9b06451.

CHAPTER 2: LITERATURE REVIEW

2.1. History and characteristics of synthetic organic dyes:

2.1.1. History of synthetic organic dyes

William Henry Perkin unintentionally invented the first synthetic organic dye (SOD) in 1865 while conducting malaria treatment research (Singh and Arora, 2011; Katheresan, Kansedo, and Lau, 2018). During his experiments, he used coal tar, and although his attempts to synthesize quinine for malaria treatment failed, they led to the discovery of an oily residue that could dye silk purple. Perkin named the dye mauveine and it is shown in **Figure 2.1**. Perkin's discovery paved the way for the discovery of many other SODs. It also had far-reaching impacts on industries such as medicine, photography, explosives, plastics, textiles, and many other industries that rely on dyes (Ziarani et al., 2018; Tkaczyk, Mitrowska, and Posyniak, 2020).

Figure 2.1: Mauveine dye (Jacopo Prisco, 2017).

2.1.2. Characteristics of synthetic organic dyes:

SODs are made from organic molecules derived from chemicals, petroleum by-products, and earth minerals. They have various applications such as fluorescent tracers, dye-sensitized solar cells, photo-redox catalysts in lasers, and paint (Ziarani *et al.*, 2018). SODs consist of two components; the first one being chromophores which are responsible for producing colour. Chromophores have a radical configuration, they are electron-accepting, and consist of conjugated double bonds containing delocalized electrons (Nidheesh, Gandhimathi, and Ramesh, 2013; Affat,

2021). They usually have an aromatic structure such as benzene, naphthalene, or anthracene (Nidheesh, Gandhimathi, and Ramesh, 2013). The most common chromophore functional groups are carbonyl (C=O), diazo (-N=N-), azomethine (-CH=N), O=(C_6H_4)=O, and nitro (NO_2) groups (Affat, 2021; Sharma, Sharma and Soni, 2021). Other chromophore groups, such as hydroxyl (OH) and amino (NR_2), increase the dye colour intensity and shift the absorption to a longer wavelength of light (Affat, 2021). The second component is auxochromes which supplement chromophores. They are commonly electron-donating groups and linked to another functional group through a conjugated system (Affat, 2021). Auxochromes have strong bonding affinity due to their characteristic high ionizing groups (Nidheesh, Gandhimathi, and Ramesh, 2013). Common auxochromes include -NH_3, -COOH, -HSO_3, and -OH (Nidheesh, Gandhimathi, and Ramesh, 2013; Shah, 2014; Sharma and Soni, 2021). Auxochromes are generally multifunctional. For instance, auxochromes introduce chromophores to textiles, increase the dye's colour affinity to textiles, increase colour intensity, and may affect water solubility by donating or removing electrons from dye molecules (Nidheesh, Gandhimathi and Ramesh, 2013; Sharma, Sharma and Soni, 2021). A dye's colour intensity can be increased by causing a bathochromic shift (i.e., absorption band shift to a longer wavelength) which can be achieved in three ways, namely: increasing the electron-accepting power of the chromophore, increasing the electron-donating power of the auxochromes and by extending the length of the conjugation (Juster, 1962).

SODs are classified according to the method of application, molecular structure, and the chromophore groups Martínez-Huitle and Brillas, 2009; Nidheesh, Gandhimathi and Ramesh, 2013; Katheresan, Kansedo, and Lau, 2018; Mokif, 2019; Affat, 2021). They are grouped into three main categories: anionic (direct, acid, azo, and reactive dyes), cationic (all basic dyes), and non-ionic (disperse dyes). In essence, anionic dyes are negatively charged, cationic dyes are positively charged, and non-ionic dyes have little to no ionic character. Dye nomenclature follows the order: method of application to materials, colour, and order number e.g., reactive red 3 (Sharma and Soni, 2021). SODs are either water-insoluble or water-soluble. Water-insoluble dyes include sulfur, vat, disperse, and pigment dyes. Water-soluble dyes are acid, basic, and reactive dyes (Nidheesh, Gandhimathi, and Ramesh, 2013; Sharma and Soni, 2021).

2.2. Dye removal methods:

Various methods exist for removing dyes from wastewater. These water treatment methods are divided into three main categories namely: chemical, physical, and biological methods (Katheresan, Kansedo, and Lau, 2018; Mokif, 2019). Different methods are used depending on the concentration and volume of the effluent (Ghaly, Farah, and Fathy, 2007). Dyes are mineralized to oxidation products such as CO_2, H_2O, NO_3^-, SO_4^-, and Cl^- (Singh and Arora, 2011; Nidheesh, Zhou, and Oturan, 2018). These methods have different advantages and limitations as mentioned in **Table 2.1** (Rafiq et al., 2021a).

Table 2.1: Advantages and disadvantages of chemical, physical, and biological dye treatment methods:

Dye removal categories	Methods	Advantages	Disadvantages	References
Chemical	Photochemical	Effective dye removal, no sludge is produced, and no foul odours.	A lot of by-products, and expansive.	(Katheresan, Kansedo, and Lau, 2018; Warade et al., 2016)
	Ozonation	Effective for azo dyes and rapid degradation. Applied in its gaseous state and does not increase the volume of treated water.	Short half-life, hazardous by-products, requires ozone destructive unit, and the stability is affected by temperature, pH, and salts.	(Katheresan, Kansedo, and Lau, 2018; Warade et al., 2016)
	Advanced Oxidation Process	Rapid, high dye removal efficiency, no chemicals consumed, and no sludge produced.	Not flexible, pH-dependent, and expansive.	(Katheresan, Kansedo, and Lau, 2018; Mokif, 2019; Crini, 2006)

	Fenton's reagent	Effective for degrading a wide range of dyes that are soluble and insoluble. Eliminates toxins in water.	High iron sludge generation results in disposal problems. Expensive, and cannot remove disperse and vat dyes. Long reaction time and only works at low pH.	(Katheresan, Kansedo, and Lau, 2018; Mokif, 2019)
	UV irradiation	No hazardous chemicals are required, no sludge production, and it reduces foul odours.	Energy intensive, high cost, and limited treatment times.	(Katheresan, Kansedo, and Lau, 2018)
Physical treatments	Adsorption	Removes various dyes from water, non-toxic, low-cost, renewable, easily recoverable, and readily available	High cost for some adsorbents.	(Katheresan, Kansedo, and Lau, 2018; Warade et al., 2016)
	Membrane filtration	Resistance to temperature, microbial attack, and adverse chemical environments. It is reusable. Effective wastewater purification.	It is unable to reduce dissolved solid content which makes recycling of the treated water difficult. High initial cost and a limited lifetime.	(Katheresan, Kansedo, and Lau, 2018; Mokif, 2019; Crini, 2006; Warade et al., 2016)

	Coagulation / flocculation	Simple, low cost, and high dye removal efficiency.	High disposal costs due to high sludge production, sludge disposal problems, and high cost of chemical reagents.	(Katheresan, Kansedo, and Lau, 2018)
	Irradiation	Effective at laboratory scale.	Expansive and requires high amounts of dissolved oxygen.	(Katheresan, Kansedo, and Lau, 2018)
Biological treatments	Biodegradation	Cost-effective, environmentally friendly, and pro-ecological.	Not effective for all dyes, slow process rate, and requires the addition of nutrients and optimum conditions	
	Fungal treatment	Flexible and can degrade a mixture of dyes simultaneously.	Slow growth, growth requires nitrogen, needs large reactors, and is unstable.	(Katheresan, Kansedo, and Lau, 2018)
	Enzyme degradation	High efficiency, cost-effective, non-toxic, and reusable. Effective for azo dyes.	Not effective for all types of dyes and limited scalability.	(Katheresan, Kansedo, and Lau, 2018; Shah, 2014)
	Aerobic-anaerobic combination	Low cost, no foam, and	Long degradation time, sludge production,	(Katheresan, Kansedo, and Lau, 2018)

	degrades a variety of dyes.	inflexibility, large area required, and toxic by-products produced.	
Algae degradation	Cheap, effective, and environmentally friendly.	Unstable.	(Katheresan, Kansedo, and Lau, 2018)

2.3. Fate of SODs:

The textile industry is one of the biggest consumers of SODs, accounting for 54% of dyes in wastewater making them one of the main sources of water pollution (Ghaly, Farah, and Fathy, 2007; Katheresan, Kansedo, and Lau, 2018; Rafiq et al., 2021a; Sharma, Sharma and Soni, 2021). Dyeing of textiles is a critical step in the textile manufacturing process and involves two processes, namely: wet and dry processes (Zafar, Fatima, and Kim, 2021). At this step, different dyes and chemicals are added to the fabric to colour and improve dye adsorption respectively (Zafar, Fatima, and Kim, 2021). For the dyeing processes, the textile industry uses organic dyestuffs, chelating agents, pH regulators, surfactants, solvents, salts, detergents, and other chemicals (Ghaly, Farah, and Fathy, 2007). More than 8000 chemicals are employed for the wet dyeing process (Nidheesh, Zhou, and Oturan, 2018; Sharma and Soni, 2021) This process requires copious amounts of water and involves operations such as sizing and de-sizing, scouring, bleaching, mercerizing, dying, printing, and finishing (Lellis *et al.*, 2019b; Mokif, 2019; Zafar, Fatima and Kim, 2021). On average, to dye 8000 kg of fabric each day, the textile sector consumes around 1.6 million litres of water (Kant, 2012; Hussain and Wahab, 2018). More than 20,000 tons of dyes are lost in dye effluents after the dyeing process due to dyes not being completely adsorbed to textiles (Katheresan, Kansedo, and Lau, 2018). The loss of dyes depends on the dye's fixative properties, which vary between 2% for cationic dyes and up to 50% for reactive dyes (Forgacs, Cserháti, and Oros, 2004). The dye effluents which consist of dyes and hazardous chemical additives (metals, chlorides, etc) are released into waterbodies such as lakes, ponds, rivers, and public sewers (Katheresan, Kansedo

and Lau, 2018; Mokif, 2019). This results in the contamination of soil, sediments, groundwater, and surface water (Yaseen and Scholz, 2016; Sharma, and Soni, 2021; Zafar, Fatima, and Kim, 2021).

The largest group of dyes are azo dyes which are characterized by the -N=N- functional group joining 2 symmetrical and/or asymmetrical identical or non-azo alkyl or aryl radicals. They constitute approximately 50-70% of synthetic dyes and are frequently discharged in wastewater (Yaseen and Scholz, 2016; Katheresan, Kansedo, and Lau, 2018; Benkhaya, M'rabet and El Harfi, 2020). Although different dyes may be present in wastewater at low concentrations, the overall concentration of dyes in wastewater ranges between 10-300 mg/L (Martínez-Huitle and Brillas, 2009; Nidheesh, Gandhimathi and Ramesh, 2013; Yaseen and Scholz, 2016; Nidheesh, Zhou and Oturan, 2018; Sharma, Sharma and Soni, 2021). This is an environmental concern because textile dye effluents are high in total organic carbon, chemical oxygen demand, biochemical oxygen demand, suspended solids, salts, and metals. They alter the pH, colour, and conductivity of natural water (Yaseen and Scholz, 2016; Benvenuti et al., 2018a; Zafar, Fatima, and Kim, 2021). Even at small traces (<1 mg/L), SODs compromise the water bodies' aesthetic due to intense colour, thus reducing light penetration in water, impairing photosynthesis, reducing symbiotic activity, and reducing the food supply for aquatic organisms (Martínez-Huitle and Brillas, 2009; Katheresan, Kansedo and Lau, 2018; Nidheesh, Zhou and Oturan, 2018; Affat, 2021; Sharma, Sharma and Soni, 2021; Zafar, Fatima and Kim, 2021). This hinders animal and plant growth (Yaseen and Scholz, 2016; Sharma and Soni, 2021). When dye-containing water is used directly in agriculture, it affects the environment and human health because dyes have toxic, carcinogenic, mutagenic, neurotoxic, and genotoxic effects (Forgacs, Cserháti and Oros, 2004; Crini, 2006; Ghaly, Farah and Fathy, 2007; Nidheesh, Gandhimathi and Ramesh, 2013; Yaseen and Scholz, 2016; Benvenuti *et al.*, 2018a; Sharma, Sharma and Soni, 2021; Zafar, Fatima and Kim, 2021; Miller *et al.*, 2022; Yousef *et al.*, 2022a). In addition, SODs are highly persistent, as well as chemically, photolytically, and biologically stable in nature due to having complex molecular structures, and xenobiotic properties (Nidheesh, Zhou, and Oturan, 2018). Therefore, SODs are difficult to decompose, thus accumulating on land and in water bodies, causing ecological problems. Moreover, they are recalcitrant organic molecules, resistant to aerobic digestion, and biodegradation, and are stable when

exposed to heat and oxidizing agents therefore making them difficult to remove from dye effluents. They, therefore, have harmful effects on humans and animals in both the short and long term (Nidheesh, Gandhimathi, and Ramesh, 2013; Katheresan, Kansedo, and Lau, 2018; Affat, 2021; Zafar, Fatima, and Kim, 2021; Yousef et al., 2022).

When SODs are degraded using conventional treatment processes, dyes can, in some cases, transform into intermediates that are more toxic than the parent dye compound (Ghaly, Farah and Fathy, 2007). It is becoming increasingly important to treat textile effluents to preserve water and the ecosystem as well as to recycle the treated water for reuse in the textile industry (Katheresan, Kansedo, and Lau, 2018; Zafar, Fatima and Kim, 2021), particularly since the current conventional methods have limitations ranging from high operational costs, poor removal efficiency, complex processes, and poor adaptability to many organic pollutants (Yousef *et al.*, 2022a).

2.4. Advanced oxidation processes

Oxidative dye removal methods have gained attention in recent years (Nidheesh, Zhou and Oturan, 2018). Advanced oxidation processes (AOPs) are one of the more powerful chemical methods for the discolouration and degradation of dyes (Ghaly, Farah and Fathy, 2007; Martínez-Huitle and Brillas, 2009; Yousef *et al.*, 2022a). AOPs have been found to be more effective than conventional chemical oxidation methods in terms of dye decolorization and COD reduction (Robinson *et al.*, 2001; Singh and Arora, 2011). AOPs utilize oxidizing agents such as hydrogen peroxide (H_2O_2) and ozone (O_3) with an inorganic catalyst such as (Fe(II), Mn(II) and TiO_2). This process is done with or without irradiation from a light source such as UV light to degrade dye molecules into smaller and harmless compounds such as CO_2 and H_2O (Harun et al., 2020; Robinson et al., 2001; Crini, 2006; Mokif, 2019).

AOPs can eliminate major classes of organic contaminants, such as SODs, from water, directly or indirectly by generating hydroxyl radicals ($OH^{\bullet}$) which are strong oxidizing agents that have the potential to completely breakdown the dyes at ambient temperatures by hydroxylating or dehydrogenating the pollutants (Ghaly, Farah and Fathy, 2007; Yousef *et al.*, 2022a). Hydroxyl radicals are better at degrading SOD

molecules because they have a higher oxidation potential of 2.80 V compared to the hydrogen peroxide potential of 1.78 V (Robinson *et al.*, 2001; Devi, Raju and Kumar, 2009; Nidheesh, Zhou and Oturan, 2018; Rafiq *et al.*, 2021a). Dye decolorization occurs through chemical oxidation where the hydroxyl groups cleave the aromatic ring of the dye molecules. The efficacy of dye removal is influenced by various factors such as UV light intensity, pH, and dye structure (Robinson *et al.*, 2001; Rafiq *et al.*, 2021a). AOPs are divided into two categories: (Arslan, Balcioğlu and Tuhkanen, 2000).

1. **Non-photochemical AOPs:** these processes include Fenton and Fenton-like processes, ozonation, O_3/H_2O_2, and wet air oxidation.
2. **Photochemical AOPs:** include homogeneous processes (UV/H_2O_2, UV/O_3, photo-Fenton process) where the photocatalyst and reactants are in the same ‘phase, and heterogeneous photocatalysis where the catalyst and reactants are in different phases. Heterogenous photocatalysis is preferred over homogenous catalysis because the catalyst can easily be separated at the end of the reaction for reuse thus reducing water treatment costs.

2.6. Photocatalysis

Photocatalysis is an effective photochemical AOP method that was discovered by Fujishima and Honda in 1972 when they presented the water-splitting capacity of TiO_2 under UV light irradiation (Ghaly, Farah and Fathy, 2007; Lee and Jang, 2014). The term photocatalysis is derived from Greek. The prefix, photo, means light. The suffix, catalysis, refers to a process in which a substance, known as a catalyst, is added to a reaction and it increases the rate of the reaction by reducing the activation energy without getting consumed or it can be regenerated at the end of the reaction (Gumerov *et al.*, 2014; Saravanan, Gracia and Stephen, 2017). Photocatalysis uses light and a semiconductor photocatalyst resulting in effective mineralization (conversion into inorganic species) of SODs provided that the photon energy is at least equal to or higher than the bandgap of the catalyst to carry out target reactions (Ghaly, Farah and Fathy, 2007). In this process, photon energy is absorbed by the photocatalyst and converted to chemical energy where photogenerated electrons and holes act as oxidizing and reducing agents thus breaking down pollutants into less harmful compounds (Yousef *et al.*, 2022a). The advantages of this method are 1) complete degradation and mineralization of SODs into less harmful compounds without having

to use toxic oxidants such as chlorine, 2) use of sunlight as a light source, 3) low cost, and 4) no waste disposal issues (Katheresan, Kansedo and Lau, 2018; Yousef *et al.*, 2022a). Sunlight is an abundant source of energy therefore this is an economically viable method since artificial light requires high electrical power which is costly (Ghaly, Farah and Fathy, 2007). This makes photocatalysis sustainable and environmentally friendly (Yousef *et al.*, 2022a). Other advantages of using this method include good reproducibility, simplicity, high efficiency, and cost-effectiveness (Yousef *et al.*, 2022a). **Scheme 2.1** below illustrates the charge carrier dynamics in the photocatalysis process.

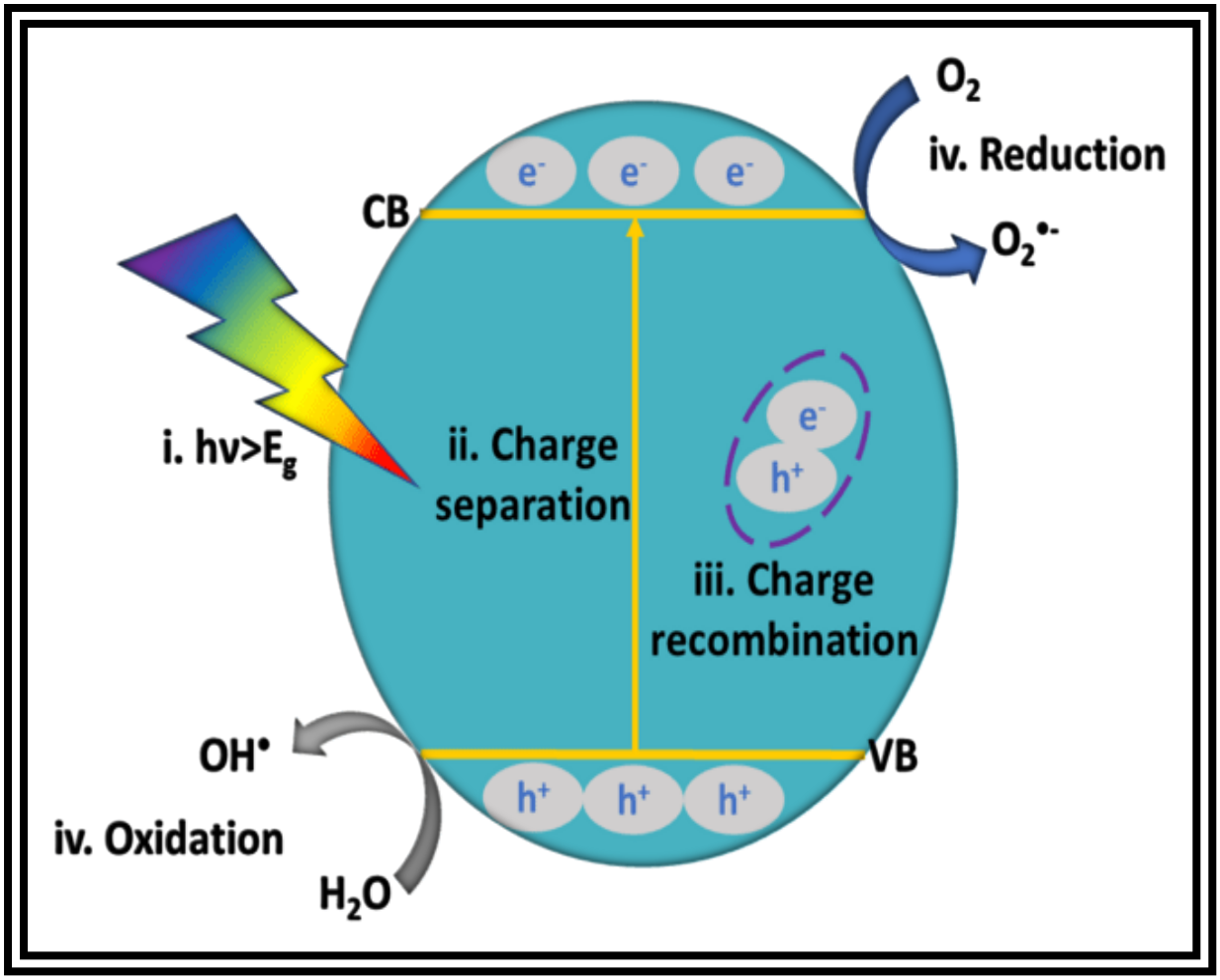

Scheme 2.1: Schematic representation of the photocatalytic process. i) light absorption ii) charge separation iii) charge recombination and iv) redox reactions on the surface of the photocatalyst.

This process is split into four steps:

i. The photocatalytic reaction is initiated when the photocatalyst absorbs light and this results in the generation of electron (e^-)-hole (h^+) pairs i.e.,

Semiconductor photocatalysts absorb photons that have a higher energy than the bandgap of the photocatalyst.

ii. This prompts inter-band transition where the charges are separated. The holes are generated in the valence band (VB) and electrons in the conduction band (CB). These electron-hole pairs are generated rapidly, within a femtosecond.

iii. The charges tend to recombine easily in the bulk or the surface of the photocatalyst. Electrostatic recombination of the photogenerated charges reduces the efficiency of a photocatalyst because the energy absorbed from the light source dissipates thus reducing the efficiency of the photocatalytic reaction.

iv. The non-recombined electron-hole pairs migrate to the photocatalyst surface and take part in redox reactions on the surface of the photocatalyst that occur through interfacial transfer. In the reduction process, the electrons in the CB react with oxygen to form superoxide anions ($O_2^{\bullet -}$). The anions react with intermediates to form H_2O_2 and water. In the oxidation reaction, holes in the VB react with water to form hydroxyl radicals ($OH^{\bullet}$). The $OH^{\bullet}$ radicals are powerful oxidizing agents that drive the degradation of dyes into smaller harmless compounds such as CO_2 and H_2O (Saravanan, Gracia and Stephen, 2017). These steps are shown in the following equations (Wong and Chu, 2003; Akpan and Hameed, 2009; Bresolin, Park and Bahnemann, 2020):

$$Semiconductor + h\nu \rightarrow Semiconductor\ (e_{CB}^- + h_{VB}^+) \quad \textbf{(2.1.)}$$

$$Semiconductor\ (e_{CB}^-) + O_2 \rightarrow O_2^{\bullet -} \quad \textbf{(2.2.)}$$

$$\mathrm{Semiconductor\ (h_{VB}^+) + H_2O \rightarrow OH^{\bullet} + H^+} \quad \textbf{(2.3.)}$$

$$O_2^{\bullet -} + H^+ \rightarrow HOO^{\bullet} \quad \textbf{(2.4.)}$$

$$2HOO^{\bullet} + O_2 \rightarrow 2\ OH^{\bullet} \quad \textbf{(2.5.)}$$

$$Dye + OH^{\bullet} \rightarrow CO_2 + H_2O \quad \textbf{(2.6.)}$$

$$Dye + Semiconductor\ (e_{CB}^-) \rightarrow reduction\ products \quad \textbf{(2.7.)}$$

$$Dye + Semiconductor\ (h_{VB}^+) \rightarrow oxidation\ products \quad \textbf{(2.8.)}$$

2.6.1. Important energy levels for photocatalytic reactions

To design new photocatalytic materials, it is crucial to have a clear understanding of the mechanism of photocatalytic reactions. **Figure 2.2** below shows the oxidation and reduction levels of typical photocatalytic reactions at pH=0 with respect to vacuum (V)

vs normal hydrogen electrode (NHE). Therefore, the photocatalyst's VB and CB energy levels need to correspond to the levels required for the target redox reactions i.e., the CB potential (eV) needs to be higher than the potential for reduction reactions of interest and the VB potential should be lower than the potential for oxidation reactions. Additionally, the energy of the photoexcited electron needs to be higher than the energy difference between the VB and CB (Kanhere and Chen, 2014; Bresolin, Park and Bahnemann, 2020).

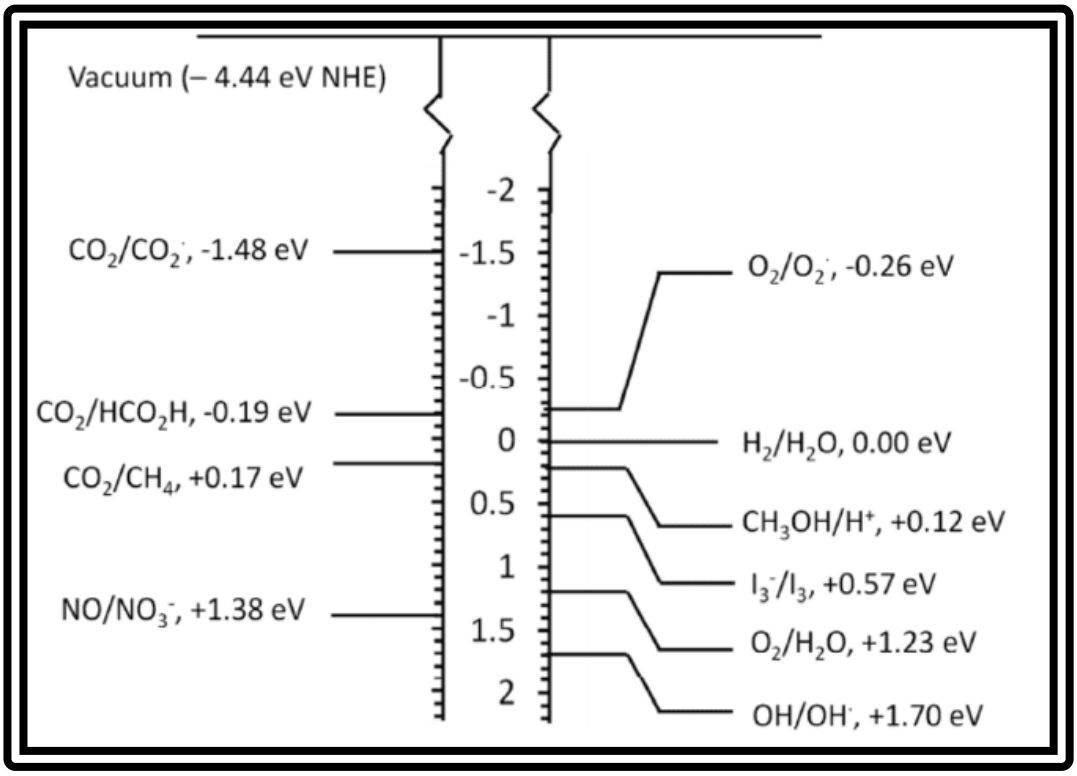

Figure 2.2: NHE energy levels for important photocatalytic reactions at pH = 0 (Kanhere and Chen, 2014).

The VB and CB potentials of the photocatalysts can be calculated using the equations below:

$$E_{CB} = \chi - E^e - 0.5E_g \quad \textbf{(2.9.)}$$

$$E_{VB} = E_{CB} + E_g \quad \textbf{(2.10.)}$$

E_{CB} and E_{VB} are the conduction and valence bands respectively. E_g is the bandgap, E^e is the energy of free electrons vs. hydrogen and χ represents the electronegativity of the photocatalyst. The formula for calculating the electronegativity is described below.

$$\chi = [x(A)^a\, x(B)^b\, x(C)^c]^{1/(a+b+c)} \quad \textbf{(2.11.)}$$

In this equation, $x(\mathrm{A})$, $x(B)$ and $x(C)$ represent the electronegativity values of elements A, B, and C which the photocatalyst is comprised of. The lower-case alphabets, a, b, and c, represent the number of the corresponding A, B and, C elements (Wang *et al.*, 2016; Channei *et al.*, 2021).

Three main approaches can be used to improve the performance of a photocatalyst:

i. Increase the ability of the photocatalyst to absorb within the visible range of the solar spectrum by tuning the bandgap. A narrow bandgap, smaller than 3 eV, enhances the optical absorbance in the visible light range. Studies have also shown that point defects such as vacancies, and the presence of interstitial atoms may reduce the bandgap.
ii. Reduce the recombination rate of the photogenerated electron-hole pairs. One of the approaches in which this can be achieved is by adding a co-catalyst.
iii. Use the VB and CB levels of the photocatalyst to evaluate the redox capacity of the material based on the target photocatalytic application. (Bresolin, Park and Bahnemann, 2020; Islam and Hossain, 2020a).

2.7. Semiconductors and heterojunctions:

2.7.1. Bandgap energy

Insulators, metals, and semiconductors are classes of solid materials that are differentiated by their conductivity and electronic band structure as shown in **Figure 2.3** below. The space between the conduction and valence bands is referred to as a bandgap. In a bandgap, there are no electronic states present. Insulators have a wide bandgap between the VB and CB and the electrons do not have enough energy to jump from the VB to the CB. In metals, the CB and VB overlap which makes them good conductors. Semiconductors have a bandgap that is small enough for photoexcited electrons to migrate from the VB to the CB. Before photon absorption, the VB is filled with charges and the CB is empty. After photon absorption, the excited electrons leave holes in the VB. The small bandgap in semiconductors allows the photogenerated electrons and holes to move freely as charge carriers. This makes them suitable for photocatalysis applications (Hoffmann *et al.*, 1995; Shaheen, 2010).

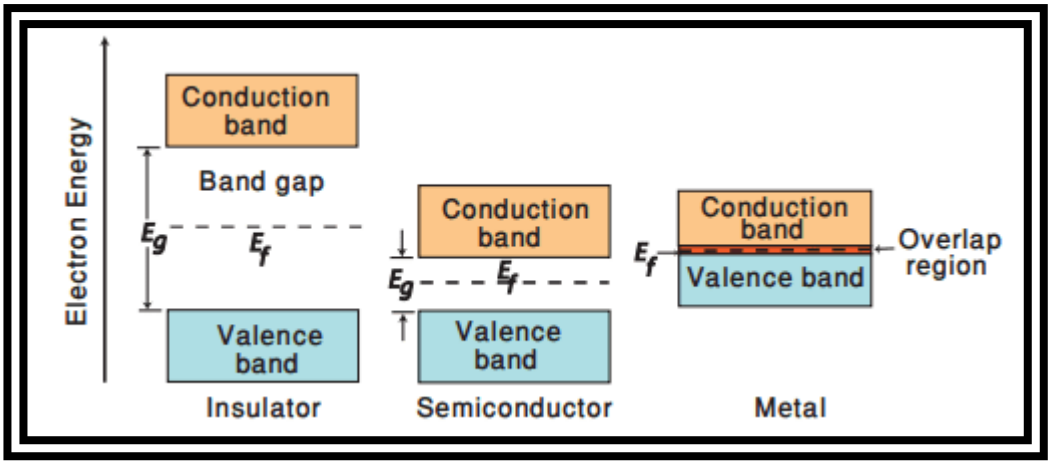

Figure 2.3: Electronic bandgap structures of insulators, semiconductors, and metals at absolute zero temperature (0 K) (Shaheen, 2010).

2.7.2. Direct and indirect bandgaps

Semiconductors have two types of bandgaps i.e., direct, and indirect bandgaps shown in **Figure 2.4.** In a direct bandgap semiconductor, the minimum energy of the CB and the maximum of the VB are at the same momentum (k) value meaning that electrons can jump directly from the VB to the CB. However, the charge recombination rate is fast. In indirect bandgap semiconductors, the minimum of the CB and the maximum of the VB are at different k values and electrons require phonon assistance to migrate to the CB. Charge recombination is slower, and this is favourable for photocatalysis (Sun, 2014).

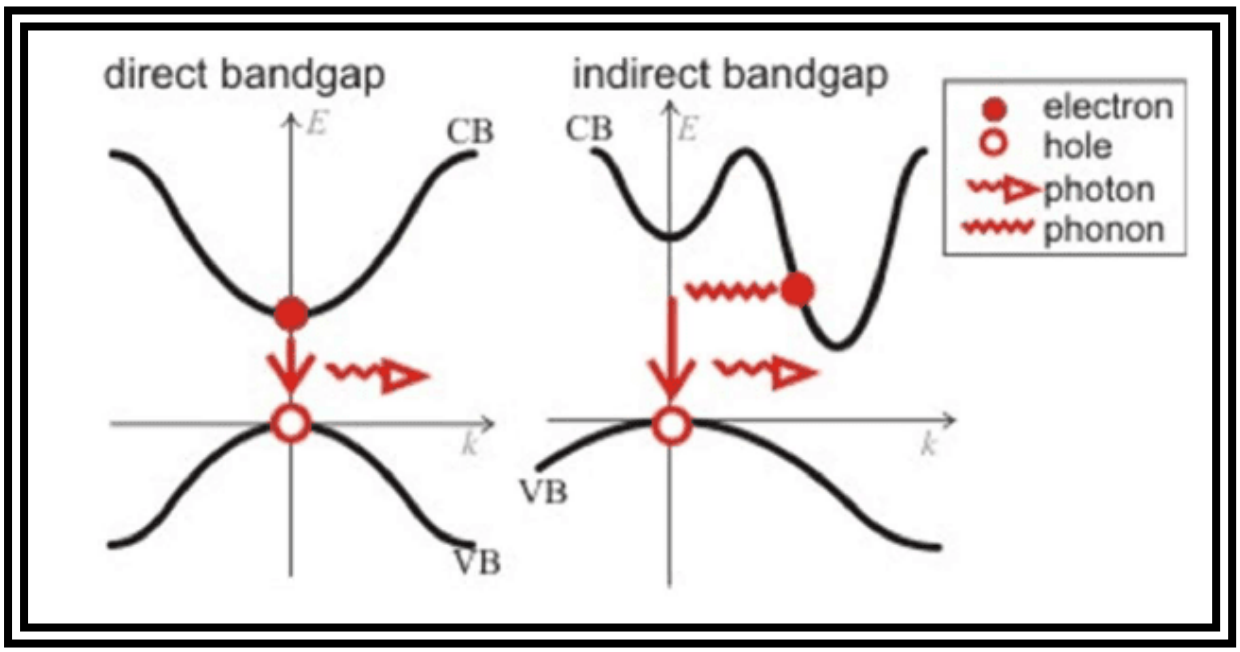

Figure 2.4: Semiconductor direct and indirect bandgaps (Jimenez-Calvo, 2019).

2.7.3. Semiconductor heterojunctions

Semiconductor nanomaterials are used as photocatalysts due to their small size. The nano-scale size of the semiconductor particles is important for surface catalysis reactions as the rate of the reactions depends on the surface area and the number of reactive sites. However, the small size can cause quantum confinement which means that the photogenerated charges are trapped between the VB and CB levels, their motion is restricted, and it increases charge recombination. This is not desirable because it reduces the efficiency of the photocatalyst. In recent years, scientists conducted research to develop solutions to reduce the recombination of electron-hole pairs to improve photocatalytic efficiency. One of the solutions is semiconductor heterostructures (Lee and Jang, 2014). This is an integrated system where two semiconductors are combined and the contact between them is referred to as a heterojunction. One semiconductor acts as a host and the other is a co-catalyst. Ideally, when creating a semiconductor heterostructure, the main photocatalyst is a semiconductor that has a narrow bandgap and it is coupled with a semiconductor that has a wide bandgap. This is ideal because photons with a short wavelength are absorbed by the main photocatalyst and the photons with a longer wavelength are absorbed by the co-catalyst (Lee and Jang, 2014; Zhu and Wang, 2017a). The mechanism for charge separation in a heterojunction is shown in **Figure 2.5** below:

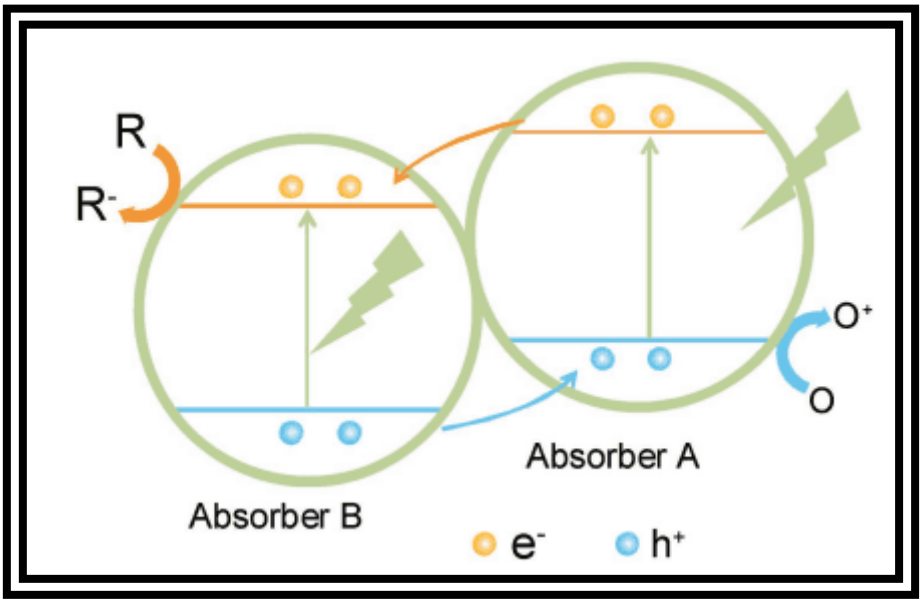

Figure 2.5: Charge separation in a heterojunction (Zhu and Wang, 2017).

A heterojunction creates an internal field that facilitates charge separation. The electrons from semiconductor A are transferred to the CB in semiconductor B. The holes from the VB in semiconductor B are transferred to the VB in semiconductor A (Zhu and Wang, 2017b). Three semiconductor heterojunction arrangements are possible based on the band energies of the semiconductors as shown in **Figure 2.6** below:

Type I heterojunction (Straddling gap structure): In the straddling structure, the CB in semiconductor A is more negative than in semiconductor B i.e., electrons will move down from CB (B) to CB (A). The VB in semiconductor A is more positive than in semiconductor B i.e., the holes in VB (B) need to move up to VB (A). This is not desirable because electrons and holes accumulate in the semiconductor that has a smaller bandgap therefore increasing the probability of charge recombination and reducing the photocatalytic performance.

Type II heterojunction (Staggered gap structure): The CB and VB in semiconductor A are more positive than the CB and VB in semiconductor B. This results in electrons from CB (B) moving down to CB (A) and holes from VB (A) moving up to VB (B) simultaneously. This is therefore the best heterojunction structure for efficient charge separation for photocatalysis.

Type III heterojunction (Broken gap structure): There is a wide energy barrier between the VBs and CBs of semiconductors A and B therefore the electrons and holes are not able to pass through the heterojunction to the respective energy bands (Kumar et al., 2020; Koe et al., 2020).

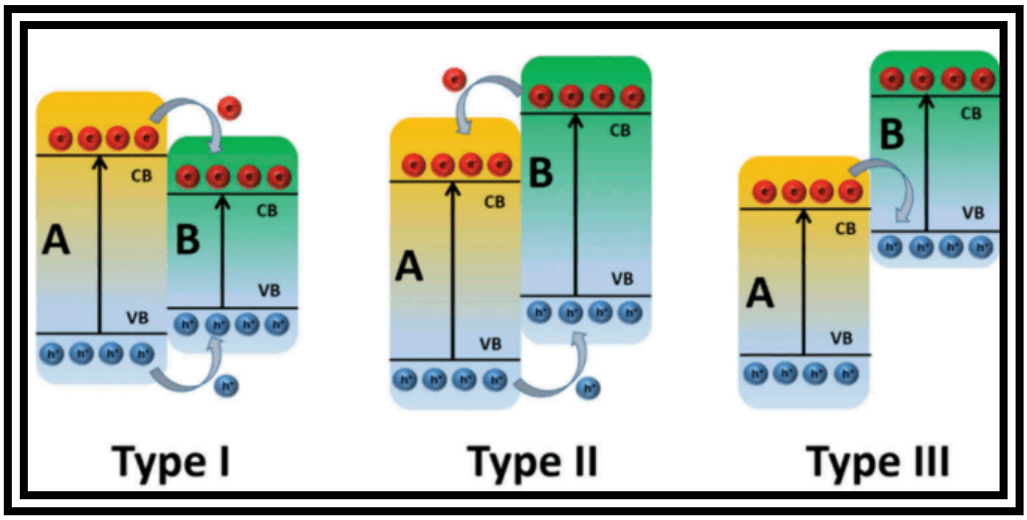

Figure 2.6: Types of semiconductor heterojunction structures (Kumar et al., 2020).

2.7.4. Heterogenous photodegradation of SODs

Heterogenous photodegradation is a process that uses light and a photocatalyst to breakdown organic pollutants into harmless substances such as water and carbon dioxide (Rafiq *et al.*, 2021b). Photocatalysts are materials that can absorb light energy to generate electron-hole pairs, which can react with oxygen and water molecules to form highly reactive species such as hydroxyl radicals (•OH). These species are capable of oxidizing organic pollutants, breaking them down into simpler and less harmful compounds (Ajmal *et al.*, 2014; Reza, Kurny and Gulshan, 2017). Photocatalytic degradation has been widely used in environmental applications such as the treatment of wastewater and industrial effluents. It offers several advantages over traditional treatment methods, including low cost, high efficiency, and minimal production of secondary pollutants (Kumar *et al.*, 2014).

2.8. Metal halide perovskites (MHPs):

Metal halide perovskites are a class of semiconductors that were discovered in 1839 by a Russian mineralogist named Perovski. The first perovskite discovered was calcium titanate ($CaTiO_3$) (Bresolin, Park and Bahnemann, 2020). MHPs have gained a lot of attention over the past 20 years in scientific research due to their interesting quantum effects, simple synthesis, as well as their visible and near-infrared optical properties (Bresolin, Park and Bahnemann, 2020). These properties include electronic structure, surface defects, long carrier lifetime, high exciton binding energy, low trap state density, high carrier mobility, high defect tolerance, long diffusion length, and high absorption coefficients (Gao *et al.*, 2019; Bresolin, Park and Bahnemann, 2020). MHPs have the general chemical formula ABX_3 as shown in **Figure 2.7** (Gao et al., 2019; Bresolin, Park and Bahnemann, 2020; Islam and Hossain, 2020b).

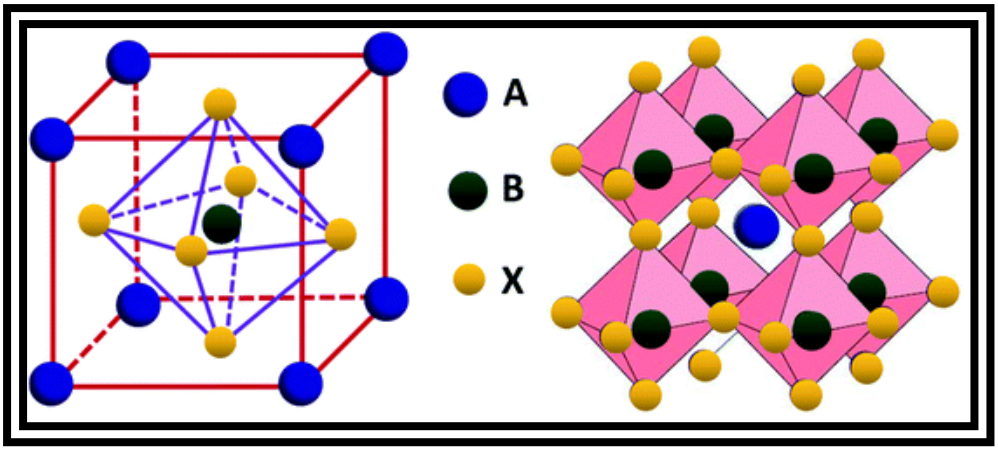

Figure 2.7: Perovskite structure (Yi et al., 2019).

The A-site represents a hybrid organic-inorganic or inorganic monovalent cation i.e., methylammonium (MA^+), cesium (Cs^+), formamidinium (FA^+), or mixed cations (Gao *et al.*, 2019; Bresolin, Park and Bahnemann, 2020). When the A-site is occupied by MA^+ or FA^+ the MHP is referred to as a hybrid organic-inorganic MHP (Bresolin, Park and Bahnemann, 2020). The cation selected for the A-site determines the orientation cage within the perovskite structure and manipulation of the cation may improve the optoelectronic properties (Bresolin, Park and Bahnemann, 2020). The size of the A-site cation affects the symmetry of the perovskite structure, when the cation is large, it distorts the B-X bond which controls the electronic properties of the perovskite. Methylammonium (MA^+) is the commonly used organic cation for solar cells because it results in low packing symmetry, higher bandgap, and higher efficiency. However, inorganic cations such as Cs^+, display better stability and they are used for different applications including photocatalysis (Bresolin, Park and Bahnemann, 2020).

The B-site is a position for metal cations that generally belong to the IVA group of the periodic table. These metal cations have a divalent oxidation state such as Pb^{2+}, Bi^{2+}, Sn^{2+}, Ge^{2+}, etc. As you go along the IVA group, the stability of the divalent oxidation state decreases due to the electron pair effect and the bandgap is affected by the electronegativity and covalent character. Although Pb-based MHPs have gained great success, the substitution of Pb with other divalent ions such as Bi, Ca, Mn, and Sr, is desirable to strike a balance between performance and environmental friendliness as well as to achieve better stability (Bresolin, Park and Bahnemann, 2020). Bismuth (Bi) is non-toxic and is used in medicine to cure stomach-related illnesses. Bi-based MHPs have presented excellent stability while Pb (lead) based ones are susceptible to

moisture. This is undesirable since it causes performance degradation (Gao *et al.*, 2019).

The X-site position contains a halide anion including I^-, Br^-, Cl^-, or a mixture of these halides (Gao *et al.*, 2019; Bresolin, Park and Bahnemann, 2020). When the X-site is occupied by a mixture of halides, the MHP is termed a mixed halide perovskite. The halide has a great impact on the valence band energy of the MHPs in accordance with their electronic features. The valence bands and associated electron band energies of MHPs have been found to decrease down the VIIA group of the periodic table i.e., from Cl^- down to I^-. The Br halide was found to improve the quality of the MHPs in terms of lattice symmetry, stability in moist environments, morphology, and optical properties (Bresolin, Park and Bahnemann, 2020).

The promising visible light absorption ability of MHPs was observed when methylammonium lead halide perovskite ($CH_3NH_3PbI_3$) was deposited on the TiO_2 electrode for solar cells. All-inorganic MHPs have developed remarkably in recent years. Researchers have discovered that different Cs-based MHPs can absorb the entire visible spectrum with surprising quantum yield efficiencies (Bresolin, Park and Bahnemann, 2020). Cs-based MHPs are also less sensitive to moisture, heat, and oxygen and therefore have better stability. It was reported that $Cs_3Bi_2I_9$ perovskite nanocrystals have unique dual optical absorption and emission features (Gao *et al.*, 2019). The discoveries of the impressive electrical and optical properties of MHPs have paved the way for MHPs to be used in various applications such as photodetectors, LEDs, memory devices, X-ray detectors, and photocatalysis (Bresolin, Park, and Bahnemann, 2020).

2.8.1. MHP synthesis

Simple and reliable synthesis methods have been developed to control the size, shape, and optical properties of MHP nanoparticles. The synthesis methods are classified as top-down or bottom-up approaches. In the top-down approach, macroscopic or larger structures are fragmented into smaller structures mechanically or chemically. The bottom-up synthesis routes start with the small molecules and ions preceded by chemical reactions which are conducted via gas- or liquid-phase to produce larger and more complex structures. The liquid phase approach has been

proven to be the best for producing high-quality colloidal MHP nanoparticles (Shamsi *et al.*, 2019).

2.8.1.1. Hot-injection synthesis for metal halide perovskites

Hot-injection synthesis is one of the most developed and popular liquid-phase methods for the synthesis of high-quality metal halide perovskite nanocrystals with controlled size and shape (Shamsi *et al.*, 2019). Hot-injection synthesis was discovered in 1993 by Murray, Norris, and Bawendi after they synthesized cadmium chalcogenides using this method (de Mello Donegá, Liljeroth and Vanmaekelbergh, 2005; Kwon and Hyeon, 2011). In this method, two solutions are prepared at high temperatures, typically above 100 °C. In the first solution, a metal halide salt, e.g., bismuth bromide, is dissolved in a solvent. In the second solution, an organic cation, e.g., cesium carbonate, is added to a mixture of capping agents. Capping agents such as oleylamine and oleic acid are commonly used (Y. Zhang *et al.*, 2020). Oleylamine is a primary capping agent and oleic acid serves as a capping agent and participates in metathesis reactions. The hot solution with the organic cation is rapidly injected into the hot metal halide solution using a syringe (Kwon and Hyeon, 2011; Shamsi *et al.*, 2019). After injection of the organic cation, rapid nucleation, and growth of perovskite nanocrystals within the solution occur (de Mello Donegá, Liljeroth and Vanmaekelbergh, 2005; Kwon and Hyeon, 2011). The size and shape of the nanocrystals can be controlled by adjusting the reaction parameters, such as temperature, the ratio of precursors to surfactants, and reaction time (Shamsi *et al.*, 2019). After the reaction is complete, the nanoparticles are typically purified with antisolvents such as hexane and isolated by centrifugation (Y. Zhang *et al.*, 2020). Hot-injection synthesis offers several advantages, such as high reproducibility, narrow size distribution, and the flexibility to tune the size and shape of the nanocrystals (Kwon and Hyeon, 2011). The experimental setup for hot-injection synthesis is shown in **Figure 2.8** below.

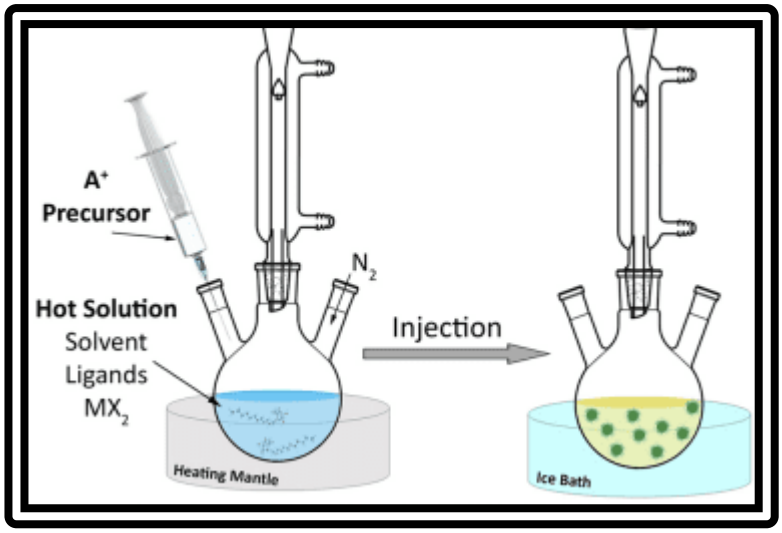

Figure 2.8: Hot-injection synthesis of colloidal MHP nanoparticles (Shamsi et al., 2019).

2.8.2. MHPs application as photocatalysts

MHPs are good candidates for use as photocatalysts because they display important factors for exceptional photocatalysis performance including easily tuneable bandgaps, longer carrier charge lifetime due to reduced recombination, long carrier diffusion length, high absorption coefficient, well-balanced charge transfer for redox reactions, bandgaps are suitable for extended light absorption in the visible light spectrum i.e., the charge carriers are effectively generated at lower energies, and high carrier charge mobility (Bresolin, Park and Bahnemann, 2020). As already stated, metal halide perovskites (MHPs) are semiconductor materials that have demonstrated promising efficacy as photocatalysts for degrading synthetic organic dyes (SODs) such as MR and RhB (Sun *et al.*, 2021). It is noteworthy to mention that these materials also face limitations, such as electron-hole recombination (deQuilettes *et al.*, 2019). To overcome charge recombination, co-catalysts can be employed. Transition metal dichalcogenides (TMDCs) like molybdenum disulfide (MoS_2) and tungsten disulfide (WS_2) are cost-effective co-catalysts that can help mitigate electron-hole recombination (Fadojutimi *et al.*, 2022), thereby enhancing the photocatalytic degradation of dyes. This is attributed to their sulfur-metal-sulfur layered structure, moderate bandgap, light absorption in the visible and ultraviolet regions, and abundance of active sites (Joseph and Aneesh, 2022). Transition metal dichalcogenides:

Many semiconductors have been used as photocatalysts as they can harvest and convert light into chemical energy (Huang et al., 2022). However, their real application is limited due to low efficacy caused by charge recombination. Noble metals such as Pt, are used as cocatalysts to enhance the efficiency of semiconductor photocatalysts. However, the low abundance and high cost of noble metals have resulted in the search for alternative materials. Transition metal dichalcogenides (TMDCs) have drawn the attention of scientists. TMDCs have various characteristics such as tuneable bandgaps, abundant active sites for photocatalytic activity, intrinsic electrical conductivity, good stability, excellent carrier mobility, increased surface area, and controllable interfaces (Yousef *et al.*, 2022a). They are used in various fields including energy conversion and storage, catalysis, electronics/optoelectronics, and sensing. TMDCs are 2D-layered structures that have three atomic layers in the form of X-M-X, where M represents the transition metal and X represents the chalcogen (Yousef *et al.*, 2022a) i.e., the metal is sandwiched between two chalcogens with weak van der Waals forces between the layers (Huang *et al.*, 2019). This makes them effective supports for semiconductor nanoparticles as they will improve charge transport through the heterojunctions formed between the TMDC and the main catalyst. It was found that the active sites that are on the exposed and under-coordinated edge sites are responsible for the catalytic activity. TMDCs show great potential as cocatalysts for semiconductor photocatalysts and are a great potential substitute for noble metal cocatalysts. MoS_2 and WS_2 are widely synthesized and studied TMDCs to date (Huang *et al.*, 2019).

Tungsten disulfide (WS_2) is a two-dimensional material that is abundant in the Earth's crust, has low toxicity, and is cheaper than other TMDCs (Yousef *et al.*, 2022a). It has impressive properties including a tuneable bandgap, high surface area, favorable electrochemical activity, high carrier mobility, biocompatibility, and photocatalytic and electronic efficiency (Yousef *et al.*, 2022a). WS_2 is a well-established photocatalyst for dye degradation and H_2 evolution (Huang *et al.*, 2022). WS_2 is an attractive material for the degradation of organic pollutants as it is a light-absorbing material due to its broad absorption spectrum (Yousef *et al.*, 2022a). WS_2 can have a low indirect bandgap (<1.5 eV) and a higher direct bandgap (>2 eV) depending on the synthesis method (Yousef *et al.*, 2022a). The relatively low bandgap increases the light absorption region to 910 nm which makes the material suitable to be used for redox

reactions required for degrading dyes (Yousef *et al.*, 2022a). The photocatalytic activity of WS_2 is inversely related to its thickness and size. The smaller the size, the larger the bandgap and the higher the photocatalytic activity as more active sites are exposed (Huang *et al.*, 2022). It is frequently used as a cocatalyst for modifying semiconductors. W is sandwiched between two S atoms with strong in-plane bonding while the layers are stacked via weak van der Waals forces (Yousef *et al.*, 2022a). WS_2 is a promising photocatalyst because it has direct bandgap transition, large spin-orbit coupling, and a strong quantum confinement effect (Yousef *et al.*, 2022a).

Since WS_2 and other semiconductors have different bandgaps, when they are coupled together, they form heterostructures that reduce recombination of photogenerated charge carriers, reduce bandgap, improve photocatalytic reactions, increase mass transfer effects, and shift the optical response to the visible light region to effectively harvest solar energy (Yousef et al., 2022, Huang et al., 2022). When the conduction band and valence band are well matched, this results in better separation of the electrons and holes (Yousef *et al.*, 2022a). When WS_2 is used as a cocatalyst, semiconductor-semiconductor or metal-semiconductor heterojunctions are fabricated, and this results in more interfaces being created. This improves charge separation, migration, and photocatalytic activity (Yousef *et al.*, 2022a). It was found that electrons transfer from WS_2 to the semiconductor and holes transfer from the semiconductor's valence band to WS_2's valence band. This results in a more efficient photogenerated charge separation which inhibits exciton recombination and improves the extent to which the semiconductor utilizes sunlight (Huang *et al.*, 2022). WS_2 has two different phases depending on the synthesis method. The phases are the prismatic trigonal phase (2H) and octahedral (1T) phase. The different phases have different properties. 2H-WS_2 is semiconducting, and 1T-WS_2 has metallic properties. The bulk hexagonal WS_2 (2H-WS_2) shows an indirect bandgap however it transitions to a direct bandgap when it is monolayered. Various synthesis techniques exist for synthesizing WS_2, this includes hydrothermal method, sol-gel, chemical deposition, liquid phase exfoliation, mechanical activation method, thermal evaporation, and colloidal method (Yousef *et al.*, 2022a).

2.8.3. Colloidal synthesis:

Material synthesis is a vital part of research regardless of the application. For this research, colloidal synthesis will be the focus of the synthesis of WS_2. Colloidal

synthesis is a wet-chemical synthesis technique that can be used to vary the size, morphology, and thickness of the synthesized materials to achieve different functionalities and it is used as a surfactant directing strategy (Pang et al., 2019; Ndala et al., 2020; Huang et al., 2019). Reaction parameters such as temperature, organic ligands, and precursors can be changed to modify the materials' physical properties (Ndala *et al.*, 2020). Colloidal chemistry is an important synthesis method due to its simple up-scalability for commercialization, tunability, and well-controlled synthesis of TMDCs (Pang *et al.*, 2019). Some of the 2D TMDC materials that have been synthesized using this method include CuS, MoS_2, TaS_2, CdS, InSe, and WS_2 (Pang *et al.*, 2019). These reactions are carried out in the presence of organic ligands containing long hydrocarbon chains such as oleylamine (OLAm) and oleic acid (OA) (Meerbach *et al.*, 2020a). The organic ligands are necessary to control the nucleation and growth of nanomaterials thus controlling the morphology and size of the nanoparticles. On the other hand, ligands hamper electron transport within nanosheets and therefore need to be removed effectively to improve catalytic performance (Meerbach *et al.*, 2020a). The synthesis of photocatalysts via the colloidal method is rarely reported because of the difficulty of removing the organic solvents which usually affects the photocatalytic activity (Meerbach *et al.*, 2020a). **Table 2.2** shows the catalysts that have been used to degrade SODs from literature.

Table 2.2: Catalysts in literature used to degrade SODS.

Catalyst	Dye degraded	Degradation efficacy and time	Reference
Perovskites			
$CsSnBr_3$	Crystal violet (cationic)	73.1% in 6 hrs	(Reyes-Pérez *et al.*, 2018; Bianca Maria Bresolin, 2021)
$CsPbCl_3$	Methyl Orange (anionic)	90% in 80 min	(Huynh *et al.*, 2020)
$CsPbCl_3$	RhB in toluene/ethane (cationic)	90% in 100 min	(Gao *et al.*, 2017; Gu *et al.*, 2023)
$CsPbBr_3$	Methyl Orange (anionic)	57.7% in 90 min	(Zhang *et al.*, 2023)

$CsPbBr_3$	RhB in toluene/ethane (cationic)	89% in 100 min	(Gao *et al.*, 2017; Gu *et al.*, 2023)
$Cs_2Bi_2I_9$-OA	Methylene blue in water (cationic)	62.1% in 60 min	(Bhattacharyya, Chaudhary, and Bhattacharjee, 2019; Bianca Maria Bresolin, 2021)
$Cs_2Bi_2Br_9$-OA	Methylene blue in water (cationic)	26.6% in 60 min	(Bhattacharyya, Chaudhary, and Bhattacharjee, 2019; Bianca Maria Bresolin, 2021)
$Cs_3Bi_2Br_9$	Methylene blue in deionized water (cationic)	99% in 100 min	(Akinbami *et al.*, 2021)
$Cs_3Bi_2Br_9$	Rhodamine B in deionized water (cationic)	100% in 100 min	(Akinbami *et al.*, 2021)
Cs_4PbBr_6	Methylene blue (cationic)	85% in 90 min	(Immanuel *et al.*, 2022)
$CsPbI_3$	Methylene Blue in ethyl alcohol (cationic)	97% in 30 min	(Q. Zhang *et al.*, 2020a)
$Cs_3Bi_2Br_9$-OA NCs	Methylene blue in isopropanol (cationic)	58.8% in 60 min	(Bhattacharyya, Chaudhary, and Bhattacharjee, 2019)
$Cs_3Bi_2Br_9$ NCs	Methylene blue in isopropanol (cationic)	66.3% in 60 min	(Bhattacharyya, Chaudhary, and Bhattacharjee, 2019)
$Cs_2AgBiBr_6$	Rhodamine B (cationic)	~98% in 2 hrs	(Zhang *et al.*, 2019)
Heterostructures			
WS_2/MoS_2	Rhodamine B (cationic)	93% in 90 min	(Kumari *et al.*, 2023)
WS_2/MoS_2	Methylene blue (cationic)	85% in 90 min	(Kumari *et al.*, 2023)
WS_2/MoS_2/BiOCl	Methylene blue (cationic)	99.36% in 240 min	(Kumari *et al.*, 2023)
ZnO/WS_2	Rhodamine B (cationic)	95.71% in 120 min	(Kumari *et al.*, 2023)

TiO_2/ WS_2	Rhodamine B (cationic)	85.1% in 120 min	(Kumari et al., 2023)
γ-$CsPbI_3$/WS_2	Methylene blue (cationic)	100% in 30 min	(Kumari et al., 2023)
$Cs_2Bi_2I_9$-OA/Ag_2S	Methylene blue in water (cationic)	88.8% in 60 min	(Bhattacharyya, Chaudhary, and Bhattacharjee, 2019; Bianca Maria Bresolin, 2021)
$Cs_2Bi_2I_9$-OA/TiO_2	Methylene blue in water (cationic)	83.5% in 120 min	(Bhattacharyya, Chaudhary, and Bhattacharjee, 2019; Bianca Maria Bresolin, 2021)
$Cs_2Bi_2Br_9$-OA/Ag_2S	Methylene blue in water (cationic)	40.13% in 60 min	(Bhattacharyya, Chaudhary, and Bhattacharjee, 2019; Bianca Maria Bresolin, 2021)
$Cs_2Bi_2Br_9$-OA/TiO_2	Methylene blue in water (cationic)	27.6% in 60 min	(Bhattacharyya, Chaudhary, and Bhattacharjee, 2019; Bianca Maria Bresolin, 2021)

2.9. Kinetics and adsorption isotherms

To gain insights into the photodegradation of dyes by transition metal dichalcogenides, researchers often apply kinetics and isotherms studies. This is owed to the reality that Kinetic and adsorption isotherms play crucial roles in explaining the degradation of synthetic organic dyes by photocatalysts. The kinetics of a degradation reaction provide insights into the rate at which the SODS are mineralized by the photocatalysts. The linear plots of the kinetic models give insights into the dye adsorption capacity of the catalyst, rate constants, and rate of adsorption are determined from the slope and intercept (Musah et al., 2022b). This information helps in understanding the efficiency and speed of the degradation, enabling the optimization of photocatalytic conditions for improved degradation performance. Kinetic data also contributes to determining the mechanism of the degradation process, shedding light on the intermediate species formed and their degradation pathways. Adsorption isotherms describe the relationship between the concentration of dye molecules in the solution and the amount of dye adsorbed onto the surface of the photocatalyst. The slopes and intercepts of the adsorption models provide valuable information about the adsorption

capacity and affinity of the photocatalyst for the dye molecules, mean free energy, single or multilayer adsorption, and physisorption or chemisorption adsorption (Musah *et al.*, 2022a). Understanding the adsorption behavior helps in assessing the interaction between the dye and the catalyst surface, which is often the initial step in the degradation process. Adsorption isotherms assist in determining parameters such as equilibrium adsorption capacity, adsorption kinetics, and the adsorption mechanism, which aid in optimizing the photocatalyst's design and performance (Ayawei, Ebelegi and Wankasi, 2017).

By considering both kinetics and adsorption isotherms, the degradation process of SODs by photocatalysts can be understood. This knowledge enables the development of efficient photocatalytic systems with improved degradation capabilities, leading to potential applications in wastewater treatment, environmental remediation, and the removal of SODs in dye-intensive industries is essential. There are six types of BET nitrogen adsorption isotherms. The shape of the isotherm indicates the physical properties of the material’s surface analysed such as the pore size distribution, surface area, and pore volume. As shown in **Figure 2.9** below.

Type I: The material is microporous, and a large portion of the exposed surface is inside the micropores.

Type II: The material is nonporous or macro-porous. The material has unrestricted mono-multilayer gas adsorption.

Type III: This type of adsorption isotherm is not common. The gas’ interaction with the adsorbed layer of gas is greater than the interaction with the material’s surface. This is referred to as adsorbate-adsorbate interactions.

Type IV: This isotherm indicates that the material is mesoporous with pores ranging between 1.5 nm to 100 nm. The quantity of gas adsorbed increases at higher pressures.

Type V: There is little interaction between the adsorbate (gas) and the adsorbent (material). The material is mesoporous.

Type VI: The material is nonporous and multilayer adsorption occurs in a stepwise manner on the nonuniform material surface.

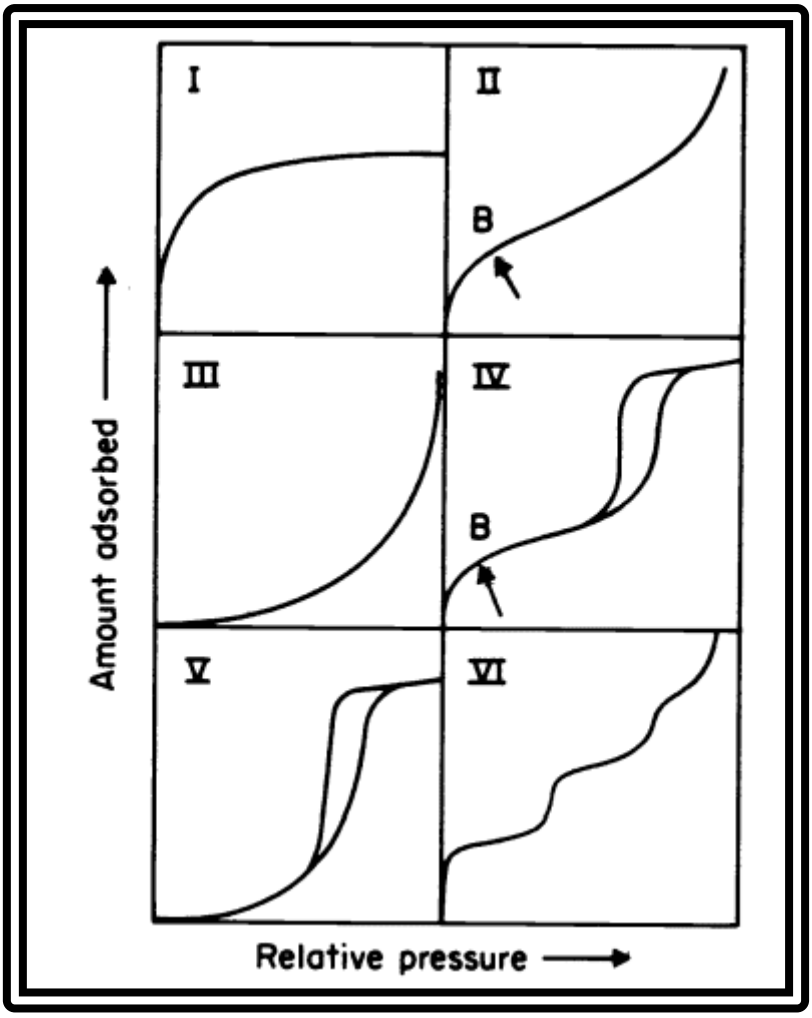

Figure 2.9: BET nitrogen adsorption isotherm Types I-VI (Sing, 1985)

References:

Affat, S.S. (2021) ‘Classifications, Advantages, Disadvantages, Toxicity Effects of Natural and Synthetic Dyes: A review’, University of Thi-Qar Journal of Science, 8(1).

Akinbami, O. et al. (2021) ‘Lead-free Rudorffite-type Cs3Bi2Br9 nanoparticles for photocatalytic degradation of rhodamine B and methylene blue’, Journal of Photochemistry and Photobiology A: Chemistry, 419, p. 113460. Available at: https://doi.org/10.1016/j.jphotochem.2021.113460.

Akpan, U.G. and Hameed, B.H. (2009) ‘Parameters affecting the photocatalytic degradation of dyes using TiO2-based photocatalysts: A review’, Journal of Hazardous Materials, 170(2–3), pp. 520–529. Available at: https://doi.org/10.1016/j.jhazmat.2009.05.039.

Arslan, I., Balcioğlu, I.A. and Tuhkanen, T. (2000) ‘Treatability of simulated reactive dye-bath wastewater by photochemical and non-photochemical advanced oxidation processes’, Journal of Environmental Science and Health, Part A, 35(5), pp. 775–793. Available at: https://doi.org/10.1080/10934520009377002.

Ayawei, N., Ebelegi, A.N. and Wankasi, D. (2017) ‘Modelling and Interpretation of Adsorption Isotherms’, Journal of Chemistry, 2017, pp. 1–11. Available at: https://doi.org/10.1155/2017/3039817.

Benkhaya, S., M’rabet, S. and El Harfi, A. (2020) ‘Classifications, properties, recent synthesis and applications of azo dyes’, Heliyon, 6(1), p. e03271. Available at: https://doi.org/10.1016/j.heliyon.2020.e03271.

Benvenuti, T. et al. (2018) ‘EVALUATION OF DIRECT PHOTOLYSIS, ELECTROOXIDATION AND PHOTOELECTROOXIDATION FOR RHODAMINE-B DEGRADATION’, Brazilian Journal of Chemical Engineering, 35(3), pp. 957–968. Available at: https://doi.org/10.1590/0104-6632.20180353s20170032.

Bhattacharya, A., Goyal, N. and Gupta, A. (2017) ‘Degradation of azo dye methyl red by alkaliphilic, halotolerant Nesterenkonia lacusekhoensis EMLA3: application in alkaline and salt-rich dyeing effluent treatment’, Extremophiles, 21(3), pp. 479–490. Available at: https://doi.org/10.1007/s00792-017-0918-2.

Bhattacharyya, S., Chaudhary, S.P. and Bhattacharjee, S. (2019) ‘Lead-Free Metal Halide Perovskite Nanocrystals for Photocatalysis in Water’, ChemRxiv [Preprint].

Bresolin, B.M., Hammouda, S. Ben and Sillanpää, M. (2019) ‘Methylammonium iodo bismuthate perovskite (CH 3 NH 3) 3 Bi 2 I 9 as new effective visible light-responsive photocatalyst for degradation of environment pollutants’, Journal of Photochemistry and Photobiology A: Chemistry, 376, pp. 116–126. Available at: https://doi.org/10.1016/j.jphotochem.2019.03.009.

Bresolin, B.-M., Park, Y. and Bahnemann, D. (2020) ‘Recent Progresses on Metal Halide Perovskite-Based Material as Potential Photocatalyst’, Catalysts, 10(6), p. 709. Available at: https://doi.org/10.3390/catal10060709.

Channei, D. et al. (2021) ‘Synthesis and Characterization of WO 3 /CeO 2 Heterostructured Nanoparticles for Photodegradation of Indigo Carmine Dye’, ACS Omega, 6(30), pp. 19771–19777. Available at: https://doi.org/10.1021/acsomega.1c02453.

Crini, G. (2006) ‘Non-conventional low-cost adsorbents for dye removal: A review’, Bioresource Technology, pp. 1061–1085. Available at: https://doi.org/10.1016/j.biortech.2005.05.001.

de Mello Donegá, C., Liljeroth, P. and Vanmaekelbergh, D. (2005) ‘Physicochemical Evaluation of the Hot-Injection Method, a Synthesis Route for Monodisperse Nanocrystals’, Small, 1(12), pp. 1152–1162. Available at: https://doi.org/10.1002/smll.200500239.

deQuilettes, D.W. et al. (2019) ‘Charge-Carrier Recombination in Halide Perovskites’, Chemical Reviews, 119(20), pp. 11007–11019. Available at: https://doi.org/10.1021/acs.chemrev.9b00169.

Devi, L.G., Raju, K.S.A. and Kumar, S.G. (2009) ‘Photodegradation of methyl red by advanced and homogeneous photo-Fenton’s processes: A comparative study and kinetic approach’, Journal of Environmental Monitoring, 11(7), pp. 1397–1404. Available at: https://doi.org/10.1039/b900936a.

Forgacs, E., Cserháti, T. and Oros, G. (2004) 'Removal of synthetic dyes from wastewaters: a review', Environment International, 30(7), pp. 953–971. Available at: https://doi.org/10.1016/j.envint.2004.02.001.

Gao, G. et al. (2017) 'Novel inorganic perovskite quantum dots for photocatalysis', Nanoscale, 9(33), pp. 12032–12038. Available at: https://doi.org/10.1039/C7NR04421F.

Ghaly, M.Y., Farah, J.Y. and Fathy, A.M. (2007) 'Enhancement of decolorization rate and COD removal from dyes containing wastewater by the addition of hydrogen peroxide under solar photocatalytic oxidation', Desalination, 217(1–3), pp. 74–84. Available at: https://doi.org/10.1016/j.desal.2007.01.013.

Gu, Y. et al. (2023) 'Nitrogen-Doped Graphene Quantum Dot-Passivated δ-Phase CsPbI3: A Water-Stable Photocatalytic Adjuvant to Degrade Rhodamine B', Molecules, 28(21). Available at: https://doi.org/10.3390/molecules28217310.

Gumerov, F.M. et al. (2014) 'Regeneration of the Catalysts by Supercritical Fluid Extraction', International Journal of Analytical Mass Spectrometry and Chromatography, 02(01), pp. 1–14. Available at: https://doi.org/10.4236/ijamsc.2014.21001.

Harun, N. et al. (2020) IMPACT OF TiO2 AND H2O2 ON PHOTOCATALYTIC DEGRADATION OF PHODAMINE B UNDER ULTRAVIOLET C (UV-C) RADIATION FOR EFFICIENT POLLUTED WASTEWATER TREATMENT, Journal of Optoelectronic and Biomedical Materials.

Hoffmann, M.R. et al. (1995) 'Environmental Applications of Semiconductor Photocatalysis', Chemical Reviews, 95(1), pp. 69–96. Available at: https://doi.org/10.1021/cr00033a004.

Huang, T. et al. (2019) 'Transition Metal Dichalcogenides in Photocatalysts', in Two Dimensional Transition Metal Dichalcogenides. Singapore: Springer Singapore, pp. 107–134. Available at: https://doi.org/10.1007/978-981-13-9045-6_4.

Huang, Y.-J. et al. (2022) 'Improved Mass-Transfer Enhances Photo-Driven Dye Degradation and H 2 Evolution over a Few-Layer WS 2 /ZnO Heterostructure', ACS

Omega, 7(2), pp. 2217–2223. Available at: https://doi.org/10.1021/acsomega.1c05756.

Hussain, T. and Wahab, A. (2018) 'A critical review of the current water conservation practices in textile wet processing', Journal of Cleaner Production, 198, pp. 806–819. Available at: https://doi.org/10.1016/j.jclepro.2018.07.051.

Huynh, K.A. *et al.* (2020) 'Halide perovskite photocatalysis: progress and perspectives', *Journal of Chemical Technology & Biotechnology*, 95(10), pp. 2579–2596. Available at: https://doi.org/10.1002/jctb.6342.

Immanuel, P.N. et al. (2022) 'Enhanced photocatalytic activity of Cs4PbBr6/WS2 hybrid nanocomposite', ChemRxiv [Preprint].

Islam, J. and Hossain, A.K.M.A. (2020a) 'Narrowing band gap and enhanced visible-light absorption of metal-doped non-toxic CsSnCl 3 metal halides for potential optoelectronic applications', RSC Advances, 10(13), pp. 7817–7827. Available at: https://doi.org/10.1039/C9RA10407K.

Jacopo Prisco (2017) The color purple: How an accidental discovery changed fashion forever, CNN.

Joseph, A. and Aneesh, P.M. (2022) 'Efficient degradation of methylene blue: A comparative study using hydrothermally synthesized SnS2, WS2 and VS2 nanostructures', Materials Research Bulletin, 146, p. 111623. Available at: https://doi.org/10.1016/j.materresbull.2021.111623.

Kanhere, P. and Chen, Z. (2014) 'A Review on Visible Light Active Perovskite-Based Photocatalysts', Molecules, 19(12), pp. 19995–20022. Available at: https://doi.org/10.3390/molecules191219995.

Kant, R. (2012) 'Textile dyeing industry an environmental hazard', Natural Science, 04(01), pp. 22–26. Available at: https://doi.org/10.4236/ns.2012.41004.

Katheresan, V., Kansedo, J. and Lau, S.Y. (2018) 'Efficiency of various recent wastewater dye removal methods: A review', Journal of Environmental Chemical Engineering, 6(4), pp. 4676–4697. Available at: https://doi.org/10.1016/j.jece.2018.06.060.

Kumari, H. *et al.* (2023) ‘A Review on Photocatalysis Used For Wastewater Treatment: Dye Degradation’, *Water, Air, & Soil Pollution*, 234(6), p. 349. Available at: https://doi.org/10.1007/s11270-023-06359-9.

Kwon, S.G. and Hyeon, T. (2011) ‘Formation Mechanisms of Uniform Nanocrystals via Hot-Injection and Heat-Up Methods’, Small, 7(19), pp. 2685–2702. Available at: https://doi.org/10.1002/smll.201002022.

Lee, J.S. and Jang, J. (2014) ‘Hetero-structured semiconductor nanomaterials for photocatalytic applications’, Journal of Industrial and Engineering Chemistry, 20(2), pp. 363–371. Available at: https://doi.org/10.1016/j.jiec.2013.11.050.

Lellis, B. et al. (2019a) ‘Effects of textile dyes on health and the environment and bioremediation potential of living organisms’, Biotechnology Research and Innovation, 3(2), pp. 275–290. Available at: https://doi.org/10.1016/j.biori.2019.09.001.

Mahdi, M.H., Mohammed, T.J. and Al-Najar, J.A. (2021) ‘Advanced Oxidation Processes (AOPs) for treatment of antibiotics in wastewater: A review’, IOP Conference Series: Earth and Environmental Science, 779(1), p. 012109. Available at: https://doi.org/10.1088/1755-1315/779/1/012109.

Martínez-Huitle, C.A. and Brillas, E. (2009) ‘Decontamination of wastewaters containing synthetic organic dyes by electrochemical methods: A general review’, Applied Catalysis B: Environmental, 87(3–4), pp. 105–145. Available at: https://doi.org/10.1016/j.apcatb.2008.09.017.

Meerbach, C. et al. (2020) ‘General Colloidal Synthesis of Transition-Metal Disulfide Nanomaterials as Electrocatalysts for Hydrogen Evolution Reaction’, ACS Applied Materials & Interfaces, 12(11), pp. 13148–13155. Available at: https://doi.org/10.1021/acsami.9b21607.

Mokif, L.A. (2019) ‘Removal Methods of Synthetic Dyes from Industrial Wastewater: A review’, Mesopo. Environ. J, 5(1), pp. 23–40. Available at: https://doi.org/10.31759/mej.2019.5.1.0040.

Musah, M. et al. (2022) ‘Adsorption Kinetics and Isotherm Models: A Review’, Caliphate Journal of Science and Technology, 4(1), pp. 20–26. Available at: https://doi.org/10.4314/cajost.v4i1.3.

Ndala, Z. et al. (2020) ‘Evaluating the Effect of Varying the Metal Precursor in the Colloidal Synthesis of MoSe2 Nanomaterials and Their Application as Electrodes in the Hydrogen Evolution Reaction’, Nanomaterials, 10(9), p. 1786. Available at: https://doi.org/10.3390/nano10091786.

Nidheesh, P.V., Gandhimathi, R. and Ramesh, S.T. (2013) ‘Degradation of dyes from aqueous solution by Fenton processes: a review’, Environmental Science and Pollution Research, 20(4), pp. 2099–2132. Available at: https://doi.org/10.1007/s11356-012-1385-z.

Nidheesh, P.V., Zhou, M. and Oturan, M.A. (2018) ‘An overview on the removal of synthetic dyes from water by electrochemical advanced oxidation processes’, Chemosphere, 197, pp. 210–227. Available at: https://doi.org/10.1016/j.chemosphere.2017.12.195.

Pang, Y. et al. (2019) ‘Photocatalysts: Colloidal Single-Layer Photocatalysts for Methanol-Storable Solar H 2 Fuel (Adv. Mater. 49/2019)’, Advanced Materials, 31(49), p. 1970348. Available at: https://doi.org/10.1002/adma.201970348.

Rafiq, A. et al. (2021a) ‘Photocatalytic degradation of dyes using semiconductor photocatalysts to clean industrial water pollution’, Journal of Industrial and Engineering Chemistry, 97, pp. 111–128. Available at: https://doi.org/10.1016/j.jiec.2021.02.017.

Reyes-Pérez, F. *et al.* (2018) ‘Visible-Light-Enhanced Photocatalytic Activity of Totally Inorganic Halide-Based Perovskite’, *ChemistrySelect*, 3(36), pp. 10226–10235. Available at: https://doi.org/10.1002/slct.201801564.

Robinson, T. et al. (2001) ‘Remediation of dyes in textile effluent: a critical review on current treatment technologies with a proposed alternative’, Bioresource Technology, 77(3), pp. 247–255. Available at: https://doi.org/10.1016/S0960-8524(00)00080-8.

Saravanan, R., Gracia, F. and Stephen, A. (2017) ‘Basic Principles, Mechanism, and Challenges of Photocatalysis’, in, pp. 19–40.

Shaheen, A. (2010) Band Structure and Electrical Conductivity in Semiconductors. Available at: https://www.researchgate.net/publication/280092391_Band_Structure_and_Electrical_Conductivity_in_Semiconductors.

Shamsi, J. et al. (2019) ‘Metal Halide Perovskite Nanocrystals: Synthesis, Post-Synthesis Modifications, and Their Optical Properties’, Chemical Reviews, 119(5), pp. 3296–3348. Available at: https://doi.org/10.1021/acs.chemrev.8b00644.

Sharma, J., Sharma, S. and Soni, V. (2021) ‘Classification and impact of synthetic textile dyes on Aquatic Flora: A review’, Regional Studies in Marine Science. Elsevier B.V. Available at: https://doi.org/10.1016/j.rsma.2021.101802.

Singh, K. and Arora, S. (2011) ‘Removal of synthetic textile dyes from wastewaters: A critical review on present treatment technologies’, Critical Reviews in Environmental Science and Technology, 41(9), pp. 807–878. Available at: https://doi.org/10.1080/10643380903218376.

Sun, J. (2014) Development of Inorganic-Organic Hybrid Materials for Waste Water Treatment. Available at: https://www.researchgate.net/publication/314081363_Development_of_Inorganic-Organic_Hybrid_Materials_for_Waste_Water_Treatment (Accessed: 23 March 2023).

Tkaczyk, A., Mitrowska, K. and Posyniak, A. (2020) ‘Synthetic organic dyes as contaminants of the aquatic environment and their implications for ecosystems: A review’, Science of the Total Environment. Elsevier B.V. Available at: https://doi.org/10.1016/j.scitotenv.2020.137222.

Vlok, E. (2006) The Textile and Clothing Industry in South Africa. Available at: https://library.fes.de/pdf-files/iez/03796/16suedafrika.pdf (Accessed: 22 March 2023).

Wang, J. et al. (2021) ‘Recent advances in metal halide perovskite photocatalysts: Properties, synthesis and applications’, Journal of Energy Chemistry. Elsevier B.V., pp. 770–785. Available at: https://doi.org/10.1016/j.jechem.2020.06.024.

Warade, A. et al. (2016) STUDY OF REMOVAL TECHNIQUES FOR DYES BY ADSORPTION: A REVIEW, IJARIIE. Available at: http://ijariie.com/AdminUploadPdf/STUDY_OF_REMOVAL_TECHNIQUES_FOR_DYES_BY_ADSORPTION__A_REVIEW_ijariie2687.pdf (Accessed: 25 March 2023).

Wong, C.C. and Chu, W. (2003) ‘The direct photolysis and photocatalytic degradation of alachlor at different TiO2 and UV sources’, Chemosphere, 50(8), pp. 981–987. Available at: https://doi.org/10.1016/S0045-6535(02)00640-9.

Yaseen, D.A. and Scholz, M. (2016) ‘Shallow pond systems planted with Lemna minor treating azo dyes’, Ecological Engineering, 94, pp. 295–305. Available at: https://doi.org/10.1016/j.ecoleng.2016.05.081.

Yousef, A. et al. (2022) ‘Recent Progress in WS2-Based Nanomaterials Employed for Photocatalytic Water Treatment’, Catalysts, 12(10), p. 1138. Available at: https://doi.org/10.3390/catal12101138.

Zafar, Z., Fatima, R. and Kim, J.-O. (2021) ‘Experimental studies on water matrix and influence of textile effluents on photocatalytic degradation of organic wastewater using Fe–TiO2 nanotubes: Towards commercial application’, Environmental Research, 197, p. 111120. Available at: https://doi.org/10.1016/j.envres.2021.111120.

Zhang, C. et al. (2023) ‘Based on Z-scheme heterojunction CsPbBr 3 /UiO-66 composite photocatalytic degradation’, Applied Organometallic Chemistry, 37(7). Available at: https://doi.org/10.1002/aoc.7122.

Zhang, Q. et al. (2020a) ‘Enhanced Photocatalytic Property of γ-CsPbI 3 Perovskite Nanocrystals with WS 2’, ACS Sustainable Chemistry & Engineering, 8(2), pp. 1219–1229. Available at: https://doi.org/10.1021/acssuschemeng.9b06451.

Zhang, Y. et al. (2020) ‘A “Tips and Tricks” Practical Guide to the Synthesis of Metal Halide Perovskite Nanocrystals’, Chemistry of Materials, 32(13), pp. 5410–5423. Available at: https://doi.org/10.1021/acs.chemmater.0c01735.

Zhang, Z. et al. (2019) ‘Stable and Highly Efficient Photocatalysis with Lead-Free Double-Perovskite of Cs 2 AgBiBr 6’, Angewandte Chemie International Edition, 58(22), pp. 7263–7267. Available at: https://doi.org/10.1002/anie.201900658.

Ziarani, G.M. et al. (2018) ‘Introduction and Importance of Synthetic Organic Dyes’, in Metal-Free Synthetic Organic Dyes. Elsevier, pp. 1–7. Available at: https://doi.org/10.1016/B978-0-12-815647-6.00001-7.

Chapter 3: RESEARCH METHODOLOGY

3.1. Chemicals and reagents:

Cesium carbonate (Cs_2CO_3, 99.995%), bismuth (III) bromide ($BiBr_3$ ≥98%), oleylamine (OLA), oleic acid (OA, technical grade, 90%), tungstic acid (H_2WO_4) (99%), thiourea ($(CS(NH_2)_2$) (ACS reagent, ≥99%), rhodamine B (≥95% HPLC), and methyl red (ACS

reagent, crystalline) were purchased from Sigma Aldrich. Sodium chloride (NaOH) pellets, nitric acid (HNO_3, 55%), hydrogen peroxide (H_2O_2, 50%, 200 vols), hexane fraction, ethanol (99,9%), and dimethyl sulfoxide (DMSO) were also purchased from ACE chemicals. Ultrapure water (UPW) with 18.2 MΩ cm resistivity was obtained from the Millipore Direct-Q water system.

3.2. Synthesis methods:

3.2.1. Hot-injection synthesis of $Cs_3Bi_2Br_9$

3.2.1.1. Preparation of Cesium Oleate (Cs-OA):

OA (5 mL) was poured into a three-necked round bottom flask under an inert atmosphere. Cs_2CO_3 (0.1 mmol) was placed in the flask and the temperature was ramped up to 150ºC. 32.5 mg in 5 ml OA. Since there was 5.015 mmol of Cs and 15.625 mmol of OA, the Cs: OA ratio was 1:3. This temperature was maintained for an hour to allow for the formation of Cs-OA (Lu *et al.*, 2019). The reaction setup is shown in **Figure 3.1**.

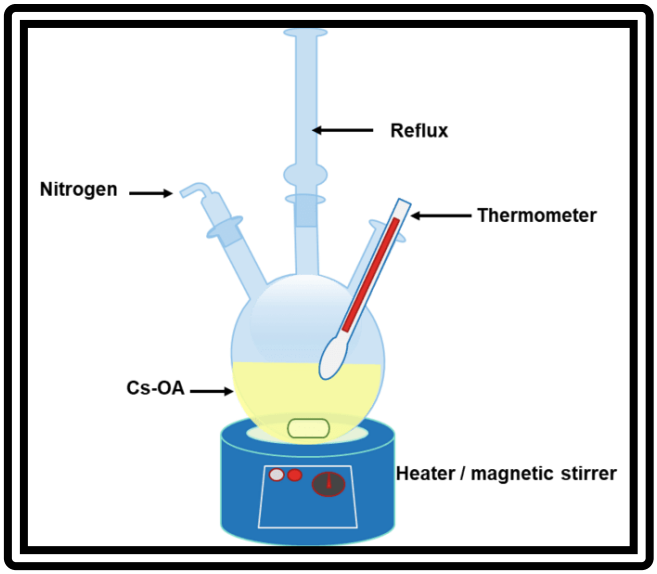

Figure 3.1: Cs-OA synthesis setup

3.2.1.2. Synthesis of Perovskite NPs by hot-injection method:

In a different 100 mL three-necked round bottom flask, $BiBr_3$ (0.3 mmol) was added to a mixture of OA (2.5 mL) and OLA (2.5 mL). The solution was heated to 210ºC and the temperature was maintained for 1 h with constant magnetic stirring. Thereafter, Cs-OA (1 mL) was injected into the solution containing $BiBr_3$ and stirred for 1 min

(Akinambi, et. al., 2021). After the addition of Cs-OA, the colloidal mixture turned yellowish-green indicating the nucleation of the $Cs_3Bi_2Br_9$ nanoparticles (Yang et al., 2017). The flask was placed in an ice bath until it cooled to room temperature. The yellowish-green nanoparticles were washed using hexane and centrifuged at 800 RPM for 10 minutes. The reaction setup and an image of the resultant product are shown in **Figure 3.2**. The product yield was 62%.

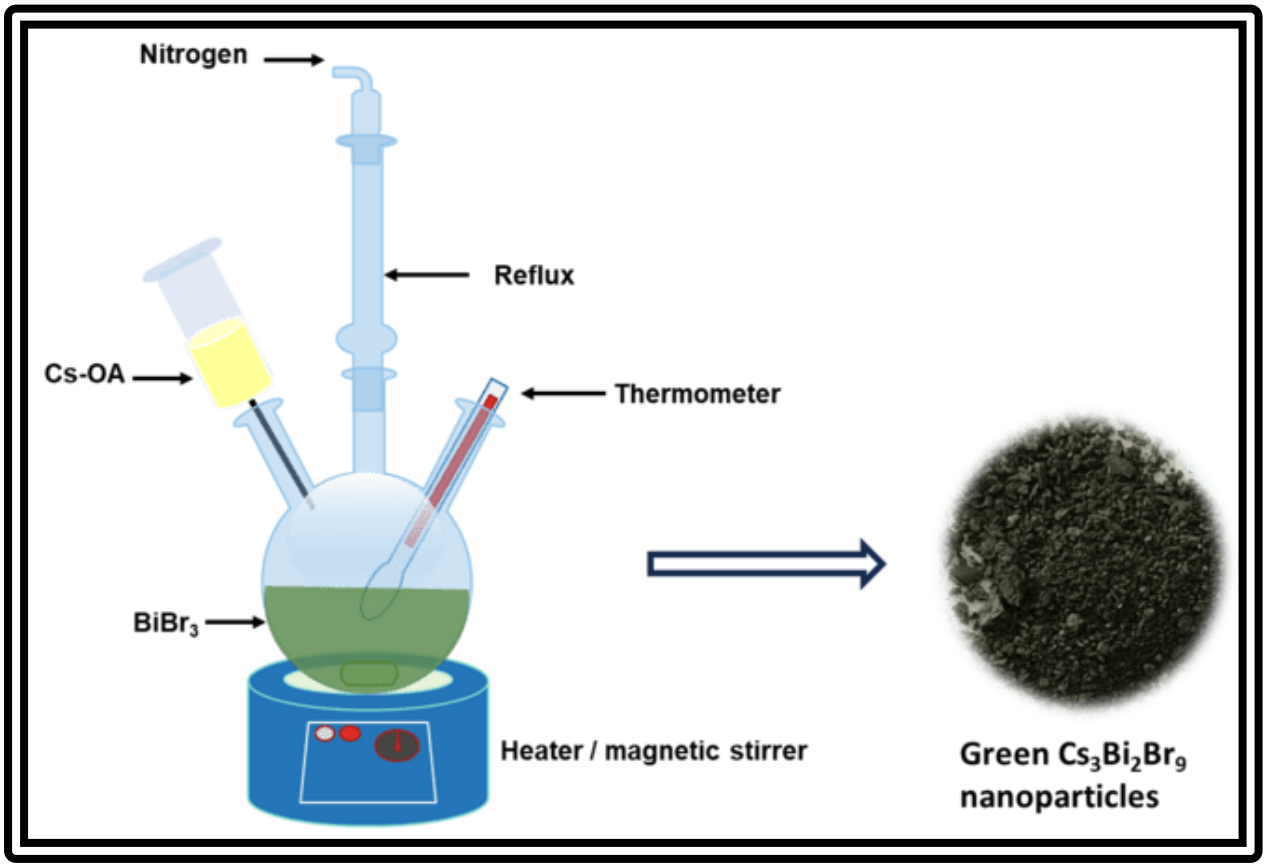

Figure 3.2: $Cs_3Bi_2Br_9$ hot-injection synthesis set-up and the synthesized nanoparticles

3.2.3. Synthesis of tungsten disulfide (WS_2)

OLA (17 mL) was degassed using nitrogen with constant stirring at 120 ℃ in a 3-neck round bottom flask for 20 minutes. H_2WO_4 (2.5 mmol) was added to OLA followed by $CS(NH_2)_2$ (10.5 mmol). The experimental setup is shown in **Figure 3.3**. The temperature was rapidly increased to 320 ºC and maintained for 150 minutes to allow the precursors to decompose and form WS_2 nanoparticles. At the end of the reaction, the black precipitate was poured into centrifuge tubes and left to cool for 5 minutes.

The nanoparticles were then flocculated with ethanol. A mixture of ethanol and hexane (1:1) was used for washing the nanoparticles multiple times, followed by centrifugation (Gqoba *et al.*, 2021). The material was left to dry at room temperature. The product yield was 89%.

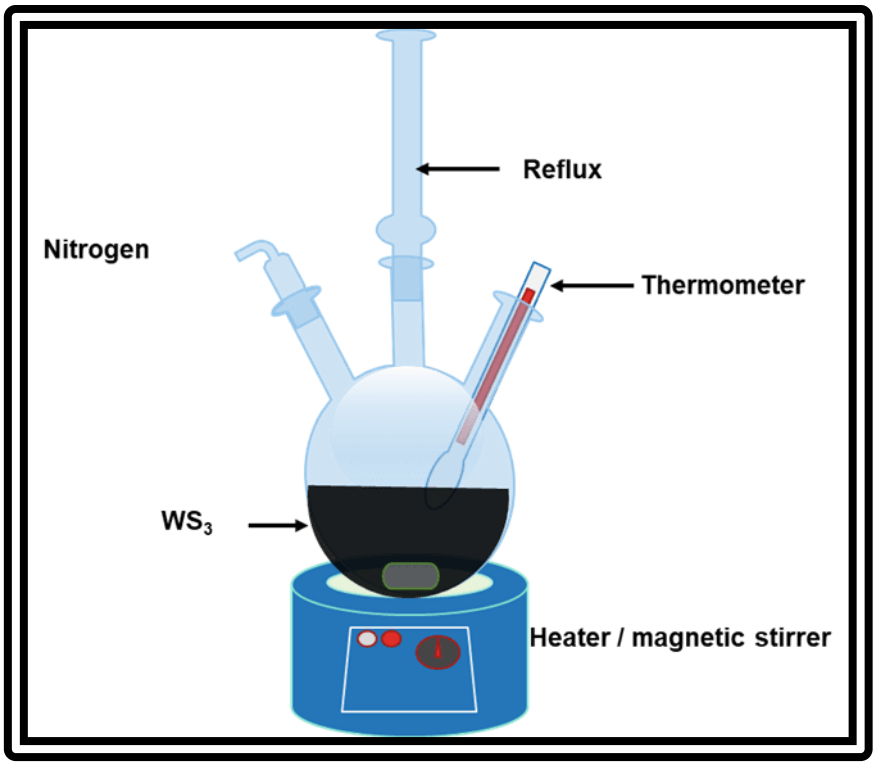

Figure 3.3: WS_2 colloidal synthesis setup

3.2.4. Preparation of $Cs_3Bi_2Br_9/WS_2$:

WS_2 (0.2 mol) and $Cs_3Bi_2Br_9$ (0.8 mol), 1:4 ratio, were placed in a centrifuge tube. DMSO (10 mL) was added to the tube. The heterogeneous mixture was ultrasonicated for 30 minutes. The resultant heterostructure was purified using ethanol and centrifuged at 8000 RPM for 10 minutes. This method is similar to the method used by (Jiang *et al.*, 2020) to prepare Cs_4PbBr_6. The heterostructure particles are shown in **Figure 3.4**. There is a van der Waals interaction expected between $Cs_3Bi_2Br_9$ and WS_2 in the heterostructure (Fang *et al.*, 2018; Singh and Ahuja, 2022).

Figure 3.4: $Cs_3Bi_2Br_9/WS_2$ nanoparticles

3.3. Characterisation techniques:

3.3.1. Powder X-ray diffraction (PXRD):

PXRD is a non-destructive characterization method that is used for analysing chemical composition, crystallographic structure, and physical properties such as grain size, lattice parameters, and phase composition (Askeland, 2011; Shand and Jin, 2020). A diffracted X-ray beam is obtained at a specific angle after a material is struck with an X-ray beam as shown in the figure below. **Figure 3.5** shows the X-rays that strike the material at certain crystallographic planes and specific angles. When the X-rays satisfy the Bragg's law conditions, i.e.

$$\sin \Theta = \frac{\lambda}{2d} \quad \textbf{(3.1)}$$

where Θ is the angle at which the X-rays hit the material, λ is the wavelength, and d is the distance between the crystallographic planes, the X-rays are thus reinforced. However, when the Bragg's law conditions are not satisfied, the diffracted X-rays are eliminated (Askeland, 2011).

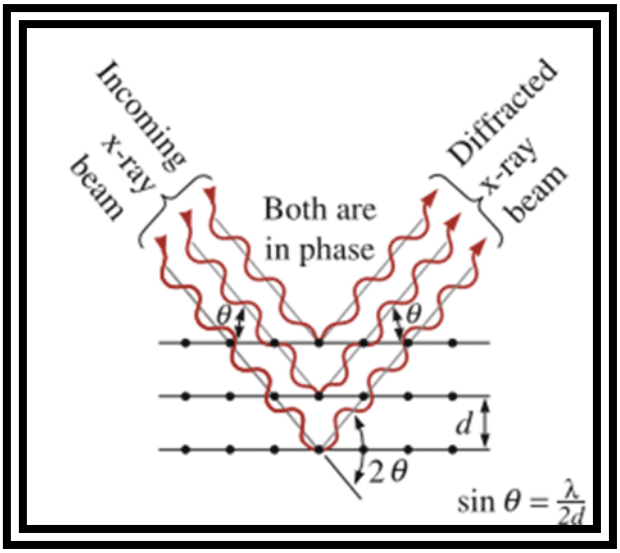

Figure 3.5: Interactions between X-rays and the material (Askeland, 2011)

A diffraction pattern is created by the X-rays' interactions with the sample, which is diffracted in accordance with Bragg's law,

$$\sin \Theta = \lambda/2dhkl \quad \textbf{(3.2)}$$

where Θ is the half-length between the diffracted and original X-ray beam, λ is the wavelength of the X-rays and d_{hkl} is the interplanar spacings between the planes (Khan et al., 2022). A diffraction pattern is produced with peaks that have different intensities. The different intensities correspond to the different growth rates of the lattice planes in different directions (Sahu and Samanta, 2021a). The identity of the material is determined by matching the diffraction pattern with similar diffraction patterns contained in common crystallographic databases such as the International Centre for Diffraction Data (ICDD) (Khan, Malik, and Bilal, 2022). The PXRD analyses were done using Bruker D2 XRD at an X-ray wavelength of 1.5406 Å.

3.3.2. Brunauer-Emmett-Teller (BET):

The BET analysis approach employs gas adsorption to determine the pore volume, pore size, and surface area of various materials, which can be porous, amorphous, or crystalline. BET surface area is measured in unit area per kilogram of sample (m^2/g). This technique employs nitrogen gas because it is abundant on the entire surface of nanomaterials. The volume of N_2 gas adsorbed in infinite layers without interlayer interaction is used to calculate the results. The Langmuir theory can be applied to each adsorbed layer of N_2 gas to calculate the BET surface area:

$$S_{BET} = = \frac{V_0 N_A s}{M_v} \quad \textbf{(3.3)}$$

Where V_0 denotes the volume of an adsorbed gas monolayer, N_A denotes Avogadro's number, M_v denotes the molar volume of the gas adsorbate, and 's' denotes the surface area of a single gas layer adsorbed onto the sample (Palchoudhury, Baalousha and Lead, 2015). The surface area helps to understand how the material interacts with its environment. The surface area affects physical properties such as moisture retention, shelf-life, and catalytic activity. For the analyses of the synthesized samples, BET analysis was conducted using the TriStar II Plus 3.03. The Barrett-Joyner-Halenda (BJH) and Dollimore-Heal (D-H) desorption methods were used to determine pore size distribution.

3.3.3. Thermogravimetric analysis (TGA):

This method is used to determine the thermal stability and volatile components of materials. The sample is placed on a pan with a weighing balance in a furnace and the changes in mass are monitored as the temperature is increased at a constant rate. TGA is run under an inert atmosphere. It can be used to determine residual metal content, moisture content, oxidation, loss of solvent, and pyrolysis (Olatunji *et al.*, 2018). TGA results were obtained using Perkin Elmer TGA 4000.

3.3.4. Transmission electron microscopy (TEM):

TEM is a powerful tool for imaging individual nanoparticles, particle size distribution, and determining crystal structures at a high resolution. A transmission electron microscope works by passing a high-energy electron beam over a sample, it detects regions of intense electron intensity by collecting electrons that are transmitted back from the material to the detector. TEM is used for analyzing particles in the nano- and micro-size scales (Sarabandi, Gharehbeglou and Jafari, 2020). The TEM images were obtained using the FEI Tecnai T12a TEM microscope. The particle size distribution curves were obtained using ImageJ.

3.3.5. Scanning electron microscopy and Energy dispersive X-ray spectroscopy (SEM-EDS):

This technique is used to analyse a sample's surface, morphology, size, and size distribution by scanning an electron beam over the surface of the material at the micro

and nanoscale. After the electrons hit the sample specimen, the sample deflects electrons and X-rays. Detectors pick up the signal of the deflected electrons, backscattered electrons, and secondary electrons to produce an image of the sample. When SEM is used with EDX spectroscopy, it can determine the chemical composition of the sample (Marshall, 1991).

3.3.6. Zeta potential analysis:

This approach determines a material's zeta potential, which is a physical property displayed by particles in suspension. It helps to predict long-term stability. It indicates the surface charge and dispersion stability of a material (Clogston & Patri, 2011a; Zeta Potential - An Introduction in 30 Minutes, 2020). It is especially important for photocatalysts as good dispersion stability results in better photocatalytic activity. High-value zeta potential (+30 or -30) is an indicator of high dispersion stability of the colloidal solution. A zeta potential of 30 or above, either negative or positive, indicates that the nanoparticles are strongly anionic or strongly cationic. Neutral nanoparticles and colloidal solutions have zeta potentials ranging from -10 to +10. The electrophoretic mobility of the nanoparticles is determined using laser Doppler velocimetry after an electric field is introduced over the sample (Zeta Potential - An Introduction in 30 Minutes, 2020). The Zetasizer nano series Nano-ZS was used to assess zeta potential. and the cells used are the Zetasizer nano series disposable folded capillary cells with gold electrodes. The zeta potential of the SODs and photocatalysts was measured as a function of pH by mixing them with UPW to make a suspension and adjusting the pH using the prepared HNO_3 and NaCl solutions.

3.3.7. Ultraviolet-visible spectroscopy UV-vis:

This technique is based on the absorbance of ultraviolet or visible light by the sample. It operates by illuminating the sample with a light source whose wavelength ranges from ultraviolet to visible light, i.e., 190-900 nm. The instrument compares the intensity of light absorbed, transmitted, or reflected by the sample to the intensity of light absorbed, transmitted, or reflected by the reference sample. to produce the absorbance spectrum (Djurisic, Chen and Leung, 2013; Quevedo *et al.*, 2021). The Analytik Jena specord 50 UV-vis spectrophotometer was used to analyse the bandgap of the photocatalysts. This technique will also be used to analyse dye photodegradation progression in the next chapter.

3.3.7.1. HOMO and LUMO levels of $Cs_3Bi_2Br_9$ and WS_2:

The valence and conduction bands of photocatalysts can be calculated using the bandgap values determined from the UV-vis results. The equations are below:

$$E_{CB} = \chi - E^e\text{-}0.5E_g \quad \textbf{(3.4)}$$

$$E_{VB} = E_{CB} + E_g \quad \textbf{(3.5)}$$

E_{CB} and E_{VB} are the valence and conduction bands respectively. E_g is the bandgap, E^e is the energy of free electrons vs. hydrogen (4.5 eV) and χ represents the electronegativity of the photocatalyst. The formula for calculating the electronegativity is described below.

$$\chi = [x(\mathrm{A})^a\, x(B)^b\, x(C)^c]^{1/(a+b+c)} \quad \textbf{(3.6)}$$

In this equation, $x(\mathrm{A})$, $x(B)$ and $x(C)$ represent the electronegativity values of elements A, B, and C which the photocatalyst is comprised of. The lower-case alphabets, a, b, and c, represent the number of the corresponding A, B, and C elements (de Barros Santos et al., 2011; Wang et al., 2016).

3.3.8. Liquid chromatography-mass spectrometry (LC-MS):

To separate distinct chemicals in a liquid sample, this technology combines two different processes: liquid chromatography and mass spectroscopy. The sample components are separated using liquid chromatography and then introduced to the mass spectrophotometer. The MS identifies positively charged ions. The information provided by the data includes the molecular weight, structure, identification, and quantity of individual sample components (Tilvi, Majik and Singh, 2014).

3.3.9. Chemical oxygen demand (COD) analysis:

COD is a water quality metric that reflects the quantity of oxygen that can be absorbed by processes in a sample and is frequently used to assess the success of a water treatment method. COD is typically defined as the amount of oxygen consumed per volume of solution(Li and Liu, 2019). COD detection quantifies the organic matter in water. The higher the COD detected, the higher the organic pollution in the water. COD measurements are done on dye samples before and after degradation. A decrease in COD indicates the adsorption of dyes onto the photocatalysts with degradation (Nagaraja *et al.*, 2012a). The COD measurements were measured using the

Spectroquant Pharo 300 spectrophotometer, the samples were added into 25-1500 mg/l COD reagent cells, and the ISCO RECORD sample reactor was used to digest/heat the samples. The blank and standard solutions were prepared and used to ensure the measurement accuracy of the spectrophotometer. A micropipette was used to measure 3 ml of each sample and the samples were added to the separate sample reagent cells. The samples and COD reagents were then mixed by inverting the cell multiple times. The cells were placed in the reactor to digest at 148ºC for 2 hours. After digestion, the samples were removed from the reactor and were aggregated for the last time. They were left to cool for 30 minutes. The COD measurements were conducted, and mineralization efficiency was calculated using the formula below.

$$Mineralization\ efficiency\% = (1 - CODt/CODi) \times 100 \quad \textbf{(3.7)}$$

Where COD_t is the COD at time t and COD_i is the COD of the initial dye sample before photodegradation.

3.4. Photodegradation experimental set-up:

The photocatalytic activity of the nanoparticles produced was determined using the setup shown in **Figure 3.6** below. The photocatalytic nanoparticles were added to aqueous solutions containing dyes at different concentrations. To establish adsorption-desorption equilibrium, the solutions were magnetically agitated for 40 minutes in the dark. Then the solar-simulated light source (180 W) provided illumination to the heterogenous mixture. The rate of photodegradation was examined using UV-vis spectroscopy, liquid chromatography-mass spectroscopy, and chemical oxygen demand (COD).

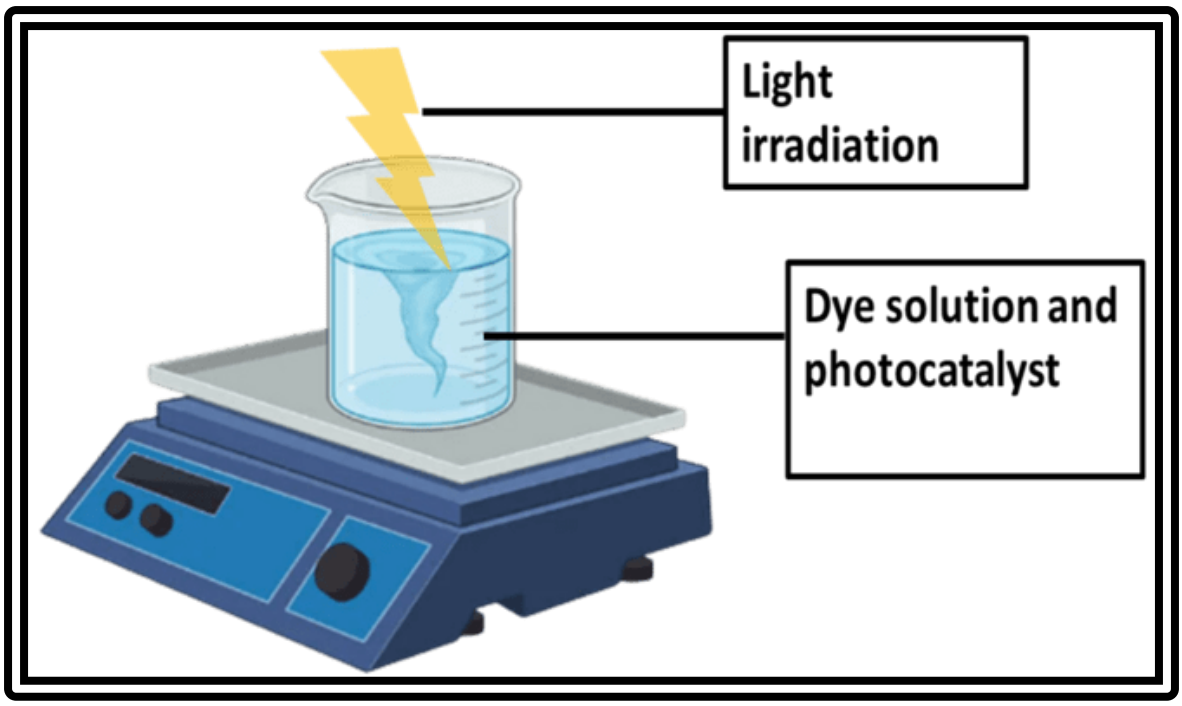

Figure 3.6: Photocatalysis experimental setup

3.5. Optimization of photodegradation efficiency:

To develop a dye degradation method that is efficient and suitable for use at an industrial scale, these parameters should be varied at a lab scale to determine the optimum conditions for dye removal (Katheresan, Kansedo and Lau, 2018). It is important to vary different parameters that influence the catalytic degradation by using the one-factor-at-a-time optimization method. This means that only one factor will be varied while the others are held constant (Abdel-Rahman *et al.*, 2020). The parameters that were varied in this project were initial dye concentration, catalyst loading, solution pH, and photodegradation cycles.

3.6. Data processing:

3.6.1. Degradation efficiency:

This refers to the percentage of dye degraded by the photocatalyst and light source. The formula is given below:

$$\eta = (A_0 - A)/A_0 \times 100 \quad \textbf{(3.8)}$$

η is degradation efficiency A_0 is the initial dye absorbance and A is the dye absorbance after the irradiation time. This formula is used for pH, dye concentration, and catalyst loading studies. It helps determine the dye degradation efficiency of the

photocatalyst under different conditions (Kozuch and Martin, 2012; Nagaraja *et al.*, 2012a; Meerbach *et al.*, 2020b).

3.6.2. Turnover number (TON) and turnover frequency (TOF):

TON and TOF are very important for determining the efficiency of a catalyst. TON is a measure of catalyst activity. In heterogeneous catalysis, it is difficult to precisely measure TON because it is dependent on the size of the catalyst surface, yet the catalyst does not have a uniform size, and the exact number of active sites on the catalyst surface cannot be determined. TOF is the number of dye molecules that can be mineralized by one catalyst molecule per second, minute, or hour (Sahraie *et al.*, 2015; Rothenberg, 2017; Hussain Chowdhury *et al.*, 2022).

Turnover number (TON) = $((moles\ of\ degraded\ dye\ during\ irradiation\ time)/(moles\ of\ photocatalyst)) \times 100$ **(3.9)**

Turnover frequency (TOF) = $TON/Time$ **(3.10)**

TOF is the maximum number of catalytic cycles reached by each accessible surface site per unit of time. TOF is the ratio of TON and time (s) (Vattikuti *et al.*, 2019; Q. Zhang *et al.*, 2020a).

3.6.3. Adsorption capacity:

This is the amount of pollutant removed by the catalyst from aqueous solution per unit time.

$$qe = (C_i - C_e) \times \frac{V}{M} \quad \textbf{(3.11)}$$

Where q_e is the adsorption capacity ($mg.g^{-1}$), C_i is the initial dye concentration, C_t is the dye concentration at time t ($mg.L^{-1}$), V is the volume of the dye solution (L), and M represents the mass of the photocatalyst (g) (Song et al., 2021).

3.6.4. Adsorption kinetic modeling:

The kinetics of SOD adsorption onto the photocatalysts can be described using the equations below:

3.6.4.1. Pseudo first-order (Largergren model)

According to this model, the rate of change in dye degradation at reaction time t is linearly proportional to the difference in dye concentration and rate of dye degradation

from solution by the adsorbent. The rate equation for investigating dye adsorption is provided by:

$$\frac{dq_t}{d_t} = k_t(q_e - q_t) \quad \textbf{(3.12)}$$

Where q_e denotes the amount of dye adsorbed at equilibrium ($mg.g^{-1}$), q_t denotes the photocatalyst's adsorption capacity of the dye at time t ($mg.g^{-1}$), and k_t represents the pseudo-first-order adsorption rate constant (min^{-1}). Photocatalytic reaction pseudo-first-order reaction rate equation:

$$\ln A_t - \ln A_0 = -kt \quad \textbf{(3.13)}$$

A_0 and A_t are the dye absorbance values at time t=0 and t=t and k is the rate constant. Equation 2 below is applied for t= 0 to t=t and $q_t = 0$ to $q_t = q_e$

$$\log (q_e - q_t) = \log(q_e) - \left(\frac{k_1}{2.303}\right)t \quad \textbf{(3.14)}$$

The $\log(q_e-q_t)$ vs t gives a linear slope from which k_t can be calculated using the slope and q_e can be calculated using the intercept (Saka, 2003; Rothenberg, 2017).

3.6.4.2. Pseudo-second-order:

The pseudo-second-order adsorption rate constant is given as the equation below:

$$\frac{dq_t}{dt} = k_2(q_e - q_t)^2 \quad \textbf{(3.15)}$$

The integrated equation for boundary conditions t=0 to t=t, and $q_t = 0$ and $q_t = q_e$ is below:

$$\frac{1}{q_e - q_t} = \frac{1}{q_e} + kt \quad \textbf{(3.16)}$$

k_2 is the rate constant for the pseudo-second-order adsorption process ($g.mg^{-1}.min^{-1}$)
The linear forms of the second-order kinetic model are expressed below:

$$\ln(q_e-q_t) - \ln(q_e)-k_1t \quad \textbf{(3.17)}$$

$$\frac{t}{q_t} = \frac{1}{k_2 q_e^2} + \frac{1}{q_e}t \quad \textbf{(3.18)}$$

The linear t/q_t vs. t plot shows how good the agreement is between the calculated and experimental q_e values at different initial concentrations (Rothenberg, 2017; Kundu and Mondal, 2019; Musah *et al.*, 2022b).

3.6.5. Adsorption isotherm modeling:

The isotherm models assist in understanding the surface properties, interaction between the catalysts and SODs at different pH conditions and concentrations.

The widely used sorption isotherms are the Langmuir, Freundlich, Dubinin–Radushkevich (D–R) models, TEMKIN, and Brunauer-Emmet-Teller (BET).

3.6.5.1. Langmuir isotherm:

The Langmuir model is based on monolayer adsorption and the notion that adsorption takes place at specific sites of the adsorbent (photocatalyst) and that once an adsorbate (dye) occupies that site, no further adsorption may take place. This adsorption isotherm employs the equation below:

$$q_e = \frac{bC_eQ^0}{1+bC_e} \quad \textbf{(3.19)}$$

Where q_e represents the quantity of the dye removed per unit weight of photocatalyst, Q^0 is the single layer adsorption capacity constant, b is the adsorption process surface energy constant, and C_e is the equilibrium dye concentration in solution.

The linear forms of the equation are:

$$\frac{C_e}{q_e} = \frac{1}{bQ^0} + \frac{C_e}{Q^0} \quad \textbf{(3.20)}$$

$$\frac{1}{q_e} = \frac{1}{Q^0} + \left[\frac{1}{bQ^0}\right]\left[\frac{1}{C_e}\right] \quad \textbf{(3.21)}$$

The ($1/q_e$ vs. $1/C_e$) plot can be used to determine $1/bQ^0$ from the slope and $1/Q^0$ from the intercept. This model uses the Langmuir isotherm separation factor (R_L) uses the expression below:

$$R_L = \frac{1}{1+bC_0} \quad \textbf{(3.22)}$$

Where C_0 is the highest initial concentration ($mg.dm^3$) and b is the Langmuir constant ($dm^3.mg$). The value of R_L indicates the isotherm types i.e., unfavourable ($R_L > 1$), favourable ($0<R_L<1$), linear ($R_L=1$), and irreversible ($R_L=0$)(Kundu and Mondal, 2019; Musah *et al.*, 2022b).

3.6.5.2. Freundlich adsorption equation:

Freundlich adsorption model is used to quantify the relationship between the amount of dye degraded per unit weight of a photocatalyst, and the dye concentration remaining in the solution at the end of the reaction. The isotherm is expressed as follows:

$$q_e = K_f C_e^{1/n} \quad \textbf{(3.23)}$$

Where q_e is the amount of the dye degraded per unit weight of the photocatalyst, n is the sorption efficiency and sorption energy constant, C_e is the adsorbate equilibrium concentration in solution, and K_f is the adsorption capacity constant.

The linear form of the equation is expressed below:

$$log q_e = log K_f + \frac{1}{n} log C_e \quad \textbf{(3.24)}$$

A linear plot of $logq_e$ vs $logC_e$ will help determine 1/n and log K_f from the slope and intercept respectively (Musah *et al.*, 2022b).

3.6.5.3. Dubinin-Radushkevic (D-R) adsorption isotherm:

The D-R adsorption isotherm model is used to determine the type of adsorption, chemisorption, or physisorption, as well as the adsorption energy. This adsorption does not assume a homogenous adsorption surface.

$$\ln q_e = \ln Q_D - B_D + [RTln(1 + \frac{1}{C_e})]^2 \quad \textbf{(3.25)}$$

Where Q_D (mol/g) denotes the maximum adsorption capacity and B_D (mol^2/KJ^2) is a D-R constant. The ln q_e vs. RT $ln(1 + \frac{1}{C_e})$ plot gives the Q_D and B_D which are derived from the slope and intercept respectively.

The equation below expresses the mean free energy (KJ/mol) required to transport one mole of the dye to the surface of the photocatalyst:

$$E = \frac{1}{\sqrt{2E_D}} \quad \textbf{(3.26)}$$

B_D (mol^2/KJ^2) represents the free energy of adsorption per mole of the dye as it moves to the surface of the photocatalyst and Q_D (mol/g) is related to the extent of adsorption of the dye (Ibrahim Abubakar, Adamu Ibrahim and Bashir Ibrahim, 2020; Musah *et al.*, 2022b).

3.6.5.4. Temkin adsorption isotherm:

Temkin adsorption isotherm assumes the adsorption heat of all the dye molecules is inversely related to the coverage of the photocatalyst surface. The equations are given below:

$$q_e = \frac{RT}{bT} \ln (k_t C_e) \quad \textbf{(3.27)}$$

$$q_e = \frac{RT}{b_T} ln\ k_t + \frac{RT}{b_T} lnC_e \quad \textbf{(3.28)}$$

Where k_t (dm^3/g) is the equilibrium binding energy, b_T (J/mol) denotes the heat of adsorption constant, R is the ideal gas constant (8.314 $JK^{-1}mol^{-1}$), and T is the temperature (K). By plotting the q_e vs. ln C_e straight line graph, $\frac{RT}{b_T}$ and $\frac{RT}{b_T} ln\ k_t$ are calculated using the slope and intercept respectively.

3.6.5.5. Redlich-Peterson (R-P) isotherm model:

This isotherm model is a hybrid of the Langmuir and Freundlich models. It provides a more accurate representation of adsorption over a wide range of concentrations and can be used in heterogeneous or homogeneous systems. The linear form of the isotherm can be expressed using the equation below:

$$\ln \frac{C_e}{q_e} = \beta lnC_e - lnK_R \quad \textbf{(3.29)}$$

Where K_R is the R-P constant ($L.g^{-1}$), and β is an exponent with a value between 0 and 1. A linear $\ln \frac{C_e}{q_e}$ vs. lnC_e plot is used to obtain the β and lnK_R values (Musah (Musah et al., 2022; Piccin et al., 2011).

References:

Abdel-Rahman, M.A. et al. (2020) “One-factor-at-a-time and response surface statistical designs for improved lactic acid production from beet molasses by Enterococcus hirae ds10,” SN Applied Sciences, 2(4), p. 573. Available at: https://doi.org/10.1007/s42452-020-2351-x.

Askeland, D.R. (2011) The Science and Engineering of Materials. Boston, MA: Springer US. Available at: https://doi.org/10.1007/978-1-4899-2895-5.

Clogston, J.D. and Patri, A.K. (2011) “Zeta Potential Measurement,” in, pp. 63–70. Available at: https://doi.org/10.1007/978-1-60327-198-1_6.

Djurisic, A.B., Chen, X.Y. and Leung, Y.H. (2013) UV-VIS and Photoluminescence Spectroscopy for Nanomaterials Characterization. Edited by C. Kumar. Berlin, Heidelberg: Springer Berlin Heidelberg. Available at: https://doi.org/10.1007/978-3-642-27594-4.

Fang, Q. *et al.* (2018) ‘Ultrafast Charge Transfer in Perovskite Nanowire/2D Transition Metal Dichalcogenide Heterostructures’, *The Journal of Physical Chemistry Letters*, 9(7), pp. 1655–1662. Available at: https://doi.org/10.1021/acs.jpclett.8b00260.

Gqoba, S.S. *et al.* (2021) ‘Hierarchical Nanoflowers of Colloidal WS2 and Their Potential Gas Sensing Properties for Room Temperature Detection of Ammonia’, *Processes*, 9(9), p. 1491. Available at: https://doi.org/10.3390/pr9091491.

Hussain Chowdhury, M.S. et al. (2022) “Decomposition of Hydrogen Peroxide using Chemical and Catalytic Methods: A Reactor-based Approach,” Asian Journal of Chemistry, 34(5), pp. 1263–1268. Available at: https://doi.org/10.14233/ajchem.2022.23729.

Ibrahim Abubakar, S., Adamu Ibrahim, M. and Bashir Ibrahim, M. (2020) “Adsorption of Methyl Orange Dye onto Raw Maize Cob and Maize Cob Activated Carbon: Isotherms and Thermodynamic Studies,” International Journal of Advanced Chemistry, 8(1), p. 147. Available at: https://doi.org/10.14419/ijac.v8i1.30676.

Katheresan, V., Kansedo, J. and Lau, S.Y. (2018) “Efficiency of various recent wastewater dye removal methods: A review,” Journal of Environmental Chemical

Engineering, 6(4), pp. 4676–4697. Available at: https://doi.org/10.1016/j.jece.2018.06.060.

Khan, A., Malik, S. and Bilal, M. (2022) Nano-Bioremediation : Fundamentals and Applications. Edited by H.M.N. Iqbal, M. Bilal, and T.A. Nguyen. Elsevier. Available at: https://doi.org/10.1016/C2020-0-00522-0.

Kozuch, S. and Martin, J.M.L. (2012) "'Turning Over' Definitions in Catalytic Cycles," ACS Catalysis, 2(12), pp. 2787–2794. Available at: https://doi.org/10.1021/cs3005264.

Kundu, A. and Mondal, A. (2019) "Kinetics, isotherm, and thermodynamic studies of methylene blue selective adsorption and photocatalysis of malachite green from aqueous solution using layered Na-intercalated Cu-doped Titania," Applied Clay Science, 183, p. 105323. Available at: https://doi.org/10.1016/j.clay.2019.105323.

Li, D. and Liu, S. (2019) "Water Quality Detection for Lakes," in Water Quality Monitoring and Management. Elsevier, pp. 221–231. Available at: https://doi.org/10.1016/B978-0-12-811330-1.00008-9.

Lu, C. et al. (2019) 'Cesium Oleate Precursor Preparation for Lead Halide Perovskite Nanocrystal Synthesis: The Influence of Excess Oleic Acid on Achieving Solubility, Conversion, and Reproducibility', Chemistry of Materials, 31(1), pp. 62–67. Available at: https://doi.org/10.1021/acs.chemmater.8b04876.

Marshall, J.L. (1991) "Scanning Electron Microscopy and Energy Dispersive X-ray (SEM/EDX) Characterization of Solder Solderability and Reliability," in Solder Joint Reliability. Boston, MA: Springer US, pp. 173–224. Available at: https://doi.org/10.1007/978-1-4615-3910-0_6.

Meerbach, C. et al. (2020) "General Colloidal Synthesis of Transition-Metal Disulfide Nanomaterials as Electrocatalysts for Hydrogen Evolution Reaction," ACS Applied Materials & Interfaces, 12(11), pp. 13148–13155. Available at: https://doi.org/10.1021/acsami.9b21607.

Musah, M. et al. (2022) "Adsorption Kinetics and Isotherm Models: A Review," Caliphate Journal of Science and Technology, 4(1), pp. 20–26. Available at: https://doi.org/10.4314/cajost.v4i1.3.

Nagaraja, R. et al. (2012) “Photocatalytic degradation of Rhodamine B dye under UV/solar light using ZnO nanopowder synthesized by solution combustion route,” Powder Technology, 215–216, pp. 91–97. Available at: https://doi.org/10.1016/j.powtec.2011.09.014.

Olatunji, O.O. et al. (2018) “Thermo-gravimetric characterization of biomass properties: A review,” IOP Conference Series: Materials Science and Engineering, 423, p. 012175. Available at: https://doi.org/10.1088/1757-899X/423/1/012175.

Palchoudhury, S., Baalousha, M. and Lead, J.R. (2015) “Methods for Measuring Concentration (Mass, Surface Area and Number) of Nanomaterials,” in, pp. 153–181. Available at: https://doi.org/10.1016/B978-0-08-099948-7.00005-1.

Piccin, J.S., Dotto, G.L. and Pinto, L.A.A. (2011) “Adsorption isotherms and thermochemical data of FD&C Red n° 40 binding by Chitosan,” Brazilian Journal of Chemical Engineering, 28(2), pp. 295–304. Available at: https://doi.org/10.1590/S0104-66322011000200014.

Quevedo, A.C. et al. (2021) “UV-Vis Spectroscopic Characterization of Nanomaterials in Aqueous Media,” Journal of Visualized Experiments [Preprint], (176). Available at: https://doi.org/10.3791/61764.

Rothenberg, G. (2017) Catalysis concepts and green applications. Weinheim Wiley-Vch Verlag Gmbh & Co.

Sahraie, N.R. et al. (2015) “Quantifying the density and utilization of active sites in non-precious metal oxygen electroreduction catalysts,” Nature Communications, 6(1), p. 8618. Available at: https://doi.org/10.1038/ncomms9618.

Sahu, S. and Samanta, P.K. (2021) “Peak Profile Analysis of X-ray Diffraction Pattern of Zinc Oxide Nanostructure,” Journal of Nano- and Electronic Physics, 13(5), pp. 05001-1-05001–4. Available at: https://doi.org/10.21272/jnep.13(5).05001.

Saka, H. (2003) “Transmission Electron Microscopy,” in Carbon Alloys. Elsevier, pp. 223–238. Available at: https://doi.org/10.1016/B978-008044163-4/50014-0.

Sarabandi, K., Gharehbeglou, P. and Jafari, S.M. (2020) “Scanning electron microscopy (SEM) of nanoencapsulated food ingredients,” in Characterization of

Nanoencapsulated Food Ingredients. Elsevier, pp. 83–130. Available at: https://doi.org/10.1016/B978-0-12-815667-4.00003-1.

Shand, M.A. and Jin, F. (2020) “Introduction – Characterization of MgO,” in Magnesia Cements. Elsevier, pp. 1–10. Available at: https://doi.org/10.1016/B978-0-12-391925-0.00006-6.

Singh, D. and Ahuja, R. (2022) ‘Two-Dimensional Perovskite/HfS_2 van der Waals Heterostructure as an Absorber Material for Photovoltaic Applications’, *ACS Applied Energy Materials*, 5(2), pp. 2300–2307. Available at: https://doi.org/10.1021/acsaem.1c03796.

Song, W. et al. (2021) “Novel BiOBr by compositing low-cost biochar for efficient ciprofloxacin removal: the synergy of adsorption and photocatalysis on the degradation kinetics and mechanism insight,” RSC Advances, 11(25), pp. 15369–15379. Available at: https://doi.org/10.1039/D1RA00941A.

Tilvi, S., Majik, M.S. and Singh, K.S. (2014) “Mass Spectrometry for Determination of Bioactive Compounds,” in, pp. 193–218. Available at: https://doi.org/10.1016/B978-0-444-63359-0.00008-2.

Vattikuti, S.V.P. et al. (2019) “Binder-free WS2/ZrO2 hybrid as a photocatalyst for organic pollutant degradation under UV/simulated sunlight and tests for H2 evolution,” Journal of Alloys and Compounds, 809, p. 151805. Available at: https://doi.org/10.1016/j.jallcom.2019.151805.

Yang, B. et al. (2017) “Lead-Free, Air-Stable All-Inorganic Cesium Bismuth Halide Perovskite Nanocrystals,” Angewandte Chemie, 129(41), pp. 12645–12649. Available at: https://doi.org/10.1002/ange.201704739.

Zeta potential - An introduction in 30 minutes (2020) Malvern Panalytical. Available at: https://www.malvernpanalytical.com/en/learn/knowledge-center/technical-notes/TN101104ZetaPotentialIntroduction (Accessed: March 27, 2023).

Zhang, Q. et al. (2020) “Enhanced Photocatalytic Property of γ-CsPbI 3 Perovskite Nanocrystals with WS 2,” ACS Sustainable Chemistry & Engineering, 8(2), pp. 1219–1229. Available at: https://doi.org/10.1021/acssuschemeng.9b06451.

CHAPTER 4: CHARACTERIZATION RESULTS

4.0. Results and discussion:

4.1. Characterization Studies:

4.1.1. Powder X-ray Diffraction (PXRD):

Figure 4.1 below shows the PXRD patterns for WS_2, $Cs_3Bi_2Br_9$, and $Cs_3Bi_2Br_9/WS_2$ materials. The WS_2 diffraction pattern has peaks at 2Θ = 14.3º, 33.6º, 39.9º, 48.7º, 58.9º, and 69.3º correspond to the (002), (100), (013), (015), (110) and (201) crystal planes respectively. It was indexed to the 01-071-4832 card for tungstenite. The diffraction pattern for WS_2 has an intense (002) peak at 2Θ = 14.3º indicating that it has a layered structure (Akple and Apevienyeku, 2018). The d_{002} interlayer spacing was calculated to be 0.6217 nm. The broad peaks are an indication that the synthesized WS_2 has defects in the crystal structure and small particle size for the WS_2 crystal structure. The $Cs_3Bi_2Br_9$ diffraction pattern had peaks positioned at 2Θ = 10.9º, 22.6º, 27.3º, 31.9º, 38.1º, 39.8º, 44.5º, 46º, 48.8º, 50.7º, 56º, 62.4º, 67.5º, 70.9º, 75º, and 78.8º which correspond to the (100), (102), (003), (202), (104), (204), (213), (212), (311), (214), (006), (206), (500), (420), (316), and (108) crystal planes, thereby indexed to the 00-044-0714 card for $Cs_3Bi_2Br_9$. The narrow peaks indicate the material is crystalline. The high crystallinity corresponds to a d_{003} lattice spacing of 0.3275 nm (Yang *et al.*, 2017b). The sharp (100) peak in $Cs_3Bi_2Br_9$ indicates the extensional orientation of the c nanoparticles (Hu *et al.*, 2018).

The diffraction peak for $Cs_3Bi_2Br_9/WS_2$ is similar to that of $Cs_3Bi_2Br_9$. The (100) and (102) peaks are significantly reduced in the $Cs_3Bi_2Br_9/WS_2$ composite diffraction pattern. The drastic reduction in the (100) and (102) peak intensities in comparison to the same peaks in the $Cs_3Bi_2Br_9$ diffraction pattern indicates that there is a higher growth rate and smaller surface area of these lattice planes (Sahu and Samanta, 2021b). The WS_2 peaks are not prominent in the $Cs_3Bi_2Br_9/WS_2$ diffraction pattern. Although the composite is comprised of WS_2 with a 20% molar percentage, the weight percentage is only 4% and the diffraction peaks are masked by the $Cs_3Bi_2Br_9$ peaks.

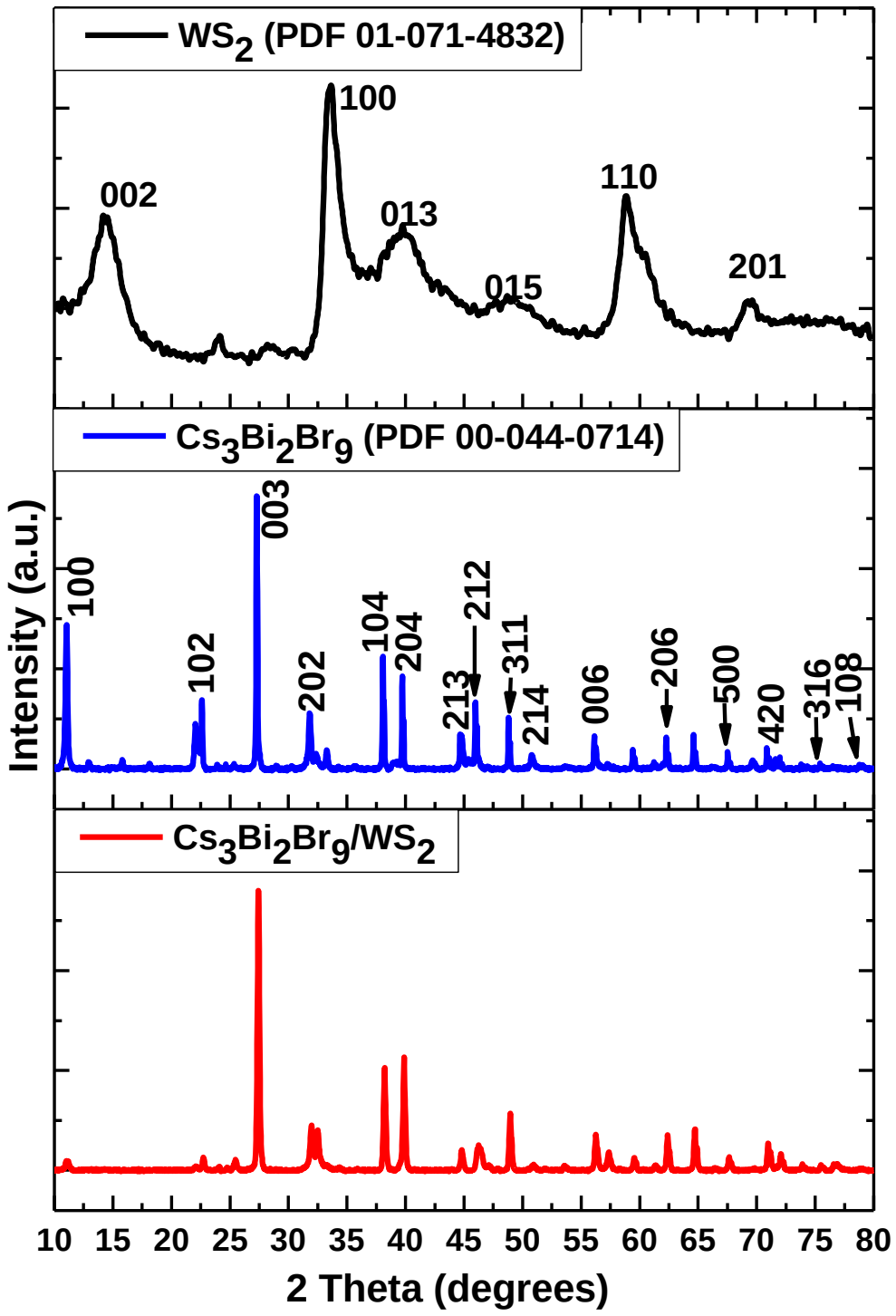

Figure 4.1: PXRD patterns for WS_2, $Cs_3Bi_2Br_9$, and $Cs_3Bi_2Br_9/WS_2$

Figure 4.2 below shows that traces of WS_2 were detected in the composite. Although small due to having a low molar composition in the heterostructure, the WS_2 diffraction peaks were visible at 2Θ = 14.2º (002), 29.2º (004), 33.6º (101), 38.9º (013), 41.1º (103), 43.8º (006), 48.7º (105), 58.9º (110), 60.6º (112), 69º (108), 76º (116), and 89º

(207). The peaks matched with the trigonal prismatic phase (3R) of WS_2 with JCPDS number 00-035-0651.

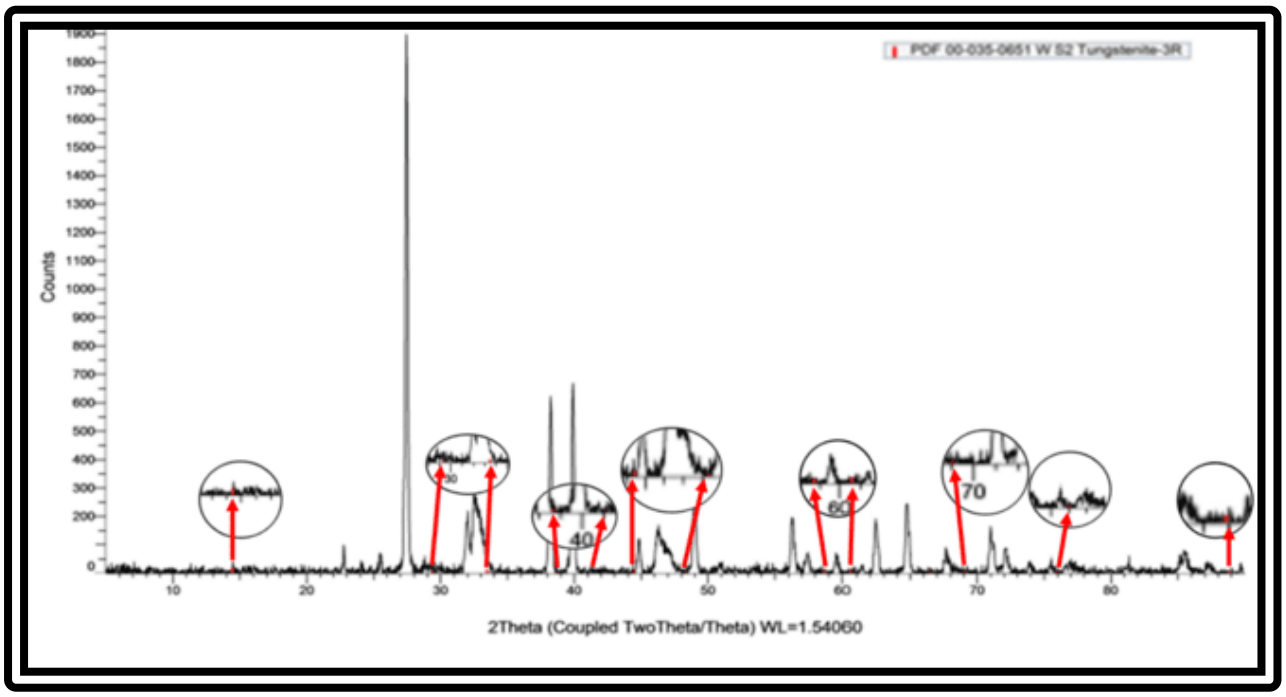

Figure 4.2: WS_2 detected in $Cs_3Bi_2Br_9/WS_2$

4.1.2. Transmission Electron Microscopy (TEM):

Figure 4.3 below shows the TEM images of WS_2, $Cs_3Bi_2Br_9$, and $Cs_3Bi_2Br_9/WS_2$. **Figure 4.3 (a-b)** shows that WS_2 had flower-petal-like morphology highlighted in a circle. TEM micrographs for $Cs_3Bi_2Br_9$ are shown in **Figure 4.3 (c-d)**. The nanoparticles were polydisperse with different morphologies. **Figure 4.3 (d-e)** shows the TEM images for $Cs_3Bi_2Br_9/WS_2$. There was a mixture of morphologies, a combination of the $Cs_3Bi_2Br_9$ nanoplates, the WS_2 nanoflower petals, as well as nanospheres. This further confirms that $Cs_3Bi_2Br_9/WS_2$ was synthesized successfully. The particles were larger in the composite micrographs in comparison to the particle sizes in the WS_2 and $CS_3Bi_2Br_9$ micrographs. This agrees with the reduction in the (100) and (102) peak intensities seen in the $Cs_3Bi_2Br_9/WS_2$ PXRD diffraction pattern that indicated a higher growth rate than $Cs_3Bi_2Br_9$.

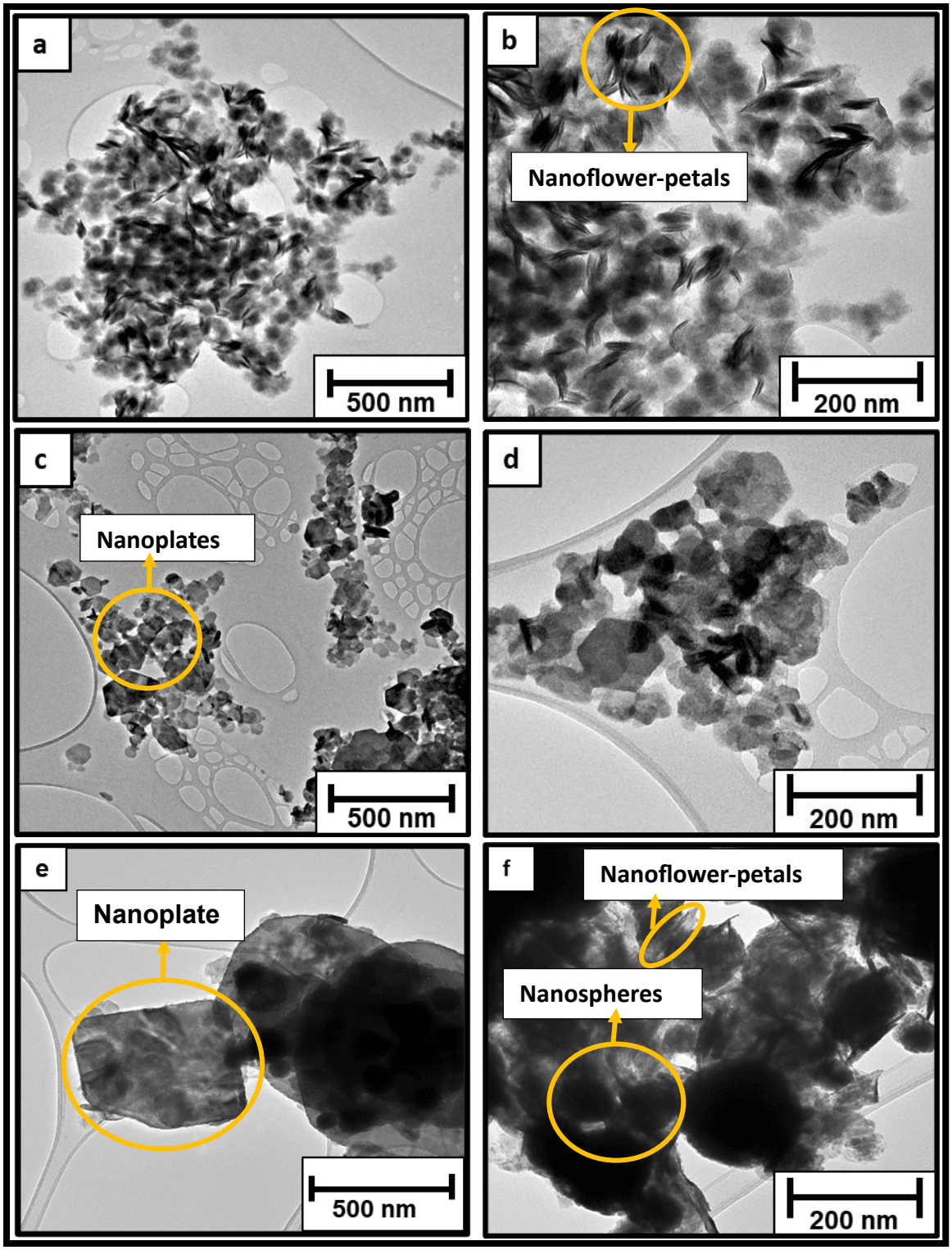

Figure 4.3: TEM images for **(a-b)** WS2 **(c-d)** Cs3Bi2Br9 **(e-f)** Cs3Bi2Br9/WS2 at 500 nm and 200 nm magnifications

4.1.3. Scanning Electron Microscopy (SEM):

The SEM images in **Figure 4.4 (a-b)** are for WS_2. The images confirmed the 3D nanoflower layered flower-petal morphology. The nanoflower petals were loosely packed and the flowers were agglomerated. **Figure 4.4 (c-d)** shows the SEM images for $Cs_3Bi_2Br_9$. It shows polydisperse 2D nanoplates with non-uniform shapes and sizes. Due to the 2D nanoplate morphology, the nanoplates were in closer contact with each other compared to WS_2. This is therefore in agreement with the larger d_{002} interlayer spacing of 0.6217 nm calculated for WS_2 compared to the d_{003} spacing of 0.3275 nm calculated for $Cs_3Bi_2Br_9$. The SEM images for $Cs_3Bi_2Br_9$ are depicted in **Figure 4.4 (e-f)**. The nanoparticles had mixed morphologies. There were agglomerated nanospheres and nanoplates. The nanoparticles were decorated with WS_2 nanoflower petals.

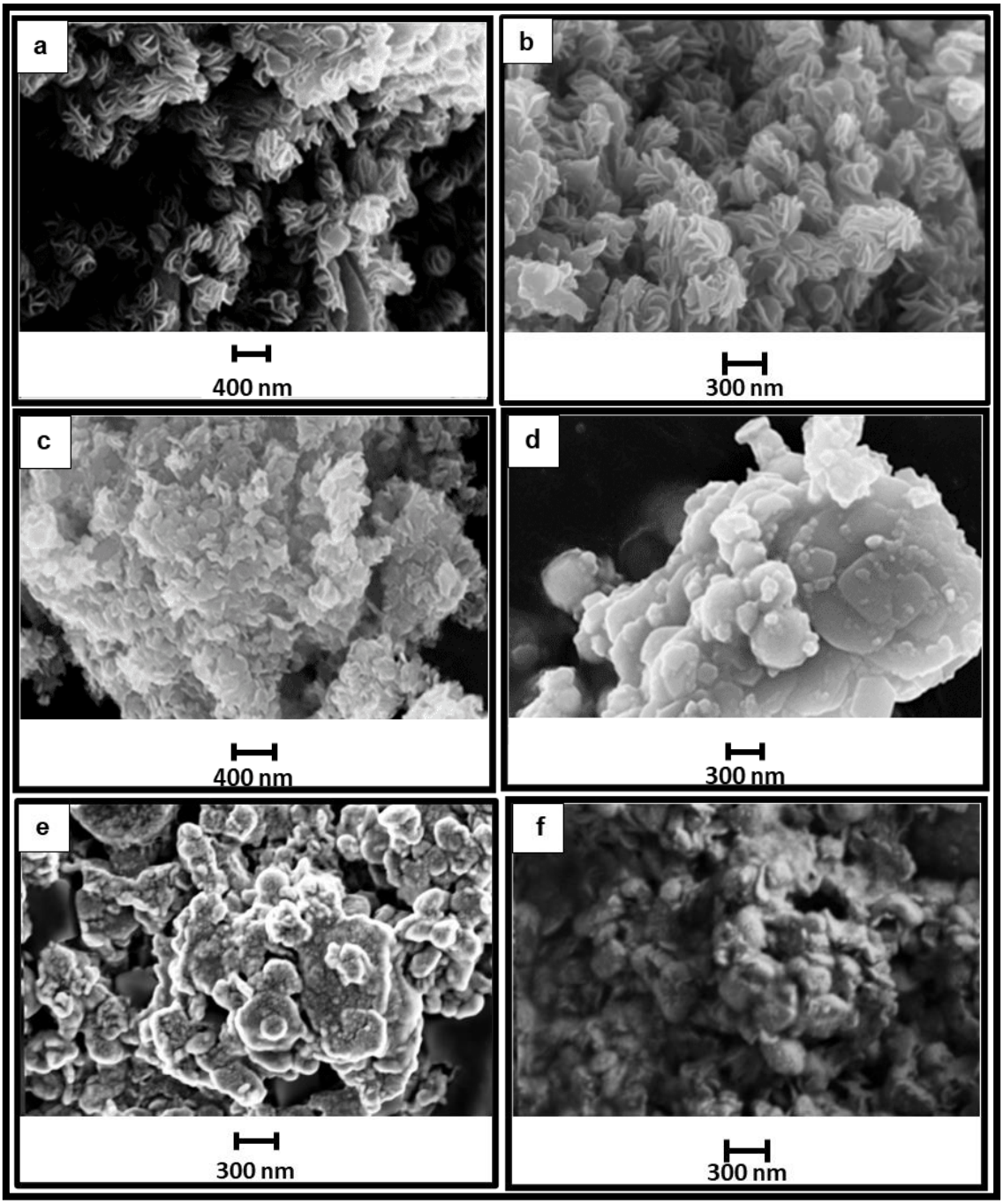

Figure 4.4. SEM analysis of **(a-b)** WS_2, **(c-d)** $Cs_3Bi_2Br_9$, and **(e-f)** $Cs_3Bi_2Br_9/WS_2$ at 400 nm and 300 nm magnifications

4.1.4. Energy Dispersive X-ray Spectroscopy (EDS) analysis:

Figure 4.5 (a) below shows the WS_2 EDS spectrum. The EDS results for WS_2 indicated that the W:S atomic ratio was close to 74:26 as shown in **Table 4.1**. **Table 4.1** shows the elemental composition of WS_2. The weight percentage of sulfur (S) was

26.17% and 73.83% for tungsten (W). This is because S has a smaller molar mass of 32.06 g/mol compared to W which has a molar mass of 183.84 g/mol.

Since the ratio of W:S is 1:2 in WS_2, the atomic percentage of S was 67.02% and 32.98% for W. This indicates that there were just over double S atoms present in the material in comparison to the number of W atoms. This proves that WS_2 was synthesized successfully. The EDS spectrum for $Cs_3Bi_2Br_9$ shows that the Cs, Bi, and Br elements were present in the sample. The carbon (C) is due to the carbon tape that the sample was placed on to keep it in place on the sample holder and oxygen (O) was due to oxidation. The elemental composition is shown in **Table 4.2** and the ratio of Cs, Bi, and Br %wt (weight percentage) was close to 1.8:1:1.9 while it should theoretically be 1:1:1.8. This could be a result of an uneven distribution of the elements throughout the sample. The EDS spectrum in **Figure 4.5 (c)** below only shows the presence of Cs, Bi, and Br in the $Cs_3Bi_2Br_9/WS_2$ sample which is similar to the pure perovskite. WS_2 may not have been detected due to not being evenly distributed throughout the sample therefore it may have not been present in the sample that was analysed.

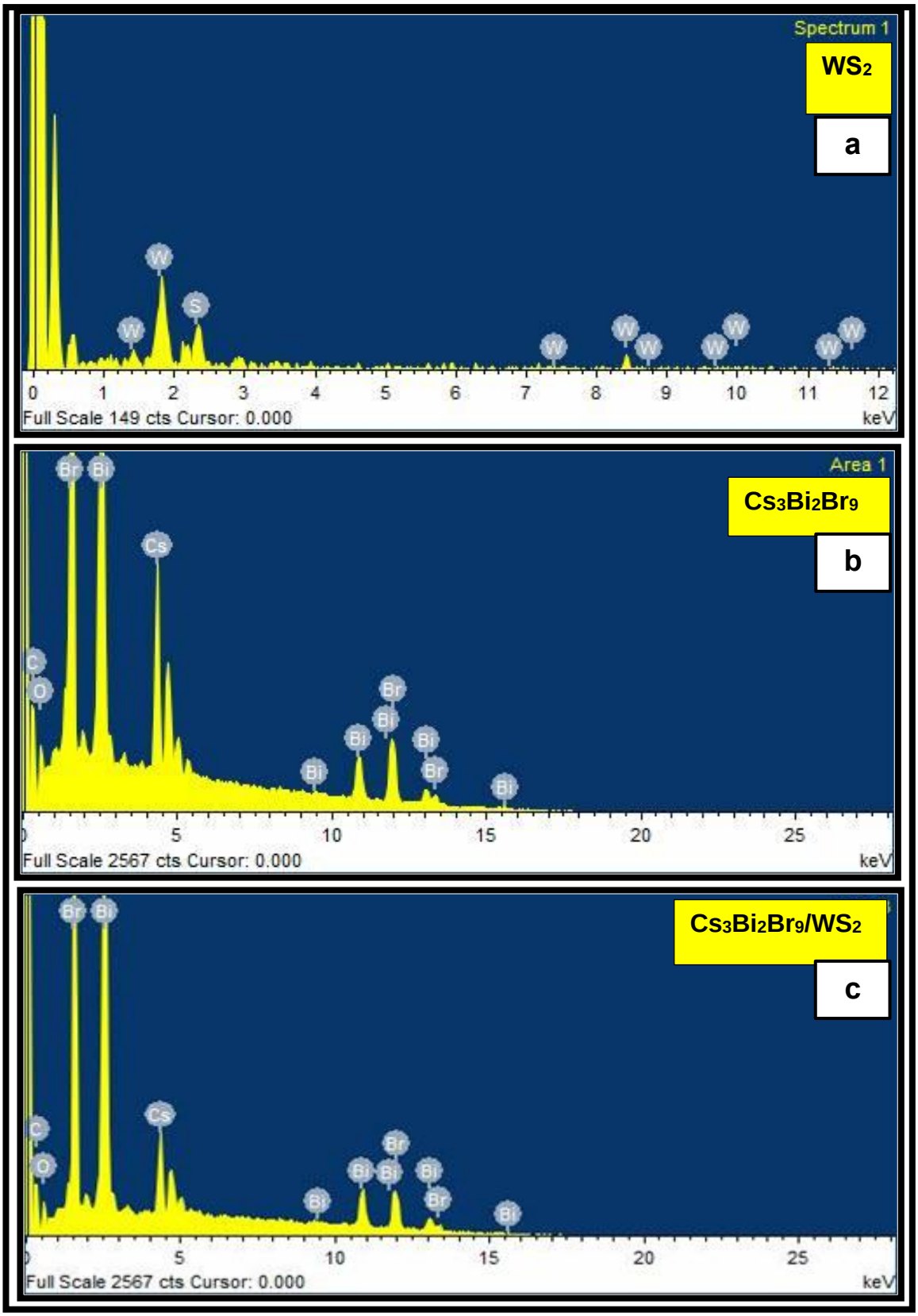

Figure 4.5: EDS spectrum for **(a)** WS_2, **(b)** $Cs_3Bi_2Br_9$, and **(c)** $Cs_3Bi_2Br_9/WS_2$.

Table 4.1: WS_2 elemental composition from EDS spectrum

Element	*Weight*	*Atomic*
S K	26.17	67.02
W M	73.83	32.98
Total	100	100

Table 4.2: Elemental composition of $Cs_3Bi_2Br_9$ and $Cs_3Bi_2Br_9/WS_2$

Element	*Weight (%) in $Cs_3Bi_2Br_9$*	*Weight (%) in $Cs_3Bi_2Br_9/WS_2$*	*Atomic (%) in $Cs_3Bi_2Br_9$*	*Atomic (%) in $Cs_3Bi_2Br_9/WS_2$*
C K	14.37	16.55	57.57	61.15
O K	3.11	5.63	9.35	15.13
Br L	31.73	15.27	19.11	8.56
Cs L	17.18	14.23	6.22	4.80
Bi M	33.62	48.32	7.74	10.36
Total	100	100	100	100

4.1.5. EDS mapping results:

EDS mapping was done to visualize the distribution of the elements in $Cs_3Bi_2Br_9$ and in the heterostructure, $Cs_3Bi_2Br_9/WS_2$. **Figure 4.6** shows the even distribution of the Cs, Bi, and Br elements in $Cs_3Bi_2Br_9$.

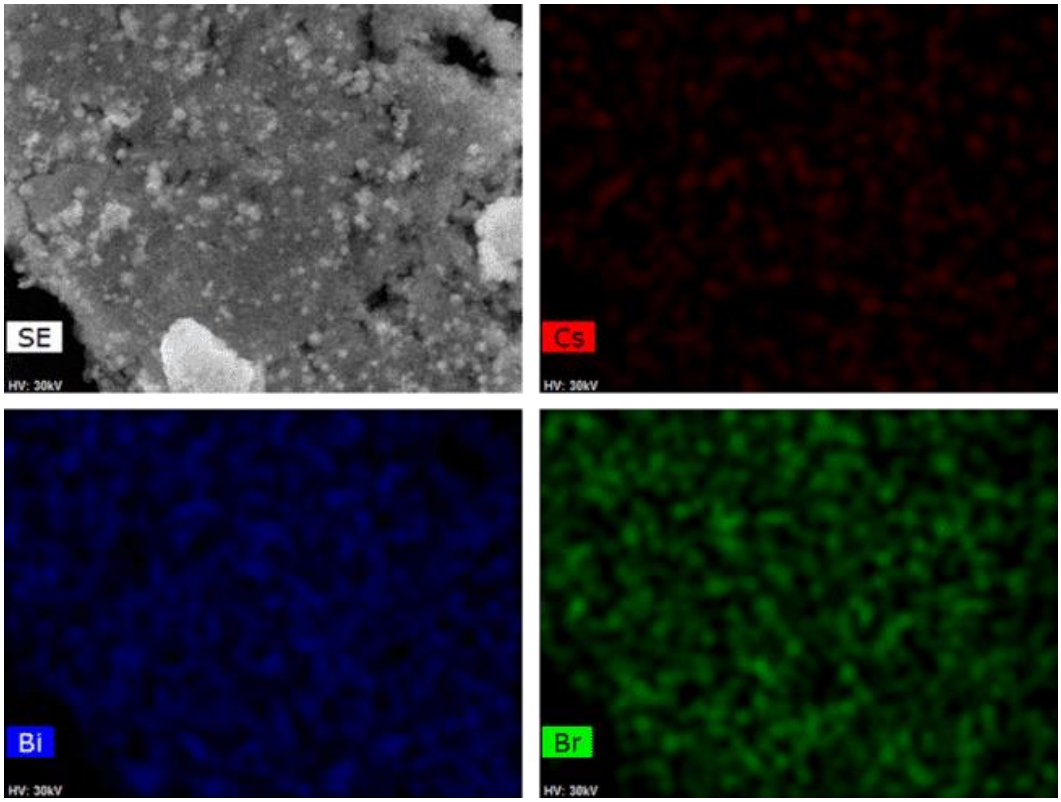

Figure 4.6: EDS mapping of $Cs_3Bi_2Br_9$

Figure 4.7 confirms the presence of WS_2 in the $Cs_3Bi_2Br_9/WS_2$ heterostructure as the distribution of the Cs, Bi, Br, W, and S elements in the heterostructure is shown.

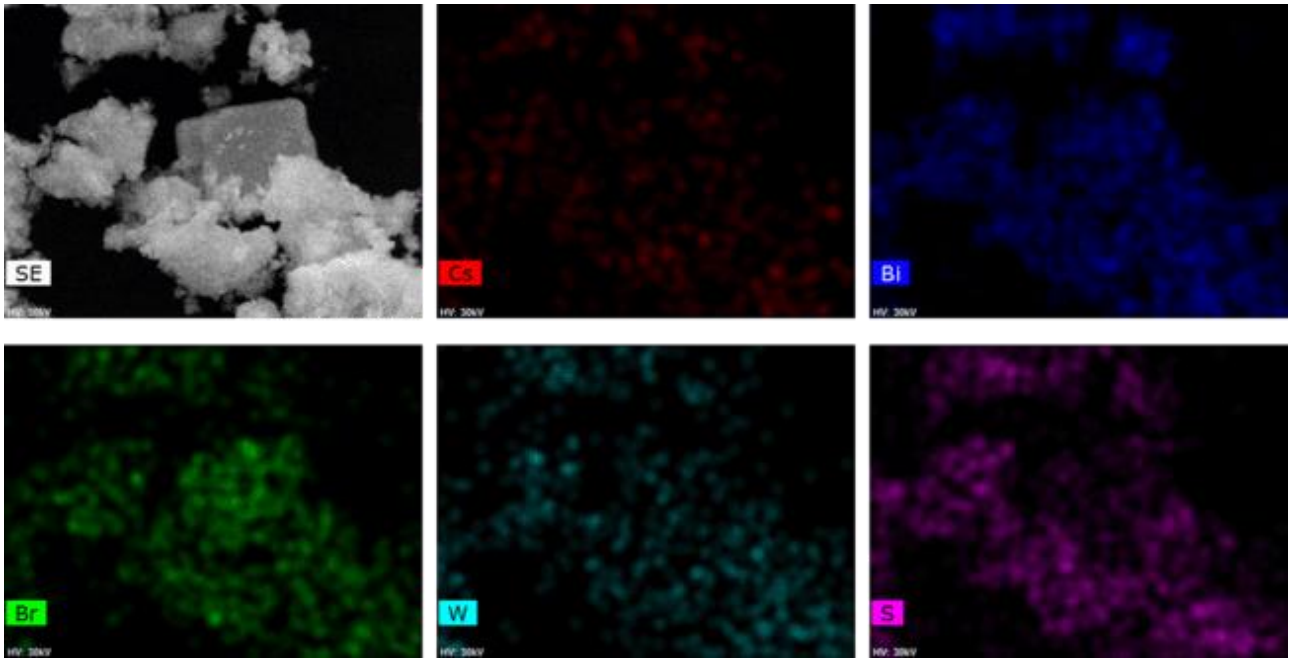

Figure 4.7: EDS mapping of the $Cs_3Bi_2Br_9/WS_2$ heterostructure

4.1.6. BET analysis:

BET analysis was conducted for $Cs_3Bi_2Br_9$ and $Cs_3Bi_2Br_9/WS_2$ and the results can be seen in **Table 4.3** and **Figure 4.8.** When comparing the BET results for $Cs_3Bi_2Br_9$ and $Cs_3Bi_2Br_9/WS_2$, the composite has higher values for BET surface area and pore size which means that the composite is better for photocatalysis. This could be attributed to the addition of the co-catalyst, WS_2, which has resulted in increased surface area and pore size. The nanoflower-petal morphology of WS_2 is layered and the spaces between the nanoflower-petals serve as additional pockets for increased catalytic sites for improved SOD degradation. $Cs_3Bi_2Br_9$ has a slightly higher pore volume of 0.094 cm^3/g compared to 0.078 cm^3/g for the composite. This suggests that $Cs_3Bi_2Br_9$ has a high number of pores which resulted in a higher pore volume than $Cs_3Bi_2Br_9/WS_2$. Both materials have high negative values for the Langmuir surface area. Additionally, the Langmuir q_{max} values were -10.8383 cm^3/g and 15.473 cm^3/g and the b values were -0.00078 1/mmHg and -0.000703 1/mmHg for $Cs_3Bi_2Br_9$ and $Cs_3Bi_2Br_9/WS_2$ respectively. This means that the Langmuir adsorption isotherm is not a suitable model for these materials as the negative values suggest that the model was concave instead of convex which makes it unfavourable (Kalam *et al.*, 2021).

Table 4.3: BET results for $Cs_3Bi_2Br_9$ and $Cs_3Bi_2Br_9/WS_2$

	$Cs_3Bi_2Br_9$	***$Cs_3Bi_2Br_9/WS_2$***
BET surface area (m^2/g)	5.4344	6.4627
Langmuir surface area (m^2/g)	-47.1745	-67.0617
Pore size (nm)	23.2299	25.9331
Pore volume (cm^3/g)	0.093577	0.078221

The BET adsorption isotherms for $Cs_3Bi_2Br_9$ and $Cs_3Bi_2Br_9/WS_2$ are shown in **Figure 4.8** below. The isotherms closely represent the Type I isotherm model indicating that both materials are microporous. However, $Cs_3Bi_2Br_9/WS_2$ adsorbed a higher quantity of gas indicating that it has larger pores than $Cs_3Bi_2Br_9$.

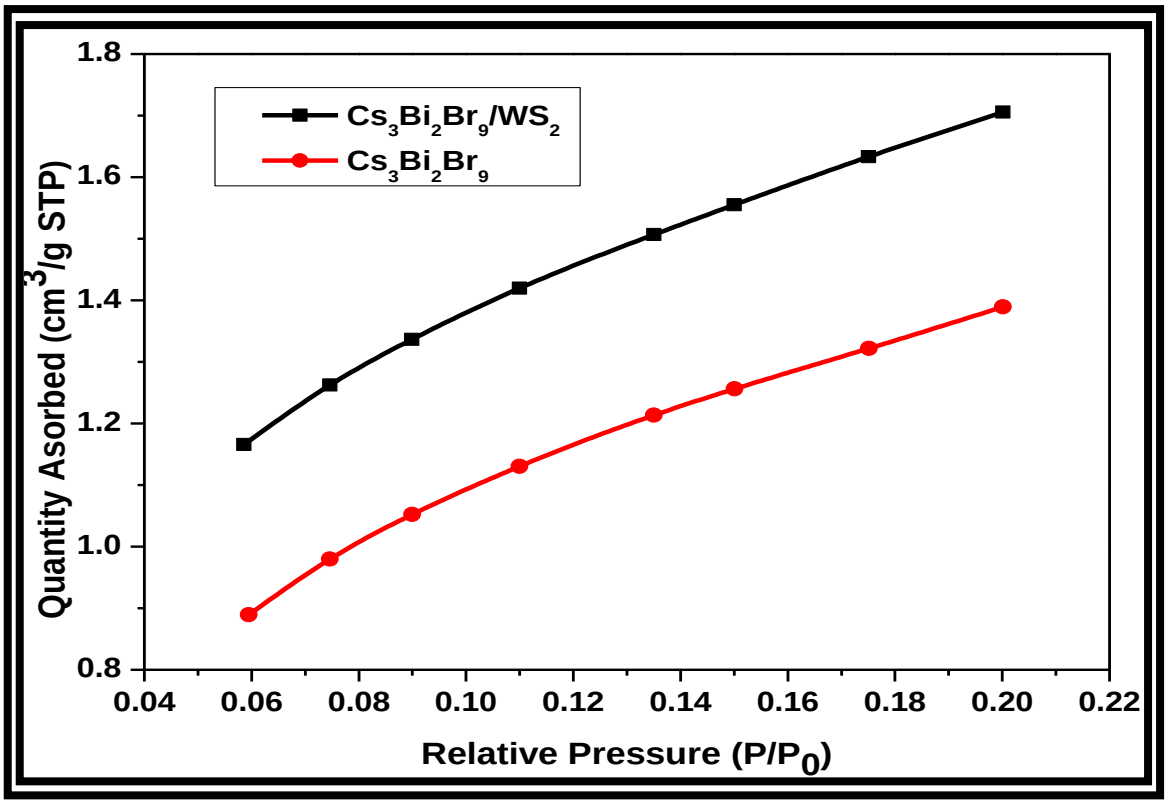

Figure 4.8: BET adsorption isotherms for $Cs_3Bi_2Br_9$ and $Cs_3Bi_2Br_9/WS_2$

4.1.7. TGA analysis:

The TGA results in **Figure 4.9** show a 24.9% weight loss for $Cs_3Bi_2Br_9/WS_2$ in the temperature range 354.6-893.5 ºC due to the decomposition of the sample. $Cs_3Bi_2Br_9$ starts to decompose at 192 ºC. The 27.6% weight loss from 192-893 ºC was due to decomposition. $Cs_3Bi_2Br_9/WS_2$ decomposed to 74.9% and $Cs_3Bi_2Br_9$ decomposed to 72.4% of the weight. The weight of the $Cs_3Bi_2Br_9/WS_2$ composite decreased slightly by 1.04% in the 120-314 ºC temperature range. This was due to the dehydroxylation of $-OH^-$ groups (Luu, C. L., et al., 2017). The small weight gain from 314-354.6 ºC could be due to oxidation, the sample may have reacted with nitrogen gas, or it could be due to the buoyancy effect where the gas surroundings become less dense at higher temperatures and the pan experiences a buoyant lift (Luu, C. L., et al., 2017).

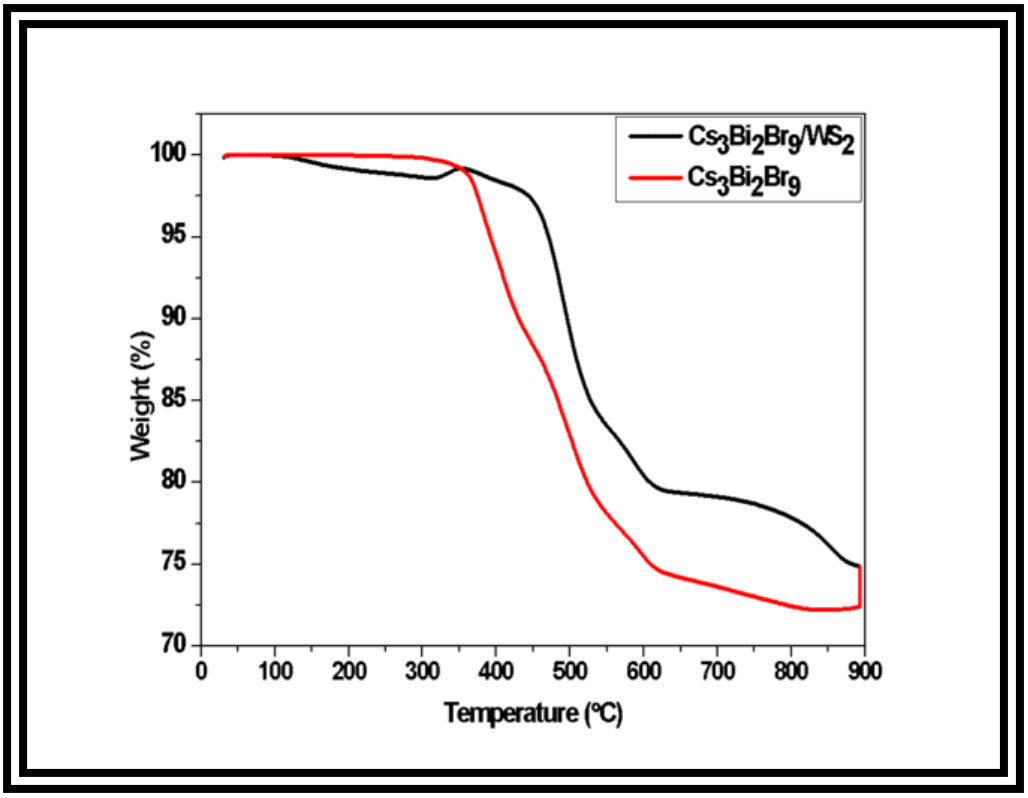

Figure 4.9: Thermogravimetric analysis of $Cs_3Bi_2Br_9$ and $Cs_3Bi_2Br_9/WS_2$

4.1.8. Zeta potential

The zeta potential results are shown below in **Figure 4.10.** $Cs_3Bi_2Br_9$ was neutral at pH 2, 7, and 10. It was cationic at pH 4, 6, and 8. It was anionic at pH 12. $Cs_3Bi_2Br_9/WS_2$ was neutral at pH 2, 4, and 6. It was anionic at pH 7, 8, and 10. It had high dispersion stability and was strongly anionic at pH 12. The synthetic dyes were characterized using this method to understand the interactions between the dyes and the synthesized materials. Methyl red (MR) was neutral at pH 2 and 7, cationic at pH 4 and 6, anionic at pH 8 and 10, and strongly anionic and stable at pH 12. Rhodamine B was strongly cationic at pH 2, neutral at pH 4, anionic at pH 7, 8, and 10, and strongly anionic at pH 12.

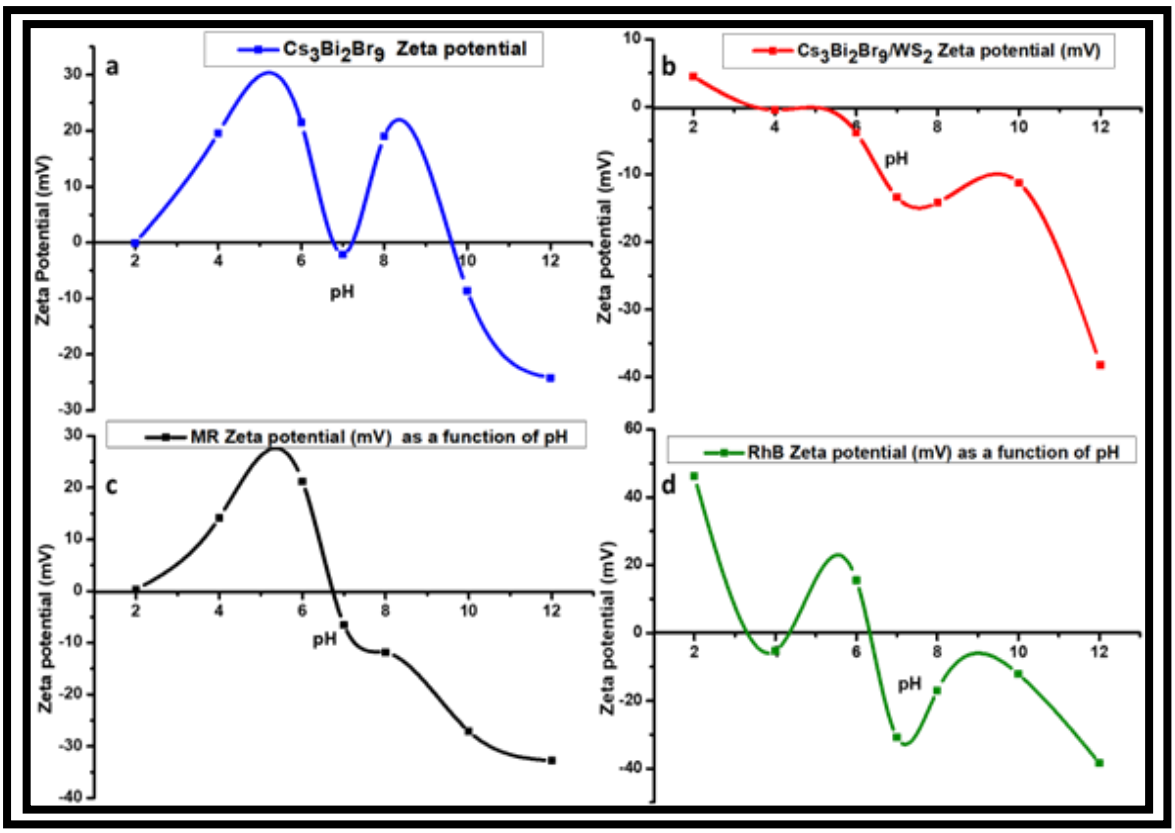

Figure 4.10: Zeta potential as a function of pH for **(a)** $Cs_3Bi_2Br_9$, **(b)** $Cs_3Bi_2Br_9/WS_2$, **(c)** Methyl red, and **(d)** Rhodamine B

4.1.9. UV-vis analysis:

This technique was used to determine the bandgaps for WS_2, $Cs_3Bi_2Br_9$, and $Cs_3Bi_2Br_9/WS_2$. Tauc plots were used to determine the bandgaps using the absorbance spectrum. This was done to understand the optical properties. **Figure 4.11** below shows that WS_2 had two UV absorption peaks at 404 nm and 608 nm thus a direct bandgap of 2.89 eV and an indirect bandgap of 1.34 eV. According to the literature, the direct bandgap of WS_2 is larger than 2 eV and the indirect bandgap is smaller than 1.5 eV (Yousef *et al.*, 2022b). The WS_2 direct bandgap reported compares well to the bandgap of 2.82 eV reported by (Gqoba *et al.*, 2021), and the indirect bandgap compares well to the 1.35 eV bandgap determined by (Cao *et al.*, 2014). $Cs_3Bi_2Br_9$ had a direct bandgap of 2.48 eV and $Cs_3Bi_2Br_9/WS_2$ had a direct bandgap of 2.81 eV. The $Cs_3Bi_2Br_9$ bandgap compared well with the 2.83 eV bandgap determined by (Akinbami *et al.*, 2021).

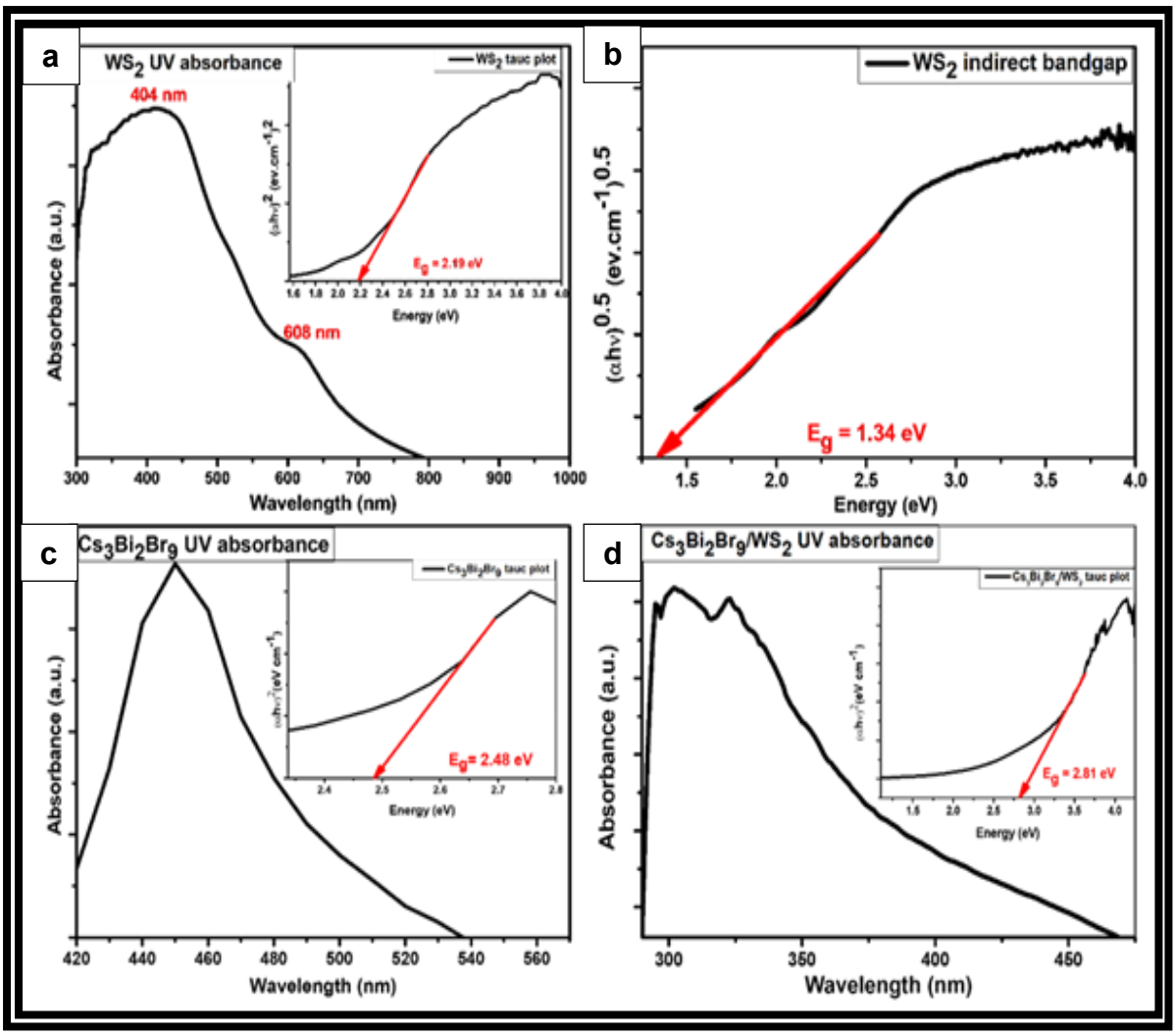

Figure 4.11: UV absorbance and Tauc plot for **(a)** WS2 direct bandgap, **(b)** WS2 indirect bandgap, **(c)** Cs3Bi2Br9 direct bandgap, and **(d)** Cs3Bi2Br9/WS2 direct bandgap

4.1.9.1. $Cs_3Bi_2Br_9/WS_2$ heterostructure:

The bandgaps of $Cs_3Bi_2Br_9$ and WS_2 were used to determine more details about the $Cs_3Bi_2Br_9/WS_2$ heterostructure. The HOMO and LUMO levels for $Cs_3Bi_2Br_9$ and WS_2 were calculated below to determine the type of heterojunction that was created.

$$Cs_3Bi_2Br_9 \text{ electronegativity} = [2.18^3 * 4.69^2 * 7.59^9]^{1/(3+2+9)} = 5.42 \text{ eV}$$

$$Cs_3Bi_2Br_9\ E_{CB} = \chi - E^e\text{-}0.5E_g$$

$$= 5.42 - 4.5 - 0.5(2.48)$$

$$= -0.32 \text{ eV}$$

$$Cs_3Bi_2Br_9\ E_{VB} = E_{CB} + E_g$$
$$= -0.32 + 2.48\ eV$$
$$= 2.16\ eV$$
$$WS_2\ electronegativity = [4.40*6.22^2]^{1/(1+2)} = 5.54\ eV$$
$$WS_2\ E_{CB} = \chi - E^e\text{-}0.5E_g$$
$$= 5.54 - 4.5 - 0.5(2.19)$$
$$= -0.055\ eV$$
$$WS_2\ E_{VB} = E_{CB} + E_g$$
$$= -0.055 + 2.19$$
$$= 2.14\ eV$$

The CB potentials for WS_2 and $Cs_3Bi_2Br_9$ were calculated to be -0.055 eV and -0.32 eV respectively. The VB potentials for WS_2 and $Cs_3Bi_2Br_9$ were 2.14 eV and 2.16 eV, respectively. $Cs_3Bi_2Br_9$ had a more negative CB potential than WS_2.

The HOMO and LUMO levels for $Cs_3Bi_2Br_9$ and WS_2 are shown in **Figure 4.12**. Since WS_2 had a smaller bandgap and was more positive than $Cs_3Bi_2Br_9$, the composite closely resembled the Type I (straddling structure) heterostructure seen in **Figure 2.6**. The electrons move down from CB ($Cs_3Bi_2Br_9$) to CB (WS_2). The VB in $Cs_3Bi_2Br_9$ is more positive than in WS_2 therefore the holes in VB ($Cs_3Bi_2Br_9$) need to move up to VB (WS_2). This is undesirable because electrons and holes would accumulate in WS_2, increasing the probability of charge recombination and reducing the photocatalytic performance. Therefore, improvements need to be made to achieve a Type II heterostructure.

However, the CB potentials were more negative than the important reduction reactions and the VB potentials were more positive than the target oxidation reactions shown in **Scheme 2.1**. Therefore, the heterostructure is still suitable for degrading dyes photo-catalytically.

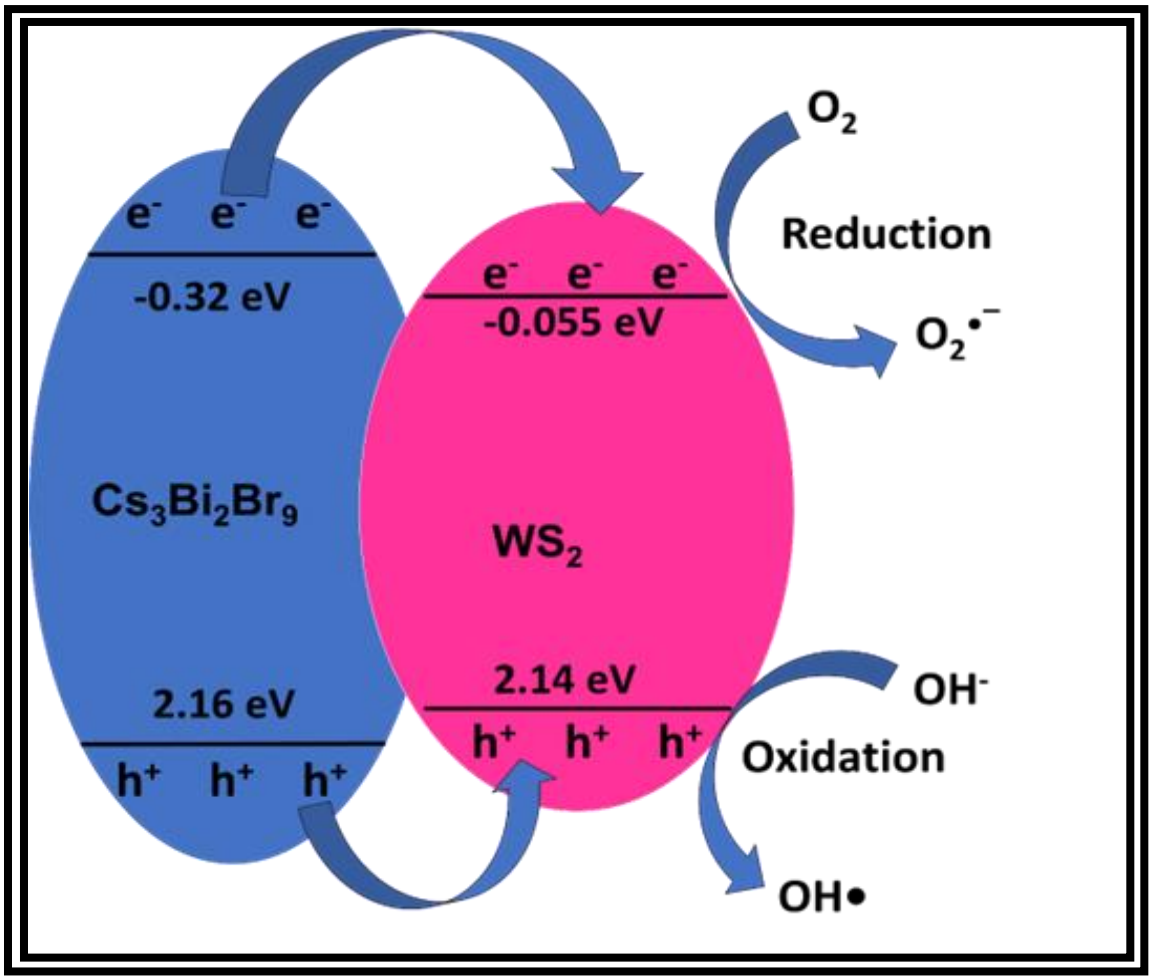

Figure 4.12: HOMO and LUMO levels for $Cs_3Bi_2Br_9$ and WS_2

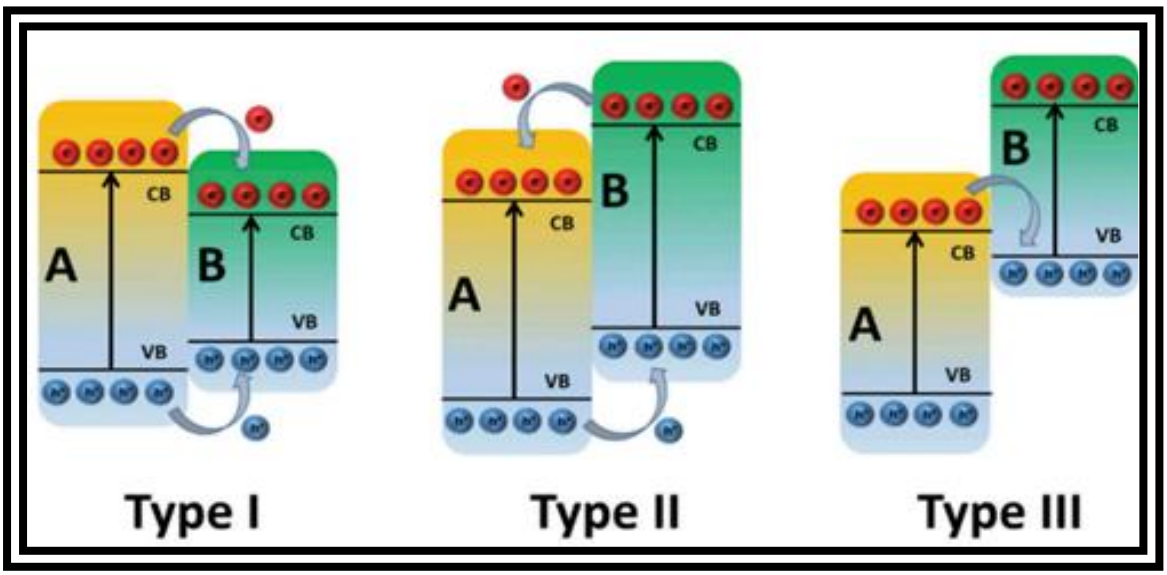

Figure 2.6: Types of semiconductor heterojunction structures (Kumar *et al.*, 2020)

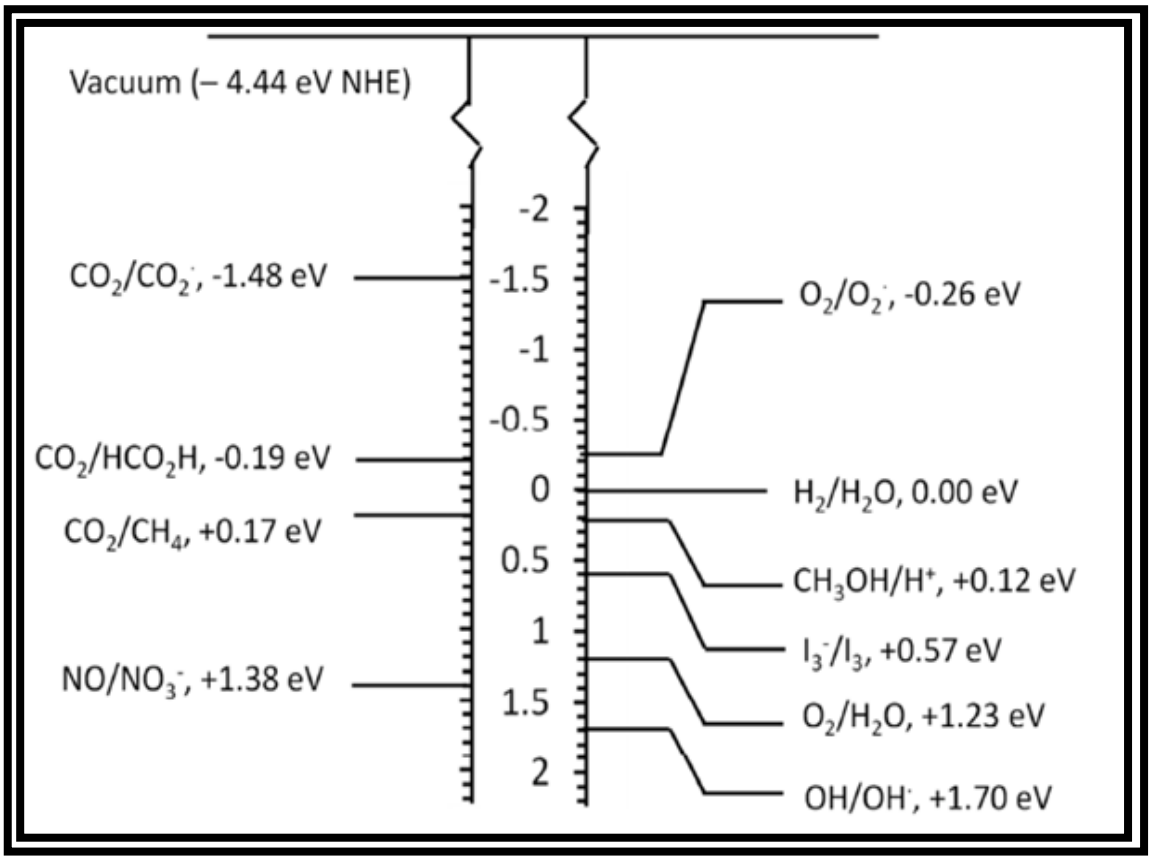

Scheme 2.1: NHE energy levels for important photocatalytic reactions at pH = 0 (Kanhere and Chen, 2014).

4.2. Conclusion:

In conclusion, the comprehensive characterization of synthesized WS_2, $Cs_3Bi_2Br_9$, and $Cs_3Bi_2Br_9/WS_2$ materials through various analytical techniques has provided valuable insights into their structural and functional properties. PXRD analysis confirmed the identity and crystal structure of WS_2 and $Cs_3Bi_2Br_9$, while TEM and SEM imaging revealed distinct morphologies for each material and its composite. EDS mapping provided elemental distribution information, highlighting the composition of the materials.

The BET analysis indicated the superior surface area of $Cs_3Bi_2Br_9/WS_2$ compared to $Cs_3Bi_2Br_9$, suggesting its potential as a more efficient photocatalyst. The TGA results suggested greater thermal stability for $Cs_3Bi_2Br_9/WS_2$, enhancing its applicability under high-temperature conditions.

Zeta potential analysis elucidated the surface charge variations of the photocatalysts and dyes under different pH conditions, providing insights into their dispersion stability and electrostatic interactions. UV-vis spectroscopy confirmed the desirable WS_2, $Cs_3Bi_2Br_9$, and $Cs_3Bi_2Br_9/WS_2$ bandgap values for photocatalytic applications. The $Cs_3Bi_2Br_9/WS_2$ heterostructure resembles a Type I heterostructure. This is undesirable as the charge carriers would be trapped in WS_2, therefore, improvements need to be made to reduce charge recombination.

Overall, the findings confirm the suitability of WS_2, $Cs_3Bi_2Br_9$, and $Cs_3Bi_2Br_9/WS_2$ for photocatalytic purposes, supported by their structural integrity, surface characteristics, thermal stability, and optical properties.

References:

Abdel-Rahman, M.A. *et al.* (2020) ‘One-factor-at-a-time and response surface statistical designs for improved lactic acid production from beet molasses by Enterococcus hirae ds10’, *SN Applied Sciences*, 2(4), p. 573. Available at: https://doi.org/10.1007/s42452-020-2351-x.

Affat, S.. S. (2021) ‘Classifications, Advantages, Disadvantages, Toxicity Effects of Natural and Synthetic Dyes: A review’, *University of Thi-Qar Journal of Science*, 8(1).

Ajmal, A. *et al.* (2014) ‘Principles and mechanisms of photocatalytic dye degradation on TiO $_2$ based photocatalysts: a comparative overview’, *RSC Adv.*, 4(70), pp. 37003–37026. Available at: https://doi.org/10.1039/C4RA06658H.

Akinbami, O. *et al.* (2021) ‘Lead-free Rudorffite-type Cs3Bi2Br9 nanoparticles for photocatalytic degradation of rhodamine B and methylene blue’, *Journal of Photochemistry and Photobiology A: Chemistry*, 419, p. 113460. Available at: https://doi.org/10.1016/j.jphotochem.2021.113460.

Akpan, U.G. and Hameed, B.H. (2009) ‘Parameters affecting the photocatalytic degradation of dyes using TiO2-based photocatalysts: A review’, *Journal of Hazardous Materials*, 170(2–3), pp. 520–529. Available at: https://doi.org/10.1016/j.jhazmat.2009.05.039.

Akple, M.S. and Apevienyeku, H.K. (2018) ‘Synthesis and density-functional-theory calculations of electronic band structure of hollow sphere WS $_2$’, *Materials Science-Poland*, 36(3), pp. 409–418. Available at: https://doi.org/10.2478/msp-2018-0052.

Al-Buriahi, A.K. *et al.* (2022) ‘Elimination of rhodamine B from textile wastewater using nanoparticle photocatalysts: A review for sustainable approaches’, *Chemosphere*, 287, p. 132162. Available at: https://doi.org/10.1016/j.chemosphere.2021.132162.

Anisuzzaman, S.M. *et al.* (2022) ‘Current Trends in the Utilization of Photolysis and Photocatalysis Treatment Processes for the Remediation of Dye Wastewater: A Short Review’, *ChemEngineering*, 6(4), p. 58. Available at: https://doi.org/10.3390/chemengineering6040058.

Arslan, I., Balcioğlu, I.A. and Tuhkanen, T. (2000) ‘Treatability of simulated reactive dye-bath wastewater by photochemical and non-photochemical advanced oxidation

processes', *Journal of Environmental Science and Health, Part A*, 35(5), pp. 775–793. Available at: https://doi.org/10.1080/10934520009377002.

Askeland, D.R. (2011) *The Science and Engineering of Materials*. Boston, MA: Springer US. Available at: https://doi.org/10.1007/978-1-4899-2895-5.

Ayawei, N., Ebelegi, A.N. and Wankasi, D. (2017) 'Modelling and Interpretation of Adsorption Isotherms', *Journal of Chemistry*, 2017, pp. 1–11. Available at: https://doi.org/10.1155/2017/3039817.

Bai, Z.-J. *et al.* (2023) 'Tuning photocatalytic performance of Cs3Bi2Br9 perovskite by g-C3N4 for C(sp3)—H bond activation', *Nano Research*, 16(5), pp. 6104–6112. Available at: https://doi.org/10.1007/s12274-022-4835-z.

Benkhaya, S., M'rabet, S. and El Harfi, A. (2020) 'Classifications, properties, recent synthesis and applications of azo dyes', *Heliyon*, 6(1), p. e03271. Available at: https://doi.org/10.1016/j.heliyon.2020.e03271.

Benvenuti, T. *et al.* (2018a) 'EVALUATION OF DIRECT PHOTOLYSIS, ELECTROOXIDATION AND PHOTOELECTROOXIDATION FOR RHODAMINE-B DEGRADATION', *Brazilian Journal of Chemical Engineering*, 35(3), pp. 957–968. Available at: https://doi.org/10.1590/0104-6632.20180353s20170032.

Benvenuti, T. *et al.* (2018b) 'EVALUATION OF DIRECT PHOTOLYSIS, ELECTROOXIDATION AND PHOTOELECTROOXIDATION FOR RHODAMINE-B DEGRADATION', *Brazilian Journal of Chemical Engineering*, 35(3), pp. 957–968. Available at: https://doi.org/10.1590/0104-6632.20180353s20170032.

Bhattacharya, A., Goyal, N. and Gupta, A. (2017) 'Degradation of azo dye methyl red by alkaliphilic, halotolerant Nesterenkonia lacusekhoensis EMLA3: application in alkaline and salt-rich dyeing effluent treatment', *Extremophiles*, 21(3), pp. 479–490. Available at: https://doi.org/10.1007/s00792-017-0918-2.

Bhattacharyya, S., Chaudhary, S.P. and Bhattacharjee, S. (2019) 'Lead-Free Metal Halide Perovskite Nanocrystals for Photocatalysis in Water', *ChemRxiv* [Preprint].

BM, V. and M, V. (2015a) 'Photocatalytic Degradation of Toxic Methyl Red Dye Using Silica Nanoparticles Synthesized from Rice Husk Ash', *Journal of Environmental &*

Analytical Toxicology, 05(06). Available at: https://doi.org/10.4172/2161-0525.1000336.

BM, V. and M, V. (2015b) 'Photocatalytic Degradation of Toxic Methyl Red Dye Using Silica Nanoparticles Synthesized from Rice Husk Ash', *Journal of Environmental & Analytical Toxicology*, 05(06). Available at: https://doi.org/10.4172/2161-0525.1000336.

Bresolin, B.M. (2021) *SYNTHESIS AND PERFORMANCE OF METAL HALIDE PEROVSKITES AS NEW VISIBLE LIGHT PHOTOCATALYSTS*.

Bresolin, Bianca Maria (2021) *SYNTHESIS AND PERFORMANCE OF METAL-HALIDE PEROVSKITES AS NEW VISIBLE LIGHT PHOTOCATALYSTS*.

Bresolin, B.M., Hammouda, S. Ben and Sillanpää, M. (2019) 'Methylammonium iodo bismuthate perovskite (CH 3 NH 3) 3 Bi 2 I 9 as new effective visible light-responsive photocatalyst for degradation of environment pollutants', *Journal of Photochemistry and Photobiology A: Chemistry*, 376, pp. 116–126. Available at: https://doi.org/10.1016/j.jphotochem.2019.03.009.

Bresolin, B.-M., Park, Y. and Bahnemann, D. (2020) 'Recent Progresses on Metal Halide Perovskite-Based Material as Potential Photocatalyst', *Catalysts*, 10(6), p. 709. Available at: https://doi.org/10.3390/catal10060709.

Cao, S. *et al.* (2014) 'Synthesis and characterization of flower-like WS2 nanospheres via a facile hydrothermal route', *Journal of Materials Science: Materials in Electronics*, 25(10), pp. 4300–4305. Available at: https://doi.org/10.1007/s10854-014-2164-z.

Channei, D. *et al.* (2021) 'Synthesis and Characterization of WO_3/CeO_2 Heterostructured Nanoparticles for Photodegradation of Indigo Carmine Dye', *ACS Omega*, 6(30), pp. 19771–19777. Available at: https://doi.org/10.1021/acsomega.1c02453.

Clogston, J.D. and Patri, A.K. (2011) 'Zeta Potential Measurement', in, pp. 63–70. Available at: https://doi.org/10.1007/978-1-60327-198-1_6.

Crini, G. (2006) 'Non-conventional low-cost adsorbents for dye removal: A review', *Bioresource Technology*, pp. 1061–1085. Available at: https://doi.org/10.1016/j.biortech.2005.05.001.

de Mello Donegá, C., Liljeroth, P. and Vanmaekelbergh, D. (2005) ‘Physicochemical Evaluation of the Hot-Injection Method, a Synthesis Route for Monodisperse Nanocrystals’, *Small*, 1(12), pp. 1152–1162. Available at: https://doi.org/10.1002/smll.200500239.

deQuilettes, D.W. *et al.* (2019) ‘Charge-Carrier Recombination in Halide Perovskites’, *Chemical Reviews*, 119(20), pp. 11007–11019. Available at: https://doi.org/10.1021/acs.chemrev.9b00169.

Devi, L.G., Raju, K.S.A. and Kumar, S.G. (2009) ‘Photodegradation of methyl red by advanced and homogeneous photo-Fenton’s processes: A comparative study and kinetic approach’, *Journal of Environmental Monitoring*, 11(7), pp. 1397–1404. Available at: https://doi.org/10.1039/b900936a.

Djurisic, A.B., Chen, X.Y. and Leung, Y.H. (2013) *UV-VIS and Photoluminescence Spectroscopy for Nanomaterials Characterization*. Edited by C. Kumar. Berlin, Heidelberg: Springer Berlin Heidelberg. Available at: https://doi.org/10.1007/978-3-642-27594-4.

Du, H. *et al.* (2022) ‘Adsorption of rhodamine B on polyvinyl chloride, polystyrene, and polyethylene terephthalate microplastics in aqueous environments’, *Environmental Technology and Innovation*, 27. Available at: https://doi.org/10.1016/j.eti.2022.102495.

Fadojutimi, P.O. *et al.* (2022) ‘Transition Metal Dichalcogenides [MX2] in Photocatalytic Water Splitting’, *Catalysts*, 12(5), p. 468. Available at: https://doi.org/10.3390/catal12050468.

Fang, Q. *et al.* (2018) ‘Ultrafast Charge Transfer in Perovskite Nanowire/2D Transition Metal Dichalcogenide Heterostructures’, *The Journal of Physical Chemistry Letters*, 9(7), pp. 1655–1662. Available at: https://doi.org/10.1021/acs.jpclett.8b00260.

Forgacs, E., Cserháti, T. and Oros, G. (2004) ‘Removal of synthetic dyes from wastewaters: a review’, *Environment International*, 30(7), pp. 953–971. Available at: https://doi.org/10.1016/j.envint.2004.02.001.

Gao, G. *et al.* (2017) ‘Novel inorganic perovskite quantum dots for photocatalysis’, *Nanoscale*, 9(33), pp. 12032–12038. Available at: https://doi.org/10.1039/C7NR04421F.

Gao, M. *et al.* (2019) ‘Controlled synthesis and photostability of blue emitting Cs 3 Bi 2 Br 9 perovskite nanocrystals by employing weak polar solvents at room temperature’, *Journal of Materials Chemistry C*, 7(12), pp. 3688–3695. Available at: https://doi.org/10.1039/C9TC00400A.

Georgiou, D. *et al.* (2002) ‘Degradation of azo-reactive dyes by ultraviolet radiation in the presence of hydrogen peroxide’, *Dyes and Pigments*, 52(2), pp. 69–78. Available at: https://doi.org/10.1016/S0143-7208(01)00078-X.

Ghaly, M.Y., Farah, J.Y. and Fathy, A.M. (2007) ‘Enhancement of decolorization rate and COD removal from dyes containing wastewater by the addition of hydrogen peroxide under solar photocatalytic oxidation’, *Desalination*, 217(1–3), pp. 74–84. Available at: https://doi.org/10.1016/j.desal.2007.01.013.

Gqoba, S.S. *et al.* (2021) ‘Hierarchical Nanoflowers of Colloidal WS2 and Their Potential Gas Sensing Properties for Room Temperature Detection of Ammonia’, *Processes*, 9(9), p. 1491. Available at: https://doi.org/10.3390/pr9091491.

Gu, Y. *et al.* (2023) ‘Nitrogen-Doped Graphene Quantum Dot-Passivated δ-Phase CsPbI3: A Water-Stable Photocatalytic Adjuvant to Degrade Rhodamine B’, *Molecules*, 28(21). Available at: https://doi.org/10.3390/molecules28217310.

Gumerov, F.M. *et al.* (2014) ‘Regeneration of the Catalysts by Supercritical Fluid Extraction’, *International Journal of Analytical Mass Spectrometry and Chromatography*, 02(01), pp. 1–14. Available at: https://doi.org/10.4236/ijamsc.2014.21001.

Harun, N. *et al.* (no date) *IMPACT OF TiO 2 AND H 2 O 2 ON PHOTOCATALYTIC DEGRADATION OF PHODAMINE B UNDER ULTRAVIOLET C (UV-C) RADIATION FOR EFFICIENT POLLUTED WASTEWATER TREATMENT*, *Journal of Optoelectronic and Biomedical Materials*. Kuala Nerus.

Hoffmann, M.R. *et al.* (1995) ‘Environmental Applications of Semiconductor Photocatalysis’, *Chemical Reviews*, 95(1), pp. 69–96. Available at: https://doi.org/10.1021/cr00033a004.

Hu, Y. *et al.* (2018) ‘Toward Exploring the Structure of Monolayer to Few-layer TaS2 by Efficient Ultrasound-free Exfoliation’, *Nanoscale Research Letters*, 13(1), p. 20. Available at: https://doi.org/10.1186/s11671-018-2439-z.

Huang, T. *et al.* (2019) ‘Transition Metal Dichalcogenides in Photocatalysts’, in *Two Dimensional Transition Metal Dichalcogenides*. Singapore: Springer Singapore, pp. 107–134. Available at: https://doi.org/10.1007/978-981-13-9045-6_4.

Huang, Y.-J. *et al.* (2022) ‘Improved Mass-Transfer Enhances Photo-Driven Dye Degradation and H $_2$ Evolution over a Few-Layer WS $_2$ /ZnO Heterostructure’, *ACS Omega*, 7(2), pp. 2217–2223. Available at: https://doi.org/10.1021/acsomega.1c05756.

Hussain Chowdhury, M.S. *et al.* (2022) ‘Decomposition of Hydrogen Peroxide using Chemical and Catalytic Methods: A Reactor-based Approach’, *Asian Journal of Chemistry*, 34(5), pp. 1263–1268. Available at: https://doi.org/10.14233/ajchem.2022.23729.

Hussain, T. and Wahab, A. (2018) ‘A critical review of the current water conservation practices in textile wet processing’, *Journal of Cleaner Production*, 198, pp. 806–819. Available at: https://doi.org/10.1016/j.jclepro.2018.07.051.

Huynh, K.A. *et al.* (2020) ‘Halide perovskite photocatalysis: progress and perspectives’, *Journal of Chemical Technology & Biotechnology*, 95(10), pp. 2579–2596. Available at: https://doi.org/10.1002/jctb.6342.

Ibrahim Abubakar, S., Adamu Ibrahim, M. and Bashir Ibrahim, M. (2020) ‘Adsorption of Methyl Orange Dye onto Raw Maize Cob and Maize Cob Activated Carbon: Isotherms and Thermodynamic Studies’, *International Journal of Advanced Chemistry*, 8(1), p. 147. Available at: https://doi.org/10.14419/ijac.v8i1.30676.

Ikram, M. *et al.* (2022) ‘Biodegradation of Azo Dye Methyl Red by Pseudomonas aeruginosa: Optimization of Process Conditions’, *International Journal of Environmental Research and Public Health*, 19(16), p. 9962. Available at: https://doi.org/10.3390/ijerph19169962.

Immanuel, P.N. *et al.* (2022) ‘Enhanced photocatalytic activity of Cs4PbBr6/WS2 hybrid nanocomposite’, *ChemRxiv* [Preprint].

Islam, J. and Hossain, A.K.M.A. (2020a) ‘Narrowing band gap and enhanced visible-light absorption of metal-doped non-toxic CsSnCl $_3$ metal halides for potential optoelectronic applications’, *RSC Advances*, 10(13), pp. 7817–7827. Available at: https://doi.org/10.1039/C9RA10407K.

Islam, J. and Hossain, A.K.M.A. (2020b) ‘Narrowing band gap and enhanced visible-light absorption of metal-doped non-toxic CsSnCl $_3$ metal halides for potential optoelectronic applications’, *RSC Advances*, 10(13), pp. 7817–7827. Available at: https://doi.org/10.1039/C9RA10407K.

Jacopo Prisco (2017) *The color purple: How an accidental discovery changed fashion forever*, *CNN*.

Jain, S.K. and Singh, V.P. (2003) ‘Water Quality Modeling’, in, pp. 743–786. Available at: https://doi.org/10.1016/S0167-5648(03)80067-9.

Jiang, J. *et al.* (2020) ‘Ultrasonication-assisted trace amount solvent synthesis of Cs4PbBr6 crystal with ultra-bright green light emission’, *APL Materials*, 8(7). Available at: https://doi.org/10.1063/5.0009852.

Jimenez-Calvo, P.I. (2019) *Synthesis, characterization, and performance of g-C3N4 based materials decorated with Au nanoparticles for (photo) catalytic applications*.

Jo, Y.K. *et al.* (2019) ‘2D inorganic nanosheet-based hybrid photocatalysts: Design, applications, and perspectives’, *Journal of Photochemistry and Photobiology C: Photochemistry Reviews*, 40, pp. 150–190. Available at: https://doi.org/10.1016/j.jphotochemrev.2018.03.002.

Joseph, A. and Aneesh, P.M. (2022) ‘Efficient degradation of methylene blue: A comparative study using hydrothermally synthesized SnS2, WS2 and VS2 nanostructures’, *Materials Research Bulletin*, 146, p. 111623. Available at: https://doi.org/10.1016/j.materresbull.2021.111623.

Kalam, S. *et al.* (2021) ‘Surfactant Adsorption Isotherms: A Review’, *ACS Omega*, 6(48), pp. 32342–32348. Available at: https://doi.org/10.1021/acsomega.1c04661.

Kanhere, P. and Chen, Z. (2014) ‘A Review on Visible Light Active Perovskite-Based Photocatalysts’, *Molecules*, 19(12), pp. 19995–20022. Available at: https://doi.org/10.3390/molecules191219995.

Kant, R. (2012) ‘Textile dyeing industry an environmental hazard’, *Natural Science*, 04(01), pp. 22–26. Available at: https://doi.org/10.4236/ns.2012.41004.

Katheresan, V., Kansedo, J. and Lau, S.Y. (2018) ‘Efficiency of various recent wastewater dye removal methods: A review’, *Journal of Environmental Chemical Engineering*, 6(4), pp. 4676–4697. Available at: https://doi.org/10.1016/j.jece.2018.06.060.

Khan, A., Malik, S. and Bilal, M. (2022) *Nano-Bioremediation : Fundamentals and Applications*. Edited by H.M.N. Iqbal, M. Bilal, and T.A. Nguyen. Elsevier. Available at: https://doi.org/10.1016/C2020-0-00522-0.

Khan, S. and Ali, J. (2018) ‘Chemical analysis of air and water’, in *Bioassays*. Elsevier, pp. 21–39. Available at: https://doi.org/10.1016/B978-0-12-811861-0.00002-4.

Koe, W.S. *et al.* (2020) ‘An overview of photocatalytic degradation: photocatalysts, mechanisms, and development of photocatalytic membrane’, *Environmental Science and Pollution Research*. Springer, pp. 2522–2565. Available at: https://doi.org/10.1007/s11356-019-07193-5.

Kozuch, S. and Martin, J.M.L. (2012) ‘“Turning Over” Definitions in Catalytic Cycles’, *ACS Catalysis*, 2(12), pp. 2787–2794. Available at: https://doi.org/10.1021/cs3005264.

Kumar, S. *et al.* (2014) ‘Nanotechnology-Based Water Treatment Strategies’, *Journal of Nanoscience and Nanotechnology*, 14(2), pp. 1838–1858. Available at: https://doi.org/10.1166/jnn.2014.9050.

Kumar, S. *et al.* (2020) ‘Nanoscale zinc oxide based heterojunctions as visible light active photocatalysts for hydrogen energy and environmental remediation’, *Catalysis Reviews*, 62(3), pp. 346–405. Available at: https://doi.org/10.1080/01614940.2019.1684649.

Kumari, H. *et al.* (2023) ‘A Review on Photocatalysis Used For Wastewater Treatment: Dye Degradation’, *Water, Air, & Soil Pollution*, 234(6), p. 349. Available at: https://doi.org/10.1007/s11270-023-06359-9.

Kundu, A. and Mondal, A. (2019) ‘Kinetics, isotherm, and thermodynamic studies of methylene blue selective adsorption and photocatalysis of malachite green from

aqueous solution using layered Na-intercalated Cu-doped Titania', *Applied Clay Science*, 183, p. 105323. Available at: https://doi.org/10.1016/j.clay.2019.105323.

Kusrini, E. *et al.* (2018) 'Textile Dye Removal from Aqueous Solution using Modified Graphite Waste/Lanthanum/Chitosan Composite', *IOP Conference Series: Materials Science and Engineering*, 316, p. 012029. Available at: https://doi.org/10.1088/1757-899X/316/1/012029.

Kwon, S.G. and Hyeon, T. (2011) 'Formation Mechanisms of Uniform Nanocrystals via Hot-Injection and Heat-Up Methods', *Small*, 7(19), pp. 2685–2702. Available at: https://doi.org/10.1002/smll.201002022.

Lee, J.S. and Jang, J. (2014) 'Hetero-structured semiconductor nanomaterials for photocatalytic applications', *Journal of Industrial and Engineering Chemistry*, 20(2), pp. 363–371. Available at: https://doi.org/10.1016/j.jiec.2013.11.050.

Lellis, B. *et al.* (2019a) 'Effects of textile dyes on health and the environment and bioremediation potential of living organisms', *Biotechnology Research and Innovation*, 3(2), pp. 275–290. Available at: https://doi.org/10.1016/j.biori.2019.09.001.

Lellis, B. *et al.* (2019b) 'Effects of textile dyes on health and the environment and bioremediation potential of living organisms', *Biotechnology Research and Innovation*, 3(2), pp. 275–290. Available at: https://doi.org/10.1016/j.biori.2019.09.001.

Li, D. and Liu, S. (2019) 'Water Quality Detection for Lakes', in *Water Quality Monitoring and Management*. Elsevier, pp. 221–231. Available at: https://doi.org/10.1016/B978-0-12-811330-1.00008-9.

Li, G. *et al.* (2010) 'Effect of the agglomeration of TiO2 nanoparticles on their photocatalytic performance in the aqueous phase', *Journal of Colloid and Interface Science*, 348(2), pp. 342–347. Available at: https://doi.org/10.1016/j.jcis.2010.04.045.

Li, Q. *et al.* (2021) 'Boosting Photocatalytic Activity and Stability of Lead-Free Cs3Bi2Br9Perovskite Nanocrystals via in Situ Growth on Monolayer 2D Ti3C2T xMXene for C-H Bond Oxidation', *ACS Applied Materials and Interfaces*, 13(23), pp. 27323–27333. Available at: https://doi.org/10.1021/acsami.1c06367.

Li, W. and Wu, H. (2017) ‘Sodium citrate functionalized reusable Fe3O4@TiO2 photocatalyst for water purification’, *Chemical Physics Letters*, 686, pp. 178–182. Available at: https://doi.org/10.1016/j.cplett.2017.08.046.

Liu, L. *et al.* (2015) ‘Simultaneous removal of cationic and anionic dyes from environmental water using montmorillonite-pillared graphene oxide’, *Journal of Chemical and Engineering Data*, 60(5), pp. 1270–1278. Available at: https://doi.org/10.1021/je5009312.

Liu, L. *et al.* (2019) ‘Application of Nanotechnology in the Removal of Heavy Metal From Water’, in *Nanomaterials for the Removal of Pollutants and Resource Reutilization*. Elsevier, pp. 83–147. Available at: https://doi.org/10.1016/B978-0-12-814837-2.00004-4.

Lu, C. *et al.* (2019) ‘Cesium Oleate Precursor Preparation for Lead Halide Perovskite Nanocrystal Synthesis: The Influence of Excess Oleic Acid on Achieving Solubility, Conversion, and Reproducibility’, *Chemistry of Materials*, 31(1), pp. 62–67. Available at: https://doi.org/10.1021/acs.chemmater.8b04876.

Mahdi, M.H., Mohammed, T.J. and Al-Najar, J.A. (2021) ‘Advanced Oxidation Processes (AOPs) for treatment of antibiotics in wastewater: A review’, *IOP Conference Series: Earth and Environmental Science*, 779(1), p. 012109. Available at: https://doi.org/10.1088/1755-1315/779/1/012109.

Marshall, J.L. (1991) ‘Scanning Electron Microscopy and Energy Dispersive X-ray (SEM/EDX) Characterization of Solder Solderability and Reliability’, in *Solder Joint Reliability*. Boston, MA: Springer US, pp. 173–224. Available at: https://doi.org/10.1007/978-1-4615-3910-0_6.

Martínez-Huitle, C.A. and Brillas, E. (2009) ‘Decontamination of wastewaters containing synthetic organic dyes by electrochemical methods: A general review’, *Applied Catalysis B: Environmental*, 87(3–4), pp. 105–145. Available at: https://doi.org/10.1016/j.apcatb.2008.09.017.

Meerbach, C. *et al.* (2020a) ‘General Colloidal Synthesis of Transition-Metal Disulfide Nanomaterials as Electrocatalysts for Hydrogen Evolution Reaction’, *ACS Applied Materials & Interfaces*, 12(11), pp. 13148–13155. Available at: https://doi.org/10.1021/acsami.9b21607.

Meerbach, C. *et al.* (2020b) ‘General Colloidal Synthesis of Transition-Metal Disulfide Nanomaterials as Electrocatalysts for Hydrogen Evolution Reaction’, *ACS Applied Materials & Interfaces*, 12(11), pp. 13148–13155. Available at: https://doi.org/10.1021/acsami.9b21607.

Miller, M.D. *et al.* (2022) ‘Potential impacts of synthetic food dyes on activity and attention in children: a review of the human and animal evidence’, *Environmental Health*, 21(1), p. 45. Available at: https://doi.org/10.1186/s12940-022-00849-9.

Milošević, M. *et al.* (2023) ‘Advanced photocatalysis mediated by TiO2/Ag/TiO2 nanoparticles modified cotton fabric’, *Cellulose*, 30(7), pp. 4749–4771. Available at: https://doi.org/10.1007/s10570-023-05165-0.

Mokif, L.A. (2019) ‘Removal Methods of Synthetic Dyes from Industrial Wastewater: A review’, *Mesopo. Environ. J*, 5(1), pp. 23–40. Available at: https://doi.org/10.31759/mej.2019.5.1.0040.

Moosavi, S. *et al.* (2020) ‘Methylene Blue Dye Photocatalytic Degradation over Synthesised Fe3O4/AC/TiO2 Nano-Catalyst: Degradation and Reusability Studies’, *Nanomaterials*, 10(12), p. 2360. Available at: https://doi.org/10.3390/nano10122360.

Musah, M. *et al.* (2022a) ‘Adsorption Kinetics and Isotherm Models: A Review’, *Caliphate Journal of Science and Technology*, 4(1), pp. 20–26. Available at: https://doi.org/10.4314/cajost.v4i1.3.

Musah, M. *et al.* (2022b) ‘Adsorption Kinetics and Isotherm Models: A Review’, *Caliphate Journal of Science and Technology*, 4(1), pp. 20–26. Available at: https://doi.org/10.4314/cajost.v4i1.3.

Muthuraman, G. and Teng, T.T. (2009) ‘Extraction of methyl red from industrial wastewater using xylene as an extractant’, *Progress in Natural Science*, 19(10), pp. 1215–1220. Available at: https://doi.org/10.1016/j.pnsc.2009.04.002.

Nagaraja, R. *et al.* (2012a) ‘Photocatalytic degradation of Rhodamine B dye under UV/solar light using ZnO nanopowder synthesized by solution combustion route’, *Powder Technology*, 215–216, pp. 91–97. Available at: https://doi.org/10.1016/j.powtec.2011.09.014.

Nagaraja, R. *et al.* (2012b) ‘Photocatalytic degradation of Rhodamine B dye under UV/solar light using ZnO nanopowder synthesized by solution combustion route’, *Powder Technology*, 215–216, pp. 91–97. Available at: https://doi.org/10.1016/j.powtec.2011.09.014.

Natarajan, T.S. *et al.* (2011) ‘Study on UV-LED/TiO2 process for degradation of Rhodamine B dye’, *Chemical Engineering Journal*, 169(1–3), pp. 126–134. Available at: https://doi.org/10.1016/j.cej.2011.02.066.

Ndala, Z. *et al.* (2020) ‘Evaluating the Effect of Varying the Metal Precursor in the Colloidal Synthesis of MoSe2 Nanomaterials and Their Application as Electrodes in the Hydrogen Evolution Reaction’, *Nanomaterials*, 10(9), p. 1786. Available at: https://doi.org/10.3390/nano10091786.

Nidheesh, P.V., Gandhimathi, R. and Ramesh, S.T. (2013) ‘Degradation of dyes from aqueous solution by Fenton processes: a review’, *Environmental Science and Pollution Research*, 20(4), pp. 2099–2132. Available at: https://doi.org/10.1007/s11356-012-1385-z.

Nidheesh, P.V., Zhou, M. and Oturan, M.A. (2018) ‘An overview on the removal of synthetic dyes from water by electrochemical advanced oxidation processes’, *Chemosphere*, 197, pp. 210–227. Available at: https://doi.org/10.1016/j.chemosphere.2017.12.195.

Olatunji, O.O. *et al.* (2018) ‘Thermo-gravimetric characterization of biomass properties: A review’, *IOP Conference Series: Materials Science and Engineering*, 423, p. 012175. Available at: https://doi.org/10.1088/1757-899X/423/1/012175.

Palchoudhury, S., Baalousha, M. and Lead, J.R. (2015) ‘Methods for Measuring Concentration (Mass, Surface Area and Number) of Nanomaterials’, in, pp. 153–181. Available at: https://doi.org/10.1016/B978-0-08-099948-7.00005-1.

Pang, Y. *et al.* (2019) ‘Photocatalysts: Colloidal Single-Layer Photocatalysts for Methanol-Storable Solar H 2 Fuel (Adv. Mater. 49/2019)’, *Advanced Materials*, 31(49), p. 1970348. Available at: https://doi.org/10.1002/adma.201970348.

Patel, B. and Shah, K. (2014) *Research review on Biodegradation of Azo Dye compounds*. Available at: https://ssrn.com/abstract=2474466.

Piaskowski, K., Świderska-Dąbrowska, R. and Zarzycki, P.K. (2018) ‘Dye removal from water and wastewater using various physical, chemical, and biological processes’, *Journal of AOAC International*, 101(5), pp. 1371–1384. Available at: https://doi.org/10.5740/jaoacint.18-0051.

Piccin, J.S., Dotto, G.L. and Pinto, L.A.A. (2011) ‘Adsorption isotherms and thermochemical data of FD&C Red n° 40 binding by Chitosan’, *Brazilian Journal of Chemical Engineering*, 28(2), pp. 295–304. Available at: https://doi.org/10.1590/S0104-66322011000200014.

Quevedo, A.C. *et al.* (2021) ‘UV-Vis Spectroscopic Characterization of Nanomaterials in Aqueous Media’, *Journal of Visualized Experiments* [Preprint], (176). Available at: https://doi.org/10.3791/61764.

Rafiq, A. *et al.* (2021a) ‘Photocatalytic degradation of dyes using semiconductor photocatalysts to clean industrial water pollution’, *Journal of Industrial and Engineering Chemistry*, 97, pp. 111–128. Available at: https://doi.org/10.1016/j.jiec.2021.02.017.

Rafiq, A. *et al.* (2021b) ‘Photocatalytic degradation of dyes using semiconductor photocatalysts to clean industrial water pollution’, *Journal of Industrial and Engineering Chemistry*, 97, pp. 111–128. Available at: https://doi.org/10.1016/j.jiec.2021.02.017.

Rand Water (no date) *Water Wise - Water Situation in South Africa*. Available at: https://waterwise.co.za/site/water/environment/situation.html (Accessed: 18 March 2023).

Rani, S. *et al.* (2016) ‘Removal of methylene blue and rhodamine B from water by zirconium oxide/graphene’, *Water Science*, 30(1), pp. 51–60. Available at: https://doi.org/10.1016/j.wsj.2016.04.001.

Rengaraj, S. *et al.* (2007) ‘Adsorption characteristics of Cu(II) onto ion exchange resins 252H and 1500H: Kinetics, isotherms and error analysis’, *Journal of Hazardous Materials*, 143(1–2), pp. 469–477. Available at: https://doi.org/10.1016/j.jhazmat.2006.09.064.

Reyes-Pérez, F. *et al.* (2018) ‘Visible-Light-Enhanced Photocatalytic Activity of Totally Inorganic Halide-Based Perovskite’, *ChemistrySelect*, 3(36), pp. 10226–10235. Available at: https://doi.org/10.1002/slct.201801564.

Reza, K.M., Kurny, A. and Gulshan, F. (2017) 'Parameters affecting the photocatalytic degradation of dyes using TiO2: a review', *Applied Water Science*, 7(4), pp. 1569–1578. Available at: https://doi.org/10.1007/s13201-015-0367-y.

Ridjal, A.T.M. *et al.* (2022) 'Study of Rhodamine B Dyes Content in Snacks of Karuwisi Traditional Market Makassar, South Sulawesi, Indonesia', *IOP Conference Series: Earth and Environmental Science*, 1027(1), p. 012012. Available at: https://doi.org/10.1088/1755-1315/1027/1/012012.

Robinson, T. *et al.* (2001) 'Remediation of dyes in textile effluent: a critical review on current treatment technologies with a proposed alternative', *Bioresource Technology*, 77(3), pp. 247–255. Available at: https://doi.org/10.1016/S0960-8524(00)00080-8.

Rothenberg, G. (2017) *Catalysis concepts and green applications*. Weinheim Wiley-Vch Verlag Gmbh & Co.

Sahraie, N.R. *et al.* (2015) 'Quantifying the density and utilization of active sites in non-precious metal oxygen electroreduction catalysts', *Nature Communications*, 6(1), p. 8618. Available at: https://doi.org/10.1038/ncomms9618.

Sahu, S. and Samanta, P.K. (2021a) 'Peak Profile Analysis of X-ray Diffraction Pattern of Zinc Oxide Nanostructure', *Journal of Nano- and Electronic Physics*, 13(5), pp. 05001-1-05001–4. Available at: https://doi.org/10.21272/jnep.13(5).05001.

Sahu, S. and Samanta, P.K. (2021b) 'Peak Profile Analysis of X-ray Diffraction Pattern of Zinc Oxide Nanostructure', *Journal of Nano- and Electronic Physics*, 13(5), pp. 05001-1-05001–4. Available at: https://doi.org/10.21272/jnep.13(5).05001.

Saka, H. (2003) 'Transmission Electron Microscopy', in *Carbon Alloys*. Elsevier, pp. 223–238. Available at: https://doi.org/10.1016/B978-008044163-4/50014-0.

Sarabandi, K., Gharehbeglou, P. and Jafari, S.M. (2020) 'Scanning electron microscopy (SEM) of nanoencapsulated food ingredients', in *Characterization of Nanoencapsulated Food Ingredients*. Elsevier, pp. 83–130. Available at: https://doi.org/10.1016/B978-0-12-815667-4.00003-1.

Saravanan, R., Gracia, F. and Stephen, A. (2017) 'Basic Principles, Mechanism, and Challenges of Photocatalysis', in, pp. 19–40. Available at: https://doi.org/10.1007/978-3-319-62446-4_2.

Shah, K. (2014) *Biodegradation of azo dye compounds IRJBB Biodegradation of azo dye compounds*. Available at: https://www.researchgate.net/publication/267623559.

Shaheen, A. (2010) *Band Structure and Electrical Conductivity in Semiconductors*. Available at: https://www.researchgate.net/publication/280092391_Band_Structure_and_Electrical_Conductivity_in_Semiconductors.

Shakir, K. *et al.* (2010) 'Removal of rhodamine B (a basic dye) and thoron (an acidic dye) from dilute aqueous solutions and wastewater simulants by ion flotation', *Water Research*, 44(5), pp. 1449–1461. Available at: https://doi.org/10.1016/j.watres.2009.10.029.

Shamsi, J. *et al.* (2019) 'Metal Halide Perovskite Nanocrystals: Synthesis, Post-Synthesis Modifications, and Their Optical Properties', *Chemical Reviews*, 119(5), pp. 3296–3348. Available at: https://doi.org/10.1021/acs.chemrev.8b00644.

Shand, M.A. and Jin, F. (2020) 'Introduction – Characterization of MgO', in *Magnesia Cements*. Elsevier, pp. 1–10. Available at: https://doi.org/10.1016/B978-0-12-391925-0.00006-6.

Sharma, J., Sharma, S. and Soni, V. (2021) 'Classification and impact of synthetic textile dyes on Aquatic Flora: A review', *Regional Studies in Marine Science*. Elsevier B.V. Available at: https://doi.org/10.1016/j.rsma.2021.101802.

Sharma, P. *et al.* (2022) 'Impact of pharmaceuticals and antibiotics waste on the river ecosystem: a growing threat', in *Ecological Significance of River Ecosystems*. Elsevier, pp. 15–36. Available at: https://doi.org/10.1016/B978-0-323-85045-2.00015-7.

Sing, K.S.W. (1985) 'Reporting physisorption data for gas/solid systems with special reference to the determination of surface area and porosity (Recommendations 1984)', *Pure and Applied Chemistry*, 57(4), pp. 603–619. Available at: https://doi.org/10.1351/pac198557040603.

Singh, D. and Ahuja, R. (2022) 'Two-Dimensional Perovskite/HfS_2 van der Waals Heterostructure as an Absorber Material for Photovoltaic Applications', *ACS Applied Energy Materials*, 5(2), pp. 2300–2307. Available at: https://doi.org/10.1021/acsaem.1c03796.

Singh, K. and Arora, S. (2011) ‘Removal of synthetic textile dyes from wastewaters: A critical review on present treatment technologies’, *Critical Reviews in Environmental Science and Technology*, 41(9), pp. 807–878. Available at: https://doi.org/10.1080/10643380903218376.

Song, W. *et al.* (2021) ‘Novel BiOBr by compositing low-cost biochar for efficient ciprofloxacin removal: the synergy of adsorption and photocatalysis on the degradation kinetics and mechanism insight’, *RSC Advances*, 11(25), pp. 15369–15379. Available at: https://doi.org/10.1039/D1RA00941A.

Speight, J.G. (2017) ‘Chemical Transformations in the Environment’, in *Environmental Organic Chemistry for Engineers*. Elsevier, pp. 305–353. Available at: https://doi.org/10.1016/B978-0-12-804492-6.00007-1.

Subramani, A.K. *et al.* (2007) ‘Photocatalytic degradation of indigo carmine dye using TiO2 impregnated activated carbon’, *Bulletin of Materials Science*, 30(1), pp. 37–41. Available at: https://doi.org/10.1007/s12034-007-0007-8.

Sun, J. (2014) *Development of Inorganic-Organic Hybrid Materials for Waste Water Treatment*. Available at: https://www.researchgate.net/publication/314081363_Development_of_Inorganic-Organic_Hybrid_Materials_for_Waste_Water_Treatment (Accessed: 23 March 2023).

Sun, J. *et al.* (2021) ‘Highly stable halide perovskite with Na incorporation for efficient photocatalytic degradation of organic dyes in water solution’, *Environmental Science and Pollution Research*, 28(36), pp. 50813–50824. Available at: https://doi.org/10.1007/s11356-021-14188-8.

Tilvi, S., Majik, M.S. and Singh, K.S. (2014) ‘Mass Spectrometry for Determination of Bioactive Compounds’, in, pp. 193–218. Available at: https://doi.org/10.1016/B978-0-444-63359-0.00008-2.

Tkaczyk, A., Mitrowska, K. and Posyniak, A. (2020) ‘Synthetic organic dyes as contaminants of the aquatic environment and their implications for ecosystems: A review’, *Science of the Total Environment*. Elsevier B.V. Available at: https://doi.org/10.1016/j.scitotenv.2020.137222.

V., L.P. and Rajagopalan, V. (2016) ‘A New Synergetic Nanocomposite for Dye Degradation in Dark and Light’, *Scientific Reports*, 6(1), p. 38606. Available at: https://doi.org/10.1038/srep38606.

Vattikuti, S.V.P. *et al.* (2019) ‘Binder-free WS2/ZrO2 hybrid as a photocatalyst for organic pollutant degradation under UV/simulated sunlight and tests for H2 evolution’, *Journal of Alloys and Compounds*, 809, p. 151805. Available at: https://doi.org/10.1016/j.jallcom.2019.151805.

Velusamy, S. *et al.* (2021) ‘A Review on Heavy Metal Ions and Containing Dyes Removal Through Graphene Oxide-Based Adsorption Strategies for Textile Wastewater Treatment’, *Chemical Record*. John Wiley and Sons Inc, pp. 1570–1610. Available at: https://doi.org/10.1002/tcr.202000153.

Wang, J. *et al.* (2021) ‘Recent advances in metal halide perovskite photocatalysts: Properties, synthesis and applications’, *Journal of Energy Chemistry*. Elsevier B.V., pp. 770–785. Available at: https://doi.org/10.1016/j.jechem.2020.06.024.

Wang, X. *et al.* (2016) ‘MO degradation by Ag–Ag2O/g-C3N4 composites under visible-light irradiation’, *SpringerPlus*, 5(1), p. 369. Available at: https://doi.org/10.1186/s40064-016-1805-5.

Weng, B. *et al.* (2019) ‘Photocorrosion Inhibition of Semiconductor-Based Photocatalysts: Basic Principle, Current Development, and Future Perspective’, *ACS Catalysis*, 9(5), pp. 4642–4687. Available at: https://doi.org/10.1021/acscatal.9b00313.

Wong, C.C. and Chu, W. (2003) ‘The direct photolysis and photocatalytic degradation of alachlor at different TiO2 and UV sources’, *Chemosphere*, 50(8), pp. 981–987. Available at: https://doi.org/10.1016/S0045-6535(02)00640-9.

World Health Organization (WHO) (2022) *Drinking-water*. Available at: https://www.who.int/news-room/fact-sheets/detail/drinking-water (Accessed: 18 March 2023).

World Health Organization (WHO) and United Nations Children’s Fund (UNICEF) (2021) *Progress on household drinking water, sanitation and hygiene 2000-2020: five*

years into the SDGs. Available at: https://washdata.org/sites/default/files/2021-07/jmp-2021-wash-households.pdf (Accessed: 18 March 2023).

Xu, C. *et al.* (2019) 'Nanostructured materials for photocatalysis', *Chemical Society Reviews*, 48(14), pp. 3868–3902. Available at: https://doi.org/10.1039/C9CS00102F.

Yang, B. *et al.* (2017a) 'Lead-Free, Air-Stable All-Inorganic Cesium Bismuth Halide Perovskite Nanocrystals', *Angewandte Chemie*, 129(41), pp. 12645–12649. Available at: https://doi.org/10.1002/ange.201704739.

Yang, B. *et al.* (2017b) 'Lead-Free, Air-Stable All-Inorganic Cesium Bismuth Halide Perovskite Nanocrystals', *Angewandte Chemie*, 129(41), pp. 12645–12649. Available at: https://doi.org/10.1002/ange.201704739.

Yaseen, D.A. and Scholz, M. (2016) 'Shallow pond systems planted with Lemna minor treating azo dyes', *Ecological Engineering*, 94, pp. 295–305. Available at: https://doi.org/10.1016/j.ecoleng.2016.05.081.

Yi, Z. *et al.* (2019) 'Will organic–inorganic hybrid halide lead perovskites be eliminated from optoelectronic applications?', *Nanoscale Advances*, 1(4), pp. 1276–1289. Available at: https://doi.org/10.1039/C8NA00416A.

Yousef, A. *et al.* (2022a) 'Recent Progress in WS2-Based Nanomaterials Employed for Photocatalytic Water Treatment', *Catalysts*, 12(10), p. 1138. Available at: https://doi.org/10.3390/catal12101138.

Yousef, A. *et al.* (2022b) 'Recent Progress in WS2-Based Nanomaterials Employed for Photocatalytic Water Treatment', *Catalysts*, 12(10), p. 1138. Available at: https://doi.org/10.3390/catal12101138.

Yousef, A. *et al.* (2022b) 'Recent Progress in WS2-Based Nanomaterials Employed for Photocatalytic Water Treatment', *Catalysts*, 12(10), p. 1138. Available at: https://doi.org/10.3390/catal12101138.

Zafar, Z., Fatima, R. and Kim, J.-O. (2021) 'Experimental studies on water matrix and influence of textile effluents on photocatalytic degradation of organic wastewater using Fe–TiO2 nanotubes: Towards commercial application', *Environmental Research*, 197, p. 111120. Available at: https://doi.org/10.1016/j.envres.2021.111120.

Zeta potential - An introduction in 30 minutes (2020) *Malvern Panalytical*. Available at: https://www.malvernpanalytical.com/en/learn/knowledge-center/technical-notes/TN101104ZetaPotentialIntroduction (Accessed: 27 March 2023).

Zhang, C. *et al.* (2023) 'Based on Z-scheme heterojunction $CsPbBr_3$ /UiO-66 composite photocatalytic degradation', *Applied Organometallic Chemistry*, 37(7). Available at: https://doi.org/10.1002/aoc.7122.

Zhang, Q. *et al.* (2020a) 'Enhanced Photocatalytic Property of γ-$CsPbI_3$ Perovskite Nanocrystals with WS_2', *ACS Sustainable Chemistry & Engineering*, 8(2), pp. 1219–1229. Available at: https://doi.org/10.1021/acssuschemeng.9b06451.

Zhang, Q. *et al.* (2020b) 'Enhanced Photocatalytic Property of γ-CsPbI3 Perovskite Nanocrystals with WS2', *ACS Sustainable Chemistry and Engineering*, 8(2), pp. 1219–1229. Available at: https://doi.org/10.1021/acssuschemeng.9b06451.

Zhang, Y. *et al.* (2020) 'A "Tips and Tricks" Practical Guide to the Synthesis of Metal Halide Perovskite Nanocrystals', *Chemistry of Materials*, 32(13), pp. 5410–5423. Available at: https://doi.org/10.1021/acs.chemmater.0c01735.

Zhang, Z. *et al.* (2019) 'Stable and Highly Efficient Photocatalysis with Lead-Free Double-Perovskite of $Cs_2AgBiBr_6$', *Angewandte Chemie International Edition*, 58(22), pp. 7263–7267. Available at: https://doi.org/10.1002/anie.201900658.

Zhu, S. and Wang, D. (2017a) 'Photocatalysis: Basic Principles, Diverse Forms of Implementations and Emerging Scientific Opportunities', *Advanced Energy Materials*, 7(23), p. 1700841. Available at: https://doi.org/10.1002/aenm.201700841.

Zhu, S. and Wang, D. (2017b) 'Photocatalysis: Basic principles, diverse forms of implementations and emerging scientific opportunities', *Advanced Energy Materials*. Wiley-VCH Verlag. Available at: https://doi.org/10.1002/aenm.201700841.

Ziarani, G.M. *et al.* (2018) 'Introduction and Importance of Synthetic Organic Dyes', in *Metal-Free Synthetic Organic Dyes*. Elsevier, pp. 1–7. Available at: https://doi.org/10.1016/B978-0-12-815647-6.00001-7.

CHAPTER 5: RESULTS AND DISCUSSION

5.0. Results and Discussion (Cont'd)

5.1. Application studies

In this chapter, the photodegradation of RhB and MR were investigated using various methods, including direct photolysis (UV), indirect photolysis (UV/H_2O_2), and heterogeneous photodegradation using $Cs_3Bi_2Br_9$ and $Cs_3Bi_2Br_9/WS_2$ catalysts, both in the absence and presence of H_2O_2. The characteristics of Methyl red and Rhodamine are outlined in **Table 5.1** below.

The effectiveness of these methods was assessed and reported. Optimization of the heterogeneous photodegradation reactions involved the manipulation of catalyst loading, initial dye concentration, and pH. Additionally, the kinetics and adsorption isotherms were examined.

Table 5.1: MR and RhB dye properties and harmful effects

Properties	**Methyl red** (LabChem, 2015; Ikram et al., 2022; Muthuraman and Teng, 2009)	**Rhodamine B** (Nagaraja et al., 2012; Yaseen and Scholz, 2016; Benvenuti et al., 2018)
Other names	Acid red-2	Basic violet 10
Molecular formula	$C_{15}H_{15}N_3O_2$	$C_{28}H_{31}ClN_2O_3$

Dye applications	Cotton, silk, viscose, and wool	Silk, cotton, leather, wool, etc It is also used in the biomedical, photochemical, and chemical industries
Chemical structure	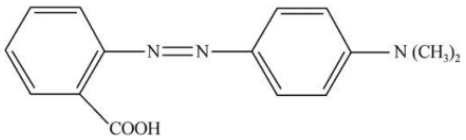	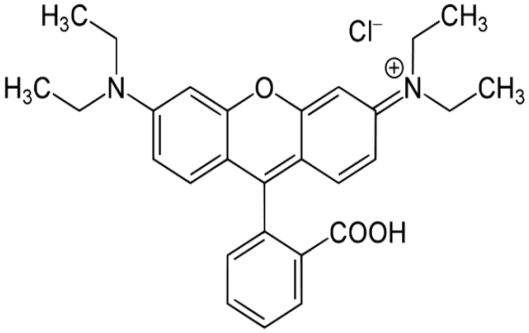
Ionic nature	Anionic	Cationic
Type of dye	Azo (N=N)	Fluorescent xanthene ($CH_2[C_6H_4]_2O$)
Side effects	Difficulty breathing, vomiting, nausea, diarrhoea, abdominal pain, cancer, hives, itching, rash, and eye irritation.	Cancer, respiratory diseases, nausea, vomiting, diarrhoea, cardiovascular disease, kidney disease/failure, liver dysfunction, hormonal imbalance, premature birth, decreased immunity, nervous system development disorders, mental health problems, learning disabilities/cognitive dysfunction, oxidative stress on cells and tissues, irritation to the eyes, respiratory tract, and skin.
Toxicity (LD50 Oral Rat)	10740 mg/kg	500 mg/kg

5.1.1. Photolysis

Photolysis of SODs is a process that involves the use of UV irradiation to break down these compounds into smaller and less harmful substances in the absence of a photocatalyst or oxidizing agent (Anisuzzaman et al., 2022, Benvenuti et al., 2018). The photolysis mechanism includes the excitation of electrons initiated by photon

absorption, and this can lead to the cleavage of the dye molecule into smaller (Speight, 2017). The effectiveness of photolysis in degrading synthetic dyes depends on several environmental and chemical factors, such as light wavelength and intensity, the concentration and chemical structure of the dye, and the presence of other compounds in the environment that can scavenge the ROS (Speight, 2017). Photolysis is a promising technique for the treatment of wastewater and surface water (Sharma *et al.*, 2022). It offers advantages over conventional treatment methods such as the ability to degrade a wide range of dyes, low cost, and minimal production of secondary pollutants. However, the process still requires further research to optimize the conditions for maximum efficiency and to develop suitable photocatalytic materials.

The photolysis mechanism is as follows (Anisuzzaman *et al.*, 2022):

$$Dye + hv + (oxygen) \longrightarrow products \quad \textbf{(5.1)}$$

$$H_2O + hv \longrightarrow OH^{\bullet} + H \quad \textbf{(5.2)}$$

$$Dye + OH^{\bullet} \longrightarrow products \quad \textbf{(5.3)}$$

5.1.1.1. Direct photolysis

Direct photolysis studies were conducted to investigate the degradation of MR and RhB under UV light irradiation in the absence of a photocatalyst. The initial dye concentration was set at 20 ppm for both dyes. The samples were prepared by dissolving the dyes in ultrapure water (UPW). The pH of the RhB solution was 4.3 after the dye had dissolved in UPW. MR is a dye that exhibits colour variations under different pH conditions. In the pH range of 4.4-6.2, MR appears red; hence, the solution pH was adjusted to 5.5 using 1M NaOH and 1M HNO_3 solutions, as this pH falls within the middle of the 4.4-6.2 range. The dye absorption spectra and degradation efficiency (DE%) graphs in **Figures 5.1 (a) and (c)** illustrate the changes in dye concentration over time. **Figures 5.1 (b)** and **(d)** demonstrate degradation efficiencies of 2.68% for MR and 3.10% for RhB respectively after 2 hours of irradiation. The low results are due to the N functional groups that are found in SODs, such as RhB and MR, which are known to cause resistance to photolysis (Ridjal *et al.*, 2022). MR displays slightly higher resistance to photolytic degradation compared to RhB. This could be attributed to the presence of the azo group (N=N) in the MR dye, which is known for its exceptional resistance to degradation (Bhattacharya, Goyal and Gupta, 2017; Bresolin, Hammouda and Sillanpää, 2019)

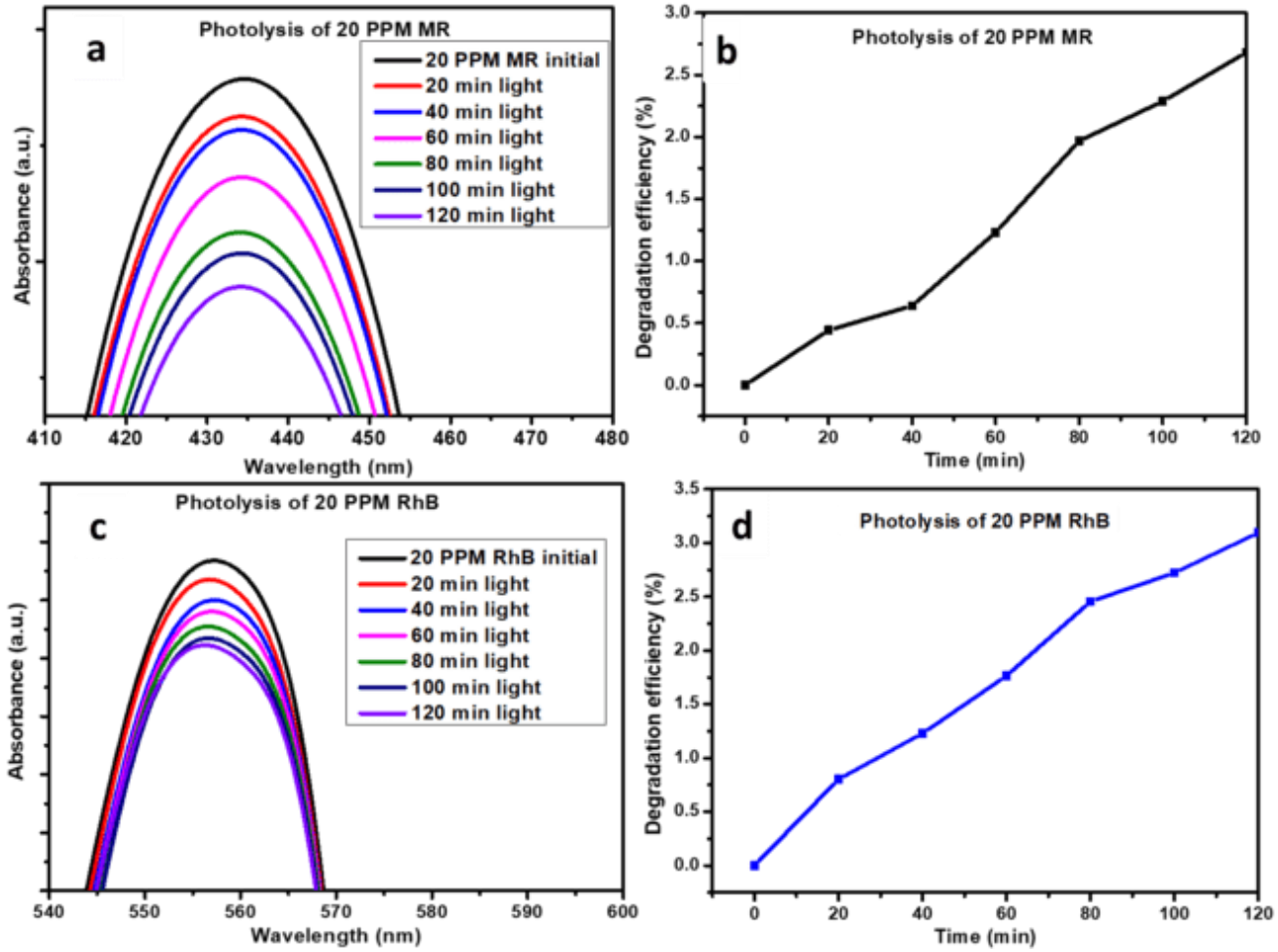

Figure 5.1. Direct photolysis study **a)** 20 ppm MR UV-vis absorbance spectrum **b)** 20 ppm MR DE% plot **c)** 20 ppm RhB UV-vis absorbance spectrum **d)** RhB DE% plot as a function of time under solar simulated light irradiation for 2 hrs

---

5.1.1.2. Photolysis with H_2O_2

To address the poor results obtained from direct photolysis, H_2O_2 was introduced to the dye solutions to explore its potential to enhance the decolorization of the dyes. The concentration of H_2O_2 added to the dye solutions was 0.3519 M. The results are presented in **Figures 5.2** and **5.3** below. Following 2 hours of irradiation under the UV light source, the colour intensity of the MR and RhB dyes was gradually reduced with an increase in irradiation time as shown in **Figures 5.2 (a)** and **(c)**. The degradation efficiency (DE%) was therefore determined to be 40.59% for MR and 52.72% for RhB as shown in **Figures 5.2 (b)** and **(d)**. **Figure 5.3** illustrates the pseudo-first-order linear fit for the photolysis reactions. The pseudo-first-order rate constant values were derived from the slope. It was observed that the rate constant increased by 14-fold for

MR and 23-fold for RhB when H_2O_2 was added to the dye solution compared to the UV photolysis results. The addition of H_2O_2 significantly improved the photolysis results because it is a strong oxidizing agent. It improves the photodegradation of dyes by increasing the number of hydroxyl radicals produced which occurs when the O-O bond is cleaved and two $OH^{\bullet}$ radicals are formed and they oxidize the organic dye compounds (Reza, Kurny, and Gulshan, 2017). However, one of the limitations associated with this method is that it requires low UV wavelengths of 200 nm < λ < 400 nm to dissociate H_2O_2 (Georgiou *et al.*, 2002; Reza, Kurny and Gulshan, 2017). The degradation of methyl blue in **Figure 5.2 (b)** shows a constant increase in degradation under UV/H_2O_2 conditions. The increase may correspond to the continuous generation of radicals as the peroxide-generated radicals continue to be produced from its atom cleavage with more reaction time. Furthermore, methyl red degradation efficiency results shown in **Figure 5.2 (b)** indicated that the degradation efficiency is higher even under dark conditions in comparison to bisphenol results shown in **Figure 5.2 (d)**. This symbolizes that it is easier to degrade methyl red dye than it is to degrade rhodamine B and related organic pollutants. However, once the UV light is set on for the degradation, there is higher removal efficiency or degradation efficiency for bisphenol in comparison to the reaction taking place between light and methyl red in **Figure 5.2 (b)**.

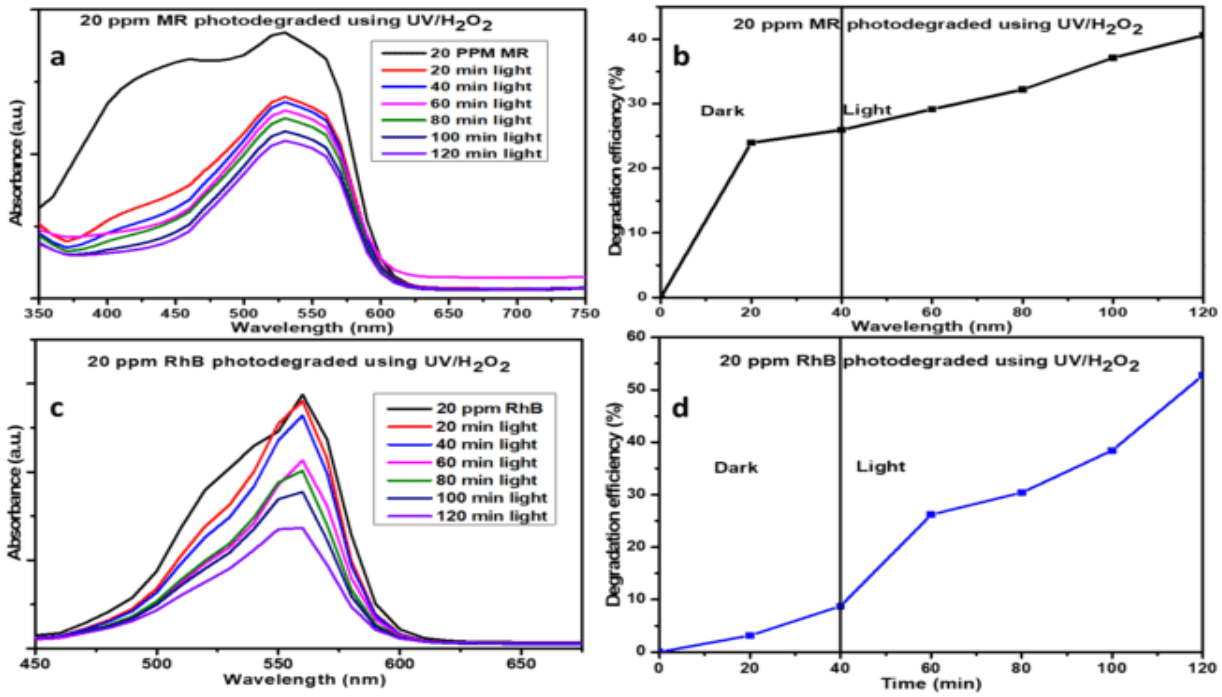

Figure 5.2. Photolysis with H_2O_2 study **a)** 20 ppm MR UV-vis absorbance spectrum **b)** 20 ppm MR DE% plot **c)** 20 ppm RhB UV-vis absorbance spectrum **d)** 20 ppm RhB DE% plot as a function of time for UV/H_2O_2 reactions

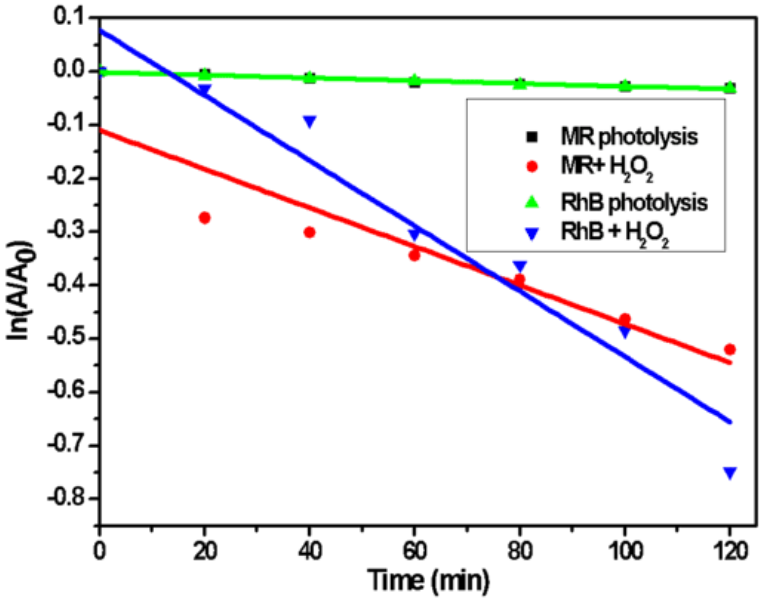

Figure 5.3: Linear pseudo-first-order model fit for MR and RhB degraded via UV and UV/H_2O_2 methods

5.1.2. Tungsten disulphide (WS_2) degradation performance:

For this project, WS_2 was utilized as a co-catalyst. MR and RhB were degraded using WS_2 with a catalyst loading of 2.4 mg/ml and UV light at 180 W. This experiment aimed to evaluate the performance of WS_2 independently. A 50 ml dye solution with a dye concentration of 20 ppm was prepared. WS_2 was added to the dye solution under constant magnetic stirring, followed by incubation in the dark for 40 minutes to reach equilibrium. Subsequently, the solution was irradiated with UV light for 2 hours, and small aliquots were taken every 20 minutes for analysis. The changes in MR and RhB UV absorbance over time are presented in **Figures 5.4 (a)** and **(c)**, while the WS_2 degradation efficiency is depicted in **Figures 5.4 (b)** and **(d)**. At the end of the photocatalytic reaction, the degradation efficiency was determined to be 62.96% for MR and 62.22% for RhB. These results are better compared to the UV and UV/H_2O_2 methods. This may be attributed to the narrow WS_2 bandgap that ensures light absorption in the visible light spectrum. The TEM and SEM images of WS_2 revealed multi-layered nanoparticles with a flower-petal-like morphology and an average particle size of 132.1 nm. The degradation in the dark was due to adsorption of the SODs to the photocatalyst (Moosavi *et al.*, 2020).

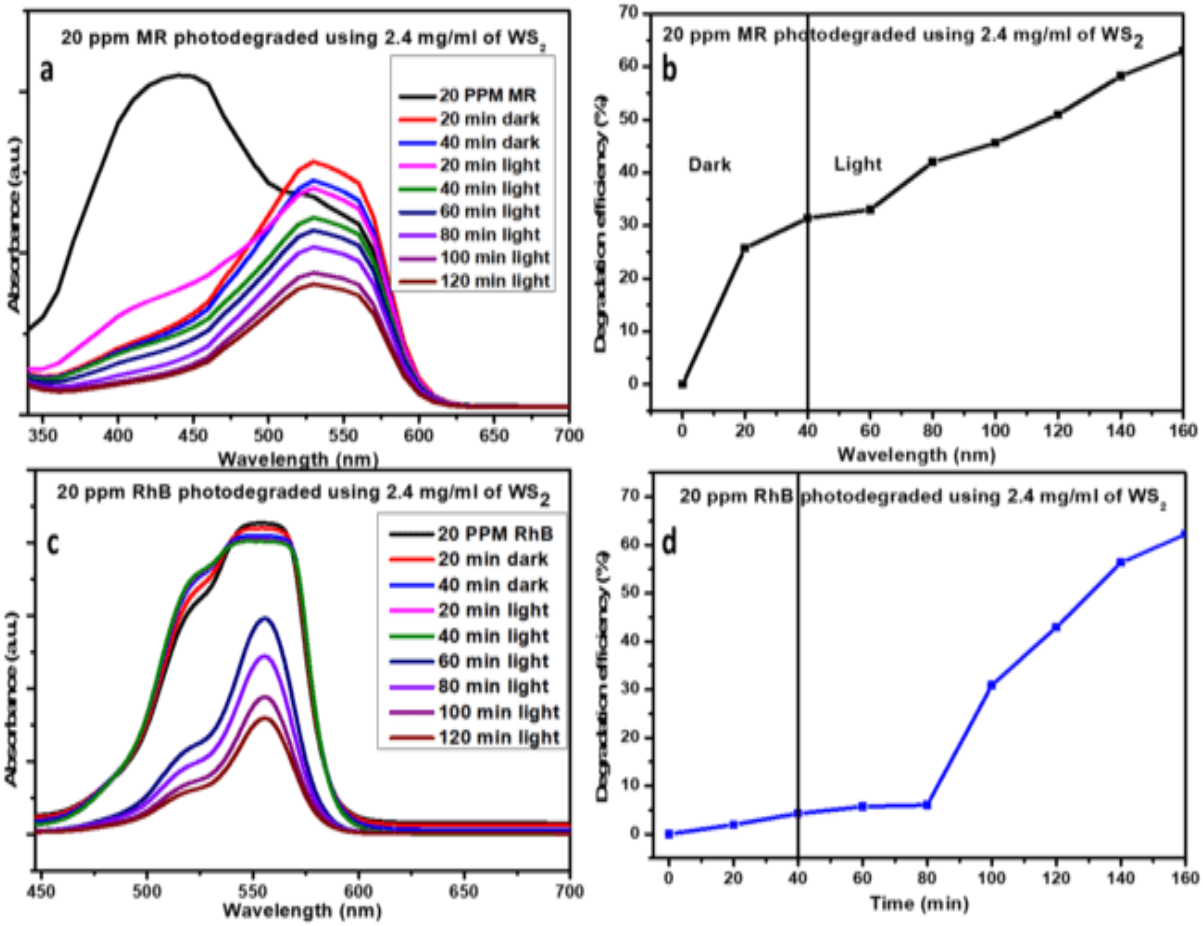

Figure 5.4. a) 20 ppm MR UV-vis absorbance spectrum **b)** 20 ppm MR DE% graph **c)** 20 ppm RhB UV-vis absorbance spectrum **d)** RhB DE% graph using 2.4 mg/ml of WS2 as a function of time

5.1.3. Cesium Bismuth Bromide ($Cs_3Bi_3Br_9$) degradation performance

In recent years, metal halide perovskites (MHPs) have been utilized for the photodegradation of dyes due to a tuneable bandgap and good charge separation. $Cs_3Bi_2Br_9$ is a lead-free MHP that has shown promising efficacy in photocatalytic dye degradation due to its excellent optical properties (Bai *et al.*, 2023). The MR and RhB dyes were degraded at pH 5.5 and 4.3, respectively, using a concentration of 2.4 mg/ml of $Cs_3Bi_2Br_9$. The initial dye concentrations were 20 ppm, and the volume of the dye solutions was 50 ml. The heterogeneous mixtures were kept in the dark for 40 minutes and then subjected to light irradiation for 120 minutes, with continuous magnetic stirring during the photocatalytic reactions. Samples were collected at 20-minute intervals for analysis. **Figures 5.5 (b)** and **(d)** demonstrated degradation efficacies of 54.32% for MR and 70.28% for RhB. These results correspond to the UV-

vis results in **Figures 5.5 (a)** and **(c)** which indicate that $Cs_3Bi_2Br_9$ degraded MR from 20 ppm to 9.136 ppm as the absorbance peak reduced by 54.32% and $Cs_3Bi_2Br_9$ degraded RhB from 20 ppm to 5.944 ppm as the absorbance peak was reduced by 70.28% at the end of the degradation time. The RhB absorbance peaks in **Figure 5.5 (c)** gradually shifted to a lower wavelength with increased UV radiation exposure, this is referred to as a hypsochromic shift from around 560 nm to 500 nm. A hypsochromic shift is due to reduced conjugation. According to literature, it is due to the stepwise N-deethylation process which produces several forms of deethylated intermediates as byproducts. These N-deethylated intermediates are as follows: N, N-diethyl-N′-ethylrhodamine (3N-Rh), N-ethyl-N′-ethylrhodamine (2N-Rh), N-ethyl rhodamine (N-Rh) and Rhodamine 110 (Rh), which have absorption peaks at around 539, 522, 510 and 498 nm, respectively (Milošević *et al.*, 2023). Referring to the zeta potential results in **Chapter 4**, we can expect electrostatic repulsion between $Cs_3Bi_2Br_9$ and MR at pH 5.5, as both the MHP surface and MR are positively charged. This explains the lower efficacy observed for MR at pH 5.5. Conversely, at pH 4.3, RhB carries a slightly negative charge while $Cs_3Bi_2Br_9$ has a high positive charge. As a result, electrostatic attraction occurs between $Cs_3Bi_2Br_9$ and RhB, leading to enhanced photodegradation efficacy.

The UV-vis spectrum and Tauc plot in **Chapter 4** for $Cs_3Bi_2Br_9$ indicated a bandgap of 2.48 eV, making it a suitable photocatalyst for light absorption in the visible and UV regions of the electromagnetic spectrum. Thus, the material can use low-cost sunlight or solar-driven light irradiation sources. This presents $Cs_3Bi_2Br_9$ as a suitable organic-polluted wastewater remediation photocatalyst of choice for developing and underdeveloped countries characterized by a limited supply of clean and safe drinkable water and low economic activities. The TEM and SEM images demonstrated that the $Cs_3Bi_2Br_9$ nanoparticles exhibit polydispersity with a mean particle size of 87.7 nm and mixed morphology. This particle size is smaller than that of WS_2, thereby increasing the surface area and facilitating greater dye-catalyst interactions. Furthermore, nanotechnology has recently emerged as a suitable water technology for dyes such as Rhodamine B and Methyl blue. This is due to the superior optoelectrical, surface morphology, porosity, and stability of photocatalysts (Kumari *et al.*, 2023).

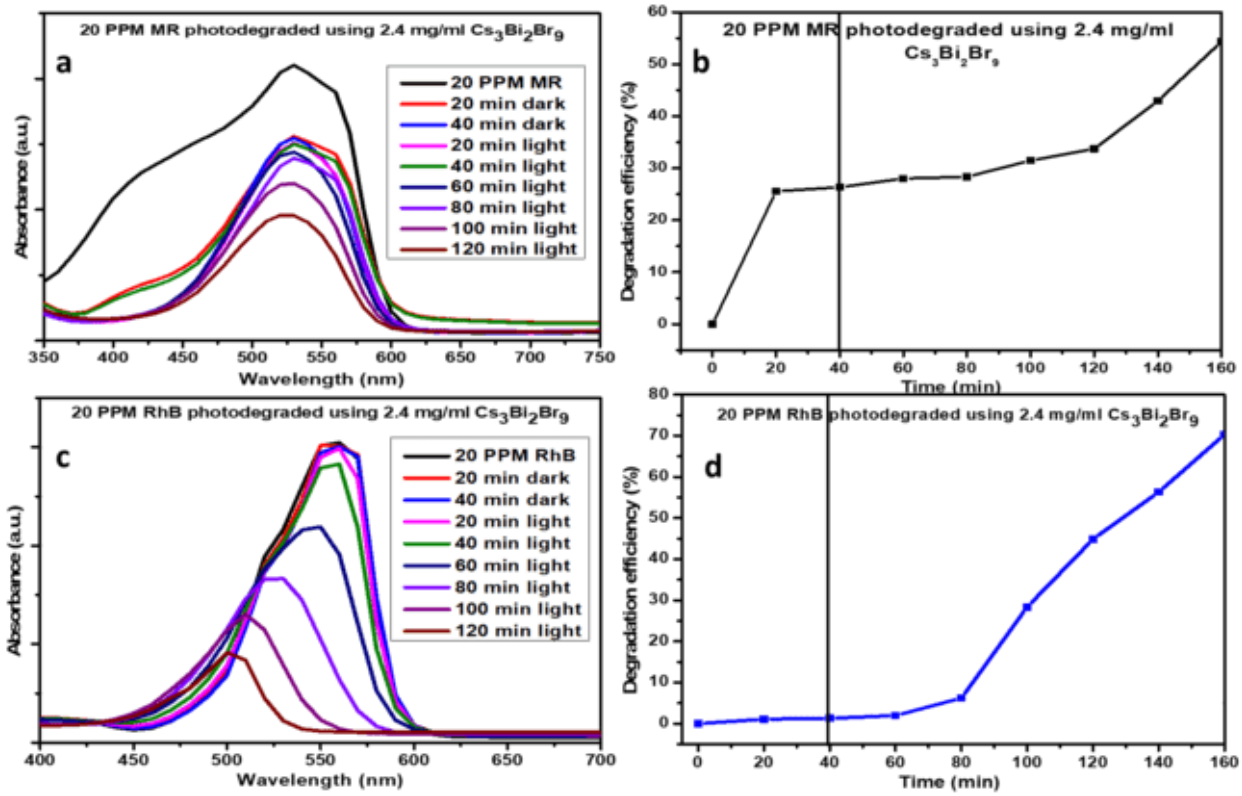

Figure **5.5. a)** MR UV-vis absorbance spectrum **b)** MR degradation efficiency graph **c)** RhB UV-vis absorbance spectrum **d)** RhB degradation efficiency graph using 2.4 mg/ml of Cs3Bi2Br9 as a function of time.

5.1.4. $Cs_3Bi_2Br_9/WS_2$ degradation performance

To enhance the degradation efficiency of $Cs_3Bi_2Br_9$, WS_2 was added as a co-catalyst at a molar percentage of 20%. The formation of the $Cs_3Bi_2Br_9/WS_2$ heterostructure was achieved through the ultrasonication method. The MR and RhB degradation reactions by $Cs_3Bi_2Br_9/WS_2$ were conducted under the same conditions as the WS_2 and $Cs_3Bi_2Br_9$ reactions. **Figure 5.6** illustrates that the composite exhibited a degradation efficacy of 89.36% for MR and 96.51% for RhB. This represents a significant improvement compared to the results obtained when using WS_2 and $Cs_3Bi_2Br_9$ individually. MR displayed a strongly positive charge within the pH range of 4-6.8, while $Cs_3Bi_2Br_9/WS_2$ had a negative surface charge within the same range. This indicates that the high degradation efficiency was attributed to the electrostatic attraction between the composite and MR, as they possessed opposite charges at pH 5.5. At pH 4.3, the composite's surface charge was negative, and RhB carried a positive charge. Consequently, this favoured the photocatalytic degradation of RhB.

The BET surface area and pore sizes of $Cs_3Bi_2Br_9$ were 5.43 m^2/g and 23.2 nm, respectively, while for the composite, they were 6.46 m^2/g and 25.9 nm. Additionally, the bandgap of $Cs_3Bi_2Br_9/WS_2$ was determined to be 2.86 eV. Therefore, $Cs_3Bi_2Br_9/WS_2$ outperformed WS_2 and $Cs_3Bi_2Br_9$ due to its higher surface area, pore size, and favourable zeta potential, all of which contributed to the effective photocatalytic degradation of MR and RhB.

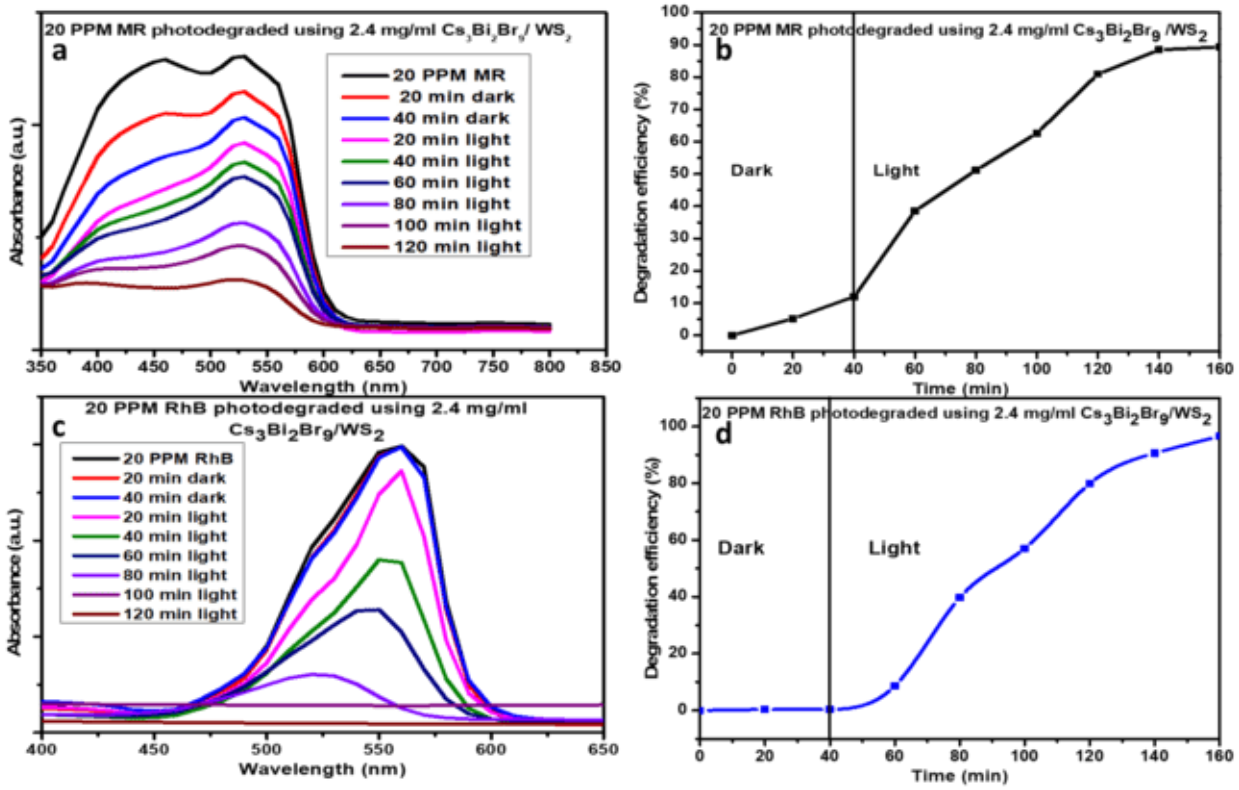

Figure 5.6 a) UV-vis absorbance spectrum for the degradation of 20 ppm MR; **b)** MR DE% plot; **c)** UV-vis absorbance spectrum for the degradation of 20 ppm RhB and **d)** RhB DE% plot using $Cs_3Bi_2Br_9/WS_2$

5.2. Optimization studies

The optimization studies were done to determine the optimum conditions for MR and RhB photodegradation reactions by $Cs_3Bi_2Br_9$ and $Cs_3Bi_2Br_9/WS_2$. The studies were done by varying one condition at a time. The optimized conditions are catalyst loading, dye concentration, and solution pH. The effect of adding hydrogen peroxide (H_2O_2) to the optimum reactions was determined.

5.2.1. Catalyst loading

For the catalyst loading studies, the concentrations of the catalysts used to degrade the dyes diluted in UPW were 0.8 mg/mL, 1.6 mg/mL, and 2.4 mg/mL. The dye concentration was 20 ppm. The pH for MR and RhB were kept at 5.5 and 4.3, respectively. **Figure 5.7 (a)-(d)** below shows the change in degradation efficiency with a change in the photocatalyst loading. In **Figure 5.7 (a)**, $Cs_3Bi_2Br_9$ had similar MR degradation efficiency percentages (DE%) in the dark at 2.4 mg/mL and 1.6 mg/mL. In the light, 1.6 mg/mL had the highest degradation efficiency of 74.04%, followed by 0.8 mg/mL and 2.4 mg/mL at 59.06% and 54.32%, respectively. A similar trend can be seen in **Figure 5.7 (b)**. The RhB degradation efficiencies were similar at the end of the reactions, with DE%s of 79.47%, 88.26%, and 70.28% for 0.8 mg/mL, 1.6 mg/mL, and 2.4 mg/mL, respectively. At 0.8 mg/mL, there are few available active sites to degrade the dye, while at 2.4 mg/mL, the higher number of nanoparticles reduces the amount of light that can penetrate the heterogeneous solution, thus reducing the efficacy of the photocatalytic reactions. The optimum $Cs_3Bi_2Br_9$ catalyst loading for degrading both MR and RhB was therefore 1.6 mg/mL.

In **Figure 5.7 (c)-(d)**, the dye DE% results were different for the $Cs_3Bi_2Br_9/WS_2$ composite. In **Figure 5.7 (c)**, the 1.6 mg/mL catalyst loading had the highest efficiency in the dark, followed by 2.4 mg/mL, while the DE% was less than 5% at 0.8 mg/mL. In the light, the optimum MR DE% was 89.36% at 2.4 mg/mL catalyst loading, 51.89% at 1.6 mg/mL, and 38.04% at 0.8 mg/mL In **Figure 5.7 (d)**, the 1.6 mg/mL $Cs_3Bi_2Br_9/WS_2$ catalyst loading had the highest DE% in the dark, while the DE%s for 0.8 mg/mL and 2.4 mg/mL were close to 0%. At the end of the 2-hour irradiation time, the 1.6 mg/mL and 2.4 mg/mL catalyst loadings achieved 93.29% and 96.51% RhB DE, respectively. Since the RhB DE%s were so close, the 1.6 mg/mL catalyst loading was chosen as the optimum catalyst loading due to its cost-effectiveness. The dyes exhibited slight degradation in the dark because the catalysts have bandgaps that are less than 3 eV, which means they not only generate ROS under light but also exhibit activity in the absence of light (V. and Rajagopalan, 2016).

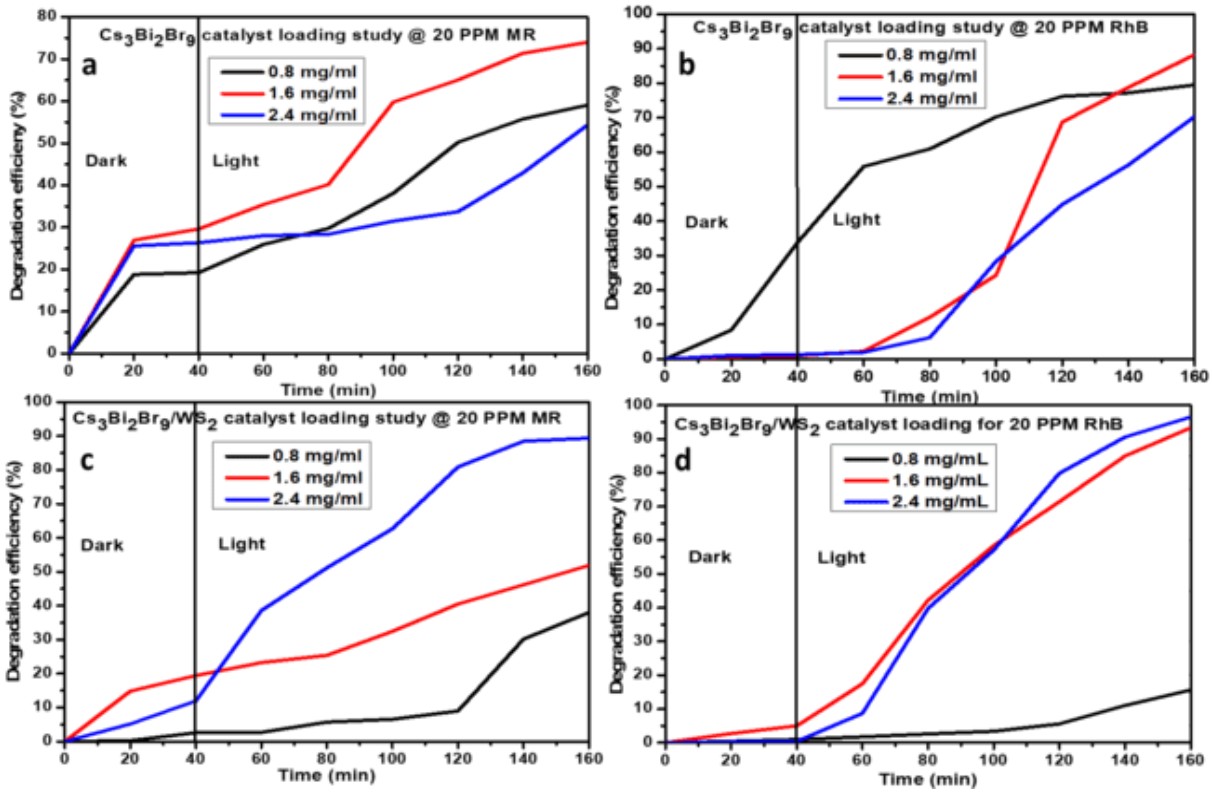

Figure 5.7. Catalyst loading study **a)** 20 ppm MR DE% using $Cs_3Bi_2Br_9$ **b)** 20 ppm RhB DE% using $Cs_3Bi_2Br_9$ **c)** 20 ppm MR DE% using $Cs_3Bi_2Br_9/WS_2$ **d)** 20 ppm RhB DE% using $Cs_3Bi_2Br_9/WS_2$ at 0.8, 1.6 and 2.4 mg/ml catalyst loading

In **Table 5.2** the MR and RhB degradation efficiencies for $Cs_3Bi_2Br_9$ and $Cs_3Bi_2Br_9/WS_2$ are given for 0.8, 1.6, and 2.4 mg/ml catalyst loading. The optimum $Cs_3Bi_2Br_9$ catalyst loading was 1.6 mg/ml for both MR and RhB with degradation efficiencies of 74.04% and 88.26% respectively. The optimum catalyst loading for $Cs_3Bi_2Br_9/WS_2$ was 2.4 mg/ml for MR and RhB with degradation efficiencies of 89.36% and 96.51% respectively.

Table 5.2. $Cs_3Bi_2Br_9$ and $Cs_3Bi_2Br_9/WS_2$ catalyst loading study DE% for MR and RhB at 20 ppm dye concentration after 2hrs of irradiation time.

Catalyst	Catalyst loading (mg/ml)	Degradation efficiency for MR (%)	Degradation efficiency for RhB (%)
$Cs_3Bi_2Br_9$	0.8	59.06	79.47
	1.6	74.04	88.26
	2.4	54.32	70.28
$Cs_3Bi_2Br_9/WS_2$	0.8	38.04	15.61
	1.6	51.89	93.29
	2.4	89.36	96.51

5.2.2. Dye concentration study for $Cs_3Bi_2Br_9$ and $Cs_3Bi_2Br_9/WS_2$

The dye concentration study was conducted using the optimum catalyst loading of the photocatalysts while keeping the pH of the dye solution constant. Since the dye concentration in textile dye effluents typically ranges between 10-200 ppm, this project examined dye concentrations of 20, 40, and 60 ppm. **Figure 5.8** illustrates the impact of the initial concentration of MR and RhB dyes on the degradation efficiency (DE%), while **Tables 5.3** and **5.4** provide a summary of the results. In **Figure 5.8 (a)**, MR was degraded using 1.6 mg/mL of $Cs_3Bi_2Br_9$. The DE% at 40 ppm and 60 ppm was 45.36% and 47.89%, respectively. The optimum dye concentration was found to be 20 ppm, resulting in a DE percentage of 74.04%. **Figure 5.8 (c)** depicts the use of $Cs_3Bi_2Br_9/WS_2$ composite at a catalyst loading of 2.4 mg/ml. For MR, the optimum concentration was again 20 ppm, achieving a DE% of 89.36%. At 40 ppm and 60 ppm, the DE percentages were 76.01% and 61.40%, respectively. The degradation trend for RhB differed between $Cs_3Bi_2Br_9$ and $Cs_3Bi_2Br_9/WS_2$, as observed in **Figure 5.8 (b)** and (**d)**. The initial RhB concentration had a significant effect on the degradation efficiency. At 40 ppm, the DE started to increase at 80 minutes of light exposure for $Cs_3Bi_2Br_9$ and 60 minutes for $Cs_3Bi_2Br_9/WS_2$. The DE percentages were negligible at 60 ppm RhB. For both photocatalysts, the optimum concentration was 20 ppm RhB, resulting in DE percentages of 88.26% and 96.51% for $Cs_3Bi_2Br_9$ and $Cs_3Bi_2Br_9/WS_2$, respectively.

The overall results indicate that the DE% decreases as the initial concentration of the dyes increases. This can be attributed to several factors, including:

1. An increase in the dye colour intensity, which reduces light absorption.
2. A decrease in the photons absorbed by the catalyst, leads to a reduction in ROS (reactive oxygen species) generation.
3. A decrease in the number of available active sites on the catalyst surface with an increase in dye concentration.

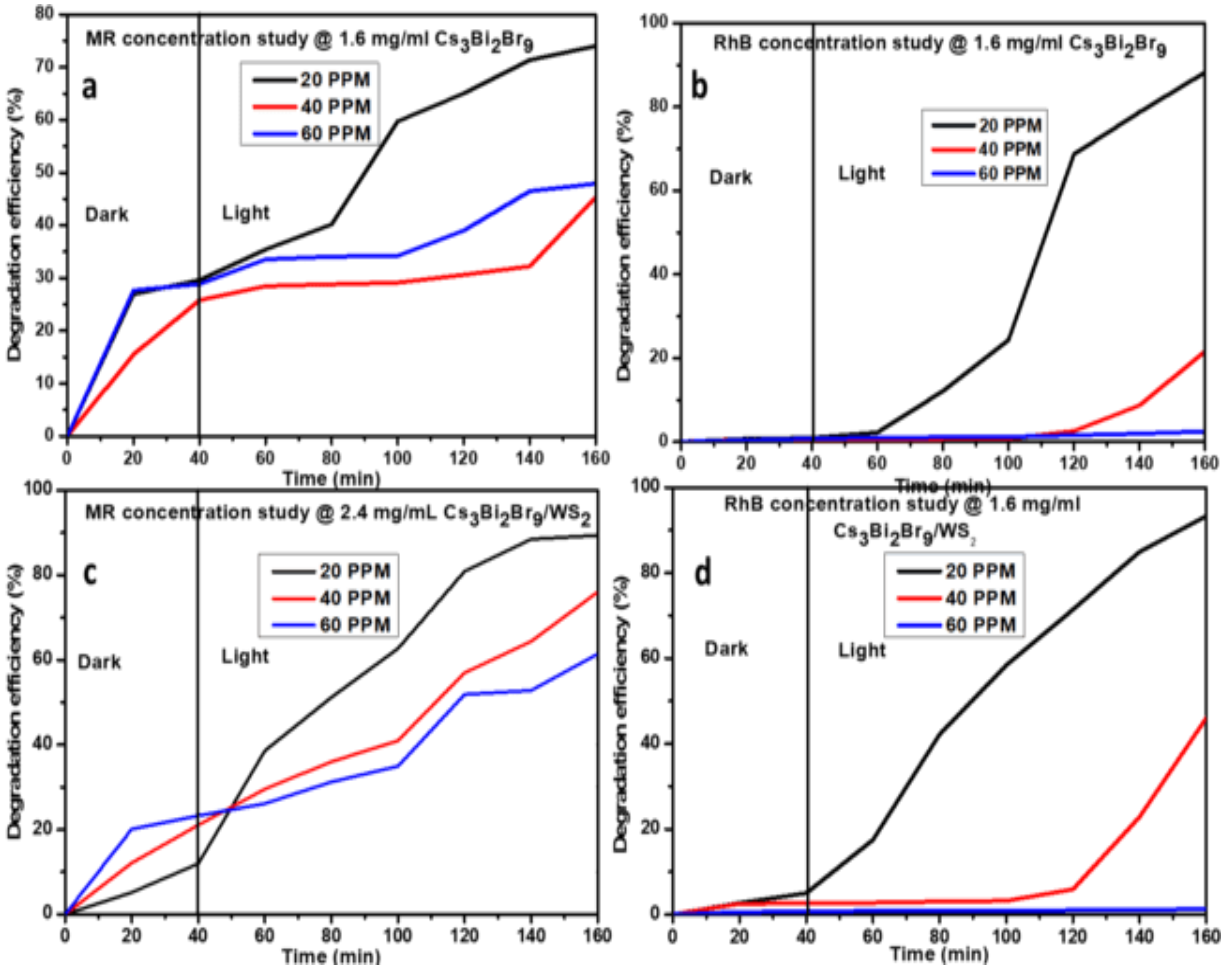

Figure 5.8. Initial concentration study **a)** MR DE% using $Cs_3Bi_2Br_9$ **b)** RhB DE% using $Cs_3Bi_2Br_9$ **c)** MR DE% using $Cs_3Bi_2Br_9/WS_2$ **d)** RhB DE% using $Cs_3Bi_2Br_9/WS_2$ at 20, 40 and 60 ppm initial dye concentrations

Table 5.3. DE% for MR and RhB at 20, 40, and 60 ppm initial dye concentration after 2 hrs of irradiation time using $Cs_3Bi_2Br_9$

Catalyst	Catalyst loading (mg/ml)	Dye concentration (ppm)	Degradation efficiency for MR at pH 5.5 (%)	Degradation efficiency for RhB at pH 4.3 (%)
$Cs_3Bi_2Br_9$	1.6	20	74.04	88.26
		40	45.36	21.55
		60	47.89	2.474

Table 5.4. DE% for MR and RhB at 20, 40, and 60 ppm initial dye concentration after 2 hrs of irradiation time using $Cs_3Bi_2Br_9/WS_2$

Catalyst	Dye concentration (ppm)	Catalyst loading (mg/ml)	Degradation efficiency for MR (%)	Catalyst loading (mg/ml)	Degradation efficiency for RhB (%)
$Cs_3Bi_2Br_9/WS_2$	20	2.4	89.36	1.6	93.29
	40		76.01		46.00
	60		61.40		1.315

5.2.3. Dye solution pH studies:

Studying the effect of the initial pH of the dye solution is important because it affects the electrostatic interaction of the dye solution and the photocatalyst, as well as the separation of photogenerated e^- - h^+ pairs on the catalyst surface. It also affects the number of hydroxyl ions and protons in the solution. An aqueous solution has more hydroxyl ions in basic pH conditions and more protons in acidic conditions (Reza, Kurny and Gulshan, 2017). **Figure 5.9** below shows how pH affects the degradation of dyes and **Figure 5.10** shows how the zeta-potential of the dye solutions and catalysts change as a function of pH. The study was done at optimum dye solution concentration and catalyst loading. The degradation of the dyes was studied at pH 2, 7, and 12 to determine how the dyes degrade in acidic, neutral, and basic conditions. **Figure 5.9 (a)** 20 ppm MR was degraded using 1.6 mg/ml of $Cs_3Bi_2Br_9$. The MR DE% was the lowest at pH 2. This is due to the zeta potential of the MR dye solution and the catalyst surface charge which are 0.29 mV and -0.058 mV, respectively. Therefore, this results in poor photodegradation of the dye as they both have a charge close to 0 mV. This could be due to a high concentration of protons present at a low pH. Protons act as hydroxyl scavengers as shown in the eqn. below (Devi, Raju and Kumar, 2009):

$$H^+ + OH^\bullet + e^- \rightarrow H_2O \quad \textbf{(5.4)}$$

At pH 12 the MR solution charge was -32.8 mV, the $Cs_3Bi_2Br_9$ zeta potential was -24.2 mV, and the MR DE% was 56.73%. Although both the dye solution and the catalyst are anionic at pH 12, there is a charge difference of 10.6 mV and this results in an improved DE compared to pH 2. Similar is true at pH 7, the MR DE is 63.57% and the zeta potential for the dye solution and the catalyst are -6.58 mV and -2.12 mV respectively. The optimum pH is at pH 5.5 with a DE of 74.04%. Based on the zeta

potential trends, the MR solution zeta potential is expected to be approximately 27 mV and the zeta potential for $Cs_3Bi_2Br_9$ is 29 mV. Since the zeta potential difference is small at pH 5.5, there could be other factors that affect the photocatalytic degradation of MR such as the colour which changes with a change in pH. At pH 2 the dye is dark red, at pH 5.5 it is reddish orange, at pH 7 it is orange and at pH 12 it is yellow. This colour change may have affected the absorbance of light and hence it the degradation of MR as well.

In **Figure 5.9 (b)** the lowest RhB DE%, 17.94%, was at pH 12. The RhB solution zeta potential was -38.4 mV at pH 12 and the difference in potential between RhB and the catalyst surface was 14.2 mV. At pH 2 the dye potential was 46.3 mV, the dye was stable and well-dispersed DE to high zeta potential. At pH 4.3 the potential was -1.12 mV and the catalyst charge was 23 mV. The optimum DE%, 97.6%, was at pH 7. The $Cs_3Bi_2Br_9$ potential was -2.12 mV and the dye solution charge was -30.8 mV. At pH 7 there is a high difference in zeta potential, and there is a balance between hydroxyl ions and free hydrogen ions resulting in high DE%. With the $Cs_3Bi_2Br_9/WS_2$ composite, there was an inverse relationship between DE% and pH for both MR and RhB shown in **Figure 5.9 (c-d)**. This shows that the dye DE% had a strong dependence on pH. The optimum pH was 2 for both MR and RhB.

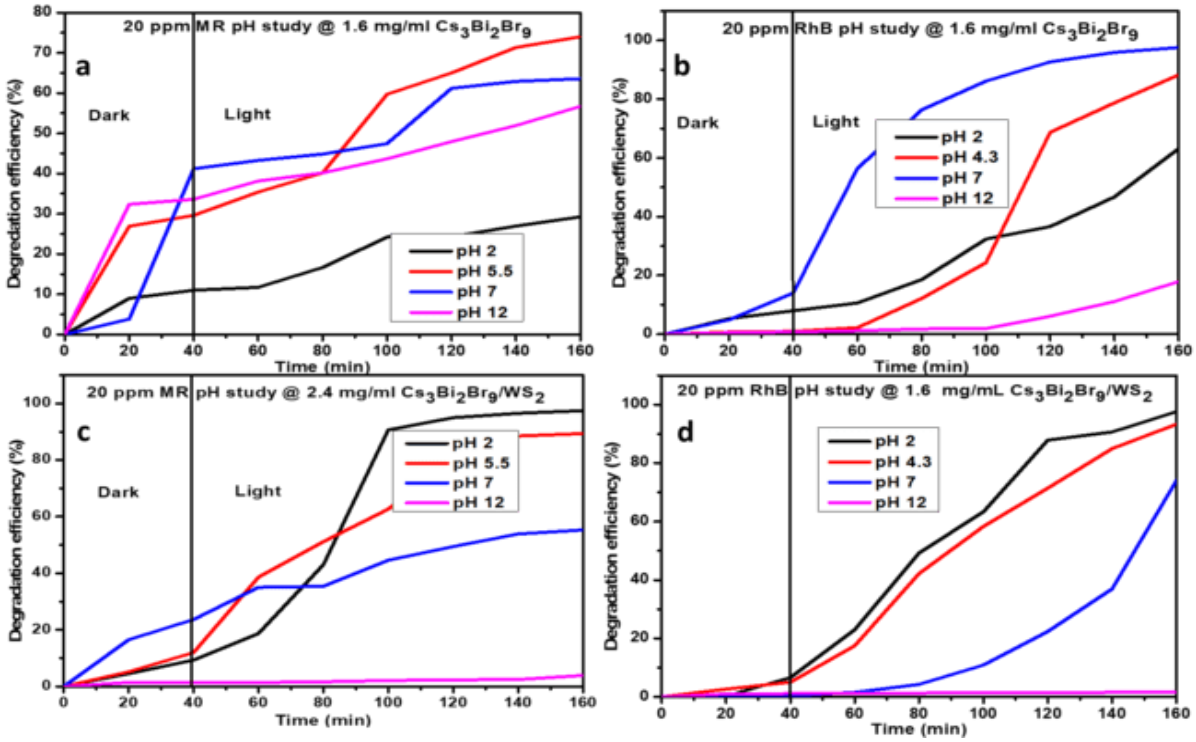

Figure 5.9. Initial dye solution pH study **a)** 20 ppm MR DE% using 1.6 mg/ml $Cs_3Bi_2Br_9$ at pH 2, 5.5, 7, and 12 **b)** 20 ppm RhB DE% using 1.6 mg/ml of $Cs_3Bi_2Br_9$ at pH 2, 7, 4.3, and 12 **c)** 20 ppm MR DE% using 2.4 mg/mL $Cs_3Bi_2Br_9/WS_2$ pH 2, 5.5, 7 and 12 **d)** RhB DE% using 1.6 mg/mL $Cs_3Bi_2Br_9/WS_2$ at pH 2, 7, 4.3, and 12

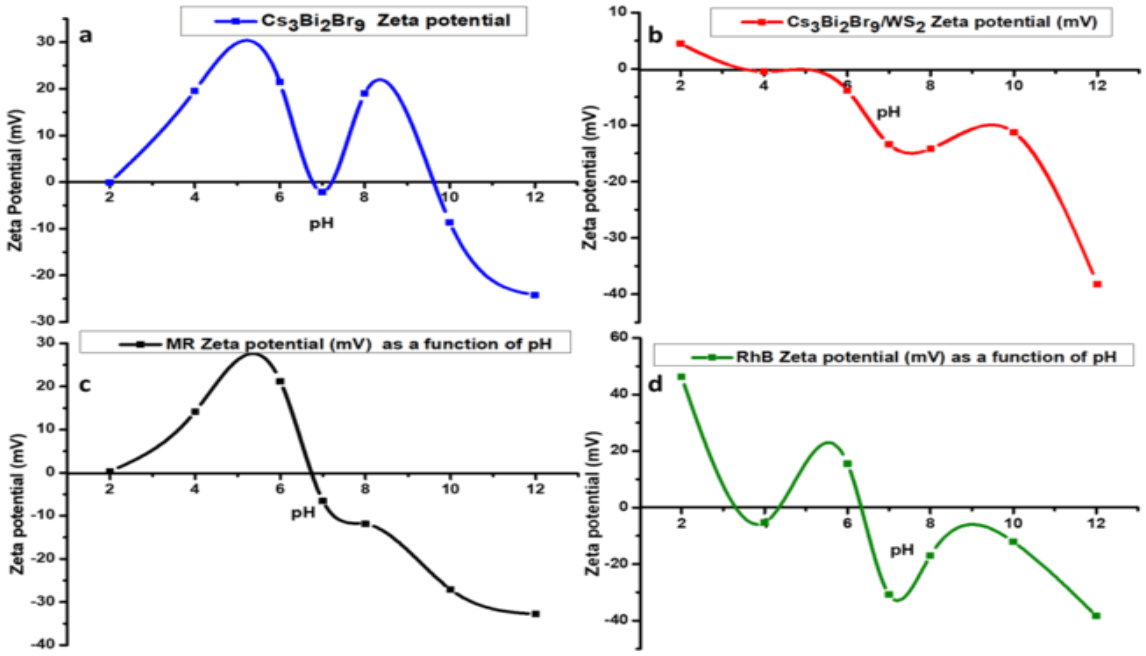

Figure 5.10 a) $Cs_3Bi_2Br_9$ zeta potential **b)** $Cs_3Bi_2Br_9/WS_2$ zetapotential **c)** MR zeta potential **d)** RhB zetapotential as a function of pH.

Table 5.5 Summary of the pH study results for 20 ppm MR and 20 ppm RhB using $Cs_3Bi_2Br_9$ and $Cs_3Bi_2Br_9/WS_2$

pH	Catalyst zeta potential (mV)	MR zeta potential (mV)	Difference between catalyst and MR zeta potential (mV)	Degradation efficiency for 20 ppm MR (%)	RhB zeta potential (mV)	Difference between catalyst and RhB zeta potential (mV)	Degradation efficiency for 20 ppm RhB (%)
				$Cs_3Bi_2Br_9$			
2	-0.0577	0.29	0.29577	29.24	46.3	46.36	63.16
4.3	23	-	-	-	-1.37	24.37	88.26
5.5	29.4	27	2.4	74.04	-	-	-
7	-2.12	-6.58	4.46	63.57	-30.8	28.68	97.60
12	-24.2	-32.8	8.6	56.73	-38.4	14.2	17.94
				$Cs_3Bi_2Br_9/WS_2$			
2	4.46	0.29	4.17	97.48	46.3	41.84	97.64
4.3	-0.38	-	-	-	-1.37	0.99	93.29
5.5	-0.91	27	27.91	89.36	-	-	-
7	-13.4	-6.58	6.82	55.28	-30.8	17.4	83.02
12	-38.2	-32.8	5.4	3.876	-38.4	0.2	1.532

5.2.4. Effect of H_2O_2

Hydrogen peroxide is an electron acceptor that is commonly used to enhance the photocatalytic degradation of organic pollutants. It improves photocatalytic degradation of dyes by generating hydroxyl radicals and it inhibits electron-hole recombination. The degradation of dyes is accelerated using H_2O_2 via the reaction mechanism below.

$$H_2O_2 + O_2^- \rightarrow OH^\bullet + OH^- + O_2^\bullet \quad \textbf{(5.5)}$$

$$H_2O_2 + hv \rightarrow 2OH^\bullet \quad \textbf{(5.6)}$$

$$H_2O_2 + e^- \rightarrow OH^- + OH^\bullet \quad \textbf{(5.7)}$$

$$H_2O_2 + 2e^- \rightarrow 2OH^- \quad \textbf{(5.8)}$$

$$H_2O_2 + 2h^+ \rightarrow 2H^+ + O_2 \quad \textbf{(5.9)}$$

$$OH^\bullet + H^+ + e^- \rightarrow H_2O \quad \textbf{(5.10)}$$

$$H_2O_2 + OH^\bullet \rightarrow OH_2^\bullet + H_2O \quad \textbf{(5.11)}$$

$$OH_2^\bullet + OH^\bullet \rightarrow H_2O + O_2 \quad \textbf{(5.12)}$$

5.2.4.1. Effect H_2O_2 on heterogeneous photocatalytic reactions:

The effect of H_2O_2 was examined by introducing H_2O_2 at a concentration of 0.3519 M to the heterogeneous catalytic reactions at optimal pH, dye concentration, and catalyst loading. The UV-vis absorbance spectra of the dye solutions and the corresponding DE% results are depicted in **Figure 5.11**, while a summary of the findings can be found in **Table 5.6**. Notably, the dyes exhibited rapid degradation in the absence of light, with the solutions clearing within 40 minutes in the light. This was significantly faster compared to the heterogeneous photocatalytic reactions, which required approximately 120 minutes of light exposure to achieve clarity in the absence of H_2O_2. **Table 5.6** presents the DE% values, revealing that the $Cs_3Bi_2Br_9/WS_2$ + H_2O_2 reactions yielded approximately 2% higher DE% compared to the $Cs_3Bi_2Br_9$ + H_2O_2 reactions for both MR and RhB.

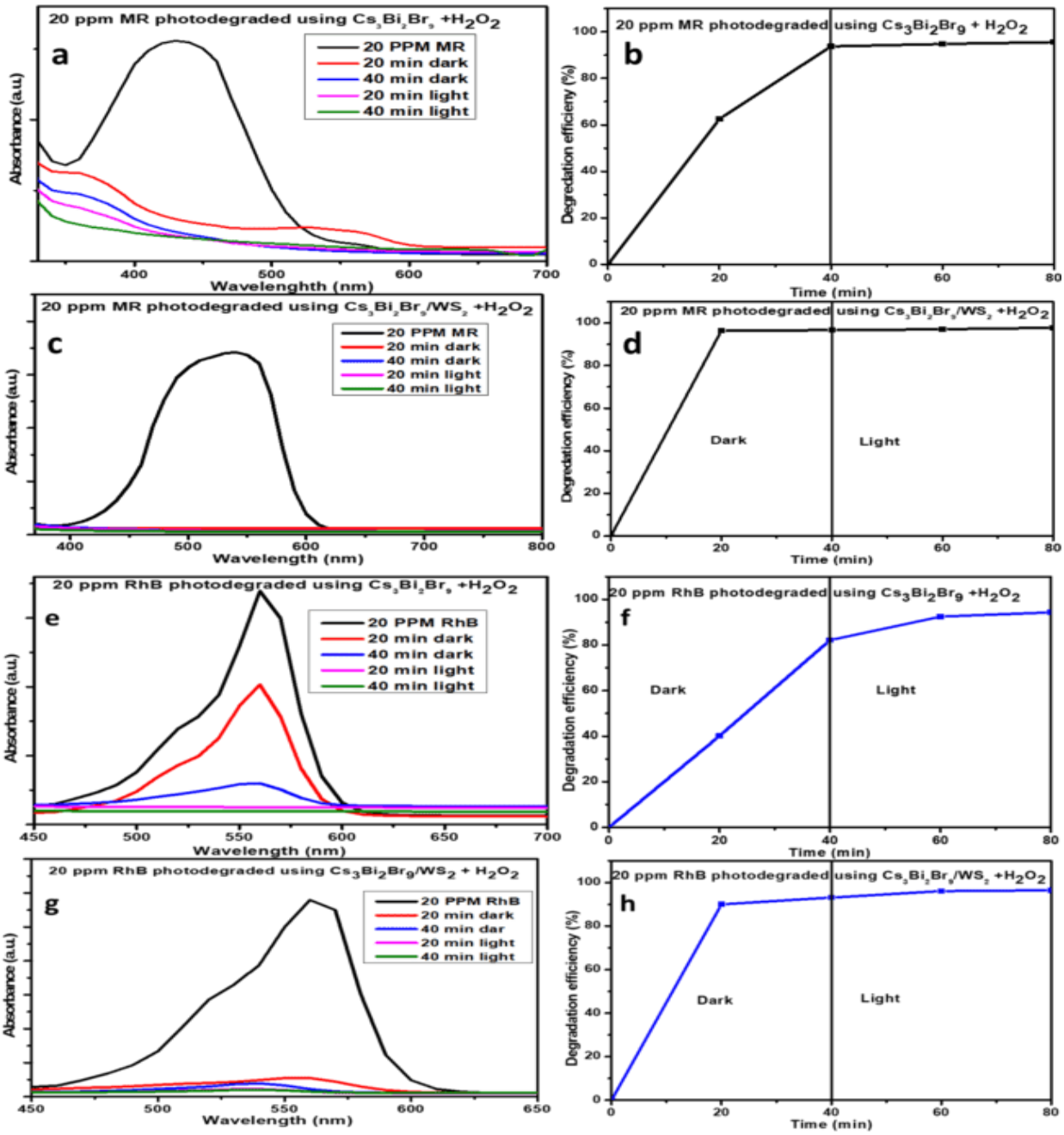

Figure 5.11 H_2O_2 effect study **a)** 20 ppm MR degraded using 1.6 mg/ml $Cs_3Bi_2Br_9$ +H_2O_2 at pH 5.5 **b)** 20 ppm MR DE% graph for reaction (a) **c)** 20 ppm MR degraded using 2.4 mg/ml $Cs_3Bi_2Br_9/WS_2$ +H_2O_2 at pH 2 **d)** 20 ppm MR DE% for reaction (c) **e)** 20 ppm RhB degraded using 1.6 mg/ml $Cs_3Bi_2Br_9$ +H_2O_2 at pH 7 **f)** 20 ppm RhB DE% for reaction (e) **g)** 20 ppm RhB degraded using 1.6 mg/ml $Cs_3Bi_2Br_9/WS_2$ +H_2O_2 at pH 2 **h)** 20 ppm RhB DE% for reaction

Table 5.6: Summary of results for H_2O_2 effect study for the optimum heterogeneous MR and RhB photodegradation reactions

Catalyst	Catalyst loading (mg/ml)	Dye	pH	H_2O_2 concentration (M)	Dye concentration (ppm)	DE (%)
$Cs_3Bi_2Br_9$ + H_2O_2	1.6	MR	5.5	0.3519	20	95.62
$Cs_3Bi_2Br_9/WS_2$ + H_2O_2	2.4	MR	2			97.83
$Cs_3Bi_2Br_9$ + H_2O_2	1.6	RhB	7			94.36
$Cs_3Bi_2Br_9/WS_2$ + H_2O_2	1.6	RhB	2			96.47

The effect of incorporating H_2O_2 can be further elucidated by considering turnover number (TON) and turnover frequency (TOF). TON represents the maximum number of catalytic cycles achieved by each active site on the catalyst. TOF, on the other hand, indicates the number of dye molecules that can be mineralized by a single catalyst molecule per unit of time (s). The equations are given below (Vattikuti *et al.*, 2019; Q. Zhang *et al.*, 2020).

Turnover number (TON) = $\left(\frac{moles\ of\ degraded\ dye\ during\ irradiation\ time}{moles\ of\ photocatalyst}\right) \times 100$ **(5.13)**

Turnover frequency (TOF) = $\frac{TON}{Time}$ **(5.14)**

Figure 5.12 presented below illustrates the turnover frequency (TOF) and turnover number (TON) for the optimized photodegradation reactions with and without the presence of H_2O_2. In the figure, "MHP" refers to $Cs_3Bi_2Br_9$, and "MHP/WS_2" refers to $Cs_3Bi_2Br_9/WS_2$. In **Figure 5.12 (a)**, the TON values for MHP and MHP/WS_2 are comparable, with values of 10.56 and 10.76, respectively, despite $Cs_3Bi_2Br_9/WS_2$ exhibiting a higher MR degradation efficiency (DE%). This can be attributed to the higher optimal catalyst loading of $Cs_3Bi_2Br_9/WS_2$ compared to $Cs_3Bi_2Br_9$. In the presence of H_2O_2, $Cs_3Bi_2Br_9$ achieved a TON of 13.63, indicating a 29% improvement in catalytic degradation of MR, whereas the composite exhibited only a 2% increase.

Figure 5.12 (b) shows the comparison of TOF for MR degradation using the catalysts in the absence of H_2O_2. $Cs_3Bi_2Br_9/WS_2$ exhibited a marginal 2% higher TOF than $Cs_3Bi_2Br_9$. However, in the presence of H_2O_2, the TOF for $Cs_3Bi_2Br_9$ was 2.6 times higher compared to its absence, while $Cs_3Bi_2Br_9/WS_2$ experienced a twofold increase in TOF. Consequently, the addition of H_2O_2 resulted in a higher TOF when used with $Cs_3Bi_2Br_9$ compared to $Cs_3Bi_2Br_9/WS_2$. This is the case because the optimum MR DE% for the composite was 97.48% whereas the optimum DE% for $Cs_3Bi_2Br_9$ was 74.04%. Therefore, the $Cs_3Bi_2Br_9$ reaction had more room for improvement compared to the $Cs_3Bi_2Br_9/WS_2$ reaction.

In **Figure 5.12 (c)**, regarding RhB, the optimum catalyst loading was 1.6 mg/ml for both $Cs_3Bi_2Br_9$ and $Cs_3Bi_2Br_9/WS_2$. The TON values were 7.82 for $Cs_3Bi_2Br_9$ and 7.56 in the presence of H_2O_2. Similarly, $Cs_3Bi_2Br_9/WS_2$ exhibited TON values of 8.984 and 8.981, with and without H_2O_2, respectively. Therefore, $Cs_3Bi_2Br_9/WS_2$ was a more effective catalyst at degrading RhB than $Cs_3Bi_2Br_9$. **Figure 5.12 (d)** shows that adding H_2O_2 increased the TOF for the $Cs_3Bi_2Br_9$ reaction by a factor of 1.94, and for the $Cs_3Bi_2Br_9/WS_2$ reaction, it resulted in a twofold increase in TOF. The TON and TOF results for RhB are smaller than the MR results because RhB has a higher molecular weight (479.02 g/mol) than MR (269.6 g/mol). This reduces the number of moles of the dye and thus lowers the TON and TOF values. In conclusion, the addition of 0.3519 M H_2O_2 to the heterogeneous catalytic reactions enhances the mineralization of dyes, enabling a twofold increase in the degradation rate compared to the reactions conducted without H_2O_2.

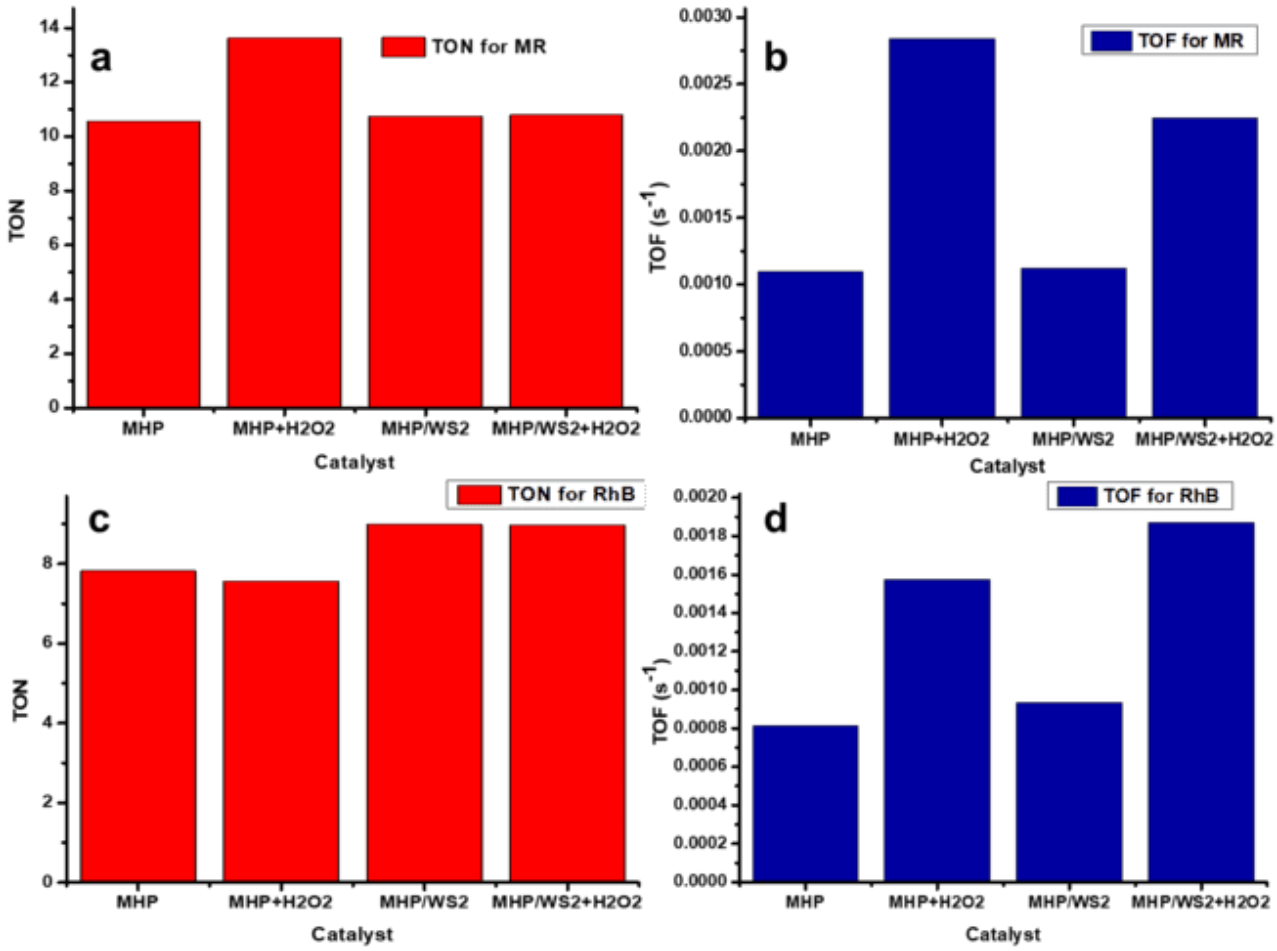

Figure 5.12 a) Turnover number for optimum MR heterogenous photodegradation reactions with and without H_2O_2 **b)** Turnover frequency for the optimum MR heterogenous photodegradation reactions with and without H_2O_2 **c)** Turnover number for optimum RhB heterogenous photodegradation reactions with and without H_2O_2 **d)** Turnover frequency for the optimum RhB heterogenous photodegradation reactions with and without H_2O_2

5.2.5. Comparison of research results to literature:

In **Table 5.7** below the optimum $Cs_3Bi_2Br_9$ and $Cs_3Bi_2Br_9/WS_2$ degradation results were compared with findings from various literature papers. Concerning the degradation of anionic dyes, $Cs_3Bi_2Br_9$ exhibited an optimum MR degradation efficiency of 74.04% within 120 min. This performance surpasses the 57.7% DE% reported for methyl orange by $CsPbBr_3$ (Zhang *et al.*, 2023). However, $Cs_3Bi_2Br_9$ was outperformed by $CsPbCl_3$, which achieved a methyl orange degradation efficiency of 90% within 80 minutes (Huynh *et al.*, 2020). In contrast, the comparison of cationic dye degradation performance comparison favours $Cs_3Bi_2Br_9$ over the anionic results. The average cationic dye degradation efficiency reported in the literature for metal halide

perovskites cited in the Table is 78.74 % within ~100 min. The lowest recorded cationic DE% was 73.1% within 6 hrs by $CsSnBr_3$ (Reyes-Pérez *et al.*, 2018; Bianca Maria Bresolin, 2021), while the highest performance was achieved by $Cs_3Bi_2Br_9$ reaching 100% within 100 min (Akinbami *et al.*, 2021). Therefore, the 97.6% DE% of RhB within 120 min compares well with the literature findings.

The heterostructure results from the literature exhibited variability; however, all the heterostructures containing WS_2 achieved degradation efficiencies exceeding 85%. According to the literature, WS_2 plays a crucial role in preventing the recombination of photogenerated charge carriers, enhancing light absorption, photocatalytic activity, and recyclability. The nanoflower structure of WS_2 increases the surface area when utilized as a co-catalyst, providing ample surface area and functional groups such as C=O and -OH, facilitating bonding with the precursor when in solution (Kumari *et al.*, 2023).

In the heterostructure studies conducted in this research, $Cs_3Bi_2Br_9/WS_2$ achieved degradation efficiencies of 97.64% and 97.48% for MR and RhB respectively, within 120 min. These results align favorably with those reported in the literature for heterostructures.

Table 5.7: MHP and heterostructure anionic and cationic dye degradation performance comparison table.

Catalyst	Dye degraded	Degradation efficacy and time	Reference
Perovskites			
$Cs_3Bi_2Br_9$	**Methyl red (anionic)**	**74.04% in 120 min**	**This study**
$Cs_3Bi_2Br_9$	**Rhodamine B (cationic)**	**97.6% in 120 min**	**This study**
$CsSnBr_3$	Crystal violet (cationic)	73.1% in 6 hrs	(Reyes-Pérez *et al.*, 2018; Bianca Maria Bresolin, 2021)
$CsPbCl_3$	Methyl Orange (anionic)	90% in 80 min	(Huynh *et al.*, 2020)
$CsPbCl_3$	RhB in toluene/ethane (cationic)	90% in 100 min	(Gao *et al.*, 2017; Gu *et al.*, 2023)

$CsPbBr_3$	Methyl Orange (anionic)	57.7% in 90 min	(Zhang *et al.*, 2023)
$CsPbBr_3$	RhB in toluene/ethane (cationic)	89% in 100 min	(Gao *et al.*, 2017; Gu *et al.*, 2023)
$Cs_2Bi_2I_9$-OA	Methylene blue in water (cationic)	62.1% in 60 min	(Bhattacharyya, Chaudhary, and Bhattacharjee, 2019; Bianca Maria Bresolin, 2021)
$Cs_2Bi_2Br_9$-OA	Methylene blue in water (cationic)	26.6% in 60 min	(Bhattacharyya, Chaudhary, and Bhattacharjee, 2019; Bianca Maria Bresolin, 2021)
$Cs_3Bi_2Br_9$	Methylene blue in deionized water (cationic)	99% in 100 min	(Akinbami *et al.*, 2021)
$Cs_3Bi_2Br_9$	Rhodamine B in deionized water (cationic)	100% in 100 min	(Akinbami *et al.*, 2021)
Cs_4PbBr_6	Methylene blue (cationic)	85% in 90 min	(Immanuel *et al.*, 2022)
$CsPbI_3$	Methylene Blue in ethyl alcohol (cationic)	97% in 30 min	(Q. Zhang *et al.*, 2020a)
$Cs_3Bi_2Br_9$-OA NCs	Methylene blue in isopropanol (cationic)	58.8% in 60 min	(Bhattacharyya, Chaudhary, and Bhattacharjee, 2019)
$Cs_3Bi_2Br_9$ NCs	Methylene blue in isopropanol (cationic)	66.3% in 60 min	(Bhattacharyya, Chaudhary, and Bhattacharjee, 2019)
$Cs_2AgBiBr_6$	Rhodamine B (cationic)	~98% in 2 hrs	(Zhang *et al.*, 2019)
Heterostructures			
$Cs_3Bi_2Br_9/WS_2$	**Methyl red (anionic)**	**97.48% in 120 min**	**This study**
$Cs_3Bi_2Br_9/WS_2$	**Rhodamine B (cationic)**	**97.64% in 120 min**	**This study**

WS_2/MoS_2	Rhodamine B (cationic)	93% in 90 min	(Kumari *et al.*, 2023)
WS_2/MoS_2	Methylene blue (cationic)	85% in 90 min	(Kumari *et al.*, 2023)
WS_2/MoS_2/BiOCl	Methylene blue (cationic)	99.36% in 240 min	(Kumari *et al.*, 2023)
ZnO/WS_2	Rhodamine B (cationic)	95.71% in 120 min	(Kumari *et al.*, 2023)
TiO_2/ WS_2	Rhodamine B (cationic)	85.1% in 120 min	(Kumari et al., 2023)
γ-$CsPbI_3/WS_2$	Methylene blue (cationic)	100% in 30 min	(Kumari et al., 2023)
$Cs_2Bi_2I_9$-OA/Ag_2S	Methylene blue in water (cationic)	88.8% in 60 min	(Bhattacharyya, Chaudhary, and Bhattacharjee, 2019; Bianca Maria Bresolin, 2021)
$Cs_2Bi_2I_9$-OA/TiO_2	Methylene blue in water (cationic)	83.5% in 120 min	(Bhattacharyya, Chaudhary, and Bhattacharjee, 2019; Bianca Maria Bresolin, 2021)
$Cs_2Bi_2Br_9$-OA/Ag_2S	Methylene blue in water (cationic)	40.13% in 60 min	(Bhattacharyya, Chaudhary, and Bhattacharjee, 2019; Bianca Maria Bresolin, 2021)
$Cs_2Bi_2Br_9$-OA/TiO_2	Methylene blue in water (cationic)	27.6% in 60 min	(Bhattacharyya, Chaudhary, and Bhattacharjee, 2019; Bianca Maria Bresolin, 2021)

5.3. Optical and structural changes to photocatalysts after degradation

After one cycle of degrading the dyes, the photocatalysts were washed with UPW multiple times, centrifuged, and left to dry at room temperature. The dried samples were then analysed to determine any optical and structural changes. UV-vis analysis was used to assess the optical changes, while PXRD was employed to investigate the structural changes.

5.3.1. Optical changes (UV-vis)

Figure 5.13 presents the optical properties of **a)** $Cs_3Bi_2Br_9$ and **b)** $Cs_3Bi_2Br_9/WS_2$ after the degradation of dyes. In the case of $Cs_3Bi_2Br_9$, the maximum absorbance shifted from 450 nm to a shorter wavelength of 442 nm. Additionally, the bandgap widened from 2.48 eV to 2.88 eV. For $Cs_3Bi_2Br_9/WS_2$, the bandgap slightly increased from 2.86 eV to 2.96 eV. Despite the increase in bandgap observed after removing the dyes in UPW, both $Cs_3Bi_2Br_9$ and $Cs_3Bi_2Br_9/WS_2$ still exhibited bandgaps smaller than 3 eV, indicating their inherent photocatalytic nature and potential for reuse.

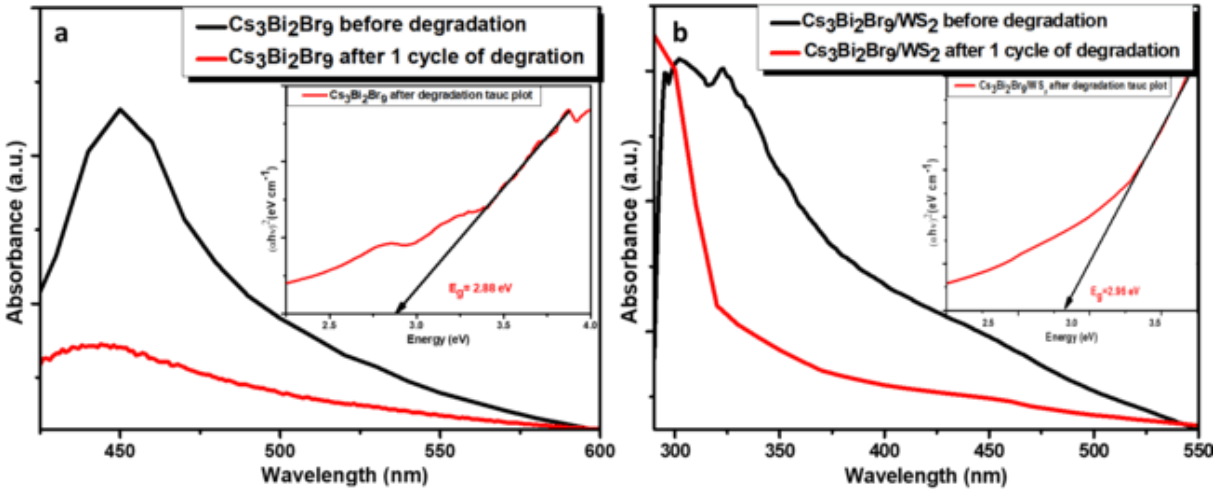

Figure 5.13 a) $Cs_3Bi_2Br_9$ UV-vis absorbance and tauc plot before and after dye degradation **b)** $Cs_3Bi_2Br_9/WS_2$ UV-vis absorbance and tauc plot before and after dye degradation

5.3.2. Structural changes (PXRD)

The PXRD patterns of the photocatalysts before and after one cycle of dye degradation are illustrated in **Figure 5.14**. In **Figure 5.14 (a)**, the intensity of the $Cs_3Bi_2Br_9$ PXRD peaks significantly decreased after degradation, with the 003 peak intensity reduced by 94.4%. Following degradation, the $Cs_3Bi_2Br_9$ PXRD pattern matched the PDF 01-073-0354 card indexed to $CsBr_3$. This observation suggests that Bi_2Br_3 may have been cleaved off during the photocatalytic reaction. In **Figure 5.14 (b)**, the $Cs_3Bi_2Br_9/WS_2$ PXRD pattern exhibited minimal changes, with a slight reduction of 33.3% in the 003-peak intensity. After degradation, the $Cs_3Bi_2Br_9/WS_2$ PXRD pattern corresponded to the PDF 01-070-0493 card indexed to $Cs_3Bi_2Br_9$. The peaks remained narrow, indicating that the catalyst still maintained its crystalline nature. Therefore, the structural changes in $Cs_3Bi_2Br_9/WS_2$ were negligible,

suggesting that it is more stable than $Cs_3Bi_2Br_9$ and can likely be reused for multiple degradation cycles compared to $Cs_3Bi_2Br_9$. These structural changes may result from photo-dissolution and photo-corrosion of the catalysts during the photodegradation reactions. Photo-corrosion refers to photoinduced decomposition, which adversely affects the durability of photocatalysts. Strategies to mitigate photo-corrosion include doping with heteroatoms, modifying the morphology of the photocatalyst, regulating the photodegradation conditions, and incorporating a co-catalyst (Weng *et al.*, 2019). Thus, it can be concluded that the use of WS_2 as a co-catalyst effectively prevented photo-corrosion, thereby improving the catalyst's durability. Researchers have also found that $Cs_3Bi_2Br_9$ is unstable in moist conditions, under light exposure, and/or in oxidative conditions, therefore creating a heterostructure with a stable photocatalytic material, like WS_2, lowers the surface energy making $Cs_3Bi_2Br_9$ more stable. This extends the lifespan of photogenerated charges as it prevents e^- - h^+ recombination thereby improving photodegradation performance (Bai *et al.*, 2023).

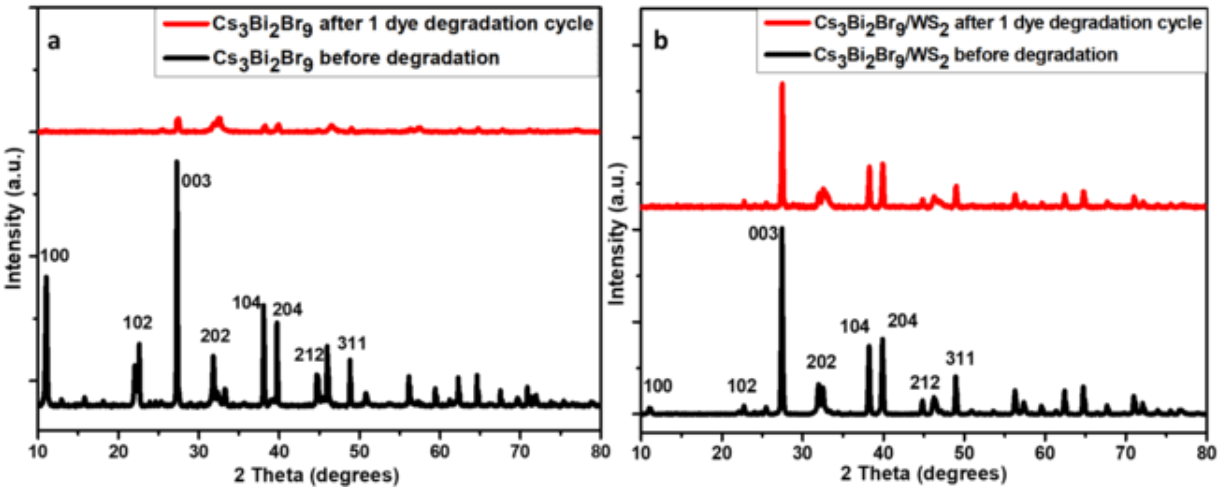

Figure 5.14 a) PXRD pattern of $Cs_3Bi_2Br_9$ before and after dye degradation **b)** $Cs_3Bi_2Br_9/WS_2$ before and after dye degradation

5.3.3. TEM images after photodegradation of dyes

Below are the TEM images of $Cs_3Bi_2Br_9$ and the heterostructure, $Cs_3Bi_2Br_9/WS_2$ after a cycle of degrading the SODs photocatalytically. After one cycle of degrading the dyes, the photocatalysts were rinsed with ultra-pure water, centrifuged, and dried. In **Figures 5.15 a-b** the $Cs_3Bi_2Br_9$ nanosheets are layered, have irregular shapes, and are polydispersed. There are also particle agglomerates present. In **Figures 5.15 c-d** the $Cs_3Bi_2Br_9/WS_2$ nanoparticles are agglomerated and the WS_2 nanopetals can be seen in **Figure 5.15 (d)** highlighted in the red block. The agglomeration of the catalysts reduces light absorption and the surface area of the photocatalysts (Li *et al.*, 2010). A reusability study would have to be conducted to determine the efficacy of the catalysts after degrading the SODs.

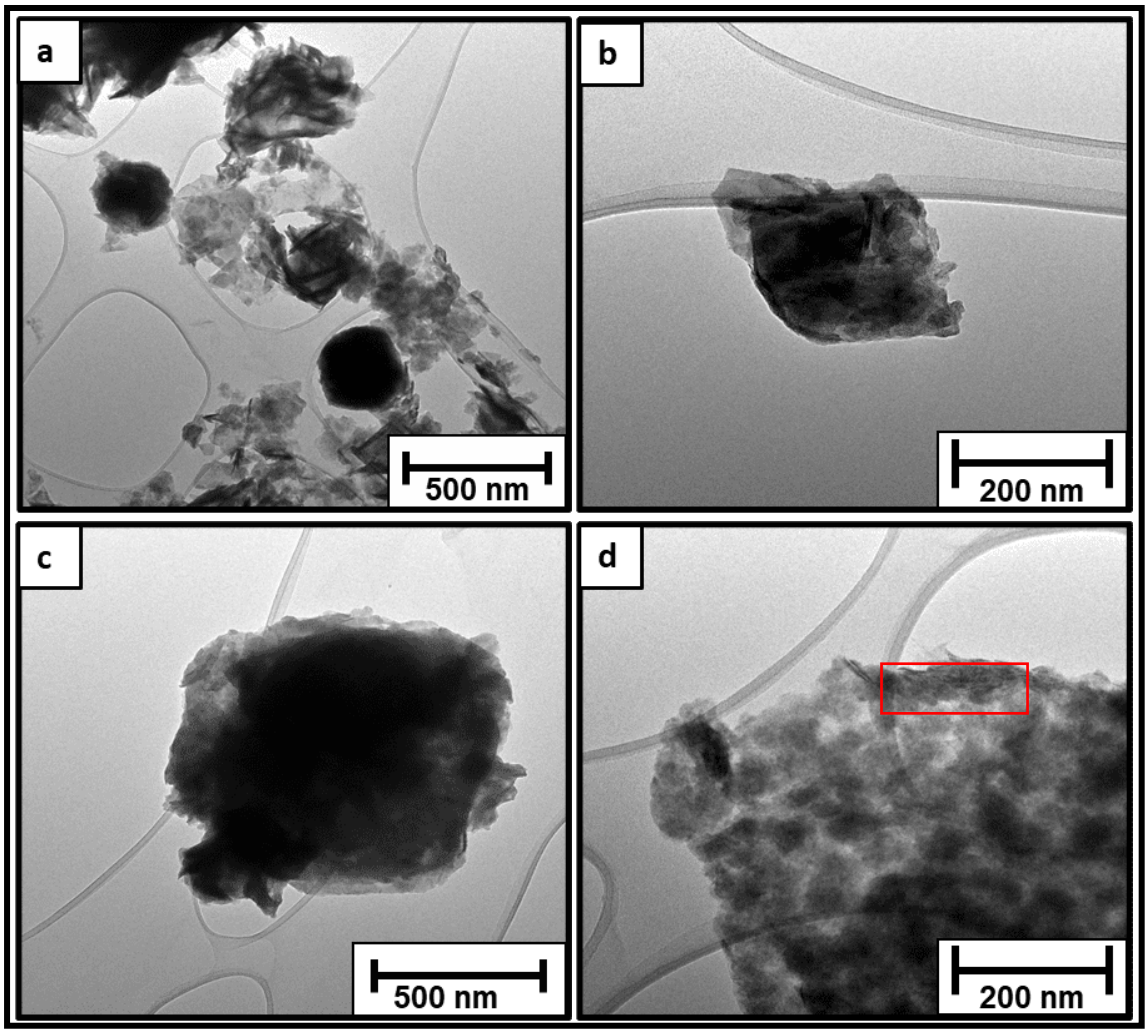

Figure 5.15 a) and **b)** $Cs_3Bi_2Br_9$ after dye degradation **c)** and **d)** $Cs_3Bi_2Br_9/WS_2$ after dye degradation

5.3.4. SEM/ EDS mapping after degradation of dyes:

SEM and EDS mapping were done after application to determine structural and compositional changes in the materials. **Figures 5.16 (a)** and (**d)** show that the $Cs_3Bi_2Br_9$ and $Cs_3Bi_2Br_9/WS_2$ materials were agglomerated as seen in the TEM images. **Figures 5.16 (b)** and **(e)** show that all the elements were still present in $Cs_3Bi_2Br_9$ and $Cs_3Bi_2Br_9/WS_2$. This suggests that the elemental integrity of the materials was still maintained. The $Cs_3Bi_2Br_9$ and $Cs_3Bi_2Br_9/WS_2$ EDX spectra are shown in **Figures 5.16 (c)** and **(f)** respectively. The relative intensities of the EDX spectra are shown in **Figures 5.16 (c)** and **(f)** below and are equal to the molar ratios of elements in the $Cs_3Bi_2Br_9$ and $Cs_3Bi_2Br_9/WS_2$ photocatalysts. The Br element did not appear in the $Cs_3Bi_2Br_9/WS_2$ EDX spectrum however, it was detected in the EDS mapping results. This could be due to the uneven distribution of the elements in the material. **Table 5.8** shows the weight percentages of the elements.

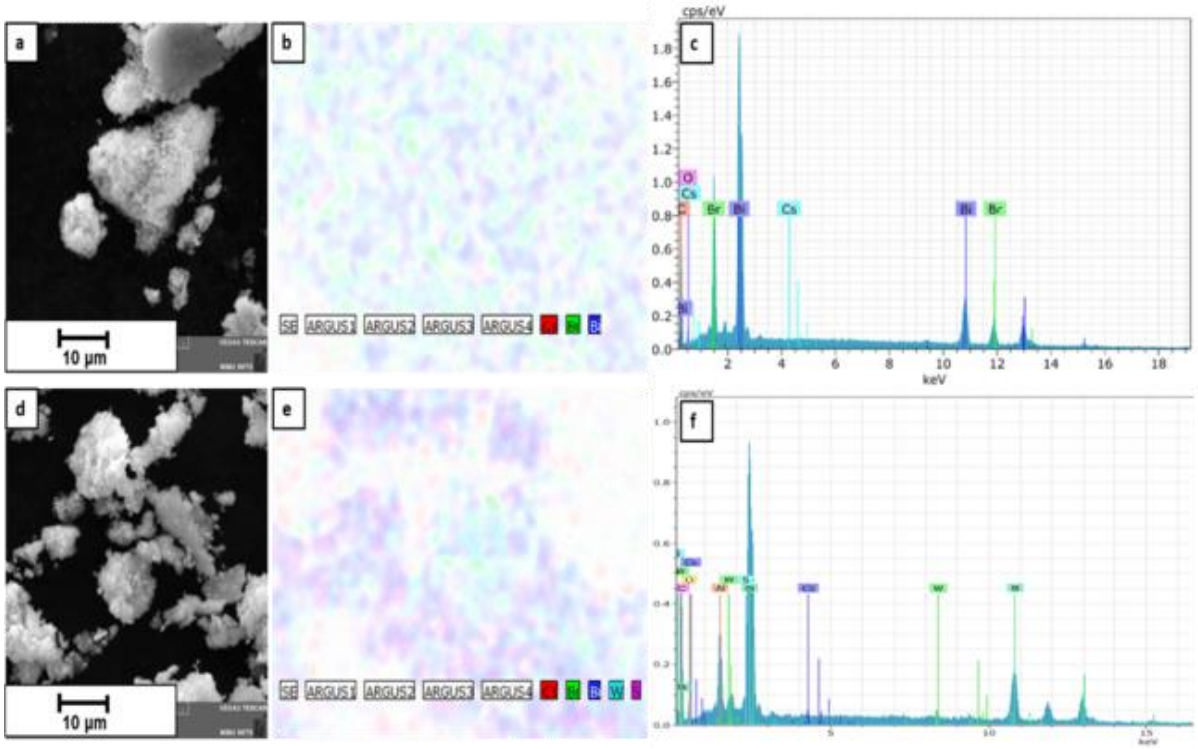

Figure 5.16 a) SEM image of $Cs_3Bi_2Br_9$ after one cycle of photodegradation reaction **b)** Elemental distribution of Cs, Br, and Bi in $Cs_3Bi_2Br_9$ **c)** $Cs_3Bi_2Br_9$ EDX plot **d)** SEM image of $Cs_3Bi_2Br_9$ after one cycle of photodegradation reaction **e)** Elemental distribution of Cs, Br, Bi, W, and S in $Cs_3Bi_2Br_9/WS_2$ **f)** $Cs_3Bi_2Br_9/WS_2$ EDX plot

Table 5.8: EDX results of $Cs_3Bi_2Br_9$ and $Cs_3Bi_2Br_9/WS_2$ after one dye degradation cycle

Elements	Weight percentage in $Cs_3Bi_2Br_9$ (%)	Weight percentage in $Cs_3Bi_2Br_9/WS_2$ (%)
O	6.468	4.272
C	10.74	11.32
Al	4.582	2.848
Cs	20.03	21.44
Bi	21.13	20.32
Br	37.05	-
W	-	28.68
S	-	11.12
Total	100	100

5.4. Qualitative and quantitative analysis:

Qualitative and quantitative analysis to determine the quality of water after dye removal and to determine the extent to which the dyes were broken down. These measurements were done for the optimum dye degradation reactions.

5.4.1. Chemical oxygen demand (COD) analysis:

COD is an estimate of oxygen which is equivalent to organic matter, such as synthetic organic dyes, that is susceptible to oxidation, and it measures the amount of oxygen consumed by the organic matter when heated in potassium dichromate solution during digestion (Jain and Singh, 2003). It is used to characterize water from waterbodies, sewage, treatment plants, and industrial effluents (Khan and Ali, 2018). COD analysis is important for various reasons such as the ones listed below:

- Quantitative measurement and degradation efficiency: By comparing the initial COD value of the dye-containing solution with the COD value after photocatalytic degradation, COD analysis helps to determine the efficacy of the photocatalysts in mineralizing the dyes as it provides a quantitative measure of the amount of organic compounds present. Therefore, a higher reduction in COD indicates a more effective degradation process, as it implies a greater removal of the SODs (Subramani *et al.*, 2007).
- Environmental impact: SODs are often non-biodegradable and can have adverse effects on ecosystems if released into the environment without proper treatment. By measuring the COD reduction, it is possible to gauge the extent

to which the photocatalytic degradation process has reduced the organic load and potentially mitigated the environmental impact (Li and Liu, 2019).

The COD measurements were conducted using the Spectroquant Pharo 300 spectrophotometer shown in **Figure 5.17 (a)**. The samples were added into 25-1500 mg/l COD reagent cells, and the ISCO RECORD sample reactor was used to digest/heat the samples as shown in **Figure 5.17 (b)**. The blank and standard solutions were prepared and used to ensure the measurement accuracy of the spectrophotometer. A micropipette was used to measure 3 ml of each sample and the measured samples were added to the separate sample reagent cells. The samples and COD reagents were then mixed by inverting the cell multiple times. The cells were placed in the reactor to digest at 148ºC for 2 hours. After digestion, the samples were removed from the reactor and aggregated for the last time. They were left to cool for 30 minutes as shown in **Figure 5.17 (c)**. The COD measurements were conducted. This is shown in **Figure 5.17 (d)**.

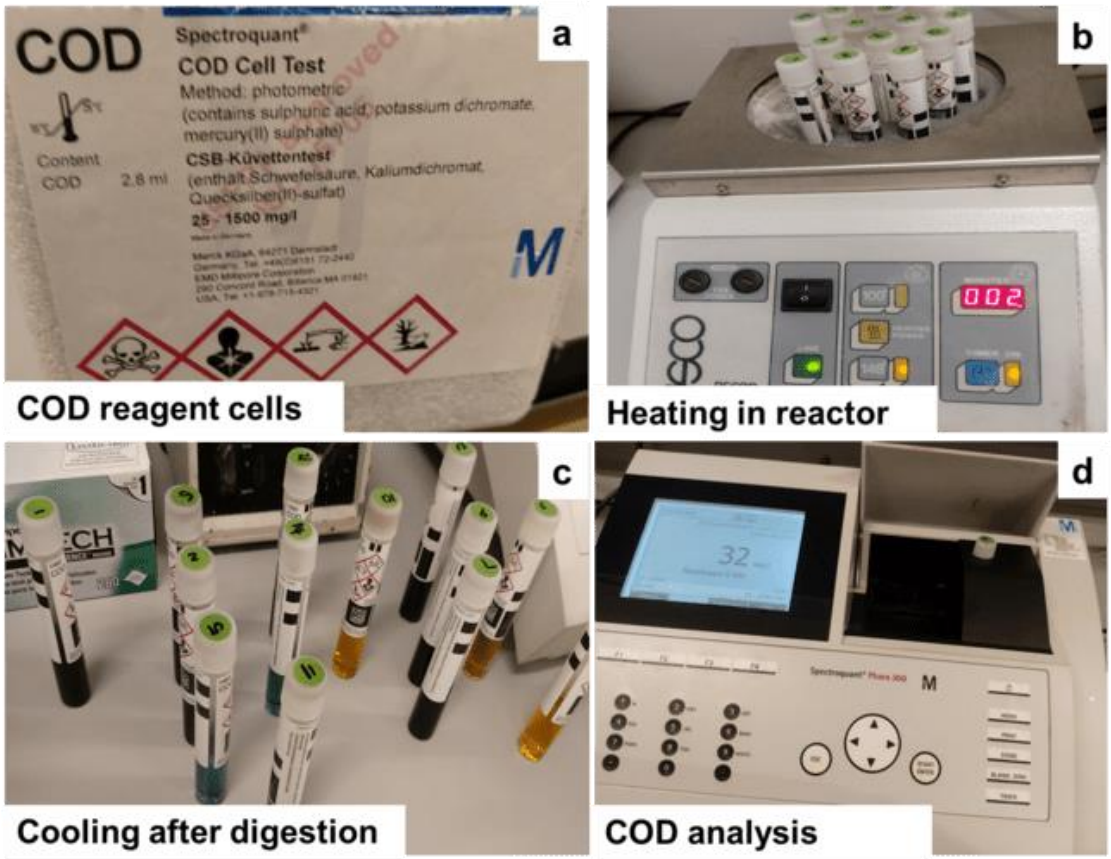

Figure 5.17: COD analysis process **a)** COD test cells **b)** reactor used for digestion **c)** samples cooling after digestion **d)** COD spectrophotometer

COD analysis was conducted for the dye samples before degradation, samples degraded under optimum conditions, and photolysis to determine if the COD levels were reduced. The results are reported in **Table 5.9** below. The initial COD levels were 6747 mg/L and 70 mg/L for MR and RhB respectively. Rajhans, G., et al., have reported that there is a positive correlation between toxicity and COD levels. Since the MR and RhB LD50 oral for rat values are 10740 mg/kg and 500 mg/kg respectively, therefore the initial COD level is much higher for MR than it is for RhB because MR is more toxic. The highest COD removal efficiency of 51.27% for MR was achieved using 1.6 mg/ml of $Cs_3Bi_2Br_9$ and 0.3519 M of H_2O_2 at pH 5.5. The COD removal efficiency was 0% for the UV/H_2O_2 and 2.4 mg/L $Cs_3Bi_2Br_9/WS_2$ at pH 2 reactions. The high COD levels are due to high levels of oxidizable material. The addition of H_2O_2 has been found to increase the COD level compared to the initial COD level due to the radical scavenging effect. The COD level could be high for 2.4 mg/L $Cs_3Bi_2Br_9/WS_2$ at pH 2 because HNO_3 and NaOH were used to adjust the pH which could have increased in oxygen-containing functional groups thus increasing the COD level. The H_2O_2 interference is more apparent in the RhB results where all samples that contained H_2O_2 had higher COD levels than the initial COD level. The highest COD removal efficiency of 42.86% was achieved using 1.6 mg/ml of $Cs_3Bi_2Br_9/WS_2$ at pH 2. Direct photolysis reduced the COD level by 17.14%. This result could be explained by the phenomenon that direct photolysis does not necessitate the addition of any oxygen-containing chemicals.

Table 5.9: MR and RhB COD levels before and after photodegradation by $Cs_3Bi_2Br_9$ and $Cs_3Bi_2Br_9$ at optimum conditions

Samples	COD level (mg/L)	COD removal efficiency (%)
MR		
20 ppm MR initial	6747	-
20 ppm MR photolysis	5258	22.07
20 ppm MR UV/H_2O_2 pH 5.5	6747	0
MR @ 1.6 mg/mL $Cs_3Bi_2Br_9$ pH 5.5	3747	44.46
MR @ 1.6 mg/mL $Cs_3Bi_2Br_9$ pH 5.5 + H_2O_2	3288	51.27
MR @ 2.4 mg/mL $Cs_3Bi_2Br_9/WS_2$ pH 2	6747	0
MR @ 2.4 mg/mL $Cs_3Bi_2Br_9/WS_2$ + H_2O_2 pH 2	3499	48.13
RhB		
20 ppm RhB initial	70	-

RhB photolysis	58	17.14
RhB UV/H_2O_2	1698	0
RhB @ 1.6 mg/mL $Cs_3Bi_2Br_9$ pH 7	175	0
RhB @ 1.6 mg/mL $Cs_3Bi_2Br_9$+ H_2O_2 pH 7	1658	0
RhB @ 1.6 mg/mL $Cs_3Bi_2Br_9/WS_2$ pH 2	40	42.86
RhB @ 1.6 mg/mL $Cs_3Bi_2Br_9/WS_2$ + H_2O_2 pH 2	1649	0

5.4.2. Mass spectroscopy analysis

Degradation pathways for methyl red and rhodamine B:

There have been various degradation pathways proposed in the literature for different types of SODs. The most effective method to determine the degradation pathway and assess the extent of degradation of SODs would involve collecting samples of the dye solution at regular time intervals during the degradation reaction. These samples can then be analysed using quantitative techniques such as mass spectrometry to identify the intermediates by examining their mass/charge (m/z) values (Natarajan et al., 2011). In a study conducted by Comparelli et al., the degradation of methyl red under UV/LED radiation in the presence of ZnO was investigated. The researchers discovered that the molecular structure of the dye is one of the factors that influence the degree of degradation. Methyl red is particularly vulnerable to attack by OH• due to the positive electronic effects resulting from the ortho positioning of the carboxyl (COOH) group in relation to the diazo (N=N) group. These positive electronic effects reduce the N=N π-overlap, thereby enhancing the reactivity between OH• and the dye (Comparelli et al., 2005). Regarding methyl red, it is believed that the hydroxyl groups primarily attack the aromatic rings, while the dimethyl amino group undergoes photolytic attack. The intermediates observed are the result of both photolytic and OH• attacks (Comparelli et al., 2005). The proposed degradation pathway is illustrated in **Scheme 5.1** below.

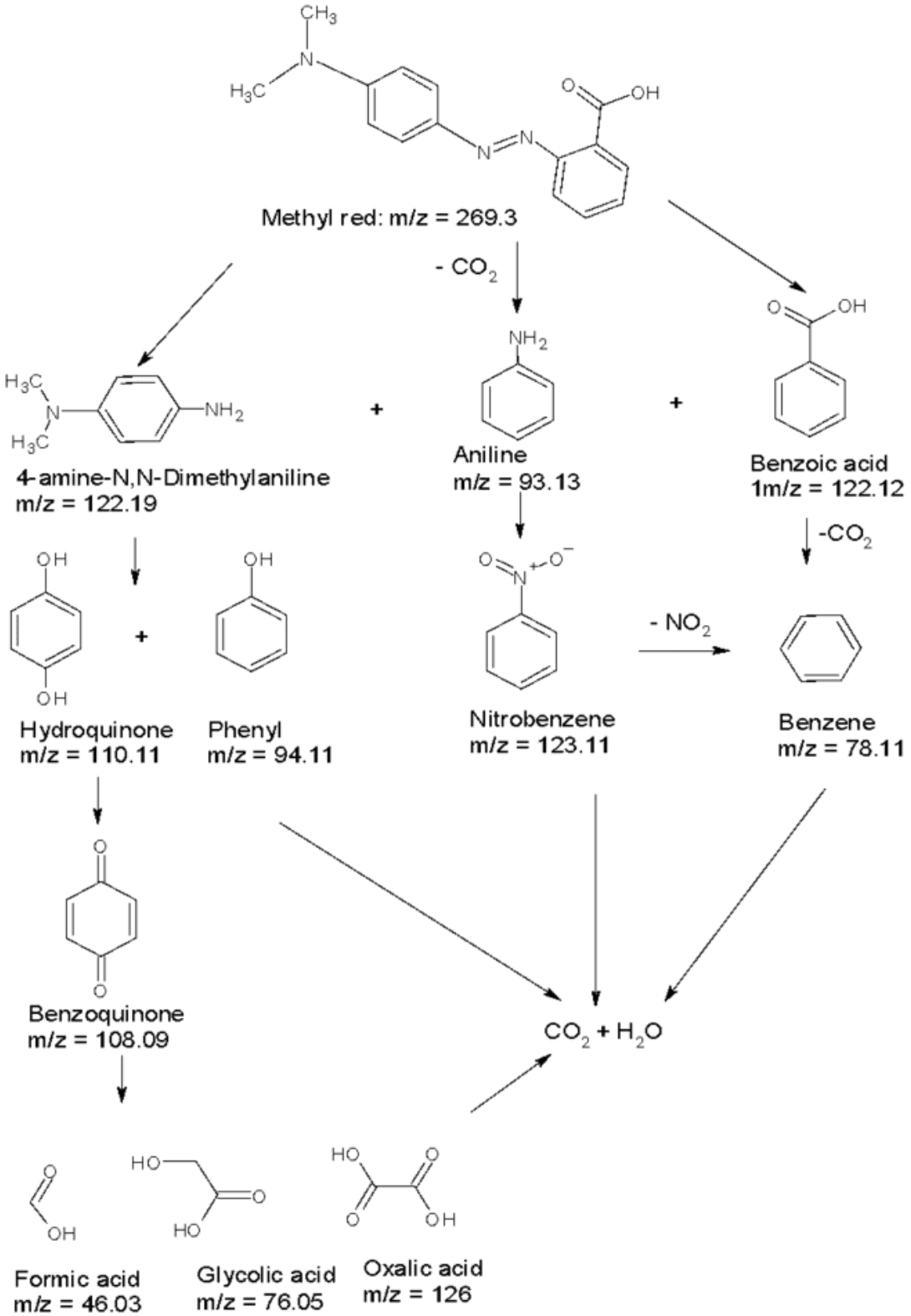

Scheme 5.1: Photodegradation pathway of methyl red (Devi, Raju and Kumar, 2009)

According to a study conducted by He et al. (2009), it was discovered that rhodamine B undergoes degradation through four distinct processes. These processes include N-de-ethylation and chromophore cleavage, which occur simultaneously. N-de-

ethylation involves a chemical reaction that leads to the detachment of ethyl (C_2H5) groups from the nitrogen (N) atoms. Intermediate compounds are formed in a stepwise manner as a result of the N-de-ethylation process, while the conjugated xanthane is cleaved by holes (h^+), hydroxyls ($OH^•$), and superoxide anions ($O_2^{•-}$). Following the N-de-ethylation and chromophore cleavage processes, the subsequent steps involve ring-opening and mineralization. These processes are also influenced by holes (h+), hydroxyls (OH•), and superoxide anions. During this stage, the xanthane rings are cleaved, and mineralization occurs. The degradation pathway for RhB is shown in **Scheme 5.2**.

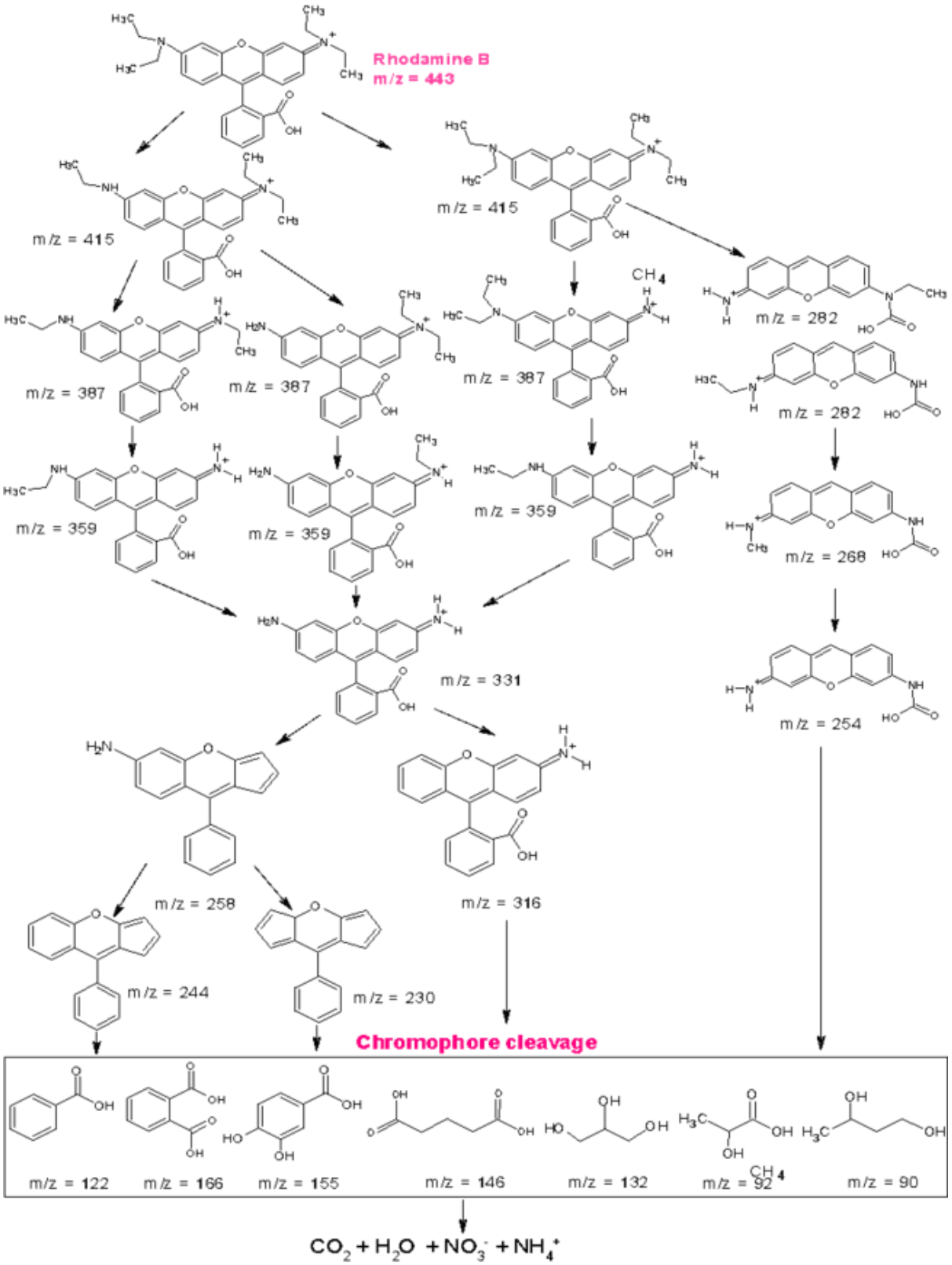

Scheme 5.2: Photodegradation pathway of rhodamine B (Natarajan et al., 2011).

The MR and RhB samples were quantitatively analysed using a liquid chromatography-mass spectrophotometer. The analysis utilized the loop method with a C18 column. Samples collected at the end of the optimum photodegradation reactions were analysed to determine the degree to which the photocatalysts degraded the dyes in the aqueous solutions. Peak intensities were converted to percentages for simplification purposes. Initially, the dye peaks exhibited 100% intensity. **Figures 5.18** and **5.19** below illustrate the RhB, MR, and other fragment peaks before and after degradation, demonstrating how the degradation of the dyes was quantified. **Table 5.10** presents the percentage of the dyes detected at the end of the photodegradation reactions. The MR and RhB dye fragments resulting from chromophore or ring cleavage, as depicted in **Schemes 5.1** and **5.2**, were identified and are shown in **Figures 5.18** and **5.19**. According to the proposed degradation pathways, these fragments occur just prior to the mineralization of the dyes. Hence, it can be assumed that the degradation of MR and RhB using $Cs_3Bi_2Br_9$ and $Cs_3Bi_2Br_9/WS_2$ follows a similar mineralization process as described in the proposed degradation pathways.

Table 5.10 reveals that $Cs_3Bi_2Br_9$ degraded MR and RhB by 70.5 - 94.1%, while $Cs_3Bi_2Br_9/WS_2$ degraded the dyes by 91.2 - 97.5% with and without H_2O_2. Therefore, $Cs_3Bi_2Br_9/WS_2$ demonstrated higher effectiveness in degrading the dyes compared to $Cs_3Bi_2Br_9$. This phenomenon can be attributed to the diminished charge recombination in $Cs_3Bi_2Br_9/WS_2$, which is facilitated by the co-catalyst. As a result, there is an increased generation of ROS, leading to a more efficient degradation of the dyes. The degradation results for RhB in the H_2O_2 reactions with both catalysts were lower compared to the results for MR. This difference could be attributed to the more complex and bulky structure of RhB when compared to MR. The addition of 0.3519 M H_2O_2 resulted in rapid dye removal within 40 minutes, whereas the photocatalysts required 120 minutes of light exposure to achieve similar dye removal efficiency in the absence of H_2O_2. The results indicate that $Cs_3Bi_2Br_9$ and $Cs_3Bi_2Br_9/WS_2$ were not only effective in removing the chromophores or pigmentation of the dyes but also in breaking down the dye molecules. Although the samples were decolorized after degradation, a longer reaction time may be necessary to completely remove the dyes from UPW.

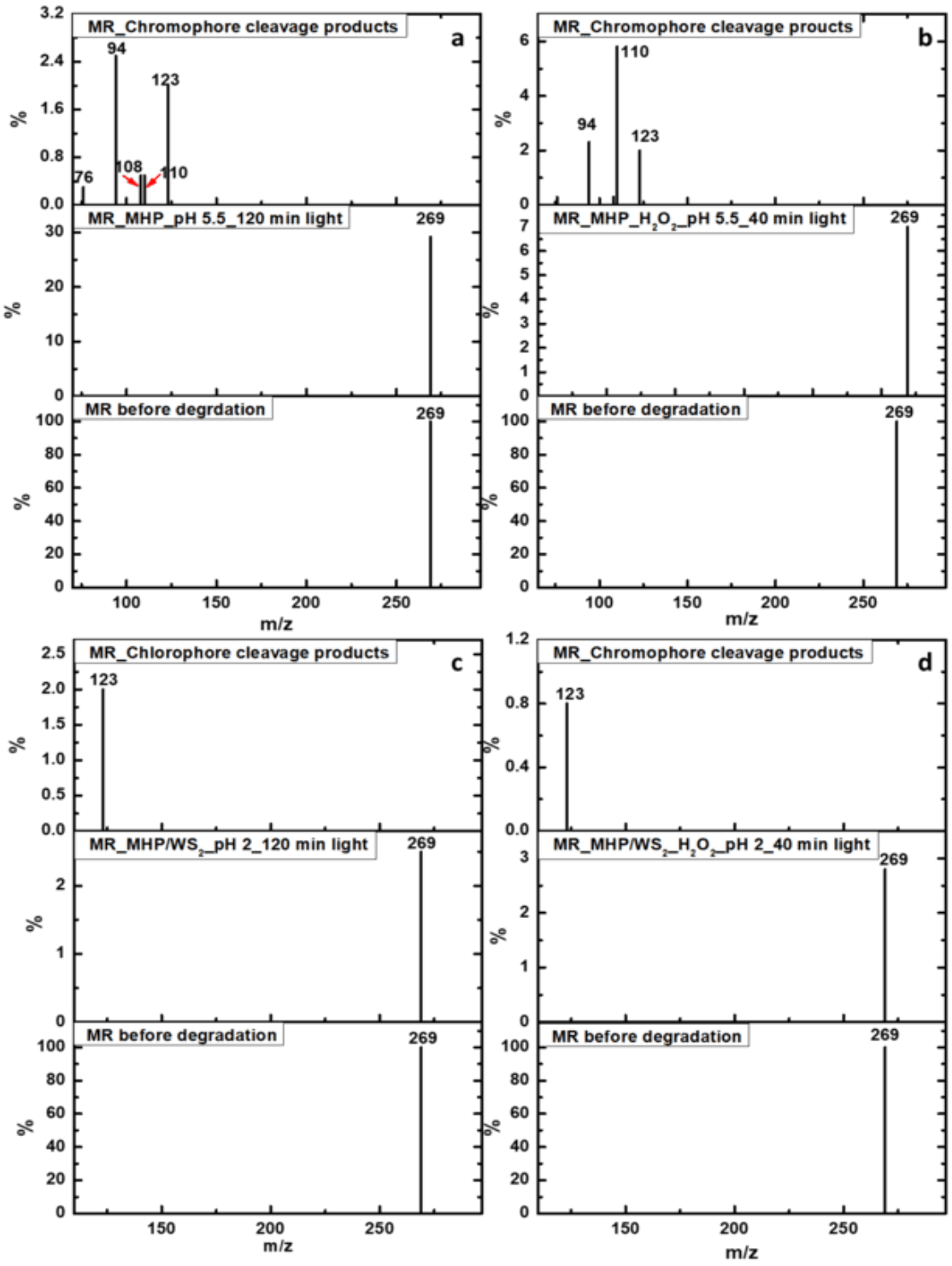

Figure 5.18: MR mass spectroscopy fragments before and after degradation

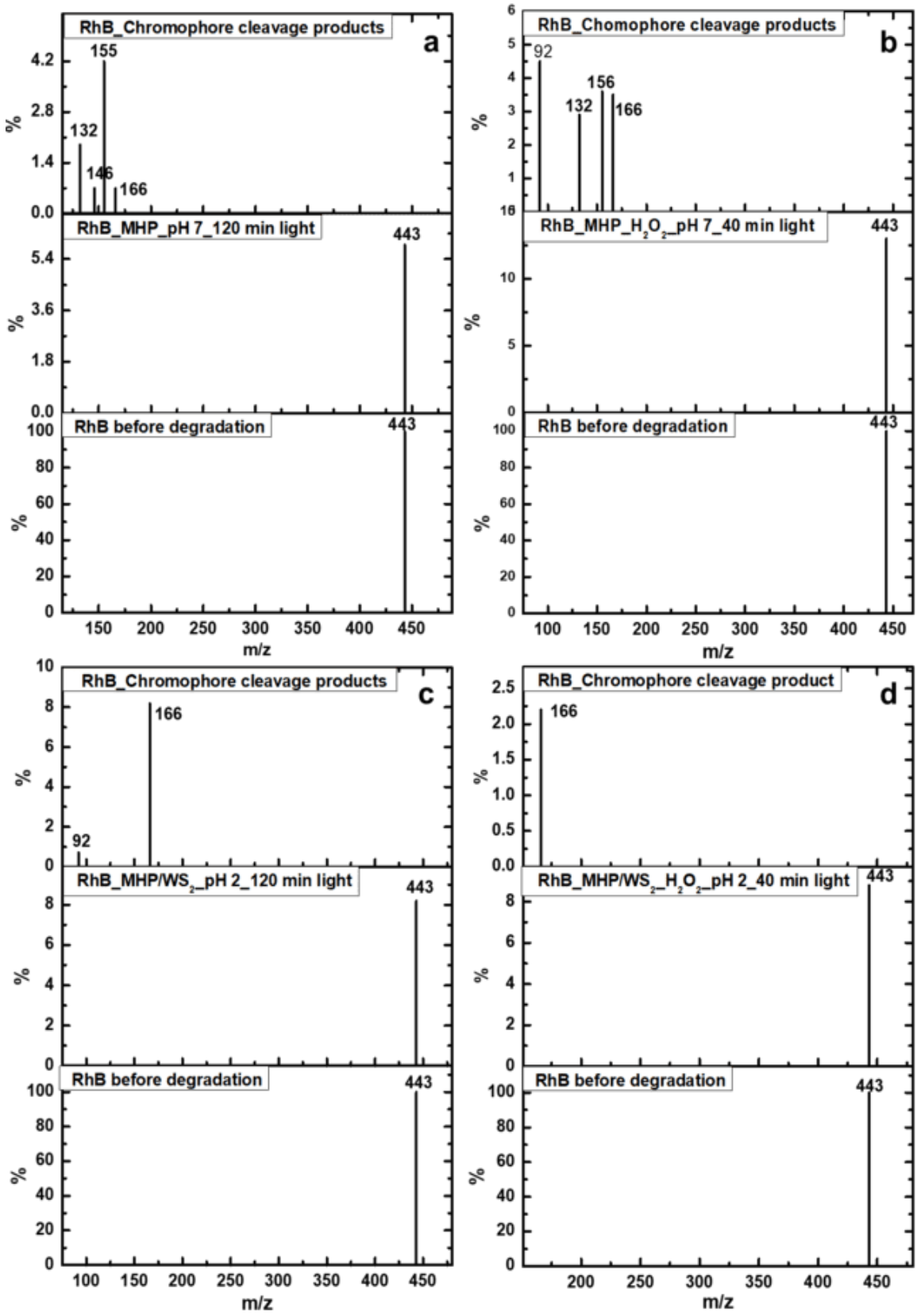

Figure 5.19: RhB mass spectroscopy fragments before and after degradation

Table 5.10: Mass spectroscopy data for the optimum MR and RhB degradation reactions

Photocatalyst	Catalyst loading	pH	Dye	% dye peak remaining after degradation	% of Dye removed
$Cs_3Bi_2Br_9$	1.6 mg/ml	5.5	MR	29.5	70.5
	1.6 mg/ml	7	RhB	5.9	94.1
$Cs_3Bi_2Br_9$ + H_2O_2	1.6 mg/ml + 0.3519 M H_2O_2	5.5	MR	7	93
	1.6 mg/ml + 0.3519 M H_2O_2	7	RhB	13	87
$Cs_3Bi_2Br_9/WS_2$	2.4 mg/ml	2	MR	2.5	97.5
	1.6 mg/ml	2	RhB	8.2	91.8
$Cs_3Bi_2Br_9/WS_2$ + H_2O_2	2.4 mg/ml + 0.3519 M H_2O_2	2	MR	2.8	97.2
	1.6 mg/ml + 0.3519 M H_2O_2	2	RhB	8.8	91.2

5.5. Kinetics:

The kinetic studies were done using the reactions with optimum degradation efficiencies. The pseudo-first-order, pseudo-second-order, Elovich, and intraparticle diffusion kinetic models were used to study the reaction kinetics. The kinetic models were fitted using the optimum MR and RhB degradation reactions. The calculated parameters are in **Tables 5.11** and **5.12**. The linear fitting of the kinetic models is shown in **Figures 5.20** and **5.21**.

5.5.1. Methyl red kinetics

The pseudo-second-order and intra-particle diffusion kinetic models had the highest R^2 values of 0.941 and 0.937, respectively, for the degradation of MR using $Cs_3Bi_2Br_9$. However, the pseudo-second-order was the best-fit model because it had the highest R^2 value. This suggests that MR was removed via chemisorption. Therefore, the rate of adsorption depends on adsorption capacity and not on the concentration of the dye.

The rate of the reaction was 1.592×10^{-3} g/mg-min and the adsorption capacity was 13.01. For $Cs_3Bi_2Br_9/WS_2$ the best fit model was pseudo-first-order with an R^2 value of 0.952. This model assumes that the dye removal rate and time have a direct relationship. Adsorption occurs via physisorption. It is common that when reaction kinetics follow a pseudo-first-order model, the adsorption occurs via adsorption through the interface.

Table 5.11: Pseudo-first-order, pseudo-second-order, intraparticle diffusion and Elovich kinetic model constants and determination coefficients for MR degradation by $Cs_3Bi_2Br_9$ and $Cs_3Bi_2Br_9/WS_2$

	Pseudo first order			**Pseudo second order**		
	R^2	**k_1 (min^{-1})**	**q_e (mg/g)**	**R^2**	**k_2**	**q_e**
$Cs_3Bi_2Br_9$	0.917	0.0333	12.5	0.941	1.59×10^{-3}	13.01
$Cs_3Bi_2Br_9/WS_2$	0.952	0.0593	27.3	-0.0899	2.14×10^{-5}	106.0
	Intraparticle diffusion			**Elovich**		
	R^2	**K_{diff}**	**C**	**R^2**	**β**	**α**
$Cs_3Bi_2Br_9$	0.937	0.822	5.71×10^{-1}	0.9206	-1.71×10^{-1}	3.38×10^{-1}
$Cs_3Bi_2Br_9/WS_2$	0.812	1.09	-2.645	0.8776	-1.47×10^{-1}	2.46×10^{-1}

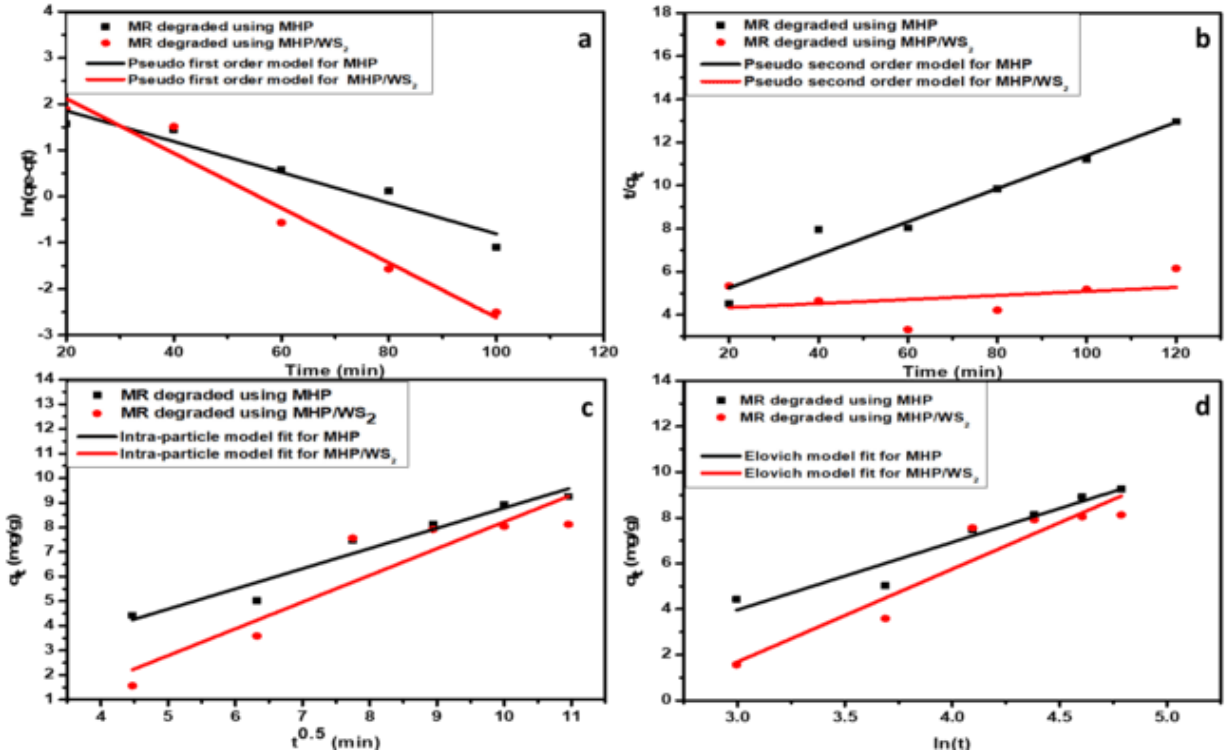

Figure 5.20: Kinetic studies for MR degradation by $Cs_3Bi_2Br_9$ and $Cs_3Bi_2Br_9/WS_2$ **(a)** Pseudo-first-order **(b)** Pseudo-second-order **(c)** Intraparticle diffusion **(d)** Elovich kinetic models

5.5.2. Rhodamine B kinetics

For the degradation of RhB, the best-fit model was pseudo-second-order for $Cs_3Bi_2Br_9$ and intraparticle diffusion for $Cs_3Bi_2Br_9/WS_2$. This means that $Cs_3Bi_2Br_9$ degrades both RhB and MR by chemisorption. The diffusion constant for $Cs_3Bi_2Br_9/WS_2$ was 5.40 $mg.g^{-1}min^{-0.5}$. The dye must diffuse through the bulk of the solution to the catalyst's surface then it diffuses into the micropores of the catalyst. The BET results indicated that $Cs_3Bi_2Br_9/WS_2$ was microporous. Intraparticle diffusion occurs through pore diffusion and surface diffusion (migration along the pore surface in which an adsorbate, dye, hops from one available adsorption site to another in a series of adsorption-desorption processes) mechanisms. Pore diffusion (diffusion in liquid-filled pores) is affected by catalyst porosity and tortuosity.

Table 5.12: Pseudo-first, pseudo-second, intraparticle diffusion and Elovich kinetic model constants and determination coefficients for RhB degradation by $Cs_3Bi_2Br_9$ and $Cs_3Bi_2Br_9/WS_2$

	Pseudo first order			**Pseudo second order**		
	R^2	**k_1 (min^{-1})**	**q_e (mg/g)**	**R^2**	**k_2**	**q_e**
$Cs_3Bi_2Br_9$	0.9637	3.94×10^{-2}	12.8	0.9995	3.47×10^{-3}	14.4
$Cs_3Bi_2Br_9/WS_2$	0.879	3.18×10^{-2}	20.4	0.7499	1.57×10^{-4}	33.3
	Intraparticle diffusion			**Elovich**		
	R^2	**K_{diff} (min^{-1})**	**c**	**R^2**	**β**	**α**
$Cs_3Bi_2Br_9$	0.977	2.93	1.46	0.914	-1.27	1.27
$Cs_3Bi_2Br_9/WS_2$	0.975	5.40	13.5	0.964	-0.573	0.674

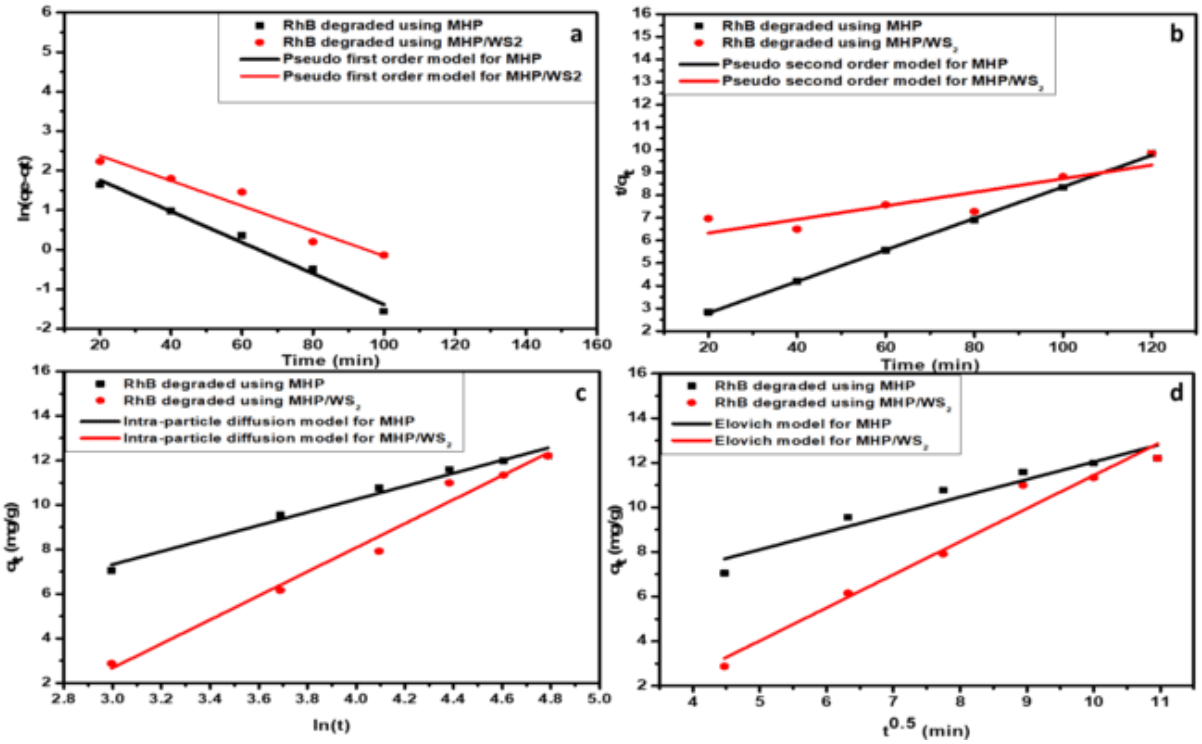

Figure 5.21: Kinetic studies for RhB degradation by $Cs_3Bi_2Br_9$ and $Cs_3Bi_2Br_9/WS_2$ **(a)** Pseudo-first-order, **(b)** Pseudo-second-order, **(c)** Intraparticle diffusion, **(d)** Elovich kinetic models

5.6. Adsorption isotherms:

The adsorption isotherms were studied at 20, 40, and 60 ppm initial concentrations. The adsorption isotherm models used are Langmuir, Frendlich, Dubinin-Radushkevic, Temkin, and Redlich-Peterson. The model with the highest R^2 value was selected as the best-fit model. The isotherm constants and coefficients are given in **Tables 5.13** and **5.14**. The linear plots are shown in **Figures 5.22** and **5.23**.

5.6.1. Methyl red adsorption isotherms

The best-fit adsorption isotherm for the degradation of MR using $Cs_3Bi_2Br_9$ was the R-P model with an R^2 value of 0.864. This model is a mixture of the Langmuir and Freundlich models. It is a more realistic model for an adsorption system that operates over a wide range of concentrations, and it does not follow ideal monolayer adsorption (Musah et al., 2022b). The R-P absorption capacity constant (K_R) was 0.1854, and the β exponent was 0.6959. The exponent lies between 0 and 1. When $0 < \beta < 0.5$, it fits Henry's law equation, and when $0.5 < \beta < 1$, it fits the Langmuir isotherm (Rengaraj *et al.*, 2007). Therefore, since it was 0.6959, it fits the Langmuir model which assumes that there was homogenous and monolayer adsorption of MR onto the $Cs_3Bi_2Br_9$ surface, and the adsorption occurred via chemisorption (Rengaraj *et al.*, 2007; Liu *et al.*, 2019). For $Cs_3Bi_2Br_9/WS_2$ the best fit model was the Temkin model with an R^2 value of 0.9977. The Temkin model accounts for the effects of the dye/catalyst interactions. This model assumes a linear decrease in heat of adsorption (ΔH_{ads}) of all the molecules as the catalyst surface coverage increases (Ayawei, Ebelegi and Wankasi, 2017). The heat of adsorption (b_T) was 728.2 J/mol and the surface coverage (k_T) was 4.483 L/g.

Table 5.13: Langmuir, Freundlich, Duninin-Radushevic, Temkin, and Redlich-Peterson adsorption isotherm model constants and determination coefficients for MR degradation by $Cs_3Bi_2Br_9$ and $Cs_3Bi_2Br_9/WS_2$.

Photocatalyst	**Langmuir**				**Freundlich**		
	R^2	**R_L**	**Q_0 (mg/L)**	**b (L/mg)**	**R^2**	**K_f**	**n**
$Cs_3Bi_2Br_9$	0.556	0.00184	2.23	9.04	0.447	5.39	3.289
$Cs_3Bi_2Br_9/WS_2$	0.9976	0.00537	5.61	3.08	0.974	6.01	3.243

	Dubinin-Radushkevic				Temkin		
	R^2	K	q_m (mg/g)	E (KJ/mol)	R^2	b_t (J/mol)	K_t (L/g)
$Cs_3Bi_2Br_9$	0.2476	-0.00135	16.38	19.2	0.3133	639.1	1.805
$Cs_3Bi_2Br_9/WS_2$	0.9786	-8.18E-4	16.15	24.7	0.9977	728.2	4.483

	Redlich-Peterson		
	R^2	K_R	β
$Cs_3Bi_2Br_9$	0.864	0.1854	0.6959
$Cs_3Bi_2Br_9/WS_2$	0.9947	0.1665	0.6917

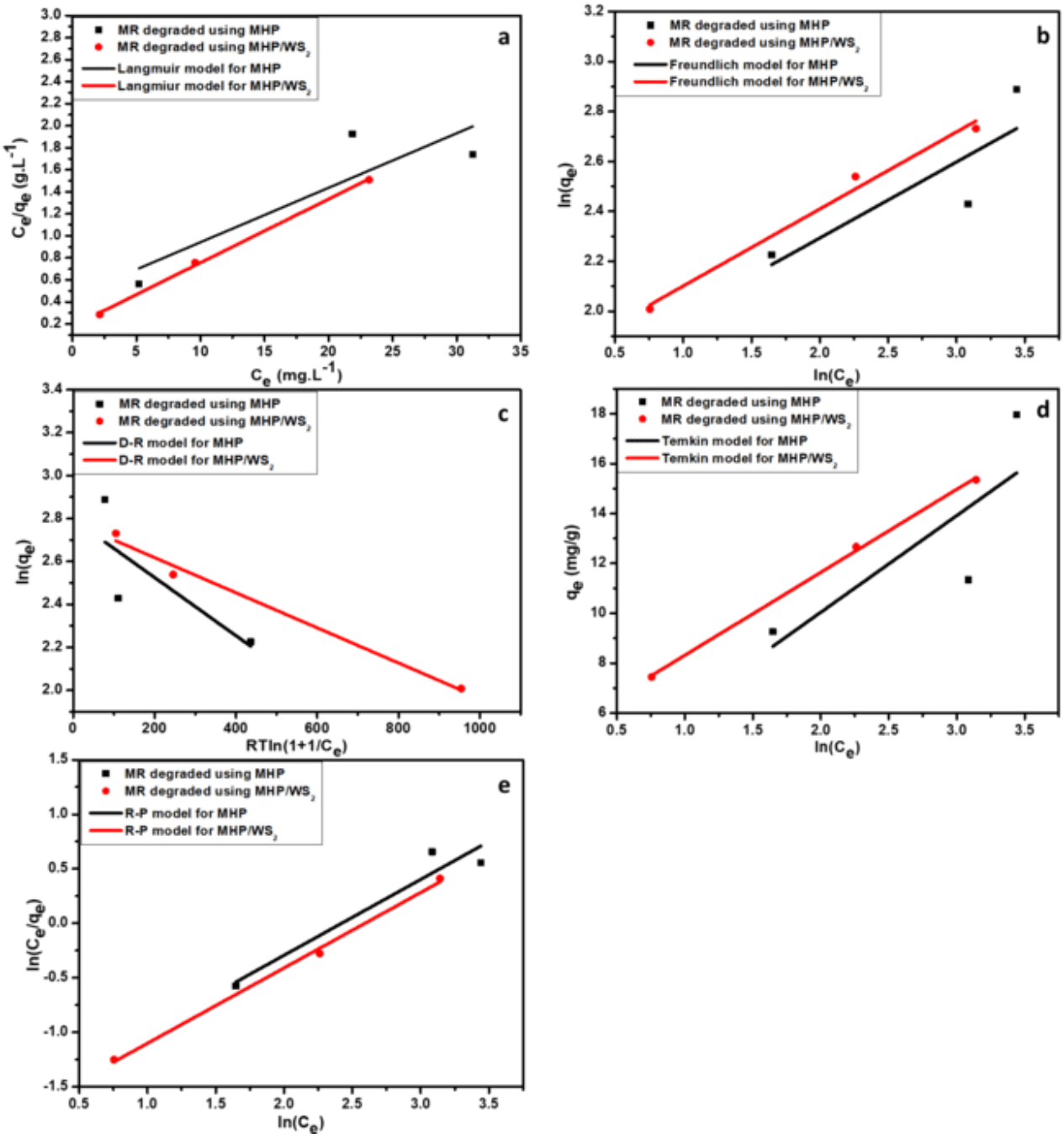

Figure 5.22: Adsorption isotherm models for MR degraded by $Cs_3Bi_2Br_9$ and $Cs_3Bi_2Br_9/WS_2$ **(a)** Langmuir isotherm, **(b)** Freundlich isotherm, **(c)** Dubinin-Radushevic isotherm, **(d)** Temkin isotherm, and **(e)** Redlich-Peterson isotherm linear fit

The best-fit model for $Cs_3Bi_2Br_9$ was the R-P model. The R-P parameter, β, was 0.4083 and the R-P isotherm constant, K_R, was 0.04589 L/g. For $Cs_3Bi_2Br_9/WS_2$ was the Langmuir model. The single layer adsorption capacity, Q_0, was 0.05377 mg/g, and the

adsorption process surface energy constant, b, was 9.963 L/mg. The Langmuir isotherm separation factor, R_L, was 0.001955 since $0<R_L<1$ which suggests that adsorption was favourable.

5.6.2. Rhodamine B adsorption isotherms

The results in **Table 5.14** indicate that the best-fit adsorption isotherm model for $Cs_3Bi_2Br_9$ was the R-P model. The R-P parameter, β, was 0.4083 and the R-P isotherm constant, K_R, was 0.04589 L/g. The best-fit model for $Cs_3Bi_2Br_9/WS_2$ is the Langmuir model. The single-layer adsorption capacity, Q_0, was 0.05377 mg/g, and the adsorption process surface energy constant, b, was 9.963 mg/g. The Langmuir isotherm separation factor, R_L, was 0.001955 and since $0< R_L<1$, it suggests that adsorption was favourable.

Table 5.14: Langmuir, Freundlich, Dubinin-Radushevic, Temkin, and Redlich-Peterson adsorption isotherm model constants and determination coefficients for RhB degradation by $Cs_3Bi_2Br_9$ and $Cs_3Bi_2Br_9/WS_2$

Isotherms	**Langmuir**				**Freundlich**		
Parameters	**R^2**	**R_L**	**Q_0 (mg/g)**	**b (L/mg)**	**R^2**	**K_f (mg/g)**	**n**
$Cs_3Bi_2Br_9$	0.6021	0.001673	0.09056	9.963	0.40239	21.79	0.62549
$Cs_3Bi_2Br_9/WS_2$	0.76873	0.001955	0.05377	8.523	-0.06078	13.88	0.52943
	Dubinin-Radushkevic				**Temkin**		
	R^2	**K**	**q_m (mg/g)**	**E (KJ/mol)**	**R^2**	**b_t (J/mol)**	**K_t (L/g)**
$Cs_3Bi_2Br_9$	0.59566	0.053	1.042E+21	3.071476	0.85534	2.860	122.9
$Cs_3Bi_2Br_9/WS_2$	-0.4259	7.998E-4	2.182	25.00313	-4.756E-4	1.981	551.3

	Redlich-Peterson		
	R^2	**K_R (L/g)**	**β**
$Cs_3Bi_2Br_9$	0.88129	0.045888	0.40831
$Cs_3Bi_2Br_9/WS_2$	0.75642	0.072068	0.573328

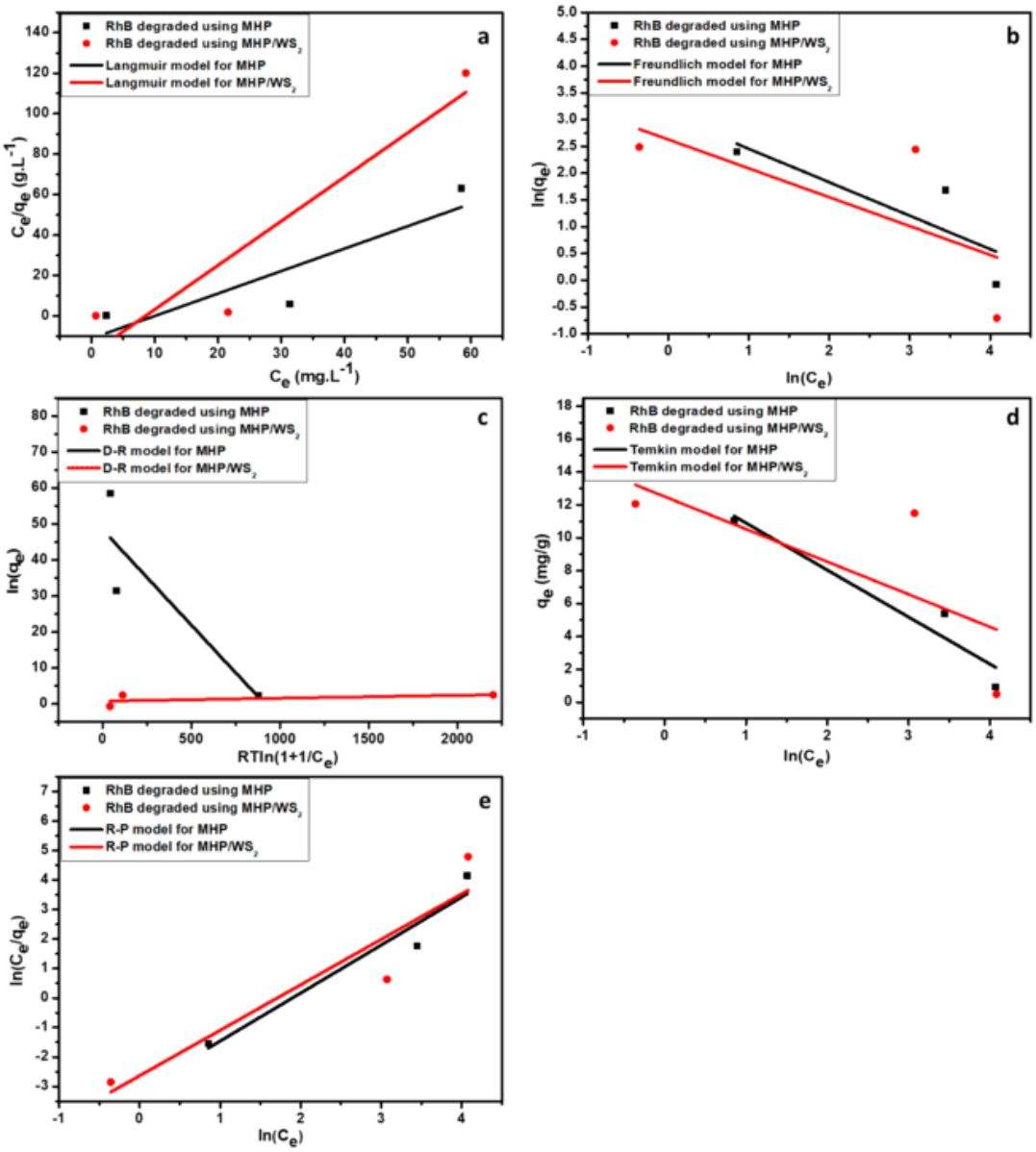

Figure 5.23: Adsorption isotherm models for RhB degraded by $Cs_3Bi_2Br_9$ and $Cs_3Bi_2Br_9/WS_2$ **(a)** Langmuir isotherm, **(b)** Freundlich isotherm, **(c)** Dubinin-Radushevic isotherm, **(d)** Temkin isotherm, and **(e)** Redlich-Peterson isotherm linear fit.

5.7. Conclusion:

In conclusion, the investigation demonstrated that direct photolysis alone exhibited minimal degradation efficiency (DE%) for Methyl Red (MR) and Rhodamine B (RhB), with values of 2.68% and 3.10%, respectively, after 2 hours of irradiation. However, the addition of UV/H_2O_2 significantly improved DE% to 40.59% for MR and 52.72% for RhB, showcasing enhanced degradation compared to direct photolysis.

Employing WS_2 as a catalyst, with specified conditions, further elevated DE% to 62.96% for MR and 62.22% for RhB. $Cs_3Bi_2Br_9$ displayed a DE% of 54.32% for MR and 70.28% for RhB under identical conditions, while the $Cs_3Bi_2Br_9/WS_2$ heterostructure yielded a remarkable DE% of 89.36% for MR and 96.51% for RhB.

Optimization studies revealed the optimum catalyst loading and dye concentration for enhanced degradation efficiency. The pH studies indicated varying optimal pH conditions for $Cs_3Bi_2Br_9$ and $Cs_3Bi_2Br_9/WS_2$, affecting the DE%. The addition of H_2O_2 to the heterogeneous reactions halved UV irradiation time, indicating improved DE% for both MR and RhB.

Post-degradation analysis revealed changes in the bandgap and structural integrity, with $Cs_3Bi_2Br_9/WS_2$ exhibiting greater stability. Agglomeration was observed in TEM images post-degradation, prompting potential recyclability studies in the future. The EDX and EDS mapping results showed that the elemental integrity remained intact.

COD removal efficiency varied between $Cs_3Bi_2Br_9$ and $Cs_3Bi_2Br_9/WS_2$, depending on the dye. Mass spectroscopy elucidated degradation pathways, while kinetics studies suggested different adsorption mechanisms for MR and RhB.

Adsorption isotherm models provided insights into adsorption behaviour, with $Cs_3Bi_2Br_9/WS_2$ displaying favourable adsorption characteristics according to the Langmuir model. Overall, the study underscores the efficacy of $Cs_3Bi_2Br_9/WS_2$ in the photocatalytic degradation of organic dyes, offering promising implications for environmental remediation applications.

References:

Abdel-Rahman, M.A. *et al.* (2020) 'One-factor-at-a-time and response surface statistical designs for improved lactic acid production from beet molasses by Enterococcus hirae ds10', *SN Applied Sciences*, 2(4), p. 573. Available at: https://doi.org/10.1007/s42452-020-2351-x.

Affat, S.. S. (2021) 'Classifications, Advantages, Disadvantages, Toxicity Effects of Natural and Synthetic Dyes: A review', *University of Thi-Qar Journal of Science*, 8(1).

Ajmal, A. *et al.* (2014) 'Principles and mechanisms of photocatalytic dye degradation on TiO $_2$ based photocatalysts: a comparative overview', *RSC Adv.*, 4(70), pp. 37003–37026. Available at: https://doi.org/10.1039/C4RA06658H.

Akinbami, O. *et al.* (2021) 'Lead-free Rudorffite-type Cs3Bi2Br9 nanoparticles for photocatalytic degradation of rhodamine B and methylene blue', *Journal of Photochemistry and Photobiology A: Chemistry*, 419, p. 113460. Available at: https://doi.org/10.1016/j.jphotochem.2021.113460.

Akpan, U.G. and Hameed, B.H. (2009) 'Parameters affecting the photocatalytic degradation of dyes using TiO2-based photocatalysts: A review', *Journal of Hazardous Materials*, 170(2–3), pp. 520–529. Available at: https://doi.org/10.1016/j.jhazmat.2009.05.039.

Akple, M.S. and Apevienyeku, H.K. (2018) 'Synthesis and density-functional-theory calculations of electronic band structure of hollow sphere WS $_2$', *Materials Science-Poland*, 36(3), pp. 409–418. Available at: https://doi.org/10.2478/msp-2018-0052.

Al-Buriahi, A.K. *et al.* (2022) 'Elimination of rhodamine B from textile wastewater using nanoparticle photocatalysts: A review for sustainable approaches', *Chemosphere*, 287, p. 132162. Available at: https://doi.org/10.1016/j.chemosphere.2021.132162.

Anisuzzaman, S.M. *et al.* (2022) 'Current Trends in the Utilization of Photolysis and Photocatalysis Treatment Processes for the Remediation of Dye Wastewater: A Short Review', *ChemEngineering*, 6(4), p. 58. Available at: https://doi.org/10.3390/chemengineering6040058.

Arslan, I., Balcioğlu, I.A. and Tuhkanen, T. (2000) 'Treatability of simulated reactive dye-bath wastewater by photochemical and non-photochemical advanced oxidation

processes', *Journal of Environmental Science and Health, Part A*, 35(5), pp. 775–793. Available at: https://doi.org/10.1080/10934520009377002.

Askeland, D.R. (2011) *The Science and Engineering of Materials*. Boston, MA: Springer US. Available at: https://doi.org/10.1007/978-1-4899-2895-5.

Ayawei, N., Ebelegi, A.N. and Wankasi, D. (2017) 'Modelling and Interpretation of Adsorption Isotherms', *Journal of Chemistry*, 2017, pp. 1–11. Available at: https://doi.org/10.1155/2017/3039817.

Bai, Z.-J. *et al.* (2023) 'Tuning photocatalytic performance of Cs3Bi2Br9 perovskite by g-C3N4 for C(sp3)—H bond activation', *Nano Research*, 16(5), pp. 6104–6112. Available at: https://doi.org/10.1007/s12274-022-4835-z.

Benkhaya, S., M'rabet, S. and El Harfi, A. (2020) 'Classifications, properties, recent synthesis and applications of azo dyes', *Heliyon*, 6(1), p. e03271. Available at: https://doi.org/10.1016/j.heliyon.2020.e03271.

Benvenuti, T. *et al.* (2018a) 'EVALUATION OF DIRECT PHOTOLYSIS, ELECTROOXIDATION AND PHOTOELECTROOXIDATION FOR RHODAMINE-B DEGRADATION', *Brazilian Journal of Chemical Engineering*, 35(3), pp. 957–968. Available at: https://doi.org/10.1590/0104-6632.20180353s20170032.

Benvenuti, T. *et al.* (2018b) 'EVALUATION OF DIRECT PHOTOLYSIS, ELECTROOXIDATION AND PHOTOELECTROOXIDATION FOR RHODAMINE-B DEGRADATION', *Brazilian Journal of Chemical Engineering*, 35(3), pp. 957–968. Available at: https://doi.org/10.1590/0104-6632.20180353s20170032.

Bhattacharya, A., Goyal, N. and Gupta, A. (2017) 'Degradation of azo dye methyl red by alkaliphilic, halotolerant Nesterenkonia lacusekhoensis EMLA3: application in alkaline and salt-rich dyeing effluent treatment', *Extremophiles*, 21(3), pp. 479–490. Available at: https://doi.org/10.1007/s00792-017-0918-2.

Bhattacharyya, S., Chaudhary, S.P. and Bhattacharjee, S. (2019) 'Lead-Free Metal Halide Perovskite Nanocrystals for Photocatalysis in Water', *ChemRxiv* [Preprint].

BM, V. and M, V. (2015a) 'Photocatalytic Degradation of Toxic Methyl Red Dye Using Silica Nanoparticles Synthesized from Rice Husk Ash', *Journal of Environmental &*

Analytical Toxicology, 05(06). Available at: https://doi.org/10.4172/2161-0525.1000336.

BM, V. and M, V. (2015b) 'Photocatalytic Degradation of Toxic Methyl Red Dye Using Silica Nanoparticles Synthesized from Rice Husk Ash', *Journal of Environmental & Analytical Toxicology*, 05(06). Available at: https://doi.org/10.4172/2161-0525.1000336.

Bresolin, B.M. (2021) *SYNTHESIS AND PERFORMANCE OF METALHALIDE PEROVSKITES AS NEW VISIBLE LIGHT PHOTOCATALYSTS*.

Bresolin, Bianca Maria (2021) *SYNTHESIS AND PERFORMANCE OF METAL-HALIDE PEROVSKITES AS NEW VISIBLE LIGHT PHOTOCATALYSTS*.

Bresolin, B.M., Hammouda, S. Ben and Sillanpää, M. (2019) 'Methylammonium iodo bismuthate perovskite (CH 3 NH 3) 3 Bi 2 I 9 as new effective visible light-responsive photocatalyst for degradation of environment pollutants', *Journal of Photochemistry and Photobiology A: Chemistry*, 376, pp. 116–126. Available at: https://doi.org/10.1016/j.jphotochem.2019.03.009.

Bresolin, B.-M., Park, Y. and Bahnemann, D. (2020) 'Recent Progresses on Metal Halide Perovskite-Based Material as Potential Photocatalyst', *Catalysts*, 10(6), p. 709. Available at: https://doi.org/10.3390/catal10060709.

Cao, S. *et al.* (2014) 'Synthesis and characterization of flower-like WS2 nanospheres via a facile hydrothermal route', *Journal of Materials Science: Materials in Electronics*, 25(10), pp. 4300–4305. Available at: https://doi.org/10.1007/s10854-014-2164-z.

Channei, D. *et al.* (2021) 'Synthesis and Characterization of WO_3 /CeO_2 Heterostructured Nanoparticles for Photodegradation of Indigo Carmine Dye', *ACS Omega*, 6(30), pp. 19771–19777. Available at: https://doi.org/10.1021/acsomega.1c02453.

Clogston, J.D. and Patri, A.K. (2011) 'Zeta Potential Measurement', in, pp. 63–70. Available at: https://doi.org/10.1007/978-1-60327-198-1_6.

Crini, G. (2006) 'Non-conventional low-cost adsorbents for dye removal: A review', *Bioresource Technology*, pp. 1061–1085. Available at: https://doi.org/10.1016/j.biortech.2005.05.001.

de Mello Donegá, C., Liljeroth, P. and Vanmaekelbergh, D. (2005) ‘Physicochemical Evaluation of the Hot-Injection Method, a Synthesis Route for Monodisperse Nanocrystals’, *Small*, 1(12), pp. 1152–1162. Available at: https://doi.org/10.1002/smll.200500239.

deQuilettes, D.W. *et al.* (2019) ‘Charge-Carrier Recombination in Halide Perovskites’, *Chemical Reviews*, 119(20), pp. 11007–11019. Available at: https://doi.org/10.1021/acs.chemrev.9b00169.

Devi, L.G., Raju, K.S.A. and Kumar, S.G. (2009) ‘Photodegradation of methyl red by advanced and homogeneous photo-Fenton’s processes: A comparative study and kinetic approach’, *Journal of Environmental Monitoring*, 11(7), pp. 1397–1404. Available at: https://doi.org/10.1039/b900936a.

Djurisic, A.B., Chen, X.Y. and Leung, Y.H. (2013) *UV-VIS and Photoluminescence Spectroscopy for Nanomaterials Characterization*. Edited by C. Kumar. Berlin, Heidelberg: Springer Berlin Heidelberg. Available at: https://doi.org/10.1007/978-3-642-27594-4.

Du, H. *et al.* (2022) ‘Adsorption of rhodamine B on polyvinyl chloride, polystyrene, and polyethylene terephthalate microplastics in aqueous environments’, *Environmental Technology and Innovation*, 27. Available at: https://doi.org/10.1016/j.eti.2022.102495.

Fadojutimi, P.O. *et al.* (2022) ‘Transition Metal Dichalcogenides [MX2] in Photocatalytic Water Splitting’, *Catalysts*, 12(5), p. 468. Available at: https://doi.org/10.3390/catal12050468.

Fang, Q. *et al.* (2018) ‘Ultrafast Charge Transfer in Perovskite Nanowire/2D Transition Metal Dichalcogenide Heterostructures’, *The Journal of Physical Chemistry Letters*, 9(7), pp. 1655–1662. Available at: https://doi.org/10.1021/acs.jpclett.8b00260.

Forgacs, E., Cserháti, T. and Oros, G. (2004) ‘Removal of synthetic dyes from wastewaters: a review’, *Environment International*, 30(7), pp. 953–971. Available at: https://doi.org/10.1016/j.envint.2004.02.001.

Gao, G. *et al.* (2017) ‘Novel inorganic perovskite quantum dots for photocatalysis’, *Nanoscale*, 9(33), pp. 12032–12038. Available at: https://doi.org/10.1039/C7NR04421F.

Gao, M. *et al.* (2019) ‘Controlled synthesis and photostability of blue emitting Cs 3 Bi 2 Br 9 perovskite nanocrystals by employing weak polar solvents at room temperature’, *Journal of Materials Chemistry C*, 7(12), pp. 3688–3695. Available at: https://doi.org/10.1039/C9TC00400A.

Georgiou, D. *et al.* (2002) ‘Degradation of azo-reactive dyes by ultraviolet radiation in the presence of hydrogen peroxide’, *Dyes and Pigments*, 52(2), pp. 69–78. Available at: https://doi.org/10.1016/S0143-7208(01)00078-X.

Ghaly, M.Y., Farah, J.Y. and Fathy, A.M. (2007) ‘Enhancement of decolorization rate and COD removal from dyes containing wastewater by the addition of hydrogen peroxide under solar photocatalytic oxidation’, *Desalination*, 217(1–3), pp. 74–84. Available at: https://doi.org/10.1016/j.desal.2007.01.013.

Gqoba, S.S. *et al.* (2021) ‘Hierarchical Nanoflowers of Colloidal WS2 and Their Potential Gas Sensing Properties for Room Temperature Detection of Ammonia’, *Processes*, 9(9), p. 1491. Available at: https://doi.org/10.3390/pr9091491.

Gu, Y. *et al.* (2023) ‘Nitrogen-Doped Graphene Quantum Dot-Passivated δ-Phase CsPbI3: A Water-Stable Photocatalytic Adjuvant to Degrade Rhodamine B’, *Molecules*, 28(21). Available at: https://doi.org/10.3390/molecules28217310.

Gumerov, F.M. *et al.* (2014) ‘Regeneration of the Catalysts by Supercritical Fluid Extraction’, *International Journal of Analytical Mass Spectrometry and Chromatography*, 02(01), pp. 1–14. Available at: https://doi.org/10.4236/ijamsc.2014.21001.

Harun, N. *et al.* (no date) *IMPACT OF TiO 2 AND H 2 O 2 ON PHOTOCATALYTIC DEGRADATION OF PHODAMINE B UNDER ULTRAVIOLET C (UV-C) RADIATION FOR EFFICIENT POLLUTED WASTEWATER TREATMENT*, *Journal of Optoelectronic and Biomedical Materials*. Kuala Nerus.

Hoffmann, M.R. *et al.* (1995) ‘Environmental Applications of Semiconductor Photocatalysis’, *Chemical Reviews*, 95(1), pp. 69–96. Available at: https://doi.org/10.1021/cr00033a004.

Hu, Y. *et al.* (2018) ‘Toward Exploring the Structure of Monolayer to Few-layer TaS2 by Efficient Ultrasound-free Exfoliation’, *Nanoscale Research Letters*, 13(1), p. 20. Available at: https://doi.org/10.1186/s11671-018-2439-z.

Huang, T. *et al.* (2019) ‘Transition Metal Dichalcogenides in Photocatalysts’, in *Two Dimensional Transition Metal Dichalcogenides*. Singapore: Springer Singapore, pp. 107–134. Available at: https://doi.org/10.1007/978-981-13-9045-6_4.

Huang, Y.-J. *et al.* (2022) ‘Improved Mass-Transfer Enhances Photo-Driven Dye Degradation and H $_2$ Evolution over a Few-Layer WS $_2$ /ZnO Heterostructure’, *ACS Omega*, 7(2), pp. 2217–2223. Available at: https://doi.org/10.1021/acsomega.1c05756.

Hussain Chowdhury, M.S. *et al.* (2022) ‘Decomposition of Hydrogen Peroxide using Chemical and Catalytic Methods: A Reactor-based Approach’, *Asian Journal of Chemistry*, 34(5), pp. 1263–1268. Available at: https://doi.org/10.14233/ajchem.2022.23729.

Hussain, T. and Wahab, A. (2018) ‘A critical review of the current water conservation practices in textile wet processing’, *Journal of Cleaner Production*, 198, pp. 806–819. Available at: https://doi.org/10.1016/j.jclepro.2018.07.051.

Huynh, K.A. *et al.* (2020) ‘Halide perovskite photocatalysis: progress and perspectives’, *Journal of Chemical Technology & Biotechnology*, 95(10), pp. 2579–2596. Available at: https://doi.org/10.1002/jctb.6342.

Ibrahim Abubakar, S., Adamu Ibrahim, M. and Bashir Ibrahim, M. (2020) ‘Adsorption of Methyl Orange Dye onto Raw Maize Cob and Maize Cob Activated Carbon: Isotherms and Thermodynamic Studies’, *International Journal of Advanced Chemistry*, 8(1), p. 147. Available at: https://doi.org/10.14419/ijac.v8i1.30676.

Ikram, M. *et al.* (2022) ‘Biodegradation of Azo Dye Methyl Red by Pseudomonas aeruginosa: Optimization of Process Conditions’, *International Journal of Environmental Research and Public Health*, 19(16), p. 9962. Available at: https://doi.org/10.3390/ijerph19169962.

Immanuel, P.N. *et al.* (2022) ‘Enhanced photocatalytic activity of Cs4PbBr6/WS2 hybrid nanocomposite’, *ChemRxiv* [Preprint].

Islam, J. and Hossain, A.K.M.A. (2020a) ‘Narrowing band gap and enhanced visible-light absorption of metal-doped non-toxic CsSnCl $_3$ metal halides for potential optoelectronic applications’, *RSC Advances*, 10(13), pp. 7817–7827. Available at: https://doi.org/10.1039/C9RA10407K.

Islam, J. and Hossain, A.K.M.A. (2020b) ‘Narrowing band gap and enhanced visible-light absorption of metal-doped non-toxic CsSnCl $_3$ metal halides for potential optoelectronic applications’, *RSC Advances*, 10(13), pp. 7817–7827. Available at: https://doi.org/10.1039/C9RA10407K.

Jacopo Prisco (2017) *The color purple: How an accidental discovery changed fashion forever*, *CNN*.

Jain, S.K. and Singh, V.P. (2003) ‘Water Quality Modeling’, in, pp. 743–786. Available at: https://doi.org/10.1016/S0167-5648(03)80067-9.

Jiang, J. *et al.* (2020) ‘Ultrasonication-assisted trace amount solvent synthesis of Cs4PbBr6 crystal with ultra-bright green light emission’, *APL Materials*, 8(7). Available at: https://doi.org/10.1063/5.0009852.

Jimenez-Calvo, P.I. (2019) *Synthesis, characterization, and performance of g-C3N4 based materials decorated with Au nanoparticles for (photo) catalytic applications* .

Jo, Y.K. *et al.* (2019) ‘2D inorganic nanosheet-based hybrid photocatalysts: Design, applications, and perspectives’, *Journal of Photochemistry and Photobiology C: Photochemistry Reviews*, 40, pp. 150–190. Available at: https://doi.org/10.1016/j.jphotochemrev.2018.03.002.

Joseph, A. and Aneesh, P.M. (2022) ‘Efficient degradation of methylene blue: A comparative study using hydrothermally synthesised SnS2, WS2 and VS2 nanostructures’, *Materials Research Bulletin*, 146, p. 111623. Available at: https://doi.org/10.1016/j.materresbull.2021.111623.

Kalam, S. *et al.* (2021) ‘Surfactant Adsorption Isotherms: A Review’, *ACS Omega*, 6(48), pp. 32342–32348. Available at: https://doi.org/10.1021/acsomega.1c04661.

Kanhere, P. and Chen, Z. (2014) ‘A Review on Visible Light Active Perovskite-Based Photocatalysts’, *Molecules*, 19(12), pp. 19995–20022. Available at: https://doi.org/10.3390/molecules191219995.

Kant, R. (2012) ‘Textile dyeing industry an environmental hazard’, *Natural Science*, 04(01), pp. 22–26. Available at: https://doi.org/10.4236/ns.2012.41004.

Katheresan, V., Kansedo, J. and Lau, S.Y. (2018) ‘Efficiency of various recent wastewater dye removal methods: A review’, *Journal of Environmental Chemical Engineering*, 6(4), pp. 4676–4697. Available at: https://doi.org/10.1016/j.jece.2018.06.060.

Khan, A., Malik, S. and Bilal, M. (2022) *Nano-Bioremediation : Fundamentals and Applications*. Edited by H.M.N. Iqbal, M. Bilal, and T.A. Nguyen. Elsevier. Available at: https://doi.org/10.1016/C2020-0-00522-0.

Khan, S. and Ali, J. (2018) ‘Chemical analysis of air and water’, in *Bioassays*. Elsevier, pp. 21–39. Available at: https://doi.org/10.1016/B978-0-12-811861-0.00002-4.

Koe, W.S. *et al.* (2020) ‘An overview of photocatalytic degradation: photocatalysts, mechanisms, and development of photocatalytic membrane’, *Environmental Science and Pollution Research*. Springer, pp. 2522–2565. Available at: https://doi.org/10.1007/s11356-019-07193-5.

Kozuch, S. and Martin, J.M.L. (2012) ‘“Turning Over” Definitions in Catalytic Cycles’, *ACS Catalysis*, 2(12), pp. 2787–2794. Available at: https://doi.org/10.1021/cs3005264.

Kumar, S. *et al.* (2014) ‘Nanotechnology-Based Water Treatment Strategies’, *Journal of Nanoscience and Nanotechnology*, 14(2), pp. 1838–1858. Available at: https://doi.org/10.1166/jnn.2014.9050.

Kumar, S. *et al.* (2020) ‘Nanoscale zinc oxide based heterojunctions as visible light active photocatalysts for hydrogen energy and environmental remediation’, *Catalysis Reviews*, 62(3), pp. 346–405. Available at: https://doi.org/10.1080/01614940.2019.1684649.

Kumari, H. *et al.* (2023) ‘A Review on Photocatalysis Used For Wastewater Treatment: Dye Degradation’, *Water, Air, & Soil Pollution*, 234(6), p. 349. Available at: https://doi.org/10.1007/s11270-023-06359-9.

Kundu, A. and Mondal, A. (2019) ‘Kinetics, isotherm, and thermodynamic studies of methylene blue selective adsorption and photocatalysis of malachite green from

aqueous solution using layered Na-intercalated Cu-doped Titania', *Applied Clay Science*, 183, p. 105323. Available at: https://doi.org/10.1016/j.clay.2019.105323.

Kusrini, E. *et al.* (2018) 'Textile Dye Removal from Aqueous Solution using Modified Graphite Waste/Lanthanum/Chitosan Composite', *IOP Conference Series: Materials Science and Engineering*, 316, p. 012029. Available at: https://doi.org/10.1088/1757-899X/316/1/012029.

Kwon, S.G. and Hyeon, T. (2011) 'Formation Mechanisms of Uniform Nanocrystals via Hot-Injection and Heat-Up Methods', *Small*, 7(19), pp. 2685–2702. Available at: https://doi.org/10.1002/smll.201002022.

Lee, J.S. and Jang, J. (2014) 'Hetero-structured semiconductor nanomaterials for photocatalytic applications', *Journal of Industrial and Engineering Chemistry*, 20(2), pp. 363–371. Available at: https://doi.org/10.1016/j.jiec.2013.11.050.

Lellis, B. *et al.* (2019a) 'Effects of textile dyes on health and the environment and bioremediation potential of living organisms', *Biotechnology Research and Innovation*, 3(2), pp. 275–290. Available at: https://doi.org/10.1016/j.biori.2019.09.001.

Lellis, B. *et al.* (2019b) 'Effects of textile dyes on health and the environment and bioremediation potential of living organisms', *Biotechnology Research and Innovation*, 3(2), pp. 275–290. Available at: https://doi.org/10.1016/j.biori.2019.09.001.

Li, D. and Liu, S. (2019) 'Water Quality Detection for Lakes', in *Water Quality Monitoring and Management*. Elsevier, pp. 221–231. Available at: https://doi.org/10.1016/B978-0-12-811330-1.00008-9.

Li, G. *et al.* (2010) 'Effect of the agglomeration of TiO2 nanoparticles on their photocatalytic performance in the aqueous phase', *Journal of Colloid and Interface Science*, 348(2), pp. 342–347. Available at: https://doi.org/10.1016/j.jcis.2010.04.045.

Li, Q. *et al.* (2021) 'Boosting Photocatalytic Activity and Stability of Lead-Free Cs3Bi2Br9Perovskite Nanocrystals via in Situ Growth on Monolayer 2D Ti3C2T xMXene for C-H Bond Oxidation', *ACS Applied Materials and Interfaces*, 13(23), pp. 27323–27333. Available at: https://doi.org/10.1021/acsami.1c06367.

Li, W. and Wu, H. (2017) ‘Sodium citrate functionalized reusable Fe3O4@TiO2 photocatalyst for water purification’, *Chemical Physics Letters*, 686, pp. 178–182. Available at: https://doi.org/10.1016/j.cplett.2017.08.046.

Liu, L. *et al.* (2015) ‘Simultaneous removal of cationic and anionic dyes from environmental water using montmorillonite-pillared graphene oxide’, *Journal of Chemical and Engineering Data*, 60(5), pp. 1270–1278. Available at: https://doi.org/10.1021/je5009312.

Liu, L. *et al.* (2019) ‘Application of Nanotechnology in the Removal of Heavy Metal From Water’, in *Nanomaterials for the Removal of Pollutants and Resource Reutilization*. Elsevier, pp. 83–147. Available at: https://doi.org/10.1016/B978-0-12-814837-2.00004-4.

Lu, C. *et al.* (2019) ‘Cesium Oleate Precursor Preparation for Lead Halide Perovskite Nanocrystal Synthesis: The Influence of Excess Oleic Acid on Achieving Solubility, Conversion, and Reproducibility’, *Chemistry of Materials*, 31(1), pp. 62–67. Available at: https://doi.org/10.1021/acs.chemmater.8b04876.

Mahdi, M.H., Mohammed, T.J. and Al-Najar, J.A. (2021) ‘Advanced Oxidation Processes (AOPs) for treatment of antibiotics in wastewater: A review’, *IOP Conference Series: Earth and Environmental Science*, 779(1), p. 012109. Available at: https://doi.org/10.1088/1755-1315/779/1/012109.

Marshall, J.L. (1991) ‘Scanning Electron Microscopy and Energy Dispersive X-ray (SEM/EDX) Characterization of Solder Solderability and Reliability’, in *Solder Joint Reliability*. Boston, MA: Springer US, pp. 173–224. Available at: https://doi.org/10.1007/978-1-4615-3910-0_6.

Martínez-Huitle, C.A. and Brillas, E. (2009) ‘Decontamination of wastewaters containing synthetic organic dyes by electrochemical methods: A general review’, *Applied Catalysis B: Environmental*, 87(3–4), pp. 105–145. Available at: https://doi.org/10.1016/j.apcatb.2008.09.017.

Meerbach, C. *et al.* (2020a) ‘General Colloidal Synthesis of Transition-Metal Disulfide Nanomaterials as Electrocatalysts for Hydrogen Evolution Reaction’, *ACS Applied Materials & Interfaces*, 12(11), pp. 13148–13155. Available at: https://doi.org/10.1021/acsami.9b21607.

Meerbach, C. *et al.* (2020b) ‘General Colloidal Synthesis of Transition-Metal Disulfide Nanomaterials as Electrocatalysts for Hydrogen Evolution Reaction’, *ACS Applied Materials & Interfaces*, 12(11), pp. 13148–13155. Available at: https://doi.org/10.1021/acsami.9b21607.

Miller, M.D. *et al.* (2022) ‘Potential impacts of synthetic food dyes on activity and attention in children: a review of the human and animal evidence’, *Environmental Health*, 21(1), p. 45. Available at: https://doi.org/10.1186/s12940-022-00849-9.

Milošević, M. *et al.* (2023) ‘Advanced photocatalysis mediated by TiO2/Ag/TiO2 nanoparticles modified cotton fabric’, *Cellulose*, 30(7), pp. 4749–4771. Available at: https://doi.org/10.1007/s10570-023-05165-0.

Mokif, L.A. (2019) ‘Removal Methods of Synthetic Dyes from Industrial Wastewater: A review’, *Mesopo. Environ. J*, 5(1), pp. 23–40. Available at: https://doi.org/10.31759/mej.2019.5.1.0040.

Moosavi, S. *et al.* (2020) ‘Methylene Blue Dye Photocatalytic Degradation over Synthesised Fe3O4/AC/TiO2 Nano-Catalyst: Degradation and Reusability Studies’, *Nanomaterials*, 10(12), p. 2360. Available at: https://doi.org/10.3390/nano10122360.

Musah, M. *et al.* (2022a) ‘Adsorption Kinetics and Isotherm Models: A Review’, *Caliphate Journal of Science and Technology*, 4(1), pp. 20–26. Available at: https://doi.org/10.4314/cajost.v4i1.3.

Musah, M. *et al.* (2022b) ‘Adsorption Kinetics and Isotherm Models: A Review’, *Caliphate Journal of Science and Technology*, 4(1), pp. 20–26. Available at: https://doi.org/10.4314/cajost.v4i1.3.

Muthuraman, G. and Teng, T.T. (2009) ‘Extraction of methyl red from industrial wastewater using xylene as an extractant’, *Progress in Natural Science*, 19(10), pp. 1215–1220. Available at: https://doi.org/10.1016/j.pnsc.2009.04.002.

Nagaraja, R. *et al.* (2012a) ‘Photocatalytic degradation of Rhodamine B dye under UV/solar light using ZnO nanopowder synthesized by solution combustion route’, *Powder Technology*, 215–216, pp. 91–97. Available at: https://doi.org/10.1016/j.powtec.2011.09.014.

Nagaraja, R. *et al.* (2012b) ‘Photocatalytic degradation of Rhodamine B dye under UV/solar light using ZnO nanopowder synthesized by solution combustion route’, *Powder Technology*, 215–216, pp. 91–97. Available at: https://doi.org/10.1016/j.powtec.2011.09.014.

Natarajan, T.S. *et al.* (2011) ‘Study on UV-LED/TiO2 process for degradation of Rhodamine B dye’, *Chemical Engineering Journal*, 169(1–3), pp. 126–134. Available at: https://doi.org/10.1016/j.cej.2011.02.066.

Ndala, Z. *et al.* (2020) ‘Evaluating the Effect of Varying the Metal Precursor in the Colloidal Synthesis of MoSe2 Nanomaterials and Their Application as Electrodes in the Hydrogen Evolution Reaction’, *Nanomaterials*, 10(9), p. 1786. Available at: https://doi.org/10.3390/nano10091786.

Nidheesh, P.V., Gandhimathi, R. and Ramesh, S.T. (2013) ‘Degradation of dyes from aqueous solution by Fenton processes: a review’, *Environmental Science and Pollution Research*, 20(4), pp. 2099–2132. Available at: https://doi.org/10.1007/s11356-012-1385-z.

Nidheesh, P.V., Zhou, M. and Oturan, M.A. (2018) ‘An overview on the removal of synthetic dyes from water by electrochemical advanced oxidation processes’, *Chemosphere*, 197, pp. 210–227. Available at: https://doi.org/10.1016/j.chemosphere.2017.12.195.

Olatunji, O.O. *et al.* (2018) ‘Thermo-gravimetric characterization of biomass properties: A review’, *IOP Conference Series: Materials Science and Engineering*, 423, p. 012175. Available at: https://doi.org/10.1088/1757-899X/423/1/012175.

Palchoudhury, S., Baalousha, M. and Lead, J.R. (2015) ‘Methods for Measuring Concentration (Mass, Surface Area and Number) of Nanomaterials’, in, pp. 153–181. Available at: https://doi.org/10.1016/B978-0-08-099948-7.00005-1.

Pang, Y. *et al.* (2019) ‘Photocatalysts: Colloidal Single-Layer Photocatalysts for Methanol-Storable Solar H 2 Fuel (Adv. Mater. 49/2019)’, *Advanced Materials*, 31(49), p. 1970348. Available at: https://doi.org/10.1002/adma.201970348.

Patel, B. and Shah, K. (2014) *Research review on Biodegradation of Azo Dye compounds*. Available at: https://ssrn.com/abstract=2474466.

Piaskowski, K., Świderska-Dąbrowska, R. and Zarzycki, P.K. (2018) ‘Dye removal from water and wastewater using various physical, chemical, and biological processes’, *Journal of AOAC International*, 101(5), pp. 1371–1384. Available at: https://doi.org/10.5740/jaoacint.18-0051.

Piccin, J.S., Dotto, G.L. and Pinto, L.A.A. (2011) ‘Adsorption isotherms and thermochemical data of FD&C Red n° 40 binding by Chitosan’, *Brazilian Journal of Chemical Engineering*, 28(2), pp. 295–304. Available at: https://doi.org/10.1590/S0104-66322011000200014.

Quevedo, A.C. *et al.* (2021) ‘UV-Vis Spectroscopic Characterization of Nanomaterials in Aqueous Media’, *Journal of Visualized Experiments* [Preprint], (176). Available at: https://doi.org/10.3791/61764.

Rafiq, A. *et al.* (2021a) ‘Photocatalytic degradation of dyes using semiconductor photocatalysts to clean industrial water pollution’, *Journal of Industrial and Engineering Chemistry*, 97, pp. 111–128. Available at: https://doi.org/10.1016/j.jiec.2021.02.017.

Rafiq, A. *et al.* (2021b) ‘Photocatalytic degradation of dyes using semiconductor photocatalysts to clean industrial water pollution’, *Journal of Industrial and Engineering Chemistry*, 97, pp. 111–128. Available at: https://doi.org/10.1016/j.jiec.2021.02.017.

Rand Water (no date) *Water Wise - Water Situation in South Africa*. Available at: https://waterwise.co.za/site/water/environment/situation.html (Accessed: 18 March 2023).

Rani, S. *et al.* (2016) ‘Removal of methylene blue and rhodamine B from water by zirconium oxide/graphene’, *Water Science*, 30(1), pp. 51–60. Available at: https://doi.org/10.1016/j.wsj.2016.04.001.

Rengaraj, S. *et al.* (2007) ‘Adsorption characteristics of Cu(II) onto ion exchange resins 252H and 1500H: Kinetics, isotherms and error analysis’, *Journal of Hazardous Materials*, 143(1–2), pp. 469–477. Available at: https://doi.org/10.1016/j.jhazmat.2006.09.064.

Reyes-Pérez, F. *et al.* (2018) ‘Visible-Light-Enhanced Photocatalytic Activity of Totally Inorganic Halide-Based Perovskite’, *ChemistrySelect*, 3(36), pp. 10226–10235. Available at: https://doi.org/10.1002/slct.201801564.

Reza, K.M., Kurny, A. and Gulshan, F. (2017) 'Parameters affecting the photocatalytic degradation of dyes using TiO2: a review', *Applied Water Science*, 7(4), pp. 1569–1578. Available at: https://doi.org/10.1007/s13201-015-0367-y.

Ridjal, A.T.M. *et al.* (2022) 'Study of Rhodamine B Dyes Content in Snacks of Karuwisi Traditional Market Makassar, South Sulawesi, Indonesia', *IOP Conference Series: Earth and Environmental Science*, 1027(1), p. 012012. Available at: https://doi.org/10.1088/1755-1315/1027/1/012012.

Robinson, T. *et al.* (2001) 'Remediation of dyes in textile effluent: a critical review on current treatment technologies with a proposed alternative', *Bioresource Technology*, 77(3), pp. 247–255. Available at: https://doi.org/10.1016/S0960-8524(00)00080-8.

Rothenberg, G. (2017) *Catalysis concepts and green applications*. Weinheim Wiley-Vch Verlag Gmbh & Co.

Sahraie, N.R. *et al.* (2015) 'Quantifying the density and utilization of active sites in non-precious metal oxygen electroreduction catalysts', *Nature Communications*, 6(1), p. 8618. Available at: https://doi.org/10.1038/ncomms9618.

Sahu, S. and Samanta, P.K. (2021a) 'Peak Profile Analysis of X-ray Diffraction Pattern of Zinc Oxide Nanostructure', *Journal of Nano- and Electronic Physics*, 13(5), pp. 05001-1-05001–4. Available at: https://doi.org/10.21272/jnep.13(5).05001.

Sahu, S. and Samanta, P.K. (2021b) 'Peak Profile Analysis of X-ray Diffraction Pattern of Zinc Oxide Nanostructure', *Journal of Nano- and Electronic Physics*, 13(5), pp. 05001-1-05001–4. Available at: https://doi.org/10.21272/jnep.13(5).05001.

Saka, H. (2003) 'Transmission Electron Microscopy', in *Carbon Alloys*. Elsevier, pp. 223–238. Available at: https://doi.org/10.1016/B978-008044163-4/50014-0.

Sarabandi, K., Gharehbeglou, P. and Jafari, S.M. (2020) 'Scanning electron microscopy (SEM) of nanoencapsulated food ingredients', in *Characterization of Nanoencapsulated Food Ingredients*. Elsevier, pp. 83–130. Available at: https://doi.org/10.1016/B978-0-12-815667-4.00003-1.

Saravanan, R., Gracia, F. and Stephen, A. (2017) 'Basic Principles, Mechanism, and Challenges of Photocatalysis', in, pp. 19–40. Available at: https://doi.org/10.1007/978-3-319-62446-4_2.

Shah, K. (2014) *Biodegradation of azo dye compounds IRJBB Biodegradation of azo dye compounds*. Available at: https://www.researchgate.net/publication/267623559.

Shaheen, A. (2010) *Band Structure and Electrical Conductivity in Semiconductors*. Available at: https://www.researchgate.net/publication/280092391_Band_Structure_and_Electrical_Conductivity_in_Semiconductors.

Shakir, K. *et al.* (2010) 'Removal of rhodamine B (a basic dye) and thoron (an acidic dye) from dilute aqueous solutions and wastewater simulants by ion flotation', *Water Research*, 44(5), pp. 1449–1461. Available at: https://doi.org/10.1016/j.watres.2009.10.029.

Shamsi, J. *et al.* (2019) 'Metal Halide Perovskite Nanocrystals: Synthesis, Post-Synthesis Modifications, and Their Optical Properties', *Chemical Reviews*, 119(5), pp. 3296–3348. Available at: https://doi.org/10.1021/acs.chemrev.8b00644.

Shand, M.A. and Jin, F. (2020) 'Introduction – Characterization of MgO', in *Magnesia Cements*. Elsevier, pp. 1–10. Available at: https://doi.org/10.1016/B978-0-12-391925-0.00006-6.

Sharma, J., Sharma, S. and Soni, V. (2021) 'Classification and impact of synthetic textile dyes on Aquatic Flora: A review', *Regional Studies in Marine Science*. Elsevier B.V. Available at: https://doi.org/10.1016/j.rsma.2021.101802.

Sharma, P. *et al.* (2022) 'Impact of pharmaceuticals and antibiotics waste on the river ecosystem: a growing threat', in *Ecological Significance of River Ecosystems*. Elsevier, pp. 15–36. Available at: https://doi.org/10.1016/B978-0-323-85045-2.00015-7.

Sing, K.S.W. (1985) 'Reporting physisorption data for gas/solid systems with special reference to the determination of surface area and porosity (Recommendations 1984)', *Pure and Applied Chemistry*, 57(4), pp. 603–619. Available at: https://doi.org/10.1351/pac198557040603.

Singh, D. and Ahuja, R. (2022) 'Two-Dimensional Perovskite/HfS_2 van der Waals Heterostructure as an Absorber Material for Photovoltaic Applications', *ACS Applied Energy Materials*, 5(2), pp. 2300–2307. Available at: https://doi.org/10.1021/acsaem.1c03796.

Singh, K. and Arora, S. (2011) ‘Removal of synthetic textile dyes from wastewaters: A critical review on present treatment technologies’, *Critical Reviews in Environmental Science and Technology*, 41(9), pp. 807–878. Available at: https://doi.org/10.1080/10643380903218376.

Song, W. *et al.* (2021) ‘Novel BiOBr by compositing low-cost biochar for efficient ciprofloxacin removal: the synergy of adsorption and photocatalysis on the degradation kinetics and mechanism insight’, *RSC Advances*, 11(25), pp. 15369–15379. Available at: https://doi.org/10.1039/D1RA00941A.

Speight, J.G. (2017) ‘Chemical Transformations in the Environment’, in *Environmental Organic Chemistry for Engineers*. Elsevier, pp. 305–353. Available at: https://doi.org/10.1016/B978-0-12-804492-6.00007-1.

Subramani, A.K. *et al.* (2007) ‘Photocatalytic degradation of indigo carmine dye using TiO2 impregnated activated carbon’, *Bulletin of Materials Science*, 30(1), pp. 37–41. Available at: https://doi.org/10.1007/s12034-007-0007-8.

Sun, J. (2014) *Development of Inorganic-Organic Hybrid Materials for Waste Water Treatment*. Available at: https://www.researchgate.net/publication/314081363_Development_of_Inorganic-Organic_Hybrid_Materials_for_Waste_Water_Treatment (Accessed: 23 March 2023).

Sun, J. *et al.* (2021) ‘Highly stable halide perovskite with Na incorporation for efficient photocatalytic degradation of organic dyes in water solution’, *Environmental Science and Pollution Research*, 28(36), pp. 50813–50824. Available at: https://doi.org/10.1007/s11356-021-14188-8.

Tilvi, S., Majik, M.S. and Singh, K.S. (2014) ‘Mass Spectrometry for Determination of Bioactive Compounds’, in, pp. 193–218. Available at: https://doi.org/10.1016/B978-0-444-63359-0.00008-2.

Tkaczyk, A., Mitrowska, K. and Posyniak, A. (2020) ‘Synthetic organic dyes as contaminants of the aquatic environment and their implications for ecosystems: A review’, *Science of the Total Environment*. Elsevier B.V. Available at: https://doi.org/10.1016/j.scitotenv.2020.137222.

V., L.P. and Rajagopalan, V. (2016) ‘A New Synergetic Nanocomposite for Dye Degradation in Dark and Light’, *Scientific Reports*, 6(1), p. 38606. Available at: https://doi.org/10.1038/srep38606.

Vattikuti, S.V.P. *et al.* (2019) ‘Binder-free WS2/ZrO2 hybrid as a photocatalyst for organic pollutant degradation under UV/simulated sunlight and tests for H2 evolution’, *Journal of Alloys and Compounds*, 809, p. 151805. Available at: https://doi.org/10.1016/j.jallcom.2019.151805.

Velusamy, S. *et al.* (2021) ‘A Review on Heavy Metal Ions and Containing Dyes Removal Through Graphene Oxide-Based Adsorption Strategies for Textile Wastewater Treatment’, *Chemical Record*. John Wiley and Sons Inc, pp. 1570–1610. Available at: https://doi.org/10.1002/tcr.202000153.

Wang, J. *et al.* (2021) ‘Recent advances in metal halide perovskite photocatalysts: Properties, synthesis and applications’, *Journal of Energy Chemistry*. Elsevier B.V., pp. 770–785. Available at: https://doi.org/10.1016/j.jechem.2020.06.024.

Wang, X. *et al.* (2016) ‘MO degradation by Ag–Ag2O/g-C3N4 composites under visible-light irradiation’, *SpringerPlus*, 5(1), p. 369. Available at: https://doi.org/10.1186/s40064-016-1805-5.

Weng, B. *et al.* (2019) ‘Photocorrosion Inhibition of Semiconductor-Based Photocatalysts: Basic Principle, Current Development, and Future Perspective’, *ACS Catalysis*, 9(5), pp. 4642–4687. Available at: https://doi.org/10.1021/acscatal.9b00313.

Wong, C.C. and Chu, W. (2003) ‘The direct photolysis and photocatalytic degradation of alachlor at different TiO2 and UV sources’, *Chemosphere*, 50(8), pp. 981–987. Available at: https://doi.org/10.1016/S0045-6535(02)00640-9.

World Health Organization (WHO) (2022) *Drinking-water*. Available at: https://www.who.int/news-room/fact-sheets/detail/drinking-water (Accessed: 18 March 2023).

World Health Organization (WHO) and United Nations Children’s Fund (UNICEF) (2021) *Progress on household drinking water, sanitation and hygiene 2000-2020: five*

years into the SDGs. Available at: https://washdata.org/sites/default/files/2021-07/jmp-2021-wash-households.pdf (Accessed: 18 March 2023).

Xu, C. *et al.* (2019) 'Nanostructured materials for photocatalysis', *Chemical Society Reviews*, 48(14), pp. 3868–3902. Available at: https://doi.org/10.1039/C9CS00102F.

Yang, B. *et al.* (2017a) 'Lead-Free, Air-Stable All-Inorganic Cesium Bismuth Halide Perovskite Nanocrystals', *Angewandte Chemie*, 129(41), pp. 12645–12649. Available at: https://doi.org/10.1002/ange.201704739.

Yang, B. *et al.* (2017b) 'Lead-Free, Air-Stable All-Inorganic Cesium Bismuth Halide Perovskite Nanocrystals', *Angewandte Chemie*, 129(41), pp. 12645–12649. Available at: https://doi.org/10.1002/ange.201704739.

Yaseen, D.A. and Scholz, M. (2016) 'Shallow pond systems planted with Lemna minor treating azo dyes', *Ecological Engineering*, 94, pp. 295–305. Available at: https://doi.org/10.1016/j.ecoleng.2016.05.081.

Yi, Z. *et al.* (2019) 'Will organic–inorganic hybrid halide lead perovskites be eliminated from optoelectronic applications?', *Nanoscale Advances*, 1(4), pp. 1276–1289. Available at: https://doi.org/10.1039/C8NA00416A.

Yousef, A. *et al.* (2022a) 'Recent Progress in WS2-Based Nanomaterials Employed for Photocatalytic Water Treatment', *Catalysts*, 12(10), p. 1138. Available at: https://doi.org/10.3390/catal12101138.

Yousef, A. *et al.* (2022b) 'Recent Progress in WS2-Based Nanomaterials Employed for Photocatalytic Water Treatment', *Catalysts*, 12(10), p. 1138. Available at: https://doi.org/10.3390/catal12101138.

Zafar, Z., Fatima, R. and Kim, J.-O. (2021) 'Experimental studies on water matrix and influence of textile effluents on photocatalytic degradation of organic wastewater using Fe–TiO2 nanotubes: Towards commercial application', *Environmental Research*, 197, p. 111120. Available at: https://doi.org/10.1016/j.envres.2021.111120.

Zeta potential - An introduction in 30 minutes (2020) *Malvern Panalytical*. Available at: https://www.malvernpanalytical.com/en/learn/knowledge-center/technical-notes/TN101104ZetaPotentialIntroduction (Accessed: 27 March 2023).

Zhang, C. *et al.* (2023) ‘Based on Z-scheme heterojunction CsPbBr $_3$ /UiO-66 composite photocatalytic degradation’, *Applied Organometallic Chemistry*, 37(7). Available at: https://doi.org/10.1002/aoc.7122.

Zhang, Q. *et al.* (2020a) ‘Enhanced Photocatalytic Property of γ-CsPbI $_3$ Perovskite Nanocrystals with WS $_2$’, *ACS Sustainable Chemistry & Engineering*, 8(2), pp. 1219–1229. Available at: https://doi.org/10.1021/acssuschemeng.9b06451.

Zhang, Q. *et al.* (2020b) ‘Enhanced Photocatalytic Property of γ-CsPbI3 Perovskite Nanocrystals with WS2’, *ACS Sustainable Chemistry and Engineering*, 8(2), pp. 1219–1229. Available at: https://doi.org/10.1021/acssuschemeng.9b06451.

Zhang, Y. *et al.* (2020) ‘A “Tips and Tricks” Practical Guide to the Synthesis of Metal Halide Perovskite Nanocrystals’, *Chemistry of Materials*, 32(13), pp. 5410–5423. Available at: https://doi.org/10.1021/acs.chemmater.0c01735.

Zhang, Z. *et al.* (2019) ‘Stable and Highly Efficient Photocatalysis with Lead-Free Double-Perovskite of Cs $_2$ AgBiBr $_6$’, *Angewandte Chemie International Edition*, 58(22), pp. 7263–7267. Available at: https://doi.org/10.1002/anie.201900658.

Zhu, S. and Wang, D. (2017a) ‘Photocatalysis: Basic Principles, Diverse Forms of Implementations and Emerging Scientific Opportunities’, *Advanced Energy Materials*, 7(23), p. 1700841. Available at: https://doi.org/10.1002/aenm.201700841.

Zhu, S. and Wang, D. (2017b) ‘Photocatalysis: Basic principles, diverse forms of implementations and emerging scientific opportunities’, *Advanced Energy Materials*. Wiley-VCH Verlag. Available at: https://doi.org/10.1002/aenm.201700841.

Ziarani, G.M. *et al.* (2018) ‘Introduction and Importance of Synthetic Organic Dyes’, in *Metal-Free Synthetic Organic Dyes*. Elsevier, pp. 1–7. Available at: https://doi.org/10.1016/B978-0-12-815647-6.00001-7.

CHAPTER 6: CONCLUSION AND FUTURE WORK

6.1. Conclusion

This project aimed to synthesize $Cs_3Bi_2Br_9$ and WS_2 through hot-injection and colloidal synthesis, respectively, as well as create the $Cs_3Bi_2Br_9/WS_2$ heterostructure via ultrasonication. The PXRD diffraction patterns indicated that these materials were successfully synthesized as WS_2 was indexed to tungstenite (PDF 01-071-4832) and $Cs_3Bi_2Br_9$ was indexed to cesium bismuth bromide (PDF 00-044-0714). The PXRD spectrum for $Cs_3Bi_2Br_9/WS_2$ matched closely with the $Cs_3Bi_2Br_9$ diffraction pattern since the heterostructure only had 4% of WS_2 present. However, traces of WS_2 were detected in the $Cs_3Bi_2Br_9/WS_2$ diffraction pattern. The EDS mapping results further confirmed the presence of WS_2. These materials were used as photocatalysts for heterogeneous photodegradation of anionic (methyl red) and cationic (rhodamine B) dyes. Additionally, the project aimed to determine the effect of H_2O_2 on photocatalytic reactions. Direct (UV) and indirect (UV/H_2O_2) photolysis reactions were conducted to examine the degradation of MR and RhB dyes in the absence of the synthesized photocatalysts and the presence of both a photocatalyst and a strong oxidizing agent. The photocatalysts underwent characterization using PXRD, UV-vis spectroscopy, zeta potential, TEM, and SEM-EDS.

The degradation percentages of MR and RhB were found to be 2.68% and 3.10%, respectively, when subjected to direct photolysis for 2 hours. These results can be attributed to the presence of N-functional groups in the dyes, which render them resistant to photolytic degradation. However, the addition of 0.3519 M H_2O_2 significantly improved the photolysis results. The degradation efficiencies (DE%) increased to 40.59% and 52.72% for MR and RhB, respectively, and the pseudo-first-order rate constant experienced a 14-fold increase for MR and a 23-fold increase for RhB. This improvement can be attributed to the powerful oxidizing properties of H_2O_2, enabling it to cleave the bonds in the dye molecules. Heterogeneous photodegradation reactions were conducted to compare the efficacy of the metal halide perovskite, $Cs_3Bi_2Br_9$, and the MHP/TMDC heterostructure, $Cs_3Bi_2Br_9/WS_2$ at 20 PPM dye concentration. The optimum DE% values for 20 PPM RhB were 70.28% and 96.51%

for $Cs_3Bi_2Br_9$ (2.4 mg/mL) and $Cs_3Bi_2Br_9/WS_2$ (2.4 mg/mL), respectively. For 20 PPM MR, the optimum DE% values were 54.32% and 89.36% for $Cs_3Bi_2Br_9$ (2.4 mg/mL) and $Cs_3Bi_2Br_9/WS_2$ (2.4 mg/mL), respectively. Optimization studies were carried out to determine the optimal catalyst loading, initial dye concentration, and pH conditions for the heterogeneous reactions. The kinetics and adsorption isotherms were also determined and are summarized in **Table 6.1**, along with the optimal conditions.

Table 6.1: Optimum results summary table

Dye	Catalyst	Catalyst loading (mg/ml)	Initial dye concentration (ppm)	pH	DE%	Adsorption isotherm	Kinetics
MR	$Cs_3Bi_2Br_9$	1.6	20	5.5	74.04	Redlich-Peterson	Pseudo second order
	$Cs_3Bi_2Br_9/WS_2$	2.4	20	2	97.48	Temkin	Pseudo first order
RhB	$Cs_3Bi_2Br_9$	1.6	20	7	97.60	Redlich-Peterson	Pseudo second order
	$Cs_3Bi_2Br_9/WS_2$	1.6	20	2	97.64	Langmuir	Intraparticle diffusion

After adding H_2O_2 to the optimized reactions, remarkable results above 90% were achieved for all reactions within just 40 minutes of light exposure. Although there were some interferences from oxygen-containing chemicals, the COD results demonstrated that the water quality improved after the degradation of the dyes. The mass spectroscopy results provided evidence that the dyes were effectively broken down during the optimized degradation reactions. Following the degradation process, the $Cs_3Bi_2Br_9$ and $Cs_3Bi_2Br_9/WS_2$ catalysts underwent analysis using PXRD and UV-vis techniques. The obtained results revealed that the heterostructure ($Cs_3Bi_2Br_9/WS_2$) exhibited greater stability compared to $Cs_3Bi_2Br_9$. Moreover, the heterostructure displayed superior degradation performance when compared to $Cs_3Bi_2Br_9$ this could be due to the addition of WS_2 which is a multilayered material that increases the active

sites for photocatalytic activity and improves charge separation. Therefore, based on the findings, it can be concluded that the $Cs_3Bi_2Br_9/WS_2$ heterostructure outperforms $Cs_3Bi_2Br_9$ in terms of both stability and degradation performance. Thus, $Cs_3Bi_2Br_9/WS_2$ has the potential to serve as a base for future inexpensive photocatalysts for the photodegradation of dyes from the textile industry.

6.2. Future work

1. Test the effects of different water matrices, such as ultrapure water, deionized water, tap water, and industrial dye effluent, on the dye degradation efficacy of the photocatalysts.
2. Investigate mixed halide metal perovskites to determine their impact on the stability and performance of metal halide perovskites.
3. Vary the molar percentage of WS_2 to find the optimal co-catalyst molar percentage.
4. Study the effects of varying H_2O_2 concentrations added to the photocatalytic reactions.
5. Degrade dyes from other classes such as disperse, direct, and reactive dyes using these materials to assess the dye degradation effectiveness of the photocatalysts across various classes.
6. Test the photocatalysts' efficacy in degrading a mixture of dyes by simulating industrial dye effluents containing a mixture of dyes, thus providing insights into their real-world applicability.
7. Produce the MHP/TMDC heterostructures using different techniques such as one-pot synthesis, ball-milling, electrospinning, and sintering.
8. Investigate the effects of dye solution volume on the photocatalytic reactions.
9. Conduct temperature studies or vary the light intensity to assess their impact on the photocatalytic reactions.